

Many-Body Perturbation Theory Approach to Raman Spectroscopy and Its Application to 2D Materials

Von der Fakultät für Mathematik, Informatik und Naturwissenschaften der RWTH
Aachen University zur Erlangung des akademischen Grades eines Doktors der
Naturwissenschaften genehmigte Dissertation

vorgelegt von

Master of Science RWTH
Sven Reichardt
aus Mönchengladbach

Berichter: Universitätsprofessor Dr. sc. ETH Christoph Stampfer
Universitätsprofessor Dr. rer. nat. Ludger Wirtz

Tag der mündlichen Prüfung: 20.04.2018

Diese Dissertation ist auf den Internetseiten der Universitätsbibliothek online
verfügbar.

Dissertation defence committee:

Prof. Dr. Ludger Wirtz, dissertation supervisor, assessor
Professor, Université du Luxembourg

Prof. Dr. Christoph Stampfer, dissertation supervisor, assessor
Professor, RWTH Aachen University

Prof. Dr. Thomas Schmidt, Chairman
Associate Professor, Université du Luxembourg

Prof. Dr. Claudia Draxl
Professor, Humboldt-Universität Berlin

Prof. Dr. Riccardo Mazzarello, Vice Chairman
Professor, RWTH Aachen University

Prof. Dr. Kristian Thygesen
Professor, Technical University of Denmark



PhD-FSTC-2018-34
The Faculty of Sciences, Technology and
Communication

Fakultät für Mathematik, Informatik und
Naturwissenschaften

MANY-BODY PERTURBATION THEORY APPROACH TO RAMAN SPECTROSCOPY AND ITS APPLICATION TO 2D MATERIALS

DISSERTATION

Defence held on 20/04/2018 in Luxembourg

to obtain the degree of

DOCTEUR DE L'UNIVERSITÉ DU LUXEMBOURG

EN PHYSIQUE

and

DOKTOR DER NATURWISSENSCHAFTEN

(DR. RER. NAT.)

by

Master of Science RWTH

Sven REICHARDT

Born on 9 August 1990 in Mönchengladbach (Germany)

Abstract

Raman spectroscopy has become one of the most important techniques for the characterization of materials, as it allows the simultaneous probing of several properties, such as electronic and vibrational excitations, at once. This versatility, however, makes its theoretical description very challenging and, up to now, no fully satisfactory and general way for the calculation of Raman spectra from first principles exists. In this thesis, we aim to fill this gap and present a coherent theory of Raman scattering within the framework of many-body perturbation theory. We develop a novel and general, correlation function-based approach for the calculation of Raman scattering rates that can potentially also be applied to ultra-fast Raman spectroscopy out of equilibrium. Besides these theoretical developments, we present concrete computational recipes for the calculation of Raman intensities that allow the inclusion of both excitonic effects and non-adiabatic effects of lattice vibrations. The latter has so far not been possible with state-of-the-art methods, which can only take into account one of the two effects. As a first test case, we apply our theory to graphene, for which we use it to study the laser frequency and Fermi energy dependence of the Raman G -peak intensity. The flexibility of our approach also allows us to demonstrate that non-resonant processes and quantum mechanical interference effects play a significant role in Raman scattering. This applies not only to graphene but also to other two-dimensional materials of current interest, such as MoTe_2 and MoS_2 . In addition to the development of a consistent and comprehensive description of Raman scattering, we derive a novel approach for the calculation of phonon frequencies and the screened electron-phonon coupling. It can be applied also to strongly correlated systems, for which the currently used methods are not entirely satisfactory or insufficient. Our new method goes beyond the limitations of the methods currently in use and will permit the computation of phonon-related quantities also in systems with strong correlation effects such as Kohn anomalies (e.g., graphene) or Peierls instabilities. Lastly, we present work on the application of (magneto-)Raman spectroscopy as a probe for many-body effects in graphene. Here we focus on the description of the phenomenon of magneto-phonon resonances and how it can be used to probe electronic excitation energies and to extract electron and phonon lifetimes.

Zusammenfassung

Raman-Spektroskopie ist zu einer der bedeutendsten Methoden zur Materialcharakterisierung geworden, da sie die gleichzeitige Untersuchung von mehreren Eigenschaften, wie z. B. elektronische Anregungen und Gitterschwingungen, erlaubt. Diese Vielseitigkeit macht ihre theoretische Beschreibung jedoch sehr herausfordernd, sodass bis heute kein allgemeiner *ab initio* Zugang existiert. Mit dieser Arbeit versuchen wir diese Lücke zu schließen und stellen eine kohärente Theorie der Raman-Streuung im Rahmen der Vielteilchenstörungstheorie vor. Wir entwickeln einen neuartigen Zugang für die Berechnung von Raman-Streuratens, der potenziell auch auf ultra-schnelle Raman-Streuung außerhalb des Gleichgewichts angewandt werden kann. Neben dieser theoretischen Arbeit präsentieren wir auch konkrete Ausdrücke für die computergestützte Berechnung von Raman-Intensitäten, die es erlauben, sowohl exzitonische Effekte als auch dynamisch behandelte Gitterschwingungen in die Rechnung miteinzubeziehen. Die gleichzeitige Berücksichtigung letzterer Aspekte ist mit bisherigen Methoden nicht möglich gewesen. Als ersten Test wenden wir unsere Theorie auf Graphen an und untersuchen die Abhängigkeit der Intensität der Raman G-Linie von der Laser- und Fermi-Energie. Unser flexibler Zugang erlaubt es uns außerdem zu zeigen, dass nicht-resonante Prozesse und Quanteninterferenzeffekte eine wesentliche Rolle im Raman-Streuprozess spielen. Dies trifft auch auf andere zweidimensionale Materialien zu, wie z. B. MoTe_2 und MoS_2 , die im Fokus der aktuellen Forschung stehen. Zusätzlich zur Entwicklung einer umfassenden Beschreibung der Raman-Streuung leiten wir einen neuartigen Ansatz zur Berechnung von Phononenfrequenzen und der abgeschirmten Elektron-Phonon-Kopplung her. Dieser kann auch auf stark korrelierte Systeme angewandt werden, für die die bislang benutzten Methoden nicht zufrieden stellend sind. Unsere neue Methode erlaubt es, die Einschränkungen aktueller Methoden zu überwinden, auch in Systemen mit starken Korrelationseffekten wie z. B. Kohn-Anomalien (wie z. B. in Graphen) oder Peierls-Instabilitäten. Zum Abschluss untersuchen wir Vielteilcheneffekte in Graphen mittels (Magneto-)Raman-Spektroskopie. Hierbei liegt der Schwerpunkt auf Magneto-Phonon-Resonanzen und wie diese dazu genutzt werden können, um elektronische Anregungsenergien und die Lebenszeiten von Elektronen und Phononen zu untersuchen.

Contents

1	Introduction	1
1.1	Aims and scope of this work	8
1.2	Structure of the thesis	11
2	Light Scattering by Matter	15
2.1	Quantization of the electromagnetic field	16
2.2	Light-matter coupling	19
2.3	Correlation function approach to inelastic light scattering	21
2.4	Generalized Fermi's golden rule approach to Raman scattering	28
3	Electronic Structure	33
3.1	The clamped nuclei approximation	34
3.2	Kohn-Sham density functional theory	36
3.3	Many-particle electronic correlation functions	49
3.3.1	General considerations and one-particle Green's function	49
3.3.2	Two-particle correlation function	60
4	Phonons	75
4.1	The adiabatic, Born-Oppenheimer approximation	76
4.2	The harmonic approximation	82
4.3	Phonons in density functional perturbation theory	88
4.4	Phonons from many-body perturbation theory	96

4.5	Physical interpretation and relation between different approximations for force constants	104
5	Electron-Phonon Interaction	113
5.1	Electron-phonon interaction Hamiltonian and Feynman rules	115
5.1.1	Electronic Hamiltonian	116
5.1.2	Phonon Hamiltonian	118
5.1.3	Electron-phonon interaction Hamiltonian	119
5.1.4	Feynman rules for perturbation theory	120
5.2	Screened electron-phonon coupling	124
5.3	Phonons beyond the adiabatic, Born- Oppenheimer approximation	134
6	One-Phonon Raman Spectroscopy	149
6.1	One-phonon Raman scattering in perturbation theory	150
6.1.1	LSZ reduction formula	151
6.1.2	Reduced scattering matrix element	160
6.2	Application to graphene: laser and Fermi energy dependence of the Ra- man scattering rate and importance of quantum interference effects . .	173
6.2.1	Theoretical details	174
6.2.2	Computational details	177
6.2.3	Laser energy dependence	179
6.2.4	Fermi energy dependence	186
6.2.5	Relevant states for the G -peak process	191
6.2.6	Summary of the results for graphene	195
6.3	Application to other 2D materials: triple-layer MoTe_2 and single-layer MoS_2	195
6.3.1	Triple-layer MoTe_2	196
6.3.2	Single-layer MoS_2	197
7	Magneto-Raman Spectroscopy for the Characterization of Graphene	201

7.1	Theory of magneto-phonon resonances in graphene	203
7.1.1	Tight-binding model for graphene	204
7.1.2	Landau levels in graphene	210
7.1.3	Magneto-phonon resonances	214
7.2	Magneto-phonon resonances as a probe for many-body effects and lifetimes	222
7.2.1	Magneto-phonon resonances as a probe for many-body effects	222
7.2.2	Tuning many-body effects in graphene	229
7.2.3	Probing electronic and phonon lifetimes with magneto-phonon resonances	240
8	Conclusions and Outlook	249
8.1	Main results of this work	249
8.2	Outlook	254
	List of Publications	257
	Bibliography	261
	Acknowledgments	281

Chapter 1

Introduction

Since its first exfoliation and the demonstration of its high electronic mobility and tunable conductivity in 2004 [1], graphene, a one-atom-thick layer of graphite, has received an ever increasing amount of attention. The reason for this lies in its remarkable electronic [2] and mechanical [3] properties. However, despite its many virtues, graphene is not without flaws when it comes to practical applications and functional devices. For example, its lack of an electronic band gap prohibits its usage as a logic transistor and all approaches to induce a band gap whilst retaining its outstanding electronic mobility have not led to a competitive on/off ratio [4].

This has sparked a desire for a “graphene-like” material with a sizable band gap. Combined with the increasing amount of expertise in exfoliating or growing graphene and in graphene device fabrication, it has led to a strong increase in attention devoted to the study of other two-dimensional materials [5, 6]. These materials, like graphene, consist of thin layers of atoms that are weakly held together by van der Waals forces, while the bonds between the atoms within each layer are of a strong, covalent nature. Two examples of this kind of materials are the insulating hexagonal boron nitride (hBN) and the family of transition metal dichalcogenides (TMDs), the most widely studied of which is the semi-conducting molybdenum disulfide (MoS_2) [7].

Although these materials are already of interest on their own, the most intriguing aspect of two-dimensional materials is the possibility to stack layers of different materials. Such a heterostructure can have new and sometimes surprising properties. One

of the earliest and by now widely used examples of these kinds of heterostructures is a stack of hexagonal boron nitride and graphene [8], in which boron nitride layers serve as a substrate and cover for a single layer of graphene. The latter is thereby effectively shielded from detrimental environmental influences, yet still remains atomically flat due to the flatness of the hBN surface. Furthermore, by carefully adjusting the orientation of the graphene lattice with respect to the underlying hBN lattice, Moiré patterns can be created, which modify the electronic properties of the heterostructure considerably [9]. The possibility to influence the electronic properties of graphene by putting it on an hBN substrate is just one example of tailoring the properties of these van der Waals heterostructures to one's needs. More sophisticated examples that also allow the fine-tuning of the heterostructure's properties soon followed [10, 11] and today there is a large amount of effort being invested into the research of such tailor-made van der Waals heterostructures [12].

However, the option to fabricate a wide variety of heterostructures with a correspondingly wide spectrum of electronic and mechanical properties comes with a need for a fast, effective, reliable, and minimally invasive method to characterize them. Transport measurements can serve as a comprehensive way to study the electronic properties of such devices. However, they necessitate further processing of the material stack, for example, due to the necessity of contacting the sample. As such, they require a sizable amount of effort and are also highly invasive. A far less invasive way for characterization is optical spectroscopy. Already optical absorption and photoluminescence experiments can yield a certain amount of information about optical and electronic properties. However, the most important optical tool for sample characterization nowadays is Raman spectroscopy, a light scattering experiment in which a part of the incident light is scattered inelastically. This effect was first observed and reported on in a series of Letters by C. V. Raman and K. S. Krishnan in 1928 [13–15].

In their original experiments, Raman and Krishnan observed that the spectrum of light from a quartz vapor lamp scattered by a fluid features lines that are not present in the spectrum of the unscattered light (see Fig. 1.1a). Already in their first Letter, Raman and Krishnan linked the appearance of these additional spectral lines to

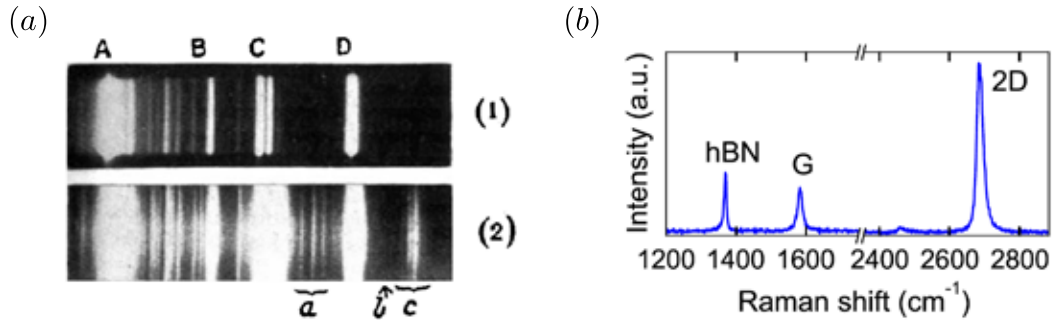


Figure 1.1: **Raman spectroscopy in the past and present.** (a) Original Raman experiment by Raman and Krishnan (1928). Panel (1) shows the spectrum of light emitted from a quartz vapor lamp whereas panel (2) shows the spectrum of the same light scattered by a fluid. (b) Modern-day Raman spectrum of an hBN-graphene-hBN heterostructure (2015). Shown is the recorded intensity of the scattered light as a function of the difference of the inverse wave lengths of the incoming and scattered light. (Figure of panel (a) reprinted by permission from Springer Nature from Raman, C. V. *et al.*, *Nature* **121**, 711 (1928). Copyright 1928 by Springer Nature. Figure of panel (b) reprinted from Neumann, C. *et al.*, *Appl. Phys. Lett.* **107**, 233105 (2015), with the permission of AIP Publishing.)

“fluctuations [of the atoms] from their normal state” [13]. Their further, more detailed studies supported this assertion as they noticed that “the diminution in frequency is of the same order of magnitude as the frequency of the molecular infra-red absorption line” [15]. This was even further supported by the fact that the shift in wavelength differed from molecule to molecule. They also noted that the frequency of the infra-red absorption line was determined by the molecule’s vibrational eigenfrequencies. By combining this information, they were able to establish a first, coherent picture of the inelastic scattering process which is nowadays known as *Raman scattering*: the incoming quantum of light interacts with the molecule and is scattered inelastically, with the lost energy having gone into a molecular excitation. This picture, for which Raman received the Nobel prize in 1930, is still the established interpretation used today. It is one of the main reasons why Raman spectroscopy has become an indispensable tool for the characterization of a wide variety of materials and substances, as it probes both optical, electronic, and vibrational/mechanical properties at once.

Experimental techniques have advanced a lot since then and today’s Raman spectroscopy experiment most often consists of exciting the sample with a potentially tunable, monochromatic laser beam. The scattered light is typically recorded with a charge-coupled device (CCD) camera after having been directed through a diffractive grating. An example of such a Raman spectrum recorded with state-of-the-art equipment is shown in Fig. 1.1b. The modern way to display such a spectrum consists of plotting the recorded light intensity as a function of the difference of the inverse wavelengths of the incoming and the scattered light,

$$\text{Raman shift} \equiv \Delta \frac{1}{\lambda} \equiv \frac{1}{\lambda_{\text{in}}} - \frac{1}{\lambda_{\text{out}}}, \quad (1.1)$$

and is usually given in units of cm^{-1} . Depending on the number of grooves on the diffractive grating, the resolution achieved with such a setup can range up to 0.5 cm^{-1} . This is precise enough to extract some properties of the sample, such as vibration, i.e., *phonon*, frequencies and related quantities such as mechanical strain with useful accuracy.

One of the prime examples for the use of Raman spectroscopy in this respect is its utilization in the characterization of graphene [16]. The relative simplicity of graphene’s electronic and vibrational band structure leads to only a small number of sizable lines in the Raman spectrum that nevertheless contain a comparatively large amount of information. Among the properties that can be extracted from the Raman peaks of graphene are the number of layers [17, 18], the average amount of mechanical strain and its short-range fluctuations [19–25], the amount and nature of charge carrier doping [23, 26–29], and the lattice temperature [30, 31]. The use of a focused laser beam in modern-day experiments also means that these properties can be probed *locally*, in contrast to the nature of a transport experiment, which is only sensitive to *global* properties of a sample. This can be exploited in a confocal setup, in which the sample can be moved relative to the laser beam, to create entire “maps” of the strain distribution [25, 32, 33], of doping domains [29, 34], or to specifically probe the edges of a sample [18, 35, 36]. More complicated Raman setups in which the sample is also exposed to a magnetic field even permit the study of many-body effects such as electronic

correlation and of electronic and phonon lifetimes [37–49]. Beyond graphene, finally, the dependence of the Raman spectrum on the frequency of the incident light can also be used to extract information on optical transition energies, i.e., to probe excitons [50].

In order to be able to extract any of the above mentioned properties of the sample from its Raman spectrum, however, a thorough theoretical understanding is required. In the case of graphene, the theoretical modeling of Raman spectra has so far been based on tight-binding or effective, relativistic Fermi liquid models for the electronic band structure [51, 52] and semi-empirical models for the vibrational band structure and the electron-phonon coupling [53]. The actual calculation of the Raman spectrum itself has usually been done within the framework of time-dependent perturbation theory [54–59] or within a simplified “double-resonance model” [17, 60–62]. These approaches led to a detailed conceptual understanding of the Raman spectrum of graphene, which has been summarized in a number of review articles and book chapters [16, 26, 63–67].

Despite the large amount of effort devoted to the study and computation of the Raman spectrum of graphene, the theoretical description is still not in an entirely satisfactory state, neither from a conceptual point of view nor from a quantitative one. Among the open problems are a proper description of the electron-phonon coupling and the phonon dispersion as well as a more complete approach to the actual calculation of the one- and two-phonon contribution to its Raman spectrum.

In the case of the electron-phonon coupling and the phonon dispersion, the main difficulty in their description lies in the sensitive dependence of the electronic screening of the Coulomb interaction between the electrons and the nuclei on the wave vector of the phonon. At certain phonon wavelengths, this screening decreases rapidly, a phenomenon that is nowadays known as a *Kohn anomaly* [68]. The fact that the breakdown of the screening only occurs within a small region around certain critical wave vectors in wave vector (i.e., *reciprocal*) space hints at the long-range correlation origin of the anomaly. Long-range correlation effects, however, are very difficult to capture within common *ab initio* approximation schemes such as density functional perturbation theory (DFPT), which often rely on local and oversimplified descriptions of the electronic

screening. These approximations are often based on the free electron gas and thus overestimate the mobility of electrons in the lattice potential of a solid and, in consequence, their screening capabilities. So far, no fully satisfying approach has been developed to deal with this problem, which is not only relevant for graphene, but concerns any metallic material with strong correlation effects. The currently accepted best attempt to describe the phonon dispersion and the electron-phonon coupling in graphene was presented by Lazzeri *et al.* [53] and yielded results that could be reconciled with experimental data for the phonon dispersion of graphite. However, as will be discussed later on in this thesis, the approach is conceptually not entirely consistent and hence an alternative approach is required.

Concerning the calculation of the Raman spectrum of graphene itself, the currently used approaches feature similar problems or are only valid within certain boundaries, such as a limited excitation frequency range. For the case of one-phonon Raman scattering, the main theoretical works so far are those of Basko [55] and Hasdeo *et al.* [58]. Both rely on a tight-binding model for the description of the electronic band structure and the electron-phonon coupling. While this semi-empirical approach works for the phonons that can partake in one-phonon Raman scattering, both works make some approximations for the calculation of the actual Raman intensity. As a result, they are not completely general and valid over the entire range of incident light frequencies.

A similar statement holds true for the previous studies of the two-phonon part of the Raman spectrum featured in the papers by Venezuela *et al.* [56] and Herziger *et al.* [57]. From a computational point of view, these works present an excellent first attempt at a perturbative calculation of two-phonon-induced Raman intensities. However, the approximations employed therein are rather inconsistent from a theoretical perspective. Conceptually, the two main problems lie in (i) the approximation to the electron-phonon coupling, which follows the one from Lazzeri *et al.* [53] and hence involves the same problems, and in (ii) the expressions given for the actual Raman intensities. For the latter, the selected approach consists of neglecting 75% of the terms appearing in the leading order of perturbation theory and modifying the remaining expressions in order to compensate for the omitted terms. While this approach yields results that are in reasonable agreement with experiment, the applied approximations have not been ad-

dressed. It therefore still remains to be understood why such an approach can describe the Raman spectrum of graphene with reasonable accuracy.

Thus, already for the relatively simple case of graphene there are several unsolved problems regarding the calculation of the Raman spectrum. For the general case of any two-dimensional material, or indeed *any* material in general, there does not yet exist an efficient, parameter-free, and entirely comprehensive approach to the computation of resonant Raman spectra entirely from *first principles*. The two main advantages of the semi-empirical, perturbative approach applied so far to graphene – the fast, tight-binding-based model and the leading-order expansion of the perturbative series – cannot simply be applied to other, more complicated two-dimensional materials. A semi-empirical tight-binding description becomes increasingly complicated the more intertwined the electronic band structure is, to the point where it can no longer be sensibly used for systems such as multi-layered TMDs. Meanwhile, the leading-order expansion of the perturbation series is inherently unable to capture non-perturbative effects such as the formation of excitons, for which an infinite series of terms of the perturbative series needs to be summed.

Up to now, there does not yet exist a comprehensive approach to the computation of Raman scattering that is able to both capture the strong excitonic effects that are important in many low-dimensional materials and also properly take into account the screening and the inherently non-adiabatic nature of the electron-phonon coupling. Instead, several approximative approaches have been suggested and applied to a variety of materials, all of them limited to the study of the one-phonon contribution to the Raman spectrum. Among these approaches are, in increasing order of complexity and accuracy: the so-called *bond polarizability model*, in which the polarizability of the interatomic chemical bonds is parametrized and fitted to experiment [69–72]; an approach based on density functional perturbation theory for the calculation of the mixed *third derivative of the total ground state energy* with respect to two external electric fields and a lattice distortion [73, 74]; and finally the computation of the *first derivative of the dielectric susceptibility with respect to static atomic displacements* via the method of finite differences [50, 75]. It should be noted that the first two of these methods assume

static electric fields. Hence they are not applicable in the resonant regime, where the finite frequency of the incoming light is important. The third approach is able to describe these resonance effects and thus also allows the study of excitonic effects, which are dominant in 2D materials such as TMDs. It is, however, unable to capture effects due to the non-static nature of lattice vibrations. Furthermore, it is computationally very expensive as it relies on the construction of supercells.

Beyond one-phonon Raman scattering, not many works have been devoted to other mechanisms of Raman scattering so far, with the exception of the above-mentioned works on the two-phonon contribution to the Raman spectrum of graphene [56, 57]. The latter has also been studied for silicon via the computation of the second derivative of the dielectric susceptibility [76]. In addition, inelastic light scattering via the excitation of an electronic transition has been studied within a tight-binding model for graphene [77]. But so far, no unified and comprehensive theoretical approach has been suggested.

1.1 Aims and scope of this work

Up to this point, we discussed the various ways in which Raman spectroscopy can be used for sample characterization and also summarized the state-of-the-art theoretical and computational approaches to the calculation of Raman spectra. In particular, we identified the main problems and challenges that still remain to be solved in order to arrive at a general, theoretically consistent, and computationally feasible description of Raman scattering. It is the main aim of our work to significantly advance the state of the art of the theoretical and computational calculation of Raman spectra and also further contribute to the use of Raman spectroscopy as a means for sample characterization. Note that many of our results and contributions to this field have already been disseminated elsewhere¹ and this thesis itself only represents a part of our work on these topics. In this work, we focus on our most recently developed theoretical approach to Raman scattering, first computational calculations, and work on the use of Raman spectroscopy within a magnetic field for probing many-body effects in graphene.

¹A full list of our contributions can be found in the [List of Publications](#).

In regards to the latter, we have seen in the summary above that Raman spectroscopy is a very versatile tool for the characterization of materials. This is especially true for graphene, for which its phenomenology has been well understood. Here, we will further explore how Raman spectroscopy in a magnetic field (also known as *magneto-Raman spectroscopy*) can serve as a probe for many-body effects. To this end, we present results of studies done in close collaboration with an experimental group. In particular, we show how magneto-Raman spectroscopy can be used to probe electronic excitation energies. In graphene, these are conventionally described in terms of an effective Fermi velocity. The latter has been shown to diverge in the absence of a magnetic field when the charge carrier density is tuned towards the charge neutrality point [78]. In the work presented here [79], we probe the charge carrier dependence of the Fermi velocity for the first time in a finite magnetic field and show that it remains *finite*, even at the charge neutrality point. Our calculations allow us to give a simple physical picture for this behavior. The insight gained in this way may also be of use for the understanding of many-body effects in other two-dimensional materials. Finally, we also show results of a study in which we used magneto-Raman spectroscopy to probe electronic and phonon lifetimes [48].

Besides this, it is one of our main goals to address some of the open theoretical problems that plague the current theoretical approaches to the calculation of Raman spectra. As such, we will present a novel method for the calculation of Raman intensities, which is based on correlation functions. This approach permits the computation of Raman scattering rates and can be used, in principle, at finite temperature and in out-of-equilibrium situations, such as present in ultra-fast optical experiments. The main focus, however, will be on the equilibrium, zero-temperature case, for which we will apply the formalism of the Lehmann-Symanzik-Zimmermann reduction [80]. It reduces the problem of the calculation of Raman intensities to the calculation of electronic correlation functions and in this way allows us to present a concrete and practically useful approach for the general calculation of Raman scattering rates.

The perturbative technique we use moreover provides a maximum of flexibility and permits both the inclusion of excitonic effects and the correct description of the screen-

ing of the electron-phonon coupling. We thus present for the first time a concrete, practical, and sound theoretical description of one-phonon-induced Raman scattering *including both excitonic and non-static phonon effects*. The inclusion of both of the latter at the same time is not possible in currently used approaches, but can be very important for Raman scattering at the onset of resonant regime in lower-dimensional, semi-conducting systems, such as transition metal dichalcogenides. In addition, our approach also offers major computational advantages over popular finite difference methods. As such, our novel theory of Raman spectroscopy significantly advances the state of the art and allows the description of all relevant physical effects within a unified framework.

Another major aspect of the theoretical work presented in this thesis is our development of a method for the calculation of phonon frequencies and the screened electron-phonon coupling both in and beyond the adiabatic, Born-Oppenheimer approximation. As already mentioned in the introduction above, currently used methods for the calculation of phonon frequencies and the screened electron-phonon coupling either rely on density functional perturbation theory or on static, finite difference techniques that are not always entirely consistent. Furthermore, these methods struggle to deal with systems with strong correlation effects, such as Kohn anomalies. We thus developed a novel, general approach based on first principles that overcomes these limitations and paves the way, for instance, for a first consistent calculation of the phonon dispersion of graphene.

However, it is beyond the scope of this thesis to also treat a full computational implementation of all of these developments. Instead, we focus the largest part of our computational efforts on the implementation of our approach for the calculation of one-phonon-induced Raman scattering rates on the level of the *independent-particle approximation*, i.e., neglecting excitonic effects. For many materials of interest, this is already sufficient to understand the qualitative behavior of the Raman intensity as a function of various tunable parameters.

We will demonstrate the validity of our approach foremost with a detailed study of the one-phonon Raman scattering intensity of graphene. Here, we will first ana-

lyze and explain its dependence on the frequency of the incident light. Our detailed study allows us to identify and investigate some of the key concepts underlying the microscopic description of Raman scattering: the presence of quantum interference effects and approximate symmetries. The former have been probed experimentally via tuning of an external electro-chemical potential [81] and our approach enables us to study this dependence on the variation of the Fermi level *ab initio*. In particular, our flexible approach allows us to study the *combined* dependence of the Raman intensity on the excitation energy and the Fermi level. Finally, we are able to address the open question of the importance of the contributions of non-resonant electronic transitions to the Raman intensity. Concretely, we will demonstrate that, contrary to the common belief that only resonant transitions contribute significantly, in graphene, a large range of transitions is important, which is again the result of quantum interference effects.

We have also applied the same analysis techniques to the case of transition metal dichalcogenides, in particular triple-layer MoTe₂ [50], for which we will summarize our most important findings. Lastly, we will also present preliminary results of ongoing work on the comparison of our new perturbative approach to the established method of finite differences of the transverse dielectric susceptibility for the case of MoS₂ [82]. As these results have already been partly disseminated elsewhere [50], we will keep the discussion of these two topics brief.

1.2 Structure of the thesis

Although we have already outlined some of the contents of this thesis in the previous section, we still want to give a more detailed overview over its structure.

We start with a discussion of light scattering by matter in Chapter 2. After reviewing the purely quantum mechanical description of free electromagnetic fields and their coupling to matter, we present our original work on the derivation of a general, correlation function-based approach to light scattering. As this approach is currently unfeasible to for a computational implementation, we also present work on an approach based on a generalized version of Fermi's golden rule. This method allows us to give concrete

recipes for the computation of Raman scattering rates for one-phonon-induced Raman scattering in the second half of this thesis.

Having discussed the description of free electromagnetic fields and their coupling to matter, we will treat the matter system in more detail starting with Chapter 3. There, we discuss the treatment of the electron-nuclei system in the clamped nuclei approximation. To obtain an effective description of a system of strongly interacting electrons, we will make use of density functional theory (DFT) within the Kohn-Sham scheme. To this end, we discuss the Kohn-Sham ansatz to density functional theory and briefly review common approximations for effective exchange-correlation potentials. The chapter concludes with a perturbative treatment of electronic correlation functions, which play an important role in all further topics presented in this thesis.

After this discussion of a purely electronic system, we will show how an effective description of the system of interacting nuclei can be obtained within the adiabatic, Born-Oppenheimer approximation in Chapter 4. Similarly to how the Kohn-Sham ansatz yields an effective description of the electronic system, we will review the harmonic approximation for the adiabatic potential for the nuclei, which leads to the notion of phonons. We then briefly review the density functional perturbation theory (DFPT) method for the calculation of the effective, harmonic potential. It is a computationally efficient way to gain a first, and in not too strongly correlated systems also accurate, estimate of the phonon frequencies. However, as there is currently no method available to calculate accurate phonon frequencies in strongly correlated systems, we will present a novel way to compute the exact phonon frequencies from many-body perturbation theory (MBPT). In the final section of this chapter, we will establish a link between our new, MBPT-based approach and the approximative DFPT method. Furthermore, we will discuss and compare a few other approximations for the calculation of adiabatic phonon frequencies.

In Chapter 5, we will go beyond the adiabatic approximation and return to the full electron-nuclei Hamiltonian. By rewriting it in a basis of phonon and Kohn-Sham electron states, we identify the electron-phonon, electron-electron, and phonon-phonon interacting Hamiltonians, which will serve as the basis for a perturbative treatment

of the fully interacting electron-nuclei system. One of the main results presented in this chapter is the derivation of a description of the screened electron-phonon coupling from MBPT. The diagrammatic description will also be compared to the treatment of the screening in DFPT, which is known to underestimate the screened electron-phonon coupling in strongly correlated systems such as graphene. Finally, we will discuss the effects of the non-adiabatic electron-phonon interaction on the exact phonon frequencies. The main focus here will lie on the a discussion of the exact one-phonon Green's function and the calculation of phonon frequencies beyond the Born-Oppenheimer approximation.

After the discussion of the basic theory and suggested improvements to the theory of the coupled electron-nuclei system, we move on to the description of Raman spectroscopy in Chapter 6, which comprises the heart of this thesis. Here, we discuss the analytical and computational calculation of one-phonon-induced Raman intensities from first principles. We start by deriving an analytical expression for the scattering matrix element in terms of a correlation function via the Lehmann-Symanzik-Zimmermann reduction formula. The needed correlation function will then be calculated diagrammatically, which leads to an explicit formula for the one-phonon Raman scattering rate that includes the correct screening of the electron-phonon interaction and takes into account excitonic effects. In addition to the theoretical developments, we also present results of concrete calculations on the level of the independent-particle approximation. Here, the full power of the perturbative formalism will be put to use in the study of the one-phonon Raman intensity of graphene. In this context, we study the laser and Fermi energy dependence of the Raman intensity and investigate the role of quantum interference effects, which play an important role in one-phonon Raman scattering in general. In the final section of this chapter, we summarize our collaborative work on the frequency dependence of the Raman spectrum of triple-layer MoTe_2 . Lastly, we briefly present ongoing work on the numerical comparison of the perturbative and finite difference methods for the calculation of Raman intensities for single-layer MoS_2 .

In the penultimate chapter of this thesis, Chapter 7, we will study the use of Ra-

man spectroscopy as a tool for sample characterization, using graphene as an example. We will focus on how Raman spectroscopy in a magnetic field can be used to examine many-body interaction effects. To this end, we use the phenomenon of magneto-phonon resonances (MPRs) as a probe and study many-body effects on the position and width of the one-phonon-induced Raman peak of graphene. After summarizing the theoretical background, we present results of a joint experimental and theoretical study of the effects of electron-electron interaction on the electronic band structure of graphene. Furthermore, we will show how MPRs can serve as a probe for electron and phonon lifetimes.

Finally, this thesis concludes with Chapter 8, in which we summarize the most important results presented in this thesis and point out various avenues for future research.

Chapter 2

Light Scattering by Matter

The focus of this chapter will be the derivation of a general and computationally feasible approach to Raman scattering, i.e., the inelastic scattering of light by matter. The main result presented here is *a novel and general correlation-function-based approach to Raman scattering* that, in principle, will allow the calculation of the Raman scattering rate for arbitrarily short time scales and out-of-equilibrium conditions and furthermore automatically takes into account all possible excitations of the matter system. However, as the general, non-equilibrium, and ultra-short time scale case is beyond the scope of this thesis, we will also offer *an alternative approach based on a generalization of Fermi's golden rule*. This approach is computationally feasible to realize and in addition allows the inclusion of only specific contributions to the Raman spectrum, by selectively computing only the desired contributions of matter excitations to the scattering rate. It hence permits the separate study of different mechanisms for inelastic light scattering, such as phonon-induced or electronic excitation/exciton-induced Raman scattering.

We employ an entirely quantum mechanical formalism to light scattering and will describe both the light and the matter degrees of freedom within the framework of quantum mechanics. As such, we will at first briefly review the quantization of the electromagnetic field before discussing its coupling to a system consisting of a fixed number of interacting electrons and nuclei. The final two sections contain original work on the derivation of the correlation function-based approach to Raman scattering and the alternative formalism based on a generalized version of Fermi's golden rule, which

is computationally feasible to realize.

2.1 Quantization of the electromagnetic field

We start with a brief review of the quantization of the electromagnetic field. We will only sketch the most important steps and introduce the quantities and notations needed for the following discussions. For a more comprehensive treatment, including a discussion of the subtleties associated with the quantization of fields describing massless particles of spin higher than 1/2, the reader is referred to the literature [83].

Since we are interested in the quantization of the free electromagnetic field, we start from Maxwell's equations in vacuum:¹

$$\begin{aligned} \nabla \cdot \mathbf{E} &= 0, & \nabla \cdot \mathbf{B} &= 0, \\ \nabla \times \mathbf{B} - \frac{1}{c} \frac{\partial}{\partial t} \mathbf{E} &= 0, & \nabla \times \mathbf{E} + \frac{1}{c} \frac{\partial}{\partial t} \mathbf{B} &= 0. \end{aligned} \quad (2.1)$$

These equations can be partially decoupled by introducing scalar and vector potentials via

$$\mathbf{B}(\mathbf{r}, t) = \nabla \times \mathbf{A}(\mathbf{r}, t), \quad \mathbf{E}(\mathbf{r}, t) = -\frac{1}{c} \frac{\partial}{\partial t} \mathbf{A}(\mathbf{r}, t) - \nabla \phi(\mathbf{r}, t). \quad (2.2)$$

The four Maxwell equations then reduce to a set of two equations only:

$$\begin{aligned} \nabla^2 \phi + \frac{1}{c} \frac{\partial}{\partial t} (\nabla \cdot \mathbf{A}) &= 0, \\ \nabla^2 \mathbf{A} - \frac{1}{c^2} \frac{\partial^2}{\partial t^2} \mathbf{A} - \nabla \left(\frac{1}{c} \frac{\partial}{\partial t} \phi + \nabla \cdot \mathbf{A} \right) &= 0. \end{aligned} \quad (2.3)$$

In order to simplify these equations even further, we note that the set of potentials (ϕ, \mathbf{A}) is not unique. Any other set (ϕ', \mathbf{A}') that is related to (ϕ, \mathbf{A}) by a *gauge transformation*

$$\phi'(\mathbf{r}, t) = \phi(\mathbf{r}, t) - \frac{1}{c} \frac{\partial}{\partial t} \chi(\mathbf{r}, t), \quad \mathbf{A}'(\mathbf{r}, t) = \mathbf{A}(\mathbf{r}, t) + \nabla \chi(\mathbf{r}, t), \quad (2.4)$$

¹We use Gaussian units for electrodynamics, with the symbol c representing the speed of light in vacuum.

with an arbitrary function $\chi(\mathbf{r}, t)$, leads to the same electromagnetic fields $\mathbf{E}(\mathbf{r}, t)$ and $\mathbf{B}(\mathbf{r}, t)$. We can use this gauge freedom to demand that the vector potential $\mathbf{A}(\mathbf{r}, t)$ obey the *Coulomb gauge* condition

$$\nabla \cdot \mathbf{A}(\mathbf{r}, t) = 0. \quad (2.5)$$

In this gauge, Eq. 2.3 reduces to

$$\begin{aligned} \nabla^2 \phi &= 0, \\ \nabla^2 \mathbf{A} - \frac{1}{c^2} \frac{\partial^2}{\partial t^2} \mathbf{A} - \nabla \left(\frac{1}{c} \frac{\partial}{\partial t} \phi \right) &= 0. \end{aligned} \quad (2.6)$$

If we further demand that the scalar potential $\phi(\mathbf{r}, t)$ vanish for $|\mathbf{r}| \rightarrow \infty$, then Laplace's equation for $\phi(\mathbf{r}, t)$ has the unique solution $\phi(\mathbf{r}, t) \equiv 0$. In this case then, the vector potential obeys the homogeneous wave equation

$$\left[\frac{1}{c^2} \frac{\partial^2}{\partial t^2} - \nabla^2 \right] \mathbf{A}(\mathbf{r}, t) = 0. \quad (2.7)$$

Note that due to the Coulomb gauge condition, only two of the three components of $\mathbf{A}(\mathbf{r}, t)$ are independent. If we treat the system as being embedded in a large but finite volume V , the general solution for the equation of motion for $\mathbf{A}(\mathbf{r}, t)$ reads:

$$\mathbf{A}(\mathbf{r}, t) = \frac{1}{\sqrt{V}} \sum_{\mathbf{k}, \mu} \left(a_{\mathbf{k}, \mu} \boldsymbol{\epsilon}_{\mathbf{k}, \mu} e^{i(\mathbf{k} \cdot \mathbf{r} - \omega_{\mathbf{k}} t)} + a_{\mathbf{k}, \mu}^* \boldsymbol{\epsilon}_{\mathbf{k}, \mu}^* e^{-i(\mathbf{k} \cdot \mathbf{r} - \omega_{\mathbf{k}} t)} \right), \quad (2.8)$$

where $\omega_{\mathbf{k}} \equiv c|\mathbf{k}|$ and $a_{\mathbf{k}, \mu} \in \mathbb{C}$. The sums run over all possible wave vectors \mathbf{k} that are compatible with the boundary condition $\mathbf{A}(\mathbf{r}, t)|_{\partial V} \equiv \mathbf{0}$ and over the two possible polarizations labeled by μ and described by two orthonormal vectors $\boldsymbol{\epsilon}_{\mathbf{k}, \mu=1,2}$ that obey $\mathbf{k} \cdot \boldsymbol{\epsilon}_{\mathbf{k}, \mu=1,2} = 0$ by virtue of the Coulomb gauge condition. In terms of the vector

potential and the eigenmodes, the Hamilton function for light reads [84]:

$$\begin{aligned}
H_L &= \int d^3r \frac{1}{8\pi} [(\mathbf{E}(\mathbf{r}, t))^2 + (\mathbf{B}(\mathbf{r}, t))^2] \\
&= \int d^3r \frac{1}{8\pi} \left[\left(\frac{1}{c} \frac{\partial}{\partial t} \mathbf{A}(\mathbf{r}, t) \right)^2 + (\nabla \times \mathbf{A}(\mathbf{r}, t))^2 \right] \\
&= \sum_{\mathbf{k}, \mu} \frac{\omega_{\mathbf{k}}^2}{2\pi c^2} a_{\mathbf{k}, \mu}^* a_{\mathbf{k}, \mu}.
\end{aligned} \tag{2.9}$$

In order to pass to the quantum theory, we promote H_L to an operator \hat{H}_L , i.e., we let $a_{\mathbf{k}, \mu} \rightarrow \alpha_{\mathbf{k}, \mu} \hat{a}_{\mathbf{k}, \mu}$ and $a_{\mathbf{k}, \mu}^* \rightarrow \alpha_{\mathbf{k}, \mu}^* \hat{a}_{\mathbf{k}, \mu}^\dagger$, where $\alpha_{\mathbf{k}, \mu}$ is a complex constant, chosen such that the Hamiltonian takes on the canonical form

$$\hat{H}_L = \sum_{\mathbf{k}, \mu} \hbar \omega_{\mathbf{k}, \mu} \hat{a}_{\mathbf{k}, \mu}^\dagger \hat{a}_{\mathbf{k}, \mu}, \tag{2.10}$$

with \hbar being the reduced Planck constant. This determines the constant up to a phase (which we set to zero) to $\alpha_{\mathbf{k}, \mu} = \sqrt{(2\pi\hbar c^2)/\omega_{\mathbf{k}}}$. In the following we will simplify the notation by adopting units in which $\hbar \equiv 1$. The operators $\hat{a}_{\mathbf{k}, \mu}$ and $\hat{a}_{\mathbf{k}, \mu}^\dagger$ are defined to obey the canonical commutation relations

$$[\hat{a}_{\mathbf{k}, \mu}, \hat{a}_{\mathbf{k}', \mu'}] = [\hat{a}_{\mathbf{k}, \mu}^\dagger, \hat{a}_{\mathbf{k}', \mu'}^\dagger] = 0, \quad [\hat{a}_{\mathbf{k}, \mu}, \hat{a}_{\mathbf{k}', \mu'}^\dagger] = \delta_{\mathbf{k}, \mathbf{k}'} \delta_{\mu, \mu'}. \tag{2.11}$$

The vector potential also becomes an operator, which, in the Schrödinger picture, reads:

$$\hat{\mathbf{A}}(\mathbf{r}) = \sum_{\mathbf{k}, \mu} \sqrt{\frac{4\pi c^2}{2\omega_{\mathbf{k}} V}} \left(\hat{a}_{\mathbf{k}, \mu} \boldsymbol{\epsilon}_{\mathbf{k}, \mu} e^{i\mathbf{k} \cdot \mathbf{r}} + \hat{a}_{\mathbf{k}, \mu}^\dagger \boldsymbol{\epsilon}_{\mathbf{k}, \mu}^* e^{-i\mathbf{k} \cdot \mathbf{r}} \right) \tag{2.12}$$

Finally, we note that the eigenvalues and eigenvectors of the free light Hamiltonian are given by

$$E_{n, \mathbf{k}, \mu} = n\omega_{\mathbf{k}} = nc|\mathbf{k}|, \quad |n, \mathbf{k}, \mu\rangle \equiv \frac{1}{\sqrt{n!}} \left(\hat{a}_{\mathbf{k}, \mu}^\dagger \right)^n |0, \mathbf{k}, \mu\rangle, \tag{2.13}$$

where $n \in \mathbb{N}_0$ and the state of lowest energy for fixed (\mathbf{k}, μ) is defined by $\hat{a}_{\mathbf{k}, \mu}|0, \mathbf{k}, \mu\rangle = 0$. The state $|n, \mathbf{k}, \mu\rangle$ is said to contain n photons of wave vector \mathbf{k} and polarization μ .

While so far we focused on the description of free electromagnetic fields and its description in a quantum theory, we will now turn to the description of the interaction of photons with matter.

2.2 Light-matter coupling

To define the coupling of matter to light, we start from the matter Hamiltonian

$$\hat{H}_M = \sum_i \frac{\hat{\mathbf{p}}_i^2}{2m} + \frac{1}{2} \sum_{\substack{i,j \\ i \neq j}} \frac{e^2}{|\hat{\mathbf{r}}_i - \hat{\mathbf{r}}_j|} + \sum_I \frac{\hat{\mathbf{P}}_I^2}{2M_I} + \frac{1}{2} \sum_{\substack{I,J \\ I \neq J}} \frac{Z_I Z_J e^2}{|\hat{\mathbf{R}}_I - \hat{\mathbf{R}}_J|} + \sum_{i,I} \frac{-Z_I e^2}{|\hat{\mathbf{r}}_i - \hat{\mathbf{R}}_I|}, \quad (2.14)$$

which describes a system of a fixed number of electrons, labeled by i , and nuclei, labeled by I , interacting with each other via the Coulomb interaction, where the nuclei carry the charges $Z_I e$. The mass of the electrons and the masses of the nuclei are denoted by m and M_I , respectively, while the electron charge is given by $-e < 0$.

To introduce a gauge-invariant coupling of the electrons and the nuclei to an external electromagnetic field, described in Coulomb gauge by a (quantized) vector potential, the momentum operators are replaced according to the minimal coupling prescription²

$$\hat{\mathbf{p}}_i \rightarrow \hat{\mathbf{p}}_i + \frac{e}{c} \hat{\mathbf{A}}(\hat{\mathbf{r}}_i), \quad \hat{\mathbf{P}}_I \rightarrow \hat{\mathbf{P}}_I - \frac{Z_I e}{c} \hat{\mathbf{A}}(\hat{\mathbf{R}}_I), \quad (2.15)$$

where the hat on the vector potential is understood to refer to the operator nature of the vector potential as acting on the Hilbert space of photons. Expanding the squares of the momentum operators in the matter Hamiltonian, we obtain

$$\begin{aligned} \hat{H}_M \rightarrow \hat{H}_M + \sum_i \frac{e}{mc} \hat{\mathbf{A}}(\hat{\mathbf{r}}_i) \cdot \hat{\mathbf{p}}_i - \sum_I \frac{Z_I e}{M_I c} \hat{\mathbf{A}}(\hat{\mathbf{R}}_I) \cdot \hat{\mathbf{P}}_I \\ + \sum_i \frac{e^2}{2mc^2} \hat{\mathbf{A}}^2(\hat{\mathbf{r}}_i) + \sum_I \frac{Z_I^2 e^2}{2M_I c^2} \hat{\mathbf{A}}^2(\hat{\mathbf{R}}_I), \end{aligned} \quad (2.16)$$

²Note that this prescription leads to a Hamilton function in the classical limit that yields the experimentally established Lorentz force law [84].

where we made use of the Coulomb gauge condition $\nabla \cdot \hat{\mathbf{A}}(\mathbf{r}) = 0$ to combine the terms of the form $\hat{\mathbf{A}}(\hat{\mathbf{r}}) \cdot \hat{\mathbf{p}} + \hat{\mathbf{p}} \cdot \hat{\mathbf{A}}(\hat{\mathbf{r}})$, which involve both $\hat{\mathbf{A}}(\hat{\mathbf{r}})$ and $\hat{\mathbf{p}}$, operators which would normally not commute (see also the last remark in Footnote 3). We will only be interested in the scattering of photons with wave lengths on the order of several hundred nm from crystalline solids with characteristic length scales on the order of several \AA , i.e., scales which are much smaller than the wave length of the incoming photon. For the purpose of taking matrix elements of the terms in the second line between eigenstates of the matter (crystal) Hamiltonian then, we can neglect the spatial variation of the vector potential. In this approximation, often referred to as the *dipole approximation* [85], the terms in the second line simply amount to a constant and will be dropped in the following. The terms in the first line can be written in a more familiar form if we define the total matter current density operator

$$\hat{\mathbf{J}}(\mathbf{r}) \equiv \sum_i (-e) \delta^{(3)}(\mathbf{r} - \hat{\mathbf{r}}_i) \frac{\hat{\mathbf{p}}_i}{m} + \sum_I (Z_I e) \delta^{(3)}(\mathbf{r} - \hat{\mathbf{R}}_I) \frac{\hat{\mathbf{P}}_I}{M_I}, \quad (2.17)$$

where $\delta^{(3)}(\mathbf{r})$ is the three-dimensional Dirac δ -distribution. Note that each term in it has the schematic form $\mathbf{J}(\mathbf{r}) \sim \varrho(\mathbf{r} - \mathbf{r}_0) \mathbf{v}$, where $\varrho(\mathbf{r} - \mathbf{r}_0)$ represents the charge density of a point particle at position \mathbf{r}_0 and \mathbf{v} its velocity, which is familiar from the classical electrodynamics of point particles.³

In terms of the matter current operator and the vector potential, the Hamiltonian for the interaction between light and matter in the approximation of neglecting the $\hat{\mathbf{A}}^2$ -terms reads:

$$\hat{\mathcal{H}}_{\text{Light-Matter}} = \frac{1}{c} \int d^3r \hat{\mathbf{A}}(\mathbf{r}) \cdot \hat{\mathbf{J}}(\mathbf{r}). \quad (2.18)$$

Despite both symbols carrying the same kind of hat, we note that $\hat{\mathbf{A}}(\mathbf{r})$ acts only on

³Note that, in general, the operators $\delta^{(3)}(\mathbf{r} - \hat{\mathbf{r}}_i)$ and $\hat{\mathbf{p}}_i$ do not commute and that, in principle, a correct passing from the classical expression to the quantum mechanical one would require one to invoke Weyl's symmetrization postulate $f(\mathbf{r})g(\mathbf{p}) \rightarrow [f(\hat{\mathbf{r}})g(\hat{\mathbf{p}}) + g(\hat{\mathbf{p}})f(\hat{\mathbf{r}})]/2$. The application of this postulate to the current would lead to the familiar form of the probability current times the electric charge, when taking the expectation value of $\hat{\mathbf{J}}(\mathbf{r})$ in a state $|\psi\rangle$: $\hbar/(2mi)[\psi^*(\mathbf{r})\nabla\psi(\mathbf{r}) - \psi(\mathbf{r})\nabla\psi^*(\mathbf{r})]$. In Coulomb gauge, however, an integration by parts of the second term reduces this expression to the non-symmetrized one of Eq. 2.17. We have already made use of this argument in the derivation of the light-matter Hamiltonian, by using the fact that $\hat{\mathbf{A}}(\hat{\mathbf{r}}) \cdot \hat{\mathbf{p}} = \hat{\mathbf{p}} \cdot \hat{\mathbf{A}}(\hat{\mathbf{r}})$ in Coulomb gauge.

the Hilbert space of photons, while $\hat{\mathbf{J}}(\mathbf{r})$ is entirely restricted to the Hilbert space on which the matter Hamiltonian acts. To emphasize that this Hamiltonian acts on the direct product of the light and matter Hilbert spaces, we write the corresponding symbol in calligraphic font. We will use this notation throughout this thesis, whenever it becomes necessary to distinguish between operators acting on a single Hilbert space or on a direct product of two different Hilbert spaces.

Having specified the total Hamiltonian in the form

$$\hat{\mathcal{H}} = \hat{\mathcal{H}}_{\text{Light}} + \hat{\mathcal{H}}_{\text{Light-Matter}} + \hat{\mathcal{H}}_{\text{Matter}}, \quad (2.19)$$

with $\hat{\mathcal{H}}_{\text{Light}} \equiv \hat{H}_L \otimes \mathbb{1}_M$ and $\hat{\mathcal{H}}_{\text{Matter}} \equiv \mathbb{1}_L \otimes \hat{H}_M$ and the three terms being given, in order, by Eqs. 2.10, 2.18, and 2.14, respectively, we can now pass on to the actual description of light scattering within the framework of quantum mechanical perturbation theory.

2.3 Correlation function approach to inelastic light scattering

For the description of light scattering, we will employ a formalism that is based on the density matrix $\hat{\rho}(t)$. We consider a system of light and matter at a time t_0 , at which the matter system shall be in thermal equilibrium with a heat bath at temperature $T = (k_B\beta)^{-1}$ while the light system shall be in a one-photon state with momentum \mathbf{k}_{in} and polarization μ , which represents the incoming photon to be scattered. The total light-matter system can then be described by an initial density matrix

$$\hat{\rho}(t_0) = |\mathbf{k}_{\text{in}}, \mu\rangle\langle\mathbf{k}_{\text{in}}, \mu| \otimes \frac{1}{Z_M} e^{-\beta\hat{H}_M}, \quad (2.20)$$

where the correct normalization of $\hat{\rho}(t_0)$ requires $Z_M = \text{tr} \hat{H}_M$, with \hat{H}_M being the matter Hamiltonian as given in Eq. 2.14.

We are interested in the probability for the inelastic scattering of the incoming photon. Assuming the interaction of light with matter to be weak, so that it can be

well approximated with the probability for the scattering of the initial photon state into *one* other photon state only, irrespective of the final state of the matter system. The total probability that at time $t > t_0$ the light-matter system is in a state of one photon with momentum \mathbf{k}_{out} and polarization ν and an arbitrary matter state is given by

$$P_{\text{scatter}} = \sum_{\alpha} (\langle \mathbf{k}_{\text{out}}, \nu | \otimes \langle \alpha |) \hat{\rho}(t) (| \mathbf{k}_{\text{out}}, \nu \rangle \otimes | \alpha \rangle), \quad (2.21)$$

where the sum over α runs over a complete set of matter states.

To find the density matrix at time t , we note that its time evolution is governed by the von Neumann equation [86]

$$i \frac{\partial}{\partial t} \hat{\rho}(t) = [\hat{\mathcal{H}}, \hat{\rho}(t)], \quad (2.22)$$

with the total Hamiltonian $\hat{\mathcal{H}}$ being given in Eq. 2.19. As the total Hamiltonian is time-independent, its solution is simply given by

$$\hat{\rho}(t) = e^{-i\hat{\mathcal{H}}(t-t_0)} \hat{\rho}(t_0) e^{+i\hat{\mathcal{H}}(t-t_0)}. \quad (2.23)$$

If we expand the matter part of $\hat{\rho}(t_0)$ in a complete set of matter states, i.e.,

$$\frac{1}{Z_{\text{M}}} e^{-\beta \hat{H}_{\text{M}}} = \frac{1}{Z_{\text{M}}} \sum_{\gamma} e^{-\beta E_{\gamma}} |\gamma\rangle \langle \gamma|, \quad (2.24)$$

where $|\gamma\rangle$ is an eigenstate of \hat{H}_{M} to the eigenvalue E_{γ} , the scattering probability reads:

$$P_{\text{scatter}} = \frac{1}{Z_{\text{M}}} \sum_{\alpha, \gamma} e^{-\beta E_{\gamma}} \left| (\langle \mathbf{k}_{\text{out}}, \nu | \otimes \langle \alpha |) e^{-i\hat{\mathcal{H}}(t-t_0)} (| \mathbf{k}_{\text{in}}, \mu \rangle \otimes | \gamma \rangle) \right|^2. \quad (2.25)$$

This expression is the intuitive generalization of the basic quantum mechanical rule to calculate probabilities: Starting from a state $|\psi(t_0)\rangle = | \mathbf{k}_{\text{in}}, \mu \rangle \otimes | \gamma \rangle$, it evolves from time t_0 to time t , i.e., $|\psi(t)\rangle = \exp(-i\hat{\mathcal{H}}(t-t_0)) |\psi(t_0)\rangle$, and one obtains the probability of finding the system in the state $| \mathbf{k}_{\text{out}}, \nu \rangle \otimes | \alpha \rangle$ by calculating $| (\langle \mathbf{k}_{\text{out}}, \nu | \otimes \langle \alpha |) |\psi(t)\rangle |^2$. If one is not interested in the matter state $|\alpha\rangle$, these probabilities have to be summed over α , and, assuming that the probability to find a particular matter state $|\gamma\rangle$ in the

initial state is given by the Boltzmann factor $Z_M^{-1} \exp(-\beta E_\gamma)$, also summed over γ with the Boltzmann factor as weight.

To evaluate the matrix elements of the time-evolution operator, we will employ a perturbative approach. To this end, we first note that the matrix elements of the light-matter Hamiltonian can be expected to be small compared to matrix elements of the free Hamiltonian $\hat{\mathcal{H}}_0 \equiv \hat{\mathcal{H}} - \hat{\mathcal{H}}_{\text{Light-Matter}}$, since, in addition to matrix elements of the charge density operators, which are also present in $\hat{\mathcal{H}}_0$, they involve a factor of $v/c \ll 1$. We would then like to expand the Hamiltonian formally into a Taylor series around $\hat{\mathcal{H}}_{\text{Light-Matter}} = 0$. However, a naïve and straightforward expansion of the exponential function is futile as a term involving $\hat{\mathcal{H}}^n$ contains terms *up to* order n in $\hat{\mathcal{H}}_{\text{Light-Matter}}$ and it is not easy to extract all terms of a given order in $\hat{\mathcal{H}}_{\text{Light-Matter}}$ in a closed form. While this problem could, in principle, be circumvented by making use of the Baker-Campbell-Hausdorff identity, this method is still rather cumbersome. Instead, a much simpler solution is provided by an approach based on passing to the *interaction picture* [83, 87–91]. The basic idea is to treat the free part of the Hamiltonian exactly, in the sense that terms of arbitrarily high power in $\hat{\mathcal{H}}_0$ are retained automatically. For this purpose, we re-write the matrix element of the time-evolution operator as

$$\begin{aligned}
& (\langle \mathbf{k}_{\text{out}}, \nu | \otimes \langle \alpha |) e^{-i\hat{\mathcal{H}}(t-t_0)} (|\mathbf{k}_{\text{in}}, \mu\rangle \otimes |\gamma\rangle) \\
&= (\langle \mathbf{k}_{\text{out}}, \nu | \otimes \langle \alpha |) e^{-i\hat{\mathcal{H}}_0 t} e^{+i\hat{\mathcal{H}}_0 t} e^{-i\hat{\mathcal{H}}(t-t_0)} e^{-i\hat{\mathcal{H}}_0 t_0} e^{+i\hat{\mathcal{H}}_0 t_0} (|\mathbf{k}_{\text{in}}, \mu\rangle \otimes |\gamma\rangle) \\
&= e^{-i(E_\alpha + \omega_{\text{out}})t} e^{+i(E_\gamma + \omega_{\text{in}})t_0} (\langle \mathbf{k}_{\text{out}}, \nu | \otimes \langle \alpha |) \hat{U}_I(t, t_0) (|\mathbf{k}_{\text{in}}, \mu\rangle \otimes |\gamma\rangle).
\end{aligned} \tag{2.26}$$

Here we used the fact that the two states are each eigenstates of the free Hamiltonian $\hat{\mathcal{H}}_0$ and introduced the abbreviations $\omega_{\text{in}} \equiv \omega_{\mathbf{k}_{\text{in}}}$ and $\omega_{\text{out}} \equiv \omega_{\mathbf{k}_{\text{out}}}$. In addition, we defined the time-evolution operator in the interaction picture as

$$\hat{U}_I(t, t_0) \equiv e^{+i\hat{\mathcal{H}}_0 t} e^{-i\hat{\mathcal{H}}(t-t_0)} e^{-i\hat{\mathcal{H}}_0 t_0}. \tag{2.27}$$

Since the oscillating exponential factors in front of the matrix element drop out after taking the absolute value, the problem of calculating the scattering probability is thus reduced to finding the matrix elements of the time-evolution operator in the interaction picture.

As is easily verified, the latter obeys the differential equation

$$i\frac{\partial}{\partial t}\hat{U}_I(t, t_0) = \hat{\mathcal{H}}_{1,I}(t)\hat{U}_I(t, t_0), \quad (2.28)$$

where we defined the interaction Hamiltonian in the interaction picture as

$$\hat{\mathcal{H}}_{1,I}(t) \equiv e^{i\hat{\mathcal{H}}_0 t} \hat{\mathcal{H}}_{\text{Light-Matter}} e^{-i\hat{\mathcal{H}}_0 t}. \quad (2.29)$$

Solving the differential equation by iteration, one finds that $\hat{U}_I(t, t_0)$ can be written in the form [83, 87–90]

$$\hat{U}_I(t, t_0) = \mathcal{T} \exp \left\{ -i \int_{t_0}^t dt' \hat{\mathcal{H}}_{1,I}(t') \right\}, \quad (2.30)$$

with \mathcal{T} being the *time-ordering symbol*, which prescribes that operators in a product are to be placed with operators at later times written to the left of those at earlier times. Most importantly though, $\hat{U}_I(t, t_0)$ can conveniently be expanded into a Taylor series by simply expanding the exponential.

Since we need the matrix elements of $\hat{U}_I(t, t_0)$ between states that include one photon only, all odd powers of $\hat{\mathcal{H}}_{1,I}$ in the expansion vanish in the matrix element as $\hat{\mathcal{H}}_{1,I}$ changes the number of photons by one. Furthermore, in the context of this thesis, we are only interested in *inelastic* light scattering, i.e., $\mathbf{k}_{\text{in}} \neq \mathbf{k}_{\text{out}}$. The lowest-order non-vanishing contribution to the scattering matrix element is then given by the second-order term in the Taylor expansion:

$$\begin{aligned} & (\langle \mathbf{k}_{\text{out}}, \nu | \otimes \langle \alpha |) \hat{U}_I(t, t_0) (| \mathbf{k}_{\text{in}}, \mu \rangle \otimes | \gamma \rangle) \\ & \simeq (\langle \mathbf{k}_{\text{out}}, \nu | \otimes \langle \alpha |) \frac{(-i)^2}{2!} \int_{t_0}^t dt_1 \int_{t_0}^t dt_2 \mathcal{T} \left[\hat{\mathcal{H}}_{1,I}(t_1) \hat{\mathcal{H}}_{1,I}(t_2) \right] (| \mathbf{k}_{\text{in}}, \mu \rangle \otimes | \gamma \rangle). \end{aligned} \quad (2.31)$$

Inserting the explicit form of $\hat{\mathcal{H}}_{1,I}$, given in Eq. 2.18, the matrix element factorizes:

$$\begin{aligned}
& (\langle \mathbf{k}_{\text{out}}, \nu | \otimes \langle \alpha |) \hat{U}_I(t, t_0) (| \mathbf{k}_{\text{in}}, \mu \rangle \otimes | \gamma \rangle) \\
& \simeq \sum_{i,j} \int_{t_0}^t dt_1 \int_{t_0}^t dt_2 \int d^3 r_1 \int d^3 r_2 \frac{(-i)^2}{2!c^2} \\
& \quad \times \langle \alpha | \mathcal{T} \left[\hat{J}_{i,I}(\mathbf{r}_1, t_1) \hat{J}_{j,I}(\mathbf{r}_2, t_2) \right] | \gamma \rangle \times \langle \mathbf{k}_{\text{out}}, \nu | \mathcal{T} \left[\hat{A}_{i,I}(\mathbf{r}_1, t_1) \hat{A}_{j,I}(\mathbf{r}_2, t_2) \right] | \mathbf{k}_{\text{in}}, \mu \rangle.
\end{aligned} \tag{2.32}$$

Here, the sums over i, j run over the three cartesian components of the vector operators. We have thus managed to decompose the problem into that of finding the matrix elements of a time-ordered product of current density operators between eigenstates of the free matter Hamiltonian and that of calculating the matrix elements of a time-ordered product of vector potential operators between eigenstates of the free light Hamiltonian. The evaluation of the former will require a more elaborate discussion that will comprise Chapters 3 through 5 and parts of Chapter 6. The latter, by contrast, is easily evaluated by applying Wick's theorem [83, 87–90] and is found to be the sum of three contributions:

$$\begin{aligned}
& \langle \mathbf{k}_{\text{out}}, \nu | \mathcal{T} \left[\hat{A}_{i,I}(\mathbf{r}_1, t_1) \hat{A}_{j,I}(\mathbf{r}_2, t_2) \right] | \mathbf{k}_{\text{in}}, \mu \rangle \\
& = \delta_{\mathbf{k}_{\text{in}}, \mathbf{k}_{\text{out}}} \delta_{\mu, \nu} \langle 0_{\text{L}} | \mathcal{T} \left[\hat{A}_{i,I}(\mathbf{r}_1, t_1) \hat{A}_{j,I}(\mathbf{r}_2, t_2) \right] | 0_{\text{L}} \rangle \\
& \quad + \frac{2\pi c^2}{\sqrt{\omega_{\text{in}} \omega_{\text{out}} V}} e^{-i(\mathbf{k}_{\text{out}} \cdot \mathbf{r}_1 - \omega_{\text{out}} t_1)} e^{+i(\mathbf{k}_{\text{in}} \cdot \mathbf{r}_2 - \omega_{\text{in}} t_2)} (\epsilon_{\mathbf{k}_{\text{out}}, \nu}^i)^* \epsilon_{\mathbf{k}_{\text{in}}, \mu}^j \\
& \quad + \frac{2\pi c^2}{\sqrt{\omega_{\text{in}} \omega_{\text{out}} V}} e^{-i(\mathbf{k}_{\text{out}} \cdot \mathbf{r}_2 - \omega_{\text{out}} t_2)} e^{+i(\mathbf{k}_{\text{in}} \cdot \mathbf{r}_1 - \omega_{\text{in}} t_1)} (\epsilon_{\mathbf{k}_{\text{out}}, \nu}^j)^* \epsilon_{\mathbf{k}_{\text{in}}, \mu}^i.
\end{aligned} \tag{2.33}$$

The first term only contributes to elastic scattering and hence we will not discuss it further. The second and third terms, however, do give a contribution to the inelastic scattering matrix element. Noting that the sum of the second and third term is symmetric under the exchange $(\mathbf{r}_1, t_1, i) \leftrightarrow (\mathbf{r}_2, t_2, j)$, we see that the pairs of sums and

integrations yield two times the same result:

$$\begin{aligned}
& (\langle \mathbf{k}_{\text{out}}, \nu | \otimes \langle \alpha |) \hat{U}_I(t, t_0) (| \mathbf{k}_{\text{in}}, \mu \rangle \otimes | \gamma \rangle) \\
& \simeq \sum_{i,j} \int_{t_0}^t dt_1 \int_{t_0}^t dt_2 \int d^3 r_1 \int d^3 r_2 \frac{-2\pi}{V \sqrt{\omega_{\text{in}} \omega_{\text{out}}}} (\epsilon_{\mathbf{k}_{\text{out}}, \nu}^i)^* \epsilon_{\mathbf{k}_{\text{in}}, \mu}^j \\
& \times e^{-i(\mathbf{k}_{\text{out}} \cdot \mathbf{r}_1 - \omega_{\text{out}} t_1)} e^{+i(\mathbf{k}_{\text{in}} \cdot \mathbf{r}_2 - \omega_{\text{in}} t_2)} \langle \alpha | \mathcal{T} \left[\hat{J}_{i,I}(\mathbf{r}_1, t_1) \hat{J}_{j,I}(\mathbf{r}_2, t_2) \right] | \gamma \rangle.
\end{aligned} \tag{2.34}$$

We can simplify the notation by introducing the spatially Fourier-transformed and projected current operators via

$$\hat{J}_{\mathbf{k}, \mu, I}(t) \equiv \epsilon_{\mathbf{k}, \mu}^* \cdot \int d^3 r e^{-i\mathbf{k} \cdot \mathbf{r}} \hat{\mathbf{J}}_I(\mathbf{r}, t), \tag{2.35}$$

whereupon the matrix element for inelastic light scattering takes on the simple form

$$\begin{aligned}
& (\langle \mathbf{k}_{\text{out}}, \nu | \otimes \langle \alpha |) \hat{U}_I(t, t_0) (| \mathbf{k}_{\text{in}}, \mu \rangle \otimes | \gamma \rangle) \\
& \simeq \frac{-2\pi}{V \sqrt{\omega_{\text{in}} \omega_{\text{out}}}} \int_{t_0}^t dt_1 \int_{t_0}^t dt_2 e^{i(\omega_{\text{out}} t_1 - \omega_{\text{in}} t_2)} \langle \alpha | \mathcal{T} \left[\hat{J}_{\mathbf{k}_{\text{out}}, \nu, I}(t_1) \hat{J}_{\mathbf{k}_{\text{in}}, \mu, I}^\dagger(t_2) \right] | \gamma \rangle.
\end{aligned} \tag{2.36}$$

Using this expression for the scattering matrix element, we arrive at the following approximation for the probability⁴ for inelastic light scattering:

$$\begin{aligned}
P_{\text{inel.}} & \simeq \frac{1}{Z_M} \sum_{\alpha, \gamma} e^{-\beta E_\gamma} \frac{(2\pi)^2}{V^2 \omega_{\text{in}} \omega_{\text{out}}} \int_{t_0}^t dt_1 \int_{t_0}^t dt_2 \int_{t_0}^t dt'_1 \int_{t_0}^t dt'_2 e^{i\omega_{\text{out}}(t_1 - t'_1)} e^{-i\omega_{\text{in}}(t_2 - t'_2)} \\
& \times \langle \gamma | \overline{\mathcal{T}} \left[\hat{J}_{\mathbf{k}_{\text{out}}, \nu, I}^\dagger(t'_1) \hat{J}_{\mathbf{k}_{\text{in}}, \mu, I}(t'_2) \right] | \alpha \rangle \langle \alpha | \mathcal{T} \left[\hat{J}_{\mathbf{k}_{\text{out}}, \nu, I}(t_1) \hat{J}_{\mathbf{k}_{\text{in}}, \mu, I}^\dagger(t_2) \right] | \gamma \rangle.
\end{aligned} \tag{2.37}$$

Here, we evaluated the squared modulus of the matrix element by multiplying it with its complex conjugate. In the complex conjugated matrix element, the time-ordering

⁴It should be noted that this expression can only be interpreted as a probability for a *small* time span $t - t_0$. When Taylor expanded, the time-evolution operator ceases to be unitary and, as a consequence, the matrix element squared is no longer guaranteed to be equal to or less than one. Compare this to the oscillating exponential $\exp(-iET)$, whose modulus squared is always equal to one, irrespective of the size of ET , but when Taylor-expanded diverges for large ET . We will not discuss this issue in more detail and instead refer the reader to the literature [86].

symbol \mathcal{T} becomes the anti-time-ordering symbol $\overline{\mathcal{T}}$, which orders the operators it acts upon so that operators at later times stand to the *right* of those at earlier times. Finally, we can simplify this expression by using the completeness relation for the intermediate matter states and by identifying the operation of taking the trace:

$$P_{\text{inel.}} \simeq \frac{(2\pi)^2}{V^2 \omega_{\text{in}} \omega_{\text{out}}} \int_{t_0}^t dt_1 \int_{t_0}^t dt_2 \int_{t_0}^t dt'_1 \int_{t_0}^t dt'_2 e^{i\omega_{\text{out}}(t_1-t'_1)} e^{-i\omega_{\text{in}}(t_2-t'_2)} \times \left\langle \overline{\mathcal{T}} \left[\hat{J}_{\mathbf{k}_{\text{out}},\nu,I}^\dagger(t'_1) \hat{J}_{\mathbf{k}_{\text{in}},\mu,I}(t'_2) \right] \mathcal{T} \left[\hat{J}_{\mathbf{k}_{\text{out}},\nu,I}(t_1) \hat{J}_{\mathbf{k}_{\text{in}},\mu,I}^\dagger(t_2) \right] \right\rangle_{\text{M}}, \quad (2.38)$$

where we identified the thermal and quantum mechanical expectation value of an operator acting on the matter part of the Hilbert space as $\langle \hat{O} \rangle_{\text{M}} \equiv Z_{\text{M}}^{-1} \text{tr} [\exp(-\beta \hat{H}_{\text{M}}) \hat{O}]$.

Equation 2.38 is one of the major results of this thesis. It expresses the probability for inelastic light scattering in a *finite* time interval in terms of a thermal correlation function of operators acting in the matter part of the Hilbert space only. As such, it provides a means to calculate the intensity of inelastically scattered light, i.e., the Raman intensity, on *arbitrarily short time scales* and *out of equilibrium*. Also note that it does not make any use of specific intermediate or final states of the matter system and hence it provides the *complete* Raman scattering probability, including *all possible matter excitations*, and not only, for instance, the contribution due to the excitation of a lattice vibration. Therefore, it can be of great value in a theoretical description of Raman spectroscopy. It can also be very useful for potential future theoretical studies of Raman scattering on ultra-short time scales, which is a likely future field of research after the advent of ultra-short pump-and-probe absorption and transmittance spectroscopy.

The needed matter correlation function, however, depends on four different time variables. Factoring in the time-independence of the total Hamiltonian, it can hence be considered to be a function of three time differences. Furthermore, it is neither the thermal average of a simple time-ordered product of operators, but instead is comprised of four terms with various time orderings. As such, it is not easy to calculate with standard, equilibrium Green's function techniques. Potentially, the Keldysh-Schwinger contour formalism for non-equilibrium Green's functions can be applied to arrive at

a practically useful expression for it. So far, however, this formalism has only been applied to correlation functions that depend on one time-difference and their products and convolutions only [91]. A detailed theoretical study of this correlation function, while highly desirable, is beyond the scope of this thesis and will be the subject of future work. Instead, we will focus on providing a detailed treatment of the equilibrium, zero-temperature case. This case is mathematically easier to handle and allows us to give concrete recipes for the computational study of Raman intensities.

2.4 Generalized Fermi's golden rule approach to Raman scattering

In order to overcome the problem of evaluating the complicated correlation function of Eq. 2.38, we will use an approach that can be thought of as a generalization of Fermi's golden rule. For this, we go back to Eq. 2.25 and approximate the matrix element for inelastic light scattering, as done in Eq. 2.36:

$$P_{\text{inel.}} \simeq \frac{1}{Z_M} \sum_{\alpha, \gamma} e^{-\beta E_\gamma} \frac{(2\pi)^2}{V^2 \omega_{\text{in}} \omega_{\text{out}}} \times \left| \int_{t_0}^t dt_1 \int_{t_0}^t dt_2 e^{i(\omega_{\text{out}} t_1 - \omega_{\text{in}} t_2)} \langle \alpha | \mathcal{T} \left[\hat{J}_{\mathbf{k}_{\text{out}}, \nu, I}(t_1) \hat{J}_{\mathbf{k}_{\text{in}}, \mu, I}^\dagger(t_2) \right] | \gamma \rangle \right|^2. \quad (2.39)$$

Note that the matrix element of the matter current density operators reads

$$\begin{aligned} & \langle \alpha | \mathcal{T} \left[\hat{J}_{\mathbf{k}_{\text{out}}, \nu, I}(t_1) \hat{J}_{\mathbf{k}_{\text{in}}, \mu, I}^\dagger(t_2) \right] | \gamma \rangle \\ &= e^{i(E_\alpha - E_\gamma)t_2} \left[e^{iE_\alpha(t_1 - t_2)} \theta(t_1 - t_2) \langle \alpha | \hat{J}_{\mathbf{k}_{\text{out}}, \nu} e^{-i\hat{H}_M(t_1 - t_2)} \hat{J}_{\mathbf{k}_{\text{in}}, \mu}^\dagger | \gamma \rangle \right. \\ & \quad \left. + e^{-iE_\gamma(t_1 - t_2)} \theta(-(t_1 - t_2)) \langle \alpha | \hat{J}_{\mathbf{k}_{\text{in}}, \mu} e^{i\hat{H}_M(t_1 - t_2)} \hat{J}_{\mathbf{k}_{\text{out}}, \nu}^\dagger | \gamma \rangle \right], \end{aligned} \quad (2.40)$$

i.e., barring the first exponential factor, it is essentially a function of $t_1 - t_2$ only. Hence it is possible and useful to write it as a Fourier integral:

$$\langle \alpha | \mathcal{T} \left[\hat{J}_{\mathbf{k}_{\text{out}}, \nu, I}(t_1) \hat{J}_{\mathbf{k}_{\text{in}}, \mu, I}^\dagger(t_2) \right] | \gamma \rangle = e^{i(E_\alpha - E_\gamma)t_2} \int \frac{d\omega}{2\pi} e^{-i\omega(t_1 - t_2)} \tilde{J}_{\mathbf{k}_{\text{out}}, \nu, \mathbf{k}_{\text{in}}, \mu}^{\alpha\gamma}(\omega), \quad (2.41)$$

where we defined the Fourier transform by

$$\tilde{J}_{\mathbf{k}_{\text{out}},\mathbf{k}_{\text{in}};\nu,\mu}^{\alpha\gamma}(\omega) \equiv \int_{-\infty}^{+\infty} dt e^{i\omega t} \langle \alpha | \mathcal{T} \left[\hat{J}_{\mathbf{k}_{\text{out}},\nu,I}(t) \hat{J}_{\mathbf{k}_{\text{in}},\mu,I}^\dagger(0) \right] | \gamma \rangle. \quad (2.42)$$

We can then perform the integration over t_1 and t_2 in Eq. 2.39, which yields

$$\begin{aligned} & \int_{t_0}^t dt_1 \int_{t_0}^t dt_2 e^{i(\omega_{\text{out}}t_1 - \omega_{\text{in}}t_2)} \langle \alpha | \mathcal{T} \left[\hat{J}_{\mathbf{k}_{\text{out}},\nu,I}(t_1) \hat{J}_{\mathbf{k}_{\text{in}},\mu,I}^\dagger(t_2) \right] | \gamma \rangle \\ &= e^{-i(\omega_{\text{in}} - \omega_{\text{out}} - E_\alpha + E_\gamma)(t - t_0)/2} (t - t_0)^2 \\ & \int \frac{d\omega}{2\pi} \text{sinc} \left[\frac{\omega - \omega_{\text{out}}}{2} (t - t_0) \right] \text{sinc} \left[\frac{\omega - \omega_{\text{in}} + E_\alpha - E_\gamma}{2} (t - t_0) \right] \tilde{J}_{\mathbf{k}_{\text{out}},\mathbf{k}_{\text{in}};\nu,\mu}^{\alpha\gamma}(\omega), \end{aligned} \quad (2.43)$$

where $\text{sinc}(x) \equiv \sin(x)/x$ denotes the cardinal sine function and we finally find an expression for the probability for inelastic light scattering:

$$\begin{aligned} P_{\text{inel.}} &\simeq \frac{1}{Z_{\text{M}}} \sum_{\alpha,\gamma} e^{-\beta E_\gamma} \frac{(2\pi)^2}{V^2 \omega_{\text{in}} \omega_{\text{out}}} (t - t_0)^4 \int \frac{d\omega}{2\pi} \int \frac{d\omega'}{2\pi} \tilde{J}_{\mathbf{k}_{\text{out}},\mathbf{k}_{\text{in}};\nu,\mu}^{\alpha\gamma}(\omega) \left[\tilde{J}_{\mathbf{k}_{\text{out}},\mathbf{k}_{\text{in}};\nu,\mu}^{\alpha\gamma}(\omega') \right]^* \\ & \times \text{sinc} \left[\frac{\omega - \omega_{\text{out}}}{2} (t - t_0) \right] \text{sinc} \left[\frac{\omega' - \omega_{\text{out}}}{2} (t - t_0) \right] \\ & \times \text{sinc} \left[\frac{\omega - \omega_{\text{in}} + E_\alpha - E_\gamma}{2} (t - t_0) \right] \text{sinc} \left[\frac{\omega' - \omega_{\text{in}} + E_\alpha - E_\gamma}{2} (t - t_0) \right]. \end{aligned} \quad (2.44)$$

If we are only interested in the scattering probability after the system is again in equilibrium, i.e., for a macroscopically long time interval, which corresponds to the limiting case $(t - t_0) \gg 2/\omega_{\text{in}}$, then we can simplify this expression considerably. In the limit $(t - t_0)\omega_{\text{in}}/2 \gg 1$, the last two cardinal sine functions in the integrand become highly oscillatory and are sharply centered around $\omega^{(\prime)} = \omega_{\text{in}} - E_\alpha + E_\gamma$. We can then approximate the integrals over ω and ω' by evaluating the prefactors in the integrand

at this value and pulling them outside the integral:

$$\begin{aligned}
P_{\text{inel.}} \xrightarrow{(t-t_0) \gg \frac{2}{\omega_{\text{in}}}} & \frac{1}{Z_{\text{M}}} \sum_{\alpha, \gamma} e^{-\beta E_{\gamma}} \frac{(2\pi)^2}{V^2 \omega_{\text{in}} \omega_{\text{out}}} (t-t_0)^2 \left| \tilde{J}_{\mathbf{k}_{\text{out}}, \nu, \mu}^{\alpha \gamma}(\omega_{\text{in}} - E_{\alpha} + E_{\gamma}) \right|^2 \\
& \times \text{sinc}^2 \left[\frac{\omega_{\text{in}} - \omega_{\text{out}} - E_{\alpha} + E_{\gamma}}{2} (t-t_0) \right] \\
& \times \left\{ (t-t_0) \int \frac{d\omega}{2\pi} \text{sinc} \left[\frac{\omega - \omega_{\text{in}} + E_{\alpha} - E_{\gamma}}{2} (t-t_0) \right] \right\}^2.
\end{aligned} \tag{2.45}$$

The integral in the last line amounts to one and we can simplify the second line with the help of the identity [86]

$$\text{sinc}^2(\omega t) = \frac{\sin^2(\omega t)}{(\omega t)^2} \xrightarrow{t \gg \frac{1}{\omega}} \frac{\pi}{t} \delta(\omega), \tag{2.46}$$

where δ denotes the Dirac δ -distribution. If we define the scattering rate, i.e., the probability per unit time for a scattering event to happen, via $\dot{P}_{\text{inel.}} \equiv P_{\text{inel.}}/(t-t_0)$, we obtain a much more simplified result, which can be interpreted as a generalization of Fermi's golden rule beyond first-order time-dependent perturbation theory:

$$\begin{aligned}
\dot{P}_{\text{inel.}} \xrightarrow{(t-t_0) \gg \frac{2}{\omega_{\text{in}}}} & \frac{1}{Z_{\text{M}}} \sum_{\alpha, \gamma} e^{-\beta E_{\gamma}} \frac{(2\pi)^2}{V^2 \omega_{\text{in}} \omega_{\text{out}}} \left| \tilde{J}_{\mathbf{k}_{\text{out}}, \nu, \mu}^{\alpha \gamma}(\omega_{\text{in}} - E_{\alpha} + E_{\gamma}) \right|^2 \\
& \times 2\pi \delta(\omega_{\text{in}} - \omega_{\text{out}} - E_{\alpha} + E_{\gamma}).
\end{aligned} \tag{2.47}$$

This expression gives the probability per unit time for one photon with momentum \mathbf{k}_{in} and polarization μ to scatter inelastically, i.e., to a state $|\mathbf{k}_{\text{out}}, \nu\rangle \neq |\mathbf{k}_{\text{in}}, \mu\rangle$ from a matter system when it interacts with the latter over a macroscopically long time period $t-t_0$. In an experimental setting, one cannot detect a photon with a precise momentum, but instead a detector always detects a scattered photon within a certain direction in a small solid angle $\Delta\Omega_{\text{D}}$ and within a small, but finite frequency interval $[\omega_{\text{D}}, \omega_{\text{D}} + \Delta\omega_{\text{D}}]$. Therefore we actually need to be interested in the total scattering rate for any photon satisfying these criteria. A similar logic applies to the source of the incoming photons, which typically emits photons into a very small, but finite solid angle $\Delta\Omega_{\text{L}}$ over a finite frequency interval $[\omega_{\text{L}}, \omega_{\text{L}} + \Delta\omega_{\text{L}}]$. If the $\Delta\Omega_{\text{D,L}}$ and $\Delta\omega_{\text{D,L}}$ are

small enough, we can approximate the total scattering rate by its value evaluated at $\omega_{\text{in}} \equiv c|\mathbf{k}_{\text{in}}| = \omega_{\text{L}}$ and $\omega_{\text{out}} \equiv c|\mathbf{k}_{\text{out}}| = \omega_{\text{D}}$ and in the direction of \mathbf{k}_{in} and \mathbf{k}_{out} , specified by the axis of the incoming light and the position of the detector, respectively, and multiply by the number of photon states in this frequency interval and solid angle:

$$N_{\text{photon states}}(c|\mathbf{k}| \in [\omega, \omega + \Delta\omega], \mathbf{k}/|\mathbf{k}| \in \Delta\Omega) = \frac{V\omega^2}{(2\pi)^3 c^3} \Delta\Omega \Delta\omega. \quad (2.48)$$

Including this kinematic factor for both the incoming and outgoing light then yields the following final expression for the scattering rate:

$$\begin{aligned} \dot{P}_{\text{inel.}} \approx & \frac{1}{Z_{\text{M}}} \sum_{\alpha, \gamma} e^{-\beta E_{\gamma}} \frac{\omega_{\text{L}} \omega_{\text{D}} \Delta\Omega_{\text{L}} \Delta\omega_{\text{L}} \Delta\Omega_{\text{D}} \Delta\omega_{\text{D}}}{(2\pi)^4 c^6} \left| \tilde{J}_{\mathbf{k}_{\text{out}}, \mathbf{k}_{\text{in}}}^{\alpha\gamma}{}_{\nu, \mu}(\omega_{\text{L}} - E_{\alpha} + E_{\gamma}) \right|^2 \\ & \times 2\pi \delta(\omega_{\text{L}} - \omega_{\text{D}} - E_{\alpha} + E_{\gamma}). \end{aligned} \quad (2.49)$$

To evaluate this expression at a finite temperature, we need knowledge of all non-vanishing matrix elements $\tilde{J}_{\mathbf{k}_{\text{out}}, \mathbf{k}_{\text{in}}}^{\alpha\gamma}{}_{\nu, \mu}(\omega_{\text{L}} - E_{\alpha} + E_{\gamma})$ for which $\exp(-\beta E_{\gamma})$ is still a sizable number, i.e., for which the state $|\gamma\rangle$ has an energy $E_{\gamma} \lesssim k_{\text{B}}T$. Here we will confine ourselves to the zero temperature limit, i.e., $\beta \rightarrow \infty$, in which the sum over γ reduces to the ground state only (which we assume to be non-degenerate):

$$\begin{aligned} \dot{P}_{\text{inel.}} = & \sum_{\alpha} \frac{\omega_{\text{L}} \omega_{\text{D}} \Delta\Omega_{\text{L}} \Delta\omega_{\text{L}} \Delta\Omega_{\text{D}} \Delta\omega_{\text{D}}}{(2\pi)^4 c^6} \left| \tilde{J}_{\mathbf{k}_{\text{out}}, \mathbf{k}_{\text{in}}}^{\alpha}{}_{\nu, \mu}(\omega_{\text{L}} - \Delta E_{\alpha}) \right|^2 \\ & \times 2\pi \delta(\omega_{\text{L}} - \omega_{\text{D}} - \Delta E_{\alpha}), \end{aligned} \quad (2.50)$$

with the understanding that the Fourier-transformed matrix element without a second state index refers to the ground state $|\Omega\rangle$ being the initial state.

$$\tilde{J}_{\mathbf{k}_{\text{out}}, \mathbf{k}_{\text{in}}}^{\alpha}{}_{\nu, \mu}(\omega) = \int_{-\infty}^{+\infty} dt e^{i\omega t} \langle \alpha | \mathcal{T} \left[\hat{J}_{\mathbf{k}_{\text{out}}, \nu, I}(t) \hat{J}_{\mathbf{k}_{\text{in}}, \mu, I}^{\dagger}(0) \right] | \Omega \rangle \quad (2.51)$$

and $\Delta E_{\alpha} \equiv E_{\alpha} - E_0$ denotes the excitation energy of the matter system associated with the transition $|\Omega\rangle \rightarrow |\alpha\rangle$.

As seen from Eq. 2.50, the inelastic, Raman scattering rate is non-zero only if the

excitation frequency ω_L and the frequency of the scattered, i.e., the detected light ω_D differ by a possible excitation frequency of the matter system. Compared to the more general result given in Eq. 2.38, the expression given in Eq. 2.50 is more cumbersome as each contribution of a state $|\alpha\rangle$ to the scattering rate has to be calculated separately, whereas the correlation function-based approach gives the full result immediately once the correlation function has been calculated. Still, the less general Eq. 2.50 also offers some advantages over the correlation function-based approach, as it (i) involves only the Fourier transform of a function of one time variable and (ii) can be computed with quantum field theoretical methods borrowed from elementary particle physics.

We also want to point out that both our correlation function-based approach as well as the Fermi golden rule-like one allow a detailed physics-oriented discussion of the phenomenon of Raman scattering. By considering only certain terms in the perturbation series for the correlation function or only certain states $|\alpha\rangle$ in the Fermi golden rule-like approach, respectively, different physical processes that contribute to the Raman spectrum can be analyzed one by one. Our approaches thus allow the identification of the most dominant mechanisms for inelastic light scattering. As an example relevant for the case of metallic solids, our methods permit both the computation of the phonon-induced part of the Raman spectrum as well as the electronic excitations/exciton-induced part of it. Within the scope of this thesis, however, we will confine ourselves to a discussion and the computation of the phonon-induced part only, which in most cases constitutes the dominant part of the Raman spectrum [85].

In order to make further progress and give concrete expressions that can be used for computational purposes, we need to find both the eigenstates and eigenvalues of the matter Hamiltonian \hat{H}_M and the matrix elements of the product of two time-ordered current density operators. We will discuss the former over the course of the next three chapters, while the latter will be tackled in Chapter 6 for the case in which the state $|\alpha\rangle$ mostly represents a quantized excitation of a lattice vibration, i.e., a phonon.

Chapter 3

Electronic Structure

The task of finding the spectrum and the eigenstates of the full matter Hamiltonian, as given in Eq. 2.14, is a highly non-trivial one. The reason for this lies in the strong Coulomb interaction between the electrons and nuclei, which makes a perturbative treatment of the electron-nuclei system challenging, as the inter-particle interaction cannot be considered a small perturbation. The coupled electron-nuclei system behaves qualitatively very much differently from a system of free particles. Nevertheless, we shall see over the course of the next three chapters how a perturbative treatment is still possible by adopting a scheme of successively more accurate approximations.

The basic idea consists of neglecting some part of the full Hamiltonian, such that the remaining part can be diagonalized exactly. The eigenfunctions of the approximated Hamiltonian then supply a basis for the full electron-nuclei Hilbert space. After expressing the exact matter Hamiltonian in this basis, a new approximation can be performed by neglecting a smaller subset of the off-diagonal matrix elements, such that the new approximated Hamiltonian is again diagonalizable. One can continue this scheme of approximating the full Hamiltonian, diagonalizing the approximated one, expressing the full Hamiltonian in terms of the newfound basis and approximating it more precisely by omitting a smaller amount of non-diagonal matrix elements, until the off-diagonal matrix elements can be considered a small enough perturbation so that they can be treated in low-order perturbation theory.

In this chapter, we will focus on the crudest approximation that still yields useful

results by reviewing the *clamped nuclei approximation (CNA)*, which yields an approximated Hamiltonian that describes a system of interacting electrons in a fixed electrostatic potential. In order to deal with the strong inter-electron Coulomb interaction, we will then review *density functional theory (DFT)* in the *Kohn-Sham (KS)* scheme, which, in its most basic form, approximates the exact two-body electron-electron interaction term of the Hamiltonian by a one-particle potential, which yields a diagonalizable Hamiltonian. Finally, we go back to the full CNA Hamiltonian and include the residual electron-electron interaction not considered in the Kohn-Sham approach in a perturbative way to obtain expressions for electronic correlation functions that will be needed in later parts of this thesis.

3.1 The clamped nuclei approximation

In order to obtain a first, reasonably accurate approximation of the matter Hamiltonian, we note that it contains a set of inherently small parameters in the form of the reciprocal masses of the nuclei, M_I^{-1} , which are very small compared to the reciprocal electron mass: $1/M_I \lesssim (1/1800) \times 1/m$. In a first approximation, we thus neglect the kinetic energy of the nuclei, which is proportional to $1/M_I$, entirely. In this *clamped nuclei approximation (CNA)*, the approximated Hamiltonian is defined as [92]¹

$$\hat{\mathcal{H}}_{\text{CNA}} \equiv \sum_i \frac{\hat{\mathbf{p}}_i^2}{2m} + \frac{1}{2} \sum_{\substack{i,j \\ i \neq j}} \frac{e^2}{|\hat{\mathbf{r}}_i - \hat{\mathbf{r}}_j|} + \sum_{i,I} \frac{-Z_I e^2}{|\hat{\mathbf{r}}_i - \hat{\mathbf{R}}_I|} + \frac{1}{2} \sum_{\substack{I,J \\ I \neq J}} \frac{Z_I Z_J e^2}{|\hat{\mathbf{R}}_I - \hat{\mathbf{R}}_J|}. \quad (3.1)$$

The absence of the nuclear momentum operators, $\hat{\mathbf{P}}_I$, means that the approximated Hamiltonian commutes with all nuclear position operators:

$$\left[\hat{\mathbf{R}}_I, \hat{\mathcal{H}}_{\text{CNA}} \right] = 0 \quad \forall I. \quad (3.2)$$

¹We again make use of a calligraphic font to denote operators that act in more than one subspace of the complete Hilbert space. In this case, $\hat{\mathcal{H}}_{\text{CNA}}$ acts on both the electronic and the nuclear part of the Hilbert space. Note that in the context of our discussion of the light-matter system, we used a non-calligraphic font to denote this kind of operator.

The eigenfunctions of $\hat{\mathcal{H}}_{\text{CNA}}$ can thus be chosen to be simultaneous eigenfunctions of all the $\hat{\mathbf{R}}_I$:²

$$|\nu, \{\mathbf{R}_I\}\rangle = |\nu(\{\mathbf{R}_I\})\rangle_e \otimes |\{\mathbf{R}_I\}\rangle_n, \quad (3.3)$$

where the subscripts “e” and “n” refer to the electronic and nuclei subspace of the electron-nuclei Hilbert space, respectively. The states $|\{\mathbf{R}_I\}\rangle_n$ are appropriately (anti-)symmetrized simultaneous eigenstates of all the $\hat{\mathbf{R}}_I$:

$$\hat{\mathbf{R}}_I |\{\mathbf{R}_I\}\rangle_n = \mathbf{R}_I |\{\mathbf{R}_I\}\rangle_n \quad \forall I, \quad (3.4)$$

while the quantum number ν distinguishes between different electronic states for a fixed nuclear configuration $\{\mathbf{R}_I\}$. The Schrödinger equation for the eigenstates of the CNA Hamiltonian then reads

$$\hat{\mathcal{H}}_{\text{CNA}} |\nu, \{\mathbf{R}_I\}\rangle = V_\nu(\{\mathbf{R}_I\}) |\nu, \{\mathbf{R}_I\}\rangle \quad (3.5)$$

and constitutes a set of independent equations, one for each fixed nuclear configuration $\{\mathbf{R}_I\}$. The ground state of $\hat{\mathcal{H}}_{\text{CNA}}$ can be found by first finding the electronic state $|0(\{\mathbf{R}_I\})\rangle_e$ that has the lowest energy for a given nuclear configuration $\{\mathbf{R}_I\}$ and then finding the nuclear configuration that minimizes the corresponding energy $V_\nu(\{\mathbf{R}_I\})$. We will denote the ground state of $\hat{\mathcal{H}}_{\text{CNA}}$ by $|0_{\text{CNA}}\rangle \equiv |0, \{\mathbf{R}_I^{(0)}\}\rangle = |\nu(\{\mathbf{R}_I^{(0)}\})\rangle_e \otimes |\{\mathbf{R}_I^{(0)}\}\rangle_n$ and the corresponding energy by $E_{0,\text{CNA}} \equiv V_0(\{\mathbf{R}_I^{(0)}\})$, with $\{\mathbf{R}_I^{(0)}\}$ being the nuclear configuration in the ground state.

From the form of the CNA Hamiltonian it is clear that the eigenvalues $V_\nu(\{\mathbf{R}_I\})$ have the form

$$V_\nu(\{\mathbf{R}_I\}) = V_\nu^{(\text{el})}(\{\mathbf{R}_I\}) + V^{(\text{nuc})}(\{\mathbf{R}_I\}), \quad (3.6)$$

²For instance, in case of a two-nuclei system, we have $\{\mathbf{R}_I\} = \{\mathbf{R}_1, \mathbf{R}_2\}$ and the wave function associated with the state $|\{\mathbf{R}_I\}\rangle_n$, $\Psi(\mathbf{r}_1, \mathbf{r}_2) \equiv {}_n\langle \mathbf{r}_1, \mathbf{r}_2 | \{\mathbf{R}_1, \mathbf{R}_2 \rangle_n$, would read

$$\Psi(\mathbf{r}_1, \mathbf{r}_2) = \frac{1}{\sqrt{2}} \left(\delta^{(3)}(\mathbf{r}_1 - \mathbf{R}_1) \delta^{(3)}(\mathbf{r}_2 - \mathbf{R}_2) \pm \delta^{(3)}(\mathbf{r}_1 - \mathbf{R}_2) \delta^{(3)}(\mathbf{r}_2 - \mathbf{R}_1) \right),$$

where the upper (lower) sign applies to bosons (fermions).

where

$$V^{(\text{nuc})}(\{\mathbf{R}_I\}) \equiv \frac{1}{2} \sum_{\substack{I,J \\ I \neq J}} \frac{Z_I Z_J e^2}{|\mathbf{R}_I - \mathbf{R}_J|} \quad (3.7)$$

is the contribution of the nuclei-nuclei Coulomb repulsion to the total energy. The electronic part of the total energy is determined from a Schrödinger equation in the electronic subspace only:

$$\hat{H}_e(\{\mathbf{R}_I\})|\nu(\{\mathbf{R}_I\})\rangle_e = V_\nu^{(\text{el})}(\{\mathbf{R}_I\})|\nu(\{\mathbf{R}_I\})\rangle_e, \quad (3.8)$$

where the Hamiltonian $\hat{H}_e(\{\mathbf{R}_I\})$ is an operator that acts in the electronic subspace only and parametrically depends on the set of all nuclear coordinates, $\{\mathbf{R}_I\}$:

$$\hat{H}_e(\{\mathbf{R}_I\}) \equiv \sum_i \frac{\hat{\mathbf{p}}_i^2}{2m} + \frac{1}{2} \sum_{\substack{i,j \\ i \neq j}} \frac{e^2}{|\hat{\mathbf{r}}_i - \hat{\mathbf{r}}_j|} + \sum_{i,I} \frac{-Z_I e^2}{|\hat{\mathbf{r}}_i - \mathbf{R}_I|.} \quad (3.9)$$

Within the clamped nuclei approximation, the problem of finding the eigenstates and -values of the electron-nuclei Hamiltonian is thus reduced to an infinite family of mutually independent, purely electronic eigenvalue problems. However, the presence of the inter-electron, two-particle Coulomb interaction term, which is too great to simply be neglected, requires another approximation if one wants to diagonalize $\hat{H}_e(\{\mathbf{R}_I\})$.

3.2 Kohn-Sham density functional theory

One possible and effective way of reducing the complexity of the problem is to replace the two-body Coulomb interaction term by an effective, one-particle potential and treat the difference between the exact two-body term and the approximated one as a small perturbation, which can then be treated within the framework of perturbation theory.

The most simple and straightforward way to approximate a two-body operator with a one-body one is by means of a *mean field approximation*, i.e., one replaces the interaction between all different pairs of two electrons by that of one electron moving in an average, not necessarily local, potential generated by all the other electrons. Math-

ematically, this physical idea is most easily implemented in the language of second quantization [90]. In this language, the inter-electron Coulomb interaction is expressed as

$$\frac{1}{2} \sum_{\substack{i,j \\ i \neq j}} \frac{e^2}{|\hat{\mathbf{r}}_i - \hat{\mathbf{r}}_j|} = \frac{1}{2} \int d^3r \int d^3r' \hat{\psi}^\dagger(\mathbf{r}) \hat{\psi}^\dagger(\mathbf{r}') \frac{e^2}{|\mathbf{r} - \mathbf{r}'|} \hat{\psi}(\mathbf{r}') \hat{\psi}(\mathbf{r}), \quad (3.10)$$

where the electron field operator is defined via $\hat{\psi}(\mathbf{r}) \equiv \sum_n \phi_n(\mathbf{r}) \hat{c}_n$, with $\{\phi_n(\mathbf{r})\}$ being a complete set of one-particle wave functions and the \hat{c}_n being the associated fermionic annihilation operators, which obey the canonical anti-commutation relations

$$\{\hat{c}_n, \hat{c}_{n'}\} = \{\hat{c}_n^\dagger, \hat{c}_{n'}^\dagger\} = 0, \quad \{\hat{c}_n, \hat{c}_{n'}^\dagger\} = \delta_{n,n'}. \quad (3.11)$$

A first, crude way to approximate the two-body operator, which depends on four electron field operators, with a one-body operator, which depends on only two electron field operators, is to replace one pair of field operators in Eq. 3.10 by their expectation value in the ground state of the resulting Hamiltonian:

$$\hat{\psi}^\dagger(\mathbf{r}) \hat{\psi}(\mathbf{r}_1) \xrightarrow{\text{HFA}} \langle 0_{\text{HF}} | \hat{\psi}^\dagger(\mathbf{r}) \hat{\psi}(\mathbf{r}_1) | 0_{\text{HF}} \rangle, \quad (3.12)$$

where \mathbf{r}_1 stands for either \mathbf{r} or \mathbf{r}' and $|0_{\text{HF}}\rangle$ denotes the ground state of the resulting Hamiltonian.³ This approximation is known as the Hartree-Fock approximation (HFA) [93–96]. The two field creation operators can be averaged pairwise with the two destruction field operators in a total of four different ways. However, due to the symmetry of the integral under the exchange of \mathbf{r} and \mathbf{r}' , only two terms are unique:

$$\begin{aligned} \frac{1}{2} \sum_{\substack{i,j \\ i \neq j}} \frac{e^2}{|\hat{\mathbf{r}}_i - \hat{\mathbf{r}}_j|} &\xrightarrow{\text{HFA}} e^2 \int d^3r \int d^3r' \hat{\psi}^\dagger(\mathbf{r}) \hat{\psi}(\mathbf{r}) \frac{\langle 0_{\text{HF}} | \hat{\psi}^\dagger(\mathbf{r}') \hat{\psi}(\mathbf{r}') | 0_{\text{HF}} \rangle}{|\mathbf{r} - \mathbf{r}'|} \\ &- e^2 \int d^3r \int d^3r' \hat{\psi}^\dagger(\mathbf{r}) \hat{\psi}(\mathbf{r}') \frac{\langle 0_{\text{HF}} | \hat{\psi}^\dagger(\mathbf{r}') \hat{\psi}(\mathbf{r}) | 0_{\text{HF}} \rangle}{|\mathbf{r} - \mathbf{r}'|}, \end{aligned} \quad (3.13)$$

³Since we are dealing with an entirely electronic problem, we dropped the subscript “e” on the states, with the understanding that all states reside in the electronic part of the electron-nuclei Hilbert space.

where the opposite sign of the second term arises from the fact that $\hat{\psi}(\mathbf{r})$ and $\hat{\psi}(\mathbf{r}')$ anti-commute. The electronic Hamiltonian in the HFA and in second quantization then takes on the form

$$\begin{aligned} \hat{H}_{\text{HF}} = & \int d^3r \hat{\psi}^\dagger(\mathbf{r}) \left(-\frac{\nabla^2}{2m} \right) \hat{\psi}(\mathbf{r}) + \int d^3r \hat{n}(\mathbf{r}) V_{\text{lat}}(\mathbf{r}; \{\mathbf{R}_I\}) \\ & + \int d^3r \hat{n}(\mathbf{r}) V_{\text{H}}(\mathbf{r}; \{\mathbf{R}_I\}) + \int d^3r \int d^3r' \hat{\psi}^\dagger(\mathbf{r}) \hat{\psi}(\mathbf{r}') \Sigma_{\text{x}}(\mathbf{r}, \mathbf{r}'; \{\mathbf{R}_I\}), \end{aligned} \quad (3.14)$$

where we defined the potential generated by the nuclei,

$$V_{\text{lat}}(\mathbf{r}; \{\mathbf{R}_I\}) \equiv \sum_I \frac{-Z_I e^2}{|\mathbf{r} - \mathbf{R}_I|} \quad (3.15)$$

and introduced the local *Hartree potential* V_{H} and the non-local (*Fock*) *exchange self-energy* Σ_{x} via

$$V_{\text{H}}(\mathbf{r}; \{\mathbf{R}_I\}) \equiv e^2 \int d^3r' \frac{n_{\text{HF}}^{(0)}(\mathbf{r}'; \{\mathbf{R}_I\})}{|\mathbf{r} - \mathbf{r}'|}, \quad (3.16)$$

$$\Sigma_{\text{x}}(\mathbf{r}, \mathbf{r}'; \{\mathbf{R}_I\}) \equiv -e^2 \frac{\langle 0_{\text{HF}}(\{\mathbf{R}_I\}) | \hat{\psi}^\dagger(\mathbf{r}') \hat{\psi}(\mathbf{r}) | 0_{\text{HF}}(\{\mathbf{R}_I\}) \rangle}{|\mathbf{r} - \mathbf{r}'|}, \quad (3.17)$$

with $\hat{n}(\mathbf{r}) \equiv \hat{\psi}^\dagger(\mathbf{r}) \hat{\psi}(\mathbf{r})$ being the charge density operator and

$$n_{\text{HF}}^{(0)}(\mathbf{r}; \{\mathbf{R}_I\}) \equiv \langle 0_{\text{HF}}(\{\mathbf{R}_I\}) | \hat{n}(\mathbf{r}) | 0_{\text{HF}}(\{\mathbf{R}_I\}) \rangle \quad (3.18)$$

being its expectation value in the self-consistent electronic ground state. Note that the ground state explicitly depends on the nuclei positions, as they appear as parameters in the Hamiltonian and hence the Hartree potential and the exchange self-energy do as well.

While the Hartree-Fock approximation yields excellent results for smaller atoms and molecules [92], it is much less viable in systems with many and partially mobile electrons. In these systems, higher-order, i.e., many-particle, correlation effects become more important. Mathematically, these are not captured in a simple mean field approach, such as the HFA, which is based around expectation values of one-body op-

erators only. Physically, many-body correlation effects are equivalent to a screening of the Coulomb interaction, which naturally play an important role in systems with many and partially mobile electrons, such as solids. As the HFA treats the Coulomb interaction as being unscreened, it severely tends to overestimate binding energies and bond strengths in these kinds of systems. For extended systems, therefore, a different approximation is required as the starting point of an efficient perturbative treatment, one that goes beyond a mean field approach and also captures higher-order correlation effects, but that still yields a diagonalizable Hamiltonian.

One such approximation has been first suggested by Kohn and Sham in 1965 [97], who built upon a work by Hohenberg and Kohn [98] on exact *density functional theory (DFT)*, published a year earlier. An extensive discussion of DFT and its practical applications can be found, for instance, in Ref. 92. Here we will just restrict ourselves to those elements of it that are needed for the work presented in this thesis as well as some motivating ideas.

The most important implication of exact DFT is the statement that all properties of a system of a fixed number of electrons, mutually interacting with each other via the pairwise Coulomb interaction and subject to an external electrostatic potential, are determined entirely by the electron density in the ground state. To put this statement into perspective, the properties of the system need not be determined from N -particle many-body wave functions, which depend on the $3N$ spatial coordinates of all the electrons, but instead can be treated as functionals of the electron density $n(\mathbf{r})$, which is a function of only *three* spatial coordinates. In particular, Hohenberg and Kohn proved two important theorems for Hamiltonians of the form

$$\begin{aligned} \hat{H} = & \int d^3r \hat{\psi}^\dagger(\mathbf{r}) \left(-\frac{\nabla^2}{2m} \right) \hat{\psi}(\mathbf{r}) + \int d^3r \hat{n}(\mathbf{r}) V_{\text{ext}}(\mathbf{r}) \\ & + \frac{1}{2} \int d^3r \int d^3r' \hat{\psi}^\dagger(\mathbf{r}) \hat{\psi}^\dagger(\mathbf{r}') \frac{e^2}{|\mathbf{r} - \mathbf{r}'|} \hat{\psi}(\mathbf{r}') \hat{\psi}(\mathbf{r}) \end{aligned} \quad (3.19)$$

which have a non-degenerate ground state:⁴

⁴The theorems also hold for degenerate ground states, as first shown by M. Levy [99–101].

1. The external potential $V_{\text{ext}}(\mathbf{r})$ is uniquely determined, up to a constant, by the ground state electron density $n^{(0)}(\mathbf{r})$, i.e., two different external potentials lead to two different electron densities. This implies in particular that all properties of the system are determined by the ground state electron density alone, since the latter fixes the external potential and hence the Hamiltonian, which in turn determines, in principle, all properties of the system.
2. The total energy of the system is a functional of the electron density $n(\mathbf{r})$ and can be written in the form

$$E[n] = E_{\text{HK}}[n] + \int d^3r n(\mathbf{r})V_{\text{ext}}(\mathbf{r}), \quad (3.20)$$

where, crucially, $E_{\text{HK}}[n]$ is a *universal* functional of the density, which is *the same for all external potentials* and can be written as $E_{\text{HK}} = T_{\text{HK}}[n] + V_{\text{HK}}[n]$, with $T_{\text{HK}}[n]$ and $V_{\text{HK}}[n]$ being functionals that yield the kinetic and inter-electron Coulomb interaction energy of the system, respectively. The ground state density $n^{(0)}(\mathbf{r})$ minimizes the functional $E[n]$.

Although these two theorems reduce, in principle, the number of degrees of freedom of the many-electron problem immensely, they do not offer a practical way to calculate the spectrum and eigenstates of the Hamiltonian, which we need for our description of inelastic light scattering. However, the fact that a *universal* energy functional for the inter-electron Coulomb interaction energy that only depends on the electron density exists offers new ways to calculate this part of the total energy. It may usefully be approximated with an expression from another, simpler-to-calculate system, such as the homogeneous electron gas, for which the Coulomb interaction energy can be calculated with the methods of perturbation theory.

Still, one needs a procedure to find not only the ground state energy or electron density of a system, but to also obtain the eigenstates and the corresponding energies of the Hamiltonian. The sole fact that the ground state electron density determines the latter *in principle* is *not* enough for this and a more concrete scheme is required. To this end, Kohn and Sham [97] introduced the idea of constructing the electron density from independent one-particle wave functions $\phi_i(\mathbf{r})$, which are eigenfunctions of an auxiliary

one-particle Hamiltonian \hat{H}_{KS} . In order to construct the auxiliary Hamiltonian, one introduces a new functional $E_{\text{KS}}[\{\phi_i\}, \{\phi_i^*\}]$ for the universal part of the energy which depends on $\phi_i(\mathbf{r})$ and $\phi_i^*(\mathbf{r})$ by demanding that

$$E_{\text{KS}}[\{\phi_i\}, \{\phi_i^*\}] = E_{\text{HK}}[n_{\text{KS}}], \quad (3.21)$$

where

$$n_{\text{KS}}(\mathbf{r}) \equiv \sum_i |\phi_i(\mathbf{r})|^2. \quad (3.22)$$

Furthermore, in order to arrive at a one-particle system, we introduce the kinetic energy part, $T_{\text{KS}}[\{\phi_i\}, \{\phi_i^*\}]$, of $E_{\text{KS}}[\{\phi_i\}, \{\phi_i^*\}]$ via:

$$T_{\text{KS}}[\{\phi_i\}, \{\phi_i^*\}] \equiv \sum_i \int d^3\mathbf{r} \phi_i^*(\mathbf{r}) \left(-\frac{\nabla^2}{2m} \right) \phi_i(\mathbf{r}) \equiv T_{\text{HK}}[n]. \quad (3.23)$$

It is also customary to split off the classical electrostatic energy, i.e., the Hartree energy

$$E_{\text{H}}[n] \equiv \frac{e^2}{2} \int d^3r \int d^3r' \frac{n(\mathbf{r})n(\mathbf{r}')}{|\mathbf{r} - \mathbf{r}'|}, \quad (3.24)$$

from the energy functional and define the remaining part as the *exchange-correlation functional*:

$$E_{\text{xc}}[n] \equiv E_{\text{HK}}[n] - T_{\text{HK}}[n] - E_{\text{H}}[n]. \quad (3.25)$$

The universal Kohn-Sham energy functional then reads

$$E_{\text{KS}}[\{\phi_i\}, \{\phi_i^*\}] = T_{\text{KS}}[\{\phi_i\}, \{\phi_i^*\}] + E_{\text{H}}[n_{\text{KS}}] + E_{\text{xc}}[n_{\text{KS}}], \quad (3.26)$$

with n_{KS} understood to be expressed in terms of the $\phi_i^{(*)}(\mathbf{r})$. Finally, we define the external energy functional by

$$E_{\text{ext}}[\{\phi_i\}, \{\phi_i^*\}] \equiv \int d^3r n_{\text{KS}}(\mathbf{r}) V_{\text{ext}}(\mathbf{r}) = \sum_i \int d^3r \phi_i^*(\mathbf{r}) V_{\text{ext}}(\mathbf{r}) \phi_i(\mathbf{r}). \quad (3.27)$$

Minimizing the total energy, $E_{\text{KS}} + E_{\text{ext}}$ under the constrain that the $\phi_i^{(*)}(\mathbf{r})$ remain

normalized, leads to the variational equation of motion

$$\frac{\delta}{\delta\phi_i^*(\mathbf{r})} \left\{ E_{\text{KS}}[\{\phi_j\}, \{\phi_j^*\}] + V_{\text{ext}}[\{\phi_j\}, \{\phi_j^*\}] - \sum_j \varepsilon_j |\phi_j(\mathbf{r})|^2 \right\} = 0, \quad (3.28)$$

in which the ε_j take on the role of Lagrange multipliers. Noting that $\partial n_{\text{KS}}(\mathbf{r})/\partial\phi_i^*(\mathbf{r}') = \phi_i(\mathbf{r})$, we arrive at a set of independent one-particle Schrödinger equations, the *Kohn-Sham (KS) equations*:

$$\left\{ -\frac{\nabla^2}{2m} + V_{\text{ext}}(\mathbf{r}) + V_{\text{H}}[n_{\text{KS}}](\mathbf{r}) + V_{\text{xc}}[n_{\text{KS}}](\mathbf{r}) \right\} \phi_i(\mathbf{r}) = \varepsilon_i \phi_i(\mathbf{r}). \quad (3.29)$$

Here, V_{H} and V_{xc} denote the one-particle Hartree and exchange-correlation *potentials*, respectively, given by

$$V_{\text{H}}[n](\mathbf{r}) \equiv \frac{\delta E_{\text{H}}[n]}{\delta n(\mathbf{r})} = e^2 \int d^3r' \frac{n(\mathbf{r}')}{|\mathbf{r} - \mathbf{r}'|}, \quad V_{\text{xc}}[n](\mathbf{r}) \equiv \frac{\delta E_{\text{xc}}[n]}{\delta n(\mathbf{r})}. \quad (3.30)$$

As mentioned above, the exchange-correlation functional can in many cases be well approximated by that of a known system. For solids with mostly mobile electrons, the exchange-correlation energy of the homogenous electron gas calculated from perturbation theory is often a reasonable approximation and was also suggested in the original paper by Kohn and Sham [97]. In modern times [92], a popular class of choices for the exchange-correlation energy functional is the semi-local approximation

$$E_{\text{xc}}^{\text{GGA}}[n] = \int d^3r n(\mathbf{r}) \varepsilon_{\text{xc}}^{\text{GGA}}(n(\mathbf{r}), \nabla n(\mathbf{r}) \dots), \quad (3.31)$$

where the dots represent higher derivatives of the electron density and the exchange-correlation density $\varepsilon_{\text{xc}}^{\text{GGA}}$ is a *function* of the charge density and its derivatives at the same point only. This approximation is known as the *generalized gradient approximation (GGA)* and is the most straightforward generalization of the entirely local *local density approximation (LDA)*

$$E_{\text{xc}}^{\text{LDA}}[n] = \int d^3r n(\mathbf{r}) \varepsilon_{\text{xc}}^{\text{LDA}}(n(\mathbf{r})). \quad (3.32)$$

In the early days of density functional theory, $\varepsilon_{\text{xc}}^{\text{LDA}}(n(\mathbf{r}))$ was suggested to be taken directly from the corresponding expressions for the homogeneous electron gas [97]. Nowadays, many different parameterizations for the exchange-correlation density and functional are available. Amongst the most popular ones for the LDA are the ones by Perdew and Zunger [102] and Perdew and Wang [103]. For the GGA, the by far most frequently used one is the parametrization by Perdew, Burke, and Ernzerhof (PBE) [104]. The calculations in this thesis were also done within one of these two approximations, as specified on a case-by-case basis.

In practice, the Kohn-Sham equations are solved self-consistently by starting with an initial guess for the KS electron density n_{KS} , calculating the *self-consistent field (SCF) potential*

$$V_{\text{scf}}(\mathbf{r}) \equiv V_{\text{ext}}(\mathbf{r}) + V_{\text{H}}[n_{\text{KS}}](\mathbf{r}) + V_{\text{xc}}[n_{\text{KS}}](\mathbf{r}), \quad (3.33)$$

solving the KS equations for the KS orbitals ϕ_i , and then finally calculating the KS electron density n_{KS} with the newly obtained KS orbitals. If the previous and the new KS electron density do not agree to within a specified tolerance, this procedure is repeated using a mixture between the old and the new KS electron density as input for the calculation of the SCF potential.⁵ This self-consistency cycle, as illustrated in Fig. 3.1, is then repeated until n_{KS} is converged. The resulting one-particle Hamiltonian can subsequently be used as a first approximation to the real Hamiltonian of the system under study.

In our case, we seek to approximate the Hamiltonian in the clamped nuclei approximation, for which the external potential is given by the potential of Eq. 3.15. For now we are interested in the case in which the nuclei are fixed in the ground state configuration $\{\mathbf{R}_I^{(0)}\}$, which, in the solid phase, typically has the nuclei arranged in a periodic lattice. In this case, there exists a set of three lattice vectors $\mathbf{t}_{1,2,3}$ that generate a Bravais lattice and a set of vectors $\boldsymbol{\tau}_\alpha$ that denote the positions of the different atoms in one unit cell of the lattice, so that every atomic position can be specified by an index

⁵A mixing of the old and new KS electron density is required to achieve convergence, as simply using the new density as input for the next step might result in oscillatory instead of converging behavior of the self-consistency cycle [92].

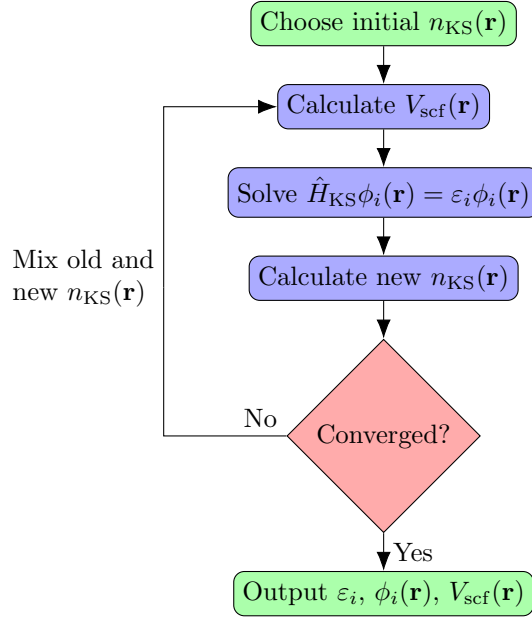


Figure 3.1: **Self-consistency cycle in Kohn-Sham density functional theory.**

n for the unit cell and an index α that runs over the different atoms within the unit cell:

$$\mathbf{R}_I^{(0)} \equiv \mathbf{R}_{n,\alpha}^{(0)} = \mathbf{R}_n + \boldsymbol{\tau}_\alpha, \quad (3.34)$$

where \mathbf{R}_n is a linear combination of the $\mathbf{t}_{1,2,3}$ with integer coefficients. The external (lattice) potential then can be written as

$$V_{\text{ext}}(\mathbf{r}) = V_{\text{lat}}(\mathbf{r}) = \sum_{n,\alpha} \frac{-Z_\alpha e^2}{|\mathbf{r} - \mathbf{R}_{n,\alpha}^{(0)}|} = \sum_{n,\alpha} \frac{-Z_\alpha e^2}{|\mathbf{r} - \mathbf{R}_n - \boldsymbol{\tau}_\alpha|}. \quad (3.35)$$

This potential is invariant under a shift $\mathbf{r} \rightarrow \mathbf{r} + \mathbf{R}_n$ as the shift can be absorbed by the summation over n . The electronic Hamiltonian as a whole and also the one-particle Kohn-Sham Hamiltonian are then invariant under these shifts, i.e., they commute with the set of the corresponding translation operators, $\{\exp(i\hat{\mathbf{p}} \cdot \mathbf{R}_n)\}$. We can then choose the eigenfunctions of the KS Hamiltonian to be eigenfunctions of *all* the $\{\exp(i\hat{\mathbf{p}} \cdot \mathbf{R}_n)\}$. These eigenfunctions can be labeled by a vector \mathbf{k} from within the Wigner-Seitz cell of the corresponding reciprocal lattice [105]. The latter is spanned by the reciprocal lattice

vectors $\mathbf{b}_{1,2,3}$, defined via $\mathbf{t}_i \cdot \mathbf{b}_j = 2\pi\delta_{i,j}$ and its Wigner-Seitz cell is also called the *first Brillouin zone (BZ)*. As a consequence, the eigenfunctions of the KS Hamiltonian can be written in the form

$$\phi_i(\mathbf{r}) \equiv \phi_{\mathbf{k},n}(\mathbf{r}) = \frac{1}{\sqrt{N}} e^{i\mathbf{k}\cdot\mathbf{r}} \chi_{\mathbf{k},n}(\mathbf{r}), \quad (3.36)$$

where n is an additional quantum number that labels the different states at a fixed \mathbf{k} , that is, the different energy bands in a solid, and N denotes the number of unit cells.⁶ The function $\chi_{\mathbf{k},n}(\mathbf{r})$ is lattice-periodic, i.e., $\chi_{\mathbf{k},n}(\mathbf{r} + \mathbf{R}_m) = \chi_{\mathbf{k},n}(\mathbf{r})$ for all lattice vectors \mathbf{R}_m , and is normalized with respect to an integration over one unit cell. The fact that the eigenfunctions of a one-particle Hamiltonian with lattice translation symmetry can be written in the form given in Eq. 3.36 has first been pointed out by F. Bloch [106] in 1929 and is nowadays known as *Bloch's theorem*. To give an example of the application of KS-DFT, we show the energy dispersion $\varepsilon_{\mathbf{k},n}$, i.e., the band structure, for graphene in Fig. 3.2. The Kohn-Sham system of independent particles is in many cases a very good approximation for the fully interacting electron system. However, the usage of a local or semi-local functional to capture the effects of exchange and correlation in an effective one-particle potential still has a few inherent shortcomings, which we want to briefly recapitulate, as they are important for some of the later work presented in this thesis.

The (semi-)local LDA and GGA functionals are modeled after the electron density dependence of the exchange and correlation energy of a homogeneous gas of free electrons. Compared to electrons under the influence of a lattice potential, electrons in a gas are much more mobile. As such, the inter-electron Coulomb interaction is significantly more screened in a gas than in a solid, which leads to larger correlation effects in the electron gas. The usage of an electron gas-inspired exchange-correlation functional for a solid-state system thus results in an overestimation of the screening of the Coulomb interaction between the electrons. In quantum mechanical terms, this has the effect that the different free-particle states are not coupled as strongly as they are in reality

⁶We work with periodic boundary conditions.

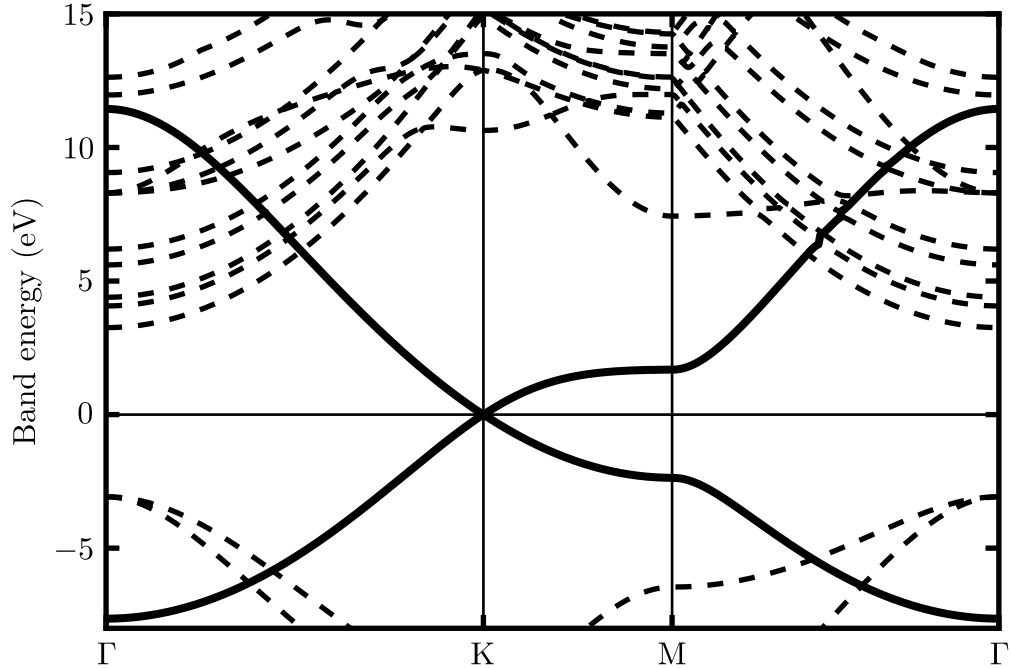


Figure 3.2: **Band structure of graphene within KS-DFT.** Band structure of graphene along the high-symmetry-line Γ - K - M - Γ of the first Brillouin zone (see Fig. 7.1 for a sketch of the first BZ). The calculation was done within the framework of Kohn-Sham density functional theory in the generalized gradient approximation (see Ref. 67 for numerical details and convergence parameters). Full lines represent the so-called π - and π^* -bands, whose wave functions can be well approximated by a linear combination of carbon p_z -like orbitals of the different atoms (also compare Section 7.1). The zero of the energy scale has been fixed to the Fermi energy, i.e., the largest energy of any occupied state.

and as a consequence the energy levels do not “repel” each other as strongly as they actually do. This implies that the use of (semi-local) exchange-correlation functionals leads to an underestimation of electronic band gaps of semi-conducting and insulating systems.

One very typical example of this problem is the case of hexagonal boron nitride (hBN), a material which is often used as a substrate for graphene. Due to the very

different electronegativities of boron and nitrogen, the electrons in the ground state tend to be much more localized on the sites of the nitrogen atoms, i.e., the electrons are much more localized in reality than in a quasi-free electron gas, which features strongly delocalized electrons. As a result, the screening of the inter-electron Coulomb interaction is severely overestimated and the band gap is thus very much underestimated. Numerically, one finds an indirect band gap of 3.9 eV for bulk hBN within density functional theory in the LDA [107]. By contrast, within many-body perturbation theory in the “GW approximation” (see next section), which features a more accurate description of the screening, one finds a sizably larger value of 5.4 eV for the indirect band gap of bulk hBN [107].

In the case of graphene, which is a semi-metallic system in which the electrons in the ground state are much more delocalized than in a typical semiconductor, the LDA and GGA give results that are much closer to the experimentally observed situation. However, the LDA and GGA still underestimate the slope of the bands near the linear crossing at the K point by roughly 12% [56]. This can again be interpreted in the quantum mechanical picture of the energy levels “not repelling each other enough”, due to a too weak, since overscreened, Coulomb interaction in the LDA and GGA.

Another consequence of the overestimation of the delocalization of the electrons caused by the use of free-electron gas-inspired functionals is the underestimation of the strength of the inter-atomic bonds, which, once again, could equally well be regarded as a consequence of the overestimation of screening effects. As a result, calculations of lattice constants and bond lengths within a local approximation to the exchange-correlation functional typically yield values that are too small compared to those observed in nature [92].

Finally, we would like to mention that the overestimation of the screening of the Coulomb interaction leads to a suppression of the long-range nature of the Coulomb interaction. This is especially relevant when considering perturbations of the lattice structure, such as lattice vibrations, which will be considered in the next chapter. A perturbation of the lattice structure from its equilibrium configuration manifests itself as a perturbation of the electrostatic lattice potential. However, due to an overestimation of electronic correlation effects, this perturbing potential will be treated as being

much more screened in LDA and GGA than it is in nature. As such, the response of the electronic system to the perturbation will be too weak. This can then manifest itself in an incorrect estimate of lattice vibration (*phonon*) frequencies as, for example, in the case of graphene [53], or in an underestimation of the influence of lattice vibrations on the electronic energy bands, such as in titanium diselenide [108]. The fact that it is mostly metallic or semi-metallic systems that are affected by the underestimation of the *response* to a perturbation can be understood from a real-space picture. As the Coulomb interaction is treated as overscreened, the inherent long-range nature of the Coulomb interaction is suppressed. As a result, electrons or nuclei located very far away from the real space location of the perturbation will not be as affected as they could be. However, in systems in which the electrons are very localized, the effect of a local perturbation on electrons very far away will not be large in any case. By contrast, in the more delocalized systems of (semi-)metals, electrons at large distances from the perturbation could in principle be affected by it, if it were not described as too short-ranged, i.e., too overscreened in local or semi-local approximations to the exchange-correlation functional.

For the work presented in this thesis, i.e., the inelastic scattering of light, foremost induced by lattice vibrations, the correct calculation of lattice vibration frequencies and correct estimation of the strength of the coupling of lattice vibrations to the electronic system is of vital importance. We will address these points in Chapters 4 and 5, in which we propose a novel theoretical approach and concrete expressions for the calculation of vibration frequencies and coupling constants. A key ingredient of the suggested approach will be a better description of electronic correlation effects. This can be achieved by using KS-DFT as a starting point of perturbation theory and treating the residual Coulomb interaction effects as a perturbation, which allows an efficient calculation of needed higher-order electronic correlation effects. We therefore dedicate the last section of this chapter to a review of the calculation of electronic correlation functions within *many-body perturbation theory (MBPT)*. As these correlation functions will play an important role in all of the following chapters, we will review them in some detail.

3.3 Many-particle electronic correlation functions

The new theoretical work presented in later parts of this thesis relies extensively on the formalism of many-particle Green's and correlation functions, i.e., expectation values of time-ordered products of electron field operators. As mentioned at the end of the last chapter, for this pioneering work, we will restrict ourselves to the case of zero temperature. In this section we shall therefore summarize the most important results and equations related to the needed electronic correlation functions. More extensive discussions can be found in the literature [91, 109, 110].

The modern treatment of correlation functions [91, 110] is typically based on a coupled set of equations known in condensed matter physics as the *Martin-Schwinger hierarchy* [111]. It consists of an infinite set of coupled integro-differential equations that link the various many-particle Green's functions with each other. The Martin-Schwinger hierarchy is a special case of the *Schwinger-Dyson equations*, which have been derived by Dyson using perturbative methods [112] and later also by Schwinger, who used functional derivative techniques [113, 114], similar to modern treatments [83, 88, 115].

For our purposes, it will be most convenient to follow Dyson's perturbative approach expressed in terms of *Feynman diagrams* [116], as this method allows us to only consider the correlation functions required for the development of our theoretical approach to Raman scattering. In particular, we will only be concerned with the one- and two-particle Green's and correlation functions, which we review over the course of the next two sections.

3.3.1 General considerations and one-particle Green's function

The the *one-particle Green's function* is defined as

$$G(1, 2) \equiv (-i)\langle 0 | \mathcal{T} \{ \hat{\psi}(1) \hat{\psi}^\dagger(2) \} | 0 \rangle. \quad (3.37)$$

Here and in the following, we use the abbreviated notation $1 \equiv (\mathbf{r}_1, t_1)$, etc., for the space-time argument of the electron field operators in the Heisenberg picture, defined

as

$$\hat{\psi}^{(\dagger)}(\mathbf{r}, t) \equiv e^{+i\hat{H}t}\hat{\psi}^{(\dagger)}(\mathbf{r})e^{-i\hat{H}t}. \quad (3.38)$$

We also use the shorter notation $\hat{H} \equiv \hat{H}_e(\{\mathbf{R}_I^{(0)}\})$ for the exact electronic Hamiltonian in the lowest-energy nuclear configuration $\{\mathbf{R}_I^{(0)}\}$ as given by Eq. 3.9, the ground state of which we denote as $|0\rangle \equiv |0(\{\mathbf{R}_I^{(0)}\})\rangle_e$.

The one-particle Green's function is the probability amplitude for an electron to travel from space-time point 2 to point 1 or vice versa in case of a hole. Its knowledge allows the calculation of the ground state expectation value of any one-particle operator. In particular, it contains information on the exact ground state charge density and even allows the calculation of the exact ground state energy [87]. We are mostly interested in it because it contains information on the exact one-particle excitation energies of the electronic system, including, for example, the band gap in a semi-conducting or insulating extended system. It will also be needed, in principle, for our review of the two-particle correlation function, presented in the next section.

The time-ordered expectation value of an arbitrary number of Heisenberg picture operators in the exact ground state of the full Hamiltonian can be calculated within the framework of time-dependent perturbation theory [83, 87–91], as already used in the previous chapter. In this formalism, the Hamiltonian is split up into two parts: $\hat{H} = \hat{H}_0 + \hat{H}_1$, where H_0 has a known (and presumed non-degenerate) ground state $|\emptyset\rangle$. One then defines the field operators in the interaction picture as

$$\hat{\psi}_I^{(\dagger)}(\mathbf{r}, t) \equiv e^{+i\hat{H}_0 t}\hat{\psi}_I^{(\dagger)}(\mathbf{r})e^{-i\hat{H}_0 t} \quad (3.39)$$

and the *non-interacting* Green's function as

$$G_0(1, 2) \equiv (-i)\langle\emptyset|\mathcal{T}\left\{\hat{\psi}_I(1)\hat{\psi}_I^\dagger(2)\right\}|\emptyset\rangle. \quad (3.40)$$

It can then be shown [83, 87–91] that the correlation function of two Heisenberg picture

field operators can be written as

$$\langle 0 | \mathcal{T} \{ \hat{\psi}(1) \hat{\psi}^\dagger(2) \} | 0 \rangle = \frac{\langle \emptyset | \mathcal{T} \left\{ \hat{\psi}_I(1) \hat{\psi}_I^\dagger(2) \exp \left[-i \int_{-\infty}^{+\infty} dt \hat{H}_{1,I}(t) \right] \right\} | \emptyset \rangle}{\langle \emptyset | \mathcal{T} \left\{ \exp \left[-i \int_{-\infty}^{+\infty} dt \hat{H}_{1,I}(t) \right] \right\} | \emptyset \rangle}, \quad (3.41)$$

where $\hat{H}_{1,I}(t) \equiv \exp(i\hat{H}_0 t) \hat{H}_1 \exp(-i\hat{H}_0 t)$ is the interaction Hamiltonian in the interaction picture.

The main challenge of the perturbative approach is then to select the reference Hamiltonian \hat{H}_0 such that both the non-interacting Green's function can be calculated exactly and the residual part $\hat{H}_1 = \hat{H} - \hat{H}_0$ of the full Hamiltonian can be considered a “small” perturbation, in the sense that the right-hand side of Eq. 3.41 can be well approximated by an exactly summable subseries of the Taylor series of the exponential function. In our concrete case, \hat{H} is the electronic Hamiltonian of Eq. 3.9, which describes a system of electrons moving in an external potential provided by a lattice of nuclei and which mutually interact with each other via the pairwise Coulomb interaction. As discussed in the last section, in many cases a first reasonable approximation of this system is provided by the non-interacting system of electrons of Kohn-Sham density functional theory. We will thus take the reference Hamiltonian to be

$$\hat{H}_0 \equiv \hat{H}_{\text{KS}}(\{\mathbf{R}_I^{(0)}\}) \equiv \int d^3r \hat{\psi}^\dagger(\mathbf{r}) \left[-\frac{\nabla^2}{2m} + V_{\text{scf}}(\mathbf{r}; \{\mathbf{R}_I^{(0)}\}) \right] \hat{\psi}(\mathbf{r}), \quad (3.42)$$

where $V_{\text{scf}}(\mathbf{r}; \{\mathbf{R}_I^{(0)}\})$ is the self-consistent potential of Eq. 3.33. The corresponding non-interacting Green's function can most easily be obtained by expanding the field operator in terms of the one-particle KS wave functions: $\hat{\psi}(\mathbf{r}) = \sum_{\mathbf{k},n} \phi_{\mathbf{k},n}(\mathbf{r}) \hat{c}_{\mathbf{k},n}$.⁷ In

⁷Here and throughout the remainder of this thesis, we understand summations over wave vectors \mathbf{k} from the first Brillouin zone to be appropriately normalized, such that, in the continuum limit, it reduces to an integration over the first Brillouin zone divided by the BZ volume: $\sum_{\mathbf{k}} \equiv V_{\text{BZ}}^{-1} \int_{\text{BZ}} d^3k = V_{\text{uc}}(2\pi)^{-3} \int_{\text{BZ}} d^3k$, with V_{uc} being the volume of the (real-space) unit cell.

this basis, the non-interacting Green's function is diagonal, i.e., it has the form

$$\begin{aligned}
G_0(1, 2) &= \sum_{\mathbf{k}, n} \phi_{\mathbf{k}, n}(\mathbf{r}_1) \phi_{\mathbf{k}, n}^*(\mathbf{r}_2) (-i) \langle \emptyset | \mathcal{T} \left\{ \hat{c}_{\mathbf{k}, n, I}(t_1) \hat{c}_{\mathbf{k}, n, I}^\dagger(t_2) \right\} | \emptyset \rangle \\
&\equiv \sum_{\mathbf{k}, n} \phi_{\mathbf{k}, n}(\mathbf{r}_1) \phi_{\mathbf{k}, n}^*(\mathbf{r}_2) \int \frac{d\omega}{2\pi} e^{-i\omega(t_1-t_2)} \tilde{G}_{0; \mathbf{k}, n}(\omega),
\end{aligned} \tag{3.43}$$

with the Fourier-transformed Green's function $\tilde{G}_{0; \mathbf{k}, n}(\omega)$ being given by

$$\begin{aligned}
\tilde{G}_{0; \mathbf{k}, n}(\omega) &\equiv \int_{-\infty}^{+\infty} dt e^{i\omega t} (-i) \langle \emptyset | \mathcal{T} \left\{ \hat{c}_{\mathbf{k}, n, I}(t) \hat{c}_{\mathbf{k}, n, I}^\dagger(0) \right\} | \emptyset \rangle \\
&= \frac{f_{\mathbf{k}, n}}{\omega - \varepsilon_{\mathbf{k}, n} - i\eta} + \frac{1 - f_{\mathbf{k}, n}}{\omega - \varepsilon_{\mathbf{k}, n} + i\eta},
\end{aligned} \tag{3.44}$$

wherein $f_{\mathbf{k}, n}$ denotes the occupancy of the state $|\mathbf{k}, n\rangle$ in the KS ground state $|\emptyset\rangle$ and η is a positive infinitesimal. Note that the *exact* one-particle Green's function $G(1, 2)$ is in general *off-diagonal* in the KS basis:

$$\begin{aligned}
G(1, 2) &= \sum_{\mathbf{k}, m, n} \phi_{\mathbf{k}, m}(\mathbf{r}_1) \phi_{\mathbf{k}, n}^*(\mathbf{r}_2) (-i) \langle 0 | \mathcal{T} \left\{ \hat{c}_{\mathbf{k}, m}(t_1) \hat{c}_{\mathbf{k}, n}^\dagger(t_2) \right\} | 0 \rangle \\
&\equiv \sum_{\mathbf{k}, m, n} \phi_{\mathbf{k}, m}(\mathbf{r}_1) \phi_{\mathbf{k}, n}^*(\mathbf{r}_2) \int \frac{d\omega}{2\pi} e^{-i\omega(t_1-t_2)} \tilde{G}_{\mathbf{k}, m, n}(\omega),
\end{aligned} \tag{3.45}$$

where

$$\tilde{G}_{\mathbf{k}, m, n}(\omega) \equiv \int_{-\infty}^{+\infty} dt e^{i\omega t} (-i) \langle 0 | \mathcal{T} \left\{ \hat{c}_{\mathbf{k}, m}(t) \hat{c}_{\mathbf{k}, n}^\dagger(0) \right\} | 0 \rangle \tag{3.46}$$

is the Fourier-transformed exact one-particle Green's function in the KS basis.

Finally, with our choice of \hat{H}_0 , the residual part of the Hamiltonian reads

$$\begin{aligned}
\hat{H}_1 \equiv \hat{H} - \hat{H}_0 &= \frac{1}{2} \int d^3r \int d^3r' \hat{\psi}^\dagger(\mathbf{r}) \hat{\psi}^\dagger(\mathbf{r}') \frac{e^2}{|\mathbf{r} - \mathbf{r}'|} \hat{\psi}(\mathbf{r}') \hat{\psi}(\mathbf{r}) \\
&\quad - \int d^3r \hat{\psi}^\dagger(\mathbf{r}) \left\{ V_{\text{H}}[n_{\text{KS}}](\mathbf{r}) + V_{\text{xc}}[n_{\text{KS}}](\mathbf{r}) \right\} \hat{\psi}(\mathbf{r}),
\end{aligned} \tag{3.47}$$

or in terms of the creation and annihilation operators for the KS one-particle states:

$$\hat{H}_1 = \sum_{\substack{\mathbf{k}, \mathbf{k}', \mathbf{q} \\ a, b, c, d}} v_{\mathbf{k}+\mathbf{q}, a; \mathbf{k}'+\mathbf{q}, b} \hat{c}_{\mathbf{k}+\mathbf{q}, a}^\dagger \hat{c}_{\mathbf{k}', d}^\dagger \hat{c}_{\mathbf{k}'+\mathbf{q}, b} \hat{c}_{\mathbf{k}, c} - \sum_{\substack{\mathbf{k} \\ a, b}} v_{\mathbf{k}}^{(\text{Hxc})} \hat{c}_{\mathbf{k}, a}^\dagger \hat{c}_{\mathbf{k}, b}, \quad (3.48)$$

where the matrix elements of the Coulomb and Hartree+xc potentials are defined as

$$v_{\substack{\mathbf{k}+\mathbf{q}, a; \mathbf{k}'+\mathbf{q}, b \\ \mathbf{k}, c; \mathbf{k}', d}} \equiv \int d^3 r \int d^3 r' \phi_{\mathbf{k}+\mathbf{q}, a}^*(\mathbf{r}) \phi_{\mathbf{k}', d}^*(\mathbf{r}') \frac{e^2}{|\mathbf{r} - \mathbf{r}'|} \phi_{\mathbf{k}'+\mathbf{q}, b}(\mathbf{r}') \phi_{\mathbf{k}, c}(\mathbf{r}) \quad (3.49)$$

$$v_{\substack{\mathbf{k} \\ a, b}}^{(\text{Hxc})} \equiv \int d^3 r \phi_{\mathbf{k}, a}^*(\mathbf{r}) \left\{ V_{\text{H}}[n_{\text{KS}}](\mathbf{r}) + V_{\text{xc}}[n_{\text{KS}}](\mathbf{r}) \right\} \phi_{\mathbf{k}, b}(\mathbf{r}). \quad (3.50)$$

Note that due to the fact that the electron density is lattice periodic, the Hartree and xc-potentials are as well and hence they conserve the (total) crystal momentum \mathbf{k} . The same is true for the Coulomb potential, which also conserves the total momentum of the two electrons interacting with each other. When passing to the interaction picture, the interaction Hamiltonian \hat{H}_1 becomes

$$\begin{aligned} \hat{H}_{1,I}(t_1) &= \frac{1}{2} \int d^3 r_1 \int d^3 r_2 \int_{-\infty}^{+\infty} dt_2 \hat{\psi}_I^\dagger(1) \hat{\psi}_I^\dagger(2) v(1, 2) \hat{\psi}_I(2) \hat{\psi}_I(1) \\ &\quad - \int d^3 r_1 \hat{\psi}_I^\dagger(1) v^{(\text{Hxc})}(\mathbf{r}_1) \hat{\psi}_I(1). \end{aligned} \quad (3.51)$$

Here we introduced the short-hand notation

$$v(1, 2) \equiv v(\mathbf{r}_1, t_1; \mathbf{r}_2, t_2) = v(\mathbf{r}_1 - \mathbf{r}_2, t_1 - t_2; \mathbf{0}, 0) \equiv \frac{e^2}{|\mathbf{r}_1 - \mathbf{r}_2|} \delta(t_1 - t_2) \quad (3.52)$$

$$v^{(\text{Hxc})}(\mathbf{r}_1) \equiv V_{\text{H}}[n_{\text{KS}}](\mathbf{r}_1) + V_{\text{xc}}[n_{\text{KS}}](\mathbf{r}_1) \quad (3.53)$$

for the Coulomb and Hartree+xc potential matrix elements in position space. Note that the instantaneous nature of the Coulomb potential is taken into account by including a factor of $\delta(t_1 - t_2)$.

According to Feynman [116], we can organize the perturbation series resulting from the right-hand side of Eq. 3.41 by associating a *Feynman diagram* with each introduced quantity, as shown in Table 3.1. In this “diagrammatic” approach, the exact one-



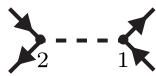
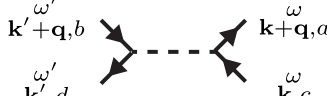
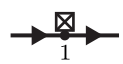
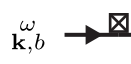




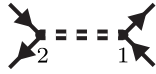
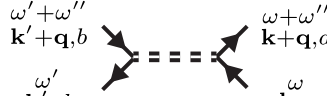
Real space	Momentum space
 = $iG_0(1, 2)$	 = $i\tilde{G}_{0;\mathbf{k},n}(\omega)$
 = $-iv(1, 2)$	 = $-iv_{\mathbf{k}+\mathbf{q},a;\mathbf{k}'+\mathbf{q},b}^{\omega}$ $\mathbf{k},c;\mathbf{k}',d$
 = $iv^{(\text{Hxc})}(\mathbf{r}_1)$	 = $iv_{\mathbf{k}}^{(\text{Hxc})}$ a,b
 = $iG(1, 2)$	 = $i\tilde{G}_{\mathbf{k},m,n}(\omega)$
 = $-i\Sigma(1, 2)$	 = $-i\tilde{\Sigma}_{\mathbf{k},m,n}(\omega)$
 = $-iW(1, 2)$	 = $-i\tilde{W}_{\mathbf{k}+\mathbf{q},a;\mathbf{k},c}^{\omega+\omega''}$ $\mathbf{k}'+\mathbf{q},b;\mathbf{k}',d$

Table 3.1: Feynman rules for the basic building blocks of electronic correlation functions and some derived quantities (separated by a horizontal line).⁹

particle Green's function is then given by the sum of all *fully connected* diagrams with two endpoints, with exactly one electron line and no Coulomb lines emerging from one of them and exactly one electron line and no Coulomb lines running into the other one.

To organize this series of diagrams, one introduces the (*one-particle-*) *irreducible self-energy* $\Sigma(1, 2)$, which is defined as i times the sum of all connected Feynman diagrams that cannot be split into two parts by cutting a single electron line only.¹⁰ The sum of all possible diagrams contributing to the exact one-particle Green's function then takes on the form of a geometric series, as shown in Fig. 3.3. On the right hand side, we can identify the exact Green's function once again, so that the diagrammatic sum

⁹Note that the index structure on the matrix elements of v and W in momentum space is different, as it will be more convenient for the later discussion of the two-particle correlation function.

¹⁰The factor of i is included so that the sum of diagrams equals $(-i)\Sigma(1, 2)$, so that in turn the factor of $(-i)$ cancels the factor of i from the factor $iG_0(1, 2)$ associated with a single electron line.

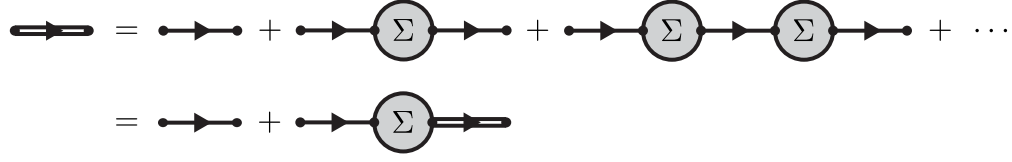


Figure 3.3: **Diagrammatic representation of Dyson's equation for the one-particle electron Green's function.**

is equivalent to Dyson's equation [112]

$$G(1, 2) = G_0(1, 2) + G_0(1, \bar{3})\Sigma(\bar{3}, \bar{4})G(\bar{4}, 2), \quad (3.54)$$

where the bar over a variable indicates that it is integrated over:

$$f(\bar{1})g(\bar{1}) \equiv \int d1 f(1)g(1) \equiv \int_{-\infty}^{+\infty} dt_1 \int d^3r_1 f(\mathbf{r}_1, t_1)g(\mathbf{r}_1, t_1). \quad (3.55)$$

A few of the leading-order terms contributing to the irreducible self-energy are shown in Fig. 3.4. Note that the exact irreducible self-energy involves subseries of diagrams

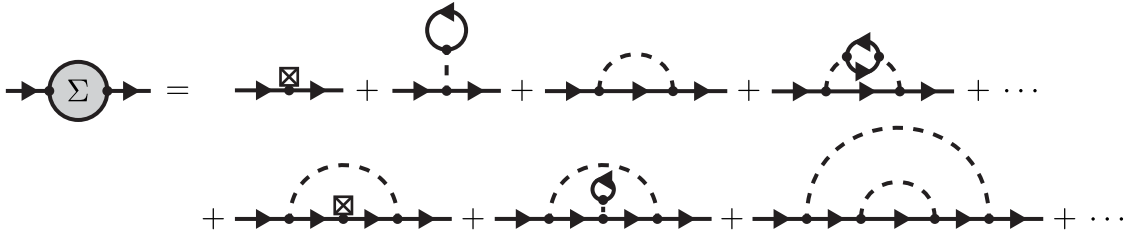


Figure 3.4: **Leading-order terms in the diagrammatic expansion of the irreducible electron self-energy.**

that can be summed up to yield the exact Green's function again (compare second row of diagrams in 3.4). It can therefore be regarded as a functional of the exact one-particle Green's function and the Kohn-Sham electron density, on which it depends through the second term in Eq. 3.47: $\Sigma(1, 2) = \Sigma[G, n_{KS}](1, 2)$. Since this second term involves only two electron field operators, the only one-particle-irreducible (sub-)diagram that can be constructed from it is simply given by the vertex associated with it. The irreducible

self-energy is then given by the sum of two parts:

$$\Sigma[G, n_{\text{KS}}](1, 2) = \Sigma_{\text{Coul.}}[G](1, 2) + \Sigma_{-\text{Hxc}}[n_{\text{KS}}](1, 2), \quad (3.56)$$

where¹¹

$$\Sigma_{-\text{Hxc}}[n_{\text{KS}}](1, 2) \equiv -v^{(\text{Hxc})}(\mathbf{r}_1)\delta(1, 2) = -\left\{V_{\text{H}}[n_{\text{KS}}](\mathbf{r}_1) + V_{\text{xc}}[n_{\text{KS}}](\mathbf{r}_1)\right\}\delta(1, 2) \quad (3.57)$$

is the contribution of the Hartree and exchange-correlation potential used in the reference KS system and $\Sigma_{\text{Coul.}}[G](1, 2)$ is given by the sum of all one-particle irreducible diagrams that involve at least one Coulomb line. Examples of this kind of diagrams are given by the last three diagrams of the first row in Fig. 3.4. Just like the exact and KS one-particle Green's functions, the irreducible self-energy can also be expanded in the basis of KS states:

$$\Sigma(1, 2) \equiv \sum_{\mathbf{k}, m, n} \phi_{\mathbf{k}, m}(\mathbf{r}_1)\phi_{\mathbf{k}, n}^*(\mathbf{r}_2) \int \frac{d\omega}{2\pi} e^{-i\omega(t_1-t_2)} \tilde{\Sigma}_{\mathbf{k}, m, n}(\omega), \quad (3.58)$$

where the conservation of crystal momentum at each vertex implies that the self-energy is diagonal in \mathbf{k} .

After a Fourier transformation, Dyson's equation takes on the form of a matrix equation in the space of electronic bands:

$$\tilde{G}_{\mathbf{k}, a, b}(\omega) = \delta_{a, b} \tilde{G}_{0; \mathbf{k}, a}(\omega) + \tilde{G}_{0; \mathbf{k}, a}(\omega) \tilde{\Sigma}_{\mathbf{k}, a, \bar{c}}(\omega) \tilde{G}_{\mathbf{k}, \bar{c}, b}(\omega), \quad (3.59)$$

where a bar over a band index implies a summation over it. Solving for the exact one-particle Green's function, one obtains the following expression for its matrix inverse in the $\eta \rightarrow 0$ limit:

$$\tilde{G}_{\mathbf{k}, a, b}^{-1}(\omega) = (\omega - \varepsilon_{\mathbf{k}, a})\delta_{a, b} - \tilde{\Sigma}_{\mathbf{k}, a, b}(\omega). \quad (3.60)$$

Thus, the exact one-particle Green's function is determined from knowledge of the matrix elements of the irreducible self-energy in the KS basis, which can be calculated diagrammatically. Note that in principle, and *especially for the purpose of further*

¹¹ $\delta(1, 2) \equiv \delta^{(3)}(\mathbf{r}_1 - \mathbf{r}_2)\delta(t_1 - t_2)$ denotes a four-dimensional δ -distribution.

derivations, it needs to be computed *self-consistently*, since it depends on the exact one-particle Green's function $\tilde{G}_{\mathbf{k},a,b}(\omega)$. In a practical calculation, however, one almost never considers the full diagrammatic series for the irreducible self-energy, but instead considers only certain subsets or subseries of diagrams. The most popular of these approximations is the so-called *GW approximation (GWA)* [91, 109, 110, 117], defined by the series of diagrams depicted in the first row of Fig. 3.5. In the second row of

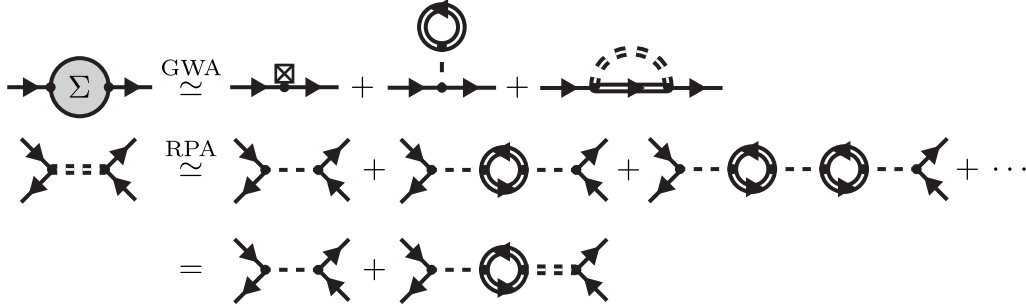


Figure 3.5: **Diagrams representing the terms retained in the GW approximation to the irreducible self-energy.**

Fig. 3.5, we defined the diagrammatic representation of the *screened* Coulomb interaction $W(1, 2) = W(2, 1)$ in the *random phase approximation (RPA)*¹², which obeys the Dyson-like equation

$$W(1, 2) = v(1, 2) + v(1, \bar{3})P(\bar{3}, \bar{4})W(\bar{4}, 2). \quad (3.61)$$

Here the *irreducible polarizability* $P(1, 2)$ is defined in analogy with the irreducible self-energy as $(-i)$ times the sum of all connected Feynman diagrams that cannot be split into two by cutting a single Coulomb line.¹³ In the RPA, it is simply given by

$$P(1, 2) \simeq P_0(1, 2) \equiv -iG(1, 2)G(2, 1). \quad (3.62)$$

¹²Note that the screened Coulomb interaction only appears in the third diagram of Fig. 3.5 and not in the second, since its inclusion in the latter would lead to a double-counting of diagrams which have already been taken into account in the diagrammatic expansion of the exact one-particle Green's function represented by the loop subdiagram.

¹³The factor of $(-i)$ is again included in the definition of the polarizability so that the sum of diagrams equals $iP(1, 2)$, so that in turn the factor of i cancels the factor of $(-i)$ included in the factor $-iv(1, 2)$ associated with a single Coulomb line.

In practical calculations, this equation is usually solved by Fourier transforming with respect to both space and time and then inverting the resulting matrix equation on a grid of reciprocal lattice vectors [109, 110]. Once the screened Coulomb interaction has been computed, the irreducible self-energy in the GWA can be calculated from

$$\Sigma(1, 2) \simeq -\delta(1, 2)v^{(\text{Hxc})}(1) - i\delta(1, 2)v(1, \bar{3})G(3, \bar{3}^+) + iG(1, 2)W(1, 2), \quad (3.63)$$

where $3^+ \equiv (\mathbf{r}_3, t_3^+) \equiv (\mathbf{r}_3, t_3 + 0^+)$ and 0^+ denotes a positive infinitesimal that is needed in order to ensure the correct ordering of electron field operators in an equal-time correlation function, which needs to follow the ordering in the interaction Hamiltonian ($\hat{\psi}^\dagger$ to the left of $\hat{\psi}$). The calculation of the self-energy is also most conveniently done in reciprocal space, from where it can be written in the KS basis by projecting on the KS wave functions.

We want to emphasize once more that for the theoretical developments presented in this thesis, the self-consistent treatment of Dyson's equation for the exact one-particle Green's function will turn out to be crucial. For many practical applications and computations, however, a self-consistent solution of Eqs. 3.54, 3.61, 3.62, and 3.63 is not necessary and instead a non-self-consistent calculation according to the scheme

$$P(1, 2) \simeq P_0(1, 2) \equiv -iG_0(1, 2)G_0(2, 1) \quad (3.64)$$

$$\rightarrow W(1, 2) \simeq W_0(1, 2) \equiv v(1, 2) + v(1, \bar{3})P_0(\bar{3}, \bar{4})W_0(\bar{4}, 2) \quad (3.65)$$

$$\rightarrow \Sigma(1, 2) \simeq \Sigma_0(1, 2) \equiv -\delta(1, 2)v^{(\text{xc})}(\mathbf{r}_1) + iG_0(1, 2)W_0(1, 2) \quad (3.66)$$

$$\rightarrow G(1, 2) \simeq G_0(1, 2) + G_0(1, \bar{3})\Sigma_0(\bar{3}, \bar{4})G(\bar{4}, 2), \quad (3.67)$$

called the G_0W_0 approximation, is sufficient for most purposes [109, 110].¹⁴

An additional approximation that is also often employed is the so-called *quasi-particle approximation (QPA)*. It is based on the observation that in many cases [109, 110], the exact Green's function can reasonably accurately be approximated by a func-

¹⁴In the third line, we simplified the expression by noting that in the non-self-consistent case the Hartree contribution reads $-iv(1, \bar{3})G_0(\bar{3}, \bar{3}^+) = e^2 \int d^3r_3 n_{\text{KS}}(\mathbf{r}_3)/|\mathbf{r}_1 - \mathbf{r}_3|$, which exactly cancels the Hartree part of the $v^{(\text{Hxc})}(1)$ contribution to the self-energy, so that only the exchange-correlation potential contribution needs to be computed explicitly.

tion with a simple pole near the unperturbed one-particle energy:¹⁵

$$\tilde{G}_{\mathbf{k},m,n}(\omega) \approx \delta_{m,n} \frac{Z_{\mathbf{k},n}^{(\text{QP})}}{\omega - \varepsilon_{\mathbf{k},n}^{(\text{QP})} + \frac{i}{2}\gamma_{\mathbf{k},n}^{(\text{QP})}}. \quad (3.68)$$

Here, the *quasi-particle weight*, *energy*, and *decay width* are defined by [109, 110]

$$Z_{\mathbf{k},n}^{(\text{QP})} \equiv 1 / \left(1 - \left. \frac{\partial \tilde{\Sigma}_{\mathbf{k},n,n}(\omega)}{\partial \omega} \right|_{\omega=\varepsilon_{\mathbf{k},n}} \right) \quad (3.69)$$

$$\varepsilon_{\mathbf{k},n}^{(\text{QP})} \equiv \varepsilon_{\mathbf{k},n} + \text{Re} \left(Z_{\mathbf{k},n}^{(\text{QP})} \tilde{\Sigma}_{\mathbf{k},n,n}(\omega) \Big|_{\omega=\varepsilon_{\mathbf{k},n}} \right) \quad (3.70)$$

$$\gamma_{\mathbf{k},n}^{(\text{QP})} \equiv -2 \text{Im} \left(Z_{\mathbf{k},n}^{(\text{QP})} \tilde{\Sigma}_{\mathbf{k},n,n}(\omega) \Big|_{\omega=\varepsilon_{\mathbf{k},n}} \right) = \begin{cases} \leq 0, & |\mathbf{k}, n\rangle \text{ occupied in } |\emptyset\rangle \\ \geq 0, & |\mathbf{k}, n\rangle \text{ not occupied in } |\emptyset\rangle \end{cases}, \quad (3.71)$$

where the sign of the decay width follows the sign of the infinitesimal η in Eq. 3.44. In the QPA, the exact Green's function is then simply given by

$$G(1, 2) \stackrel{QPA}{\approx} G^{(\text{QP})}(1, 2) \equiv \sum_{\mathbf{k},n} \phi_{\mathbf{k},n}(\mathbf{r}_1) \phi_{\mathbf{k},n}^*(\mathbf{r}_2) \int \frac{d\omega}{2\pi} e^{-i\omega(t_1-t_2)} \frac{Z_{\mathbf{k},n}^{(\text{QP})}}{\omega - \varepsilon_{\mathbf{k},n}^{(\text{QP})} + \frac{i}{2}\gamma_{\mathbf{k},n}^{(\text{QP})}} \quad (3.72)$$

and describes non-interacting (“quasi-”)particles of energy $\varepsilon_{\mathbf{k},n}^{(\text{QP})}$, which possess a *finite* lifetime $\tau_{\mathbf{k},n} = 1/\gamma_{\mathbf{k},n}^{(\text{QP})}$, as easily seen by evaluating the frequency integral. The QPA is sensible as long as the quasi-particle decay width are reasonably smaller than the quasi-particle energies. This approximation often serves as the starting point for the calculation of the two-particle Green's function, to which we turn in the next section.

¹⁵Here we further assumed for simplicity that the exact Green's function near the quasi-particle pole can be well approximated as being diagonal in the KS basis, which is often a reasonable approximation [109, 110]. In case this approximation is not good, one first needs to diagonalize the exact Green's function by solving the eigenvalue problem given in Eq. 3.60.

3.3.2 Two-particle correlation function

The one-particle Green's function, treated in the previous section, contains information on the propagation of one electron, or, equivalently, on the correlation between the values of the electron field at one pair of points in space and time. For many topics discussed in this thesis, higher-order correlations are of even bigger importance, however, in particular correlations between the values of the electron field at *two* pairs of space-time points. In a more intuitive language, this is equivalent to the correlated propagation of two charge carriers (two electrons, two holes, or one electron and one hole). This correlated propagation amplitude is given by the two-particle Green's function

$$G^{(2)}(1, 2; 3, 4) \equiv (-i)^2 \langle 0 | \mathcal{T} \left\{ \hat{\psi}(1) \hat{\psi}(4) \hat{\psi}^\dagger(2) \hat{\psi}^\dagger(3) \right\} | 0 \rangle. \quad (3.73)$$

As it describes the correlated movement of two charge carriers, it also contains information on two-particle scattering amplitudes and furthermore also on possible bound states (called *excitons*), in case of the two charge carriers being one electron and one hole. Since it will be needed in several instances throughout this thesis, we will review the most important aspects of its calculation.

To begin with, we re-write the ground state expectation value of a time-ordered product of four electron field operators in the Heisenberg picture in the interaction picture:

$$\begin{aligned} & \langle 0 | \mathcal{T} \left\{ \hat{\psi}(1) \hat{\psi}(4) \hat{\psi}^\dagger(2) \hat{\psi}^\dagger(3) \right\} | 0 \rangle \\ &= \frac{\langle \emptyset | \mathcal{T} \left\{ \hat{\psi}_I(1) \hat{\psi}_I(4) \hat{\psi}_I^\dagger(2) \hat{\psi}_I^\dagger(3) \exp \left[-i \int_{-\infty}^{+\infty} dt \hat{H}_{1,I}(t) \right] \right\} | \emptyset \rangle}{\langle \emptyset | \mathcal{T} \left\{ \exp \left[-i \int_{-\infty}^{+\infty} dt \hat{H}_{1,I}(t) \right] \right\} | \emptyset \rangle}, \end{aligned} \quad (3.74)$$

where the definitions of the various operators were given in the previous section. The right-hand side can again be expanded in terms of the elementary Feynman diagrams of Table 3.1. To organize the various diagrams, we employ the *skeleton expansion* [91, 115], which consists of summing certain subseries of diagrams exactly and using the result as part of a larger diagram. For the case of the two-particle Green's function, this

amounts to first summing the Dyson series for each appearing non-interacting one-particle Green's function and then replacing the latter in larger diagrams with the *exact* one-particle Green's function. This is done with the understanding that all other one-particle irreducible diagrams are to be omitted, as these have already been taken into account via Dyson's equation and the irreducible self-energy. Within the skeleton expansion, a selection of leading-order diagrams contributing to the two-particle Green's function are shown in Fig. 3.6. The first two terms constitute the *independent-particle*

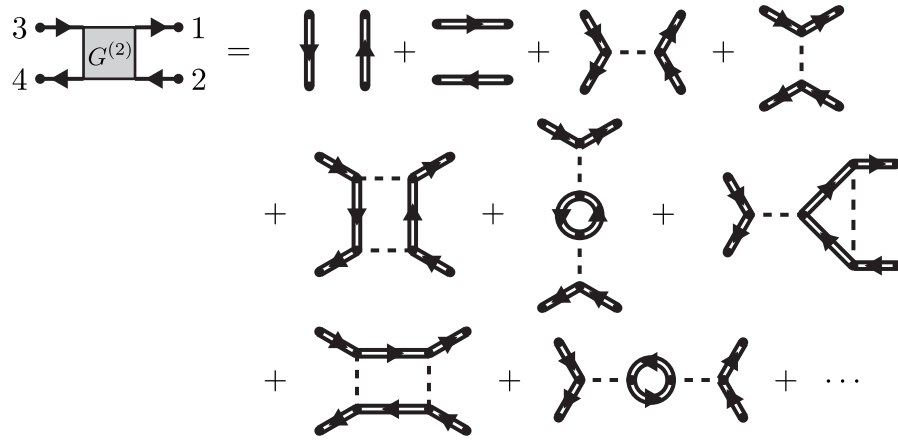


Figure 3.6: **Examples of leading-order terms in the diagrammatic expansion of the two-particle Green's function.**

approximation:

$$\begin{aligned}
 G^{(2)}(1, 2; 3, 4) &\stackrel{\text{IPA}}{\simeq} (-i)^2 \left[-\langle 0 | \mathcal{T} \{ \hat{\psi}(1) \hat{\psi}^\dagger(2) \} | 0 \rangle \langle 0 | \mathcal{T} \{ \hat{\psi}(4) \hat{\psi}^\dagger(3) \} | 0 \rangle \right. \\
 &\quad \left. \langle 0 | \mathcal{T} \{ \hat{\psi}(1) \hat{\psi}^\dagger(3) \} | 0 \rangle \langle 0 | \mathcal{T} \{ \hat{\psi}(4) \hat{\psi}^\dagger(2) \} | 0 \rangle \right] \quad (3.75) \\
 &= -G(1, 2)G(4, 3) + G(1, 3)G(4, 2),
 \end{aligned}$$

where the minus sign of the first term arises from the anti-commuting nature of the electron field operators. In this approximation, the propagation of the two charge carriers is uncorrelated, i.e., the two charge carriers move independent of each other. From Fig. 3.6 it becomes clear that the second term appears repeatedly as a subdiagram in the diagrammatic expansion of the two-particle Green's function, while the first term

only appears once in the very leading order. It thus has become common [109, 110] to introduce the *two-particle correlation function*

$$\begin{aligned}
 L(1, 2; 3, 4) &\equiv G^{(2)}(1, 2; 3, 4) + G(1, 2)G(4, 3) \\
 &\stackrel{\text{IPA}}{\simeq} G(1, 3)G(4, 2) \equiv L_0(1, 2; 3, 4),
 \end{aligned}
 \tag{3.76}$$

where in the second line we defined its independent-particle version. We diagrammatically represent the two-particle correlation functions $L(1, 2; 3, 4)$ and $L_0(1, 2; 3, 4)$ as shown in Fig. 3.7.

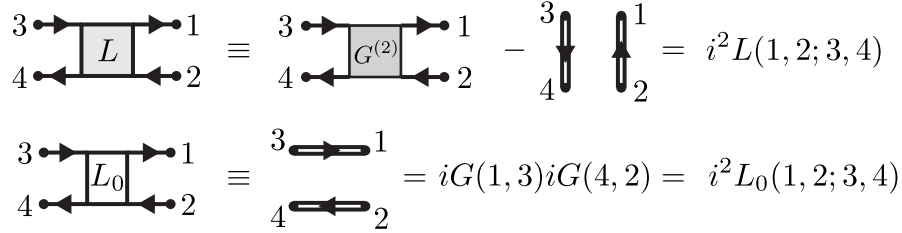


Figure 3.7: **Diagrammatic representation of the two-particle correlation function.**

The perturbation series for $L(1, 2; 3, 4)$ can be organized even further and cast into a Dyson-like equation by introducing the notion of the (*two-particle-*) *irreducible interaction kernel* $K^{(2)}(1, 2; 3, 4)$, akin to the (*one-particle-*) irreducible self-energy. We define it as the sum of all diagrams that do not fall into two pieces if only two electron lines are cut. The leading-order terms contributing to the irreducible interaction kernel are depicted in Fig. 3.8. As in the case of the irreducible self-energy, we can take more subseries of diagrams into account by replacing the Coulomb interaction lines by lines representing the screened Coulomb interaction, in all but the first diagram, as an inclusion of the screened Coulomb interaction there would render the diagram *two-particle reducible*. For example, the consideration of the first row of diagrams and including the screened Coulomb interaction would lead to the following expression for the interaction

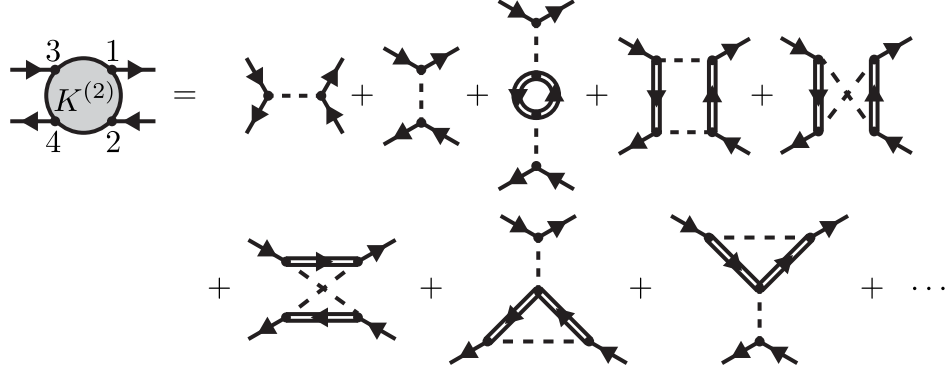


Figure 3.8: **Leading order terms in the diagrammatic expansion of the irreducible interaction kernel.**

kernel:

$$\begin{aligned}
 (-i)^2 K^{(2)}(1, 2; 3, 4) \simeq & i\delta(1, 2)\delta(3, 4)v(1, 3) - i\delta(1, 3)\delta(2, 4)W(1, 2) \\
 & - G(1, 2)W(1, 3)G(4, 3)W(2, 4) - G(1, 2)W(1, 4)G(4, 3)W(2, 3).
 \end{aligned}
 \tag{3.77}$$

Note that we have defined the diagrammatic representation of the two-particle interaction kernel to correspond to $(-i)^2 K^{(2)}(1, 2; 3, 4)$, similar to how we defined the diagrammatic representation of the irreducible self-energy to correspond to $(-i)\Sigma(1, 2)$.¹⁶ The additional minus signs in the first, third, and fourth terms arise due to the anti-commuting nature of the fermion field operators. Equivalently, one notes that these diagrams, when inserted into another diagram, would lead to an additional closed fermion loop, and hence this minus sign corresponds to the minus sign that is normally prescribed to be included for a closed fermion loop [83, 87–89, 91, 115].

The exact two-particle-irreducible interaction kernel obeys the relation

$$K^{(2)}(1, 2; 3, 4) = \frac{\delta\Sigma_{\text{Coul.}}(1, 2)}{\delta G(3, 4)},
 \tag{3.78}$$

where $\delta/\delta G(3, 4)$ denotes a functional derivative. This identity plays an important role

¹⁶This is done so that the factors of $\pm i$ cancel between the interaction kernel and the two-particle correlation function, whose diagrammatic representation corresponds to $i^2 L(1, 2; 3, 4)$, similar to how a single-particle line corresponds to $iG(1, 2)$.

in later chapters of this thesis. To illustrate its validity, consider the case of the GW approximation to the self-energy:

$$\Sigma_{\text{Coul.}}(1, 2) \stackrel{\text{GWA}}{\simeq} -iv(1, \bar{3})G(\bar{3}, \bar{3}^+) + iG(1, 2)W[G](1, 2) \quad (3.79)$$

(compare Eq. 3.63) and hence

$$\begin{aligned} K^{(2)}(1, 2; 3, 4) \stackrel{\text{GWA}}{\simeq} & -i\delta(1, 2)\delta(3, 4)v(1, 3) + i\delta(1, 3)\delta(2, 4)W(1, 2) \\ & + G(1, 2)W(1, 3)G(4, 3)W(2, 4) + G(1, 2)W(1, 4)G(4, 3)W(2, 3). \end{aligned} \quad (3.80)$$

Here, the functional derivative of $W[G](1, 2)$ was computed via the relation

$$W^{-1}(1, \bar{3})W(\bar{3}, 2) = \delta(1, 2) \Rightarrow \frac{\delta W(1, 2)}{\delta G(3, 4)} = -W(1, \bar{5}) \frac{\delta W^{-1}(\bar{5}, \bar{6})}{\delta G(3, 4)} W(\bar{6}, 2), \quad (3.81)$$

with the functional derivative of the inverse of $W(1, 2)$ being easily obtained from

$$W^{-1}(1, 2) = v^{-1}(1, 2) - P(1, 2) \stackrel{\text{RPA}}{\simeq} v^{-1}(1, 2) + iG(1, 2)G(2, 1), \quad (3.82)$$

according to Eq. 3.62. This result matches that obtained via the diagrammatic expansion, given in Eq. 3.77. The general proof is best done diagrammatically and can be found in the literature [91].

In terms of the two-particle-irreducible interaction kernel, the perturbative expansion for the two-particle correlation function $L(1, 2; 3, 4)$ takes on the diagrammatic form shown in Fig. 3.9. This diagrammatic identity corresponds to the integral equation

$$L(1, 2; 3, 4) = L_0(1, 2; 3, 4) + L_0(1, 2; \bar{5}, \bar{6})K^{(2)}(\bar{5}, \bar{6}; \bar{7}, \bar{8})L(\bar{7}, \bar{8}; 3, 4), \quad (3.83)$$

which is known as the *Bethe-Salpeter equation (BSE)*, after E. Salpeter and H. Bethe, who derived it in 1951 and used it to find the binding energy of the deuteron [118]. It was also discussed extensively by G. Wick [119] and R. Cutkosky [120], while modern treatments within the context of condensed matter systems can be found in Refs. 109 and 110.

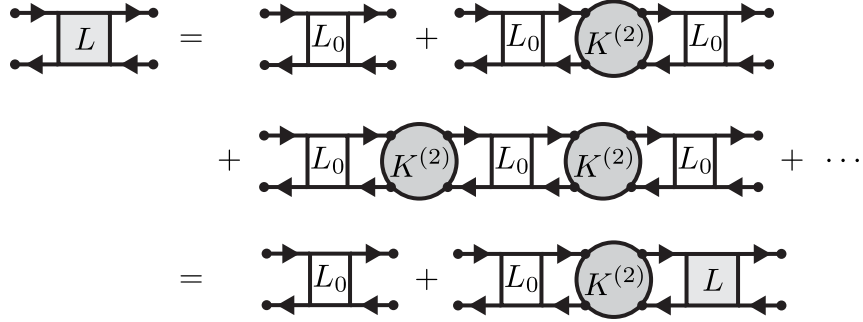


Figure 3.9: **Diagrammatic representation of the Bethe-Salpeter equation for the two-particle correlation function.**

The BSE describes the correlated movement of two charge carriers by taking into account all possible ways in which the two particles can interact with each other. While it was first employed in nuclear physics [118] and relativistic quantum electrodynamics [119, 120], its arguably main application nowadays lies in the domain of condensed matter physics, where it is almost exclusively used for the study of optical properties [109, 110]. The prime example for its use in the context of the latter is the calculation of optical absorption spectra, i.e., the rate with which an incoming light wave of a certain frequency creates electronic excitations. In materials in which the inter-electron Coulomb interaction is not highly screened, such as semi-conductors and low-dimensional materials, the optically excited electron-hole pairs can form bound states with a sizable binding energy. By explicitly considering the Coulomb interaction between the electron and the hole, the BSE allows the inclusion of bound state effects on the absorption spectrum.

Returning to our technical exposition of the BSE, for the content presented in this thesis, it is most useful to pass to the KS basis and consider the Fourier transform:

$$\begin{aligned}
 F(1, 2; 3, 4) \equiv & \sum_{\substack{\mathbf{k}, \mathbf{k}', \mathbf{q} \\ a, b, c, d}} \phi_{\mathbf{k}+\mathbf{q}, a}(\mathbf{r}_1) \phi_{\mathbf{k}', d}(\mathbf{r}_4) \phi_{\mathbf{k}'+\mathbf{q}, b}^*(\mathbf{r}_2) \phi_{\mathbf{k}, c}^*(\mathbf{r}_3) \int \frac{d\omega}{2\pi} \int \frac{d\omega'}{2\pi} \int \frac{d\omega''}{2\pi} \\
 & \times e^{-i\omega(t_1-t_3)} e^{-i\omega'(t_4-t_2)} e^{-i\omega''(t_1-t_2)} \tilde{F}_{\substack{\mathbf{k}+\mathbf{q}, a; \mathbf{k}, c \\ \mathbf{k}'+\mathbf{q}, b; \mathbf{k}', d}}(\omega, \omega', \omega''),
 \end{aligned} \tag{3.84}$$

where F is either one of L or $K^{(2)}$, whose Fourier transforms can only depend on three

different crystal momenta \mathbf{k} , \mathbf{k}' , and \mathbf{q} and three different frequencies ω , ω' , and ω'' , due to the discrete translational symmetry of the ground state and time translation invariance, respectively. The three crystal momenta and frequencies are defined such that the momentum and frequency flows mimic those depicted in the Feynman diagram for the screened Coulomb interaction \tilde{W} in Table 3.1. They are also also illustrated in Fig. 3.10. The graphical illustrations provided by the Feynman diagrams can be interpreted in the following way: On the left-hand side of the graphical equation shown in Fig. 3.10, an incoming electron line carries (crystal) momentum \mathbf{k} and frequency ω into the interaction process, while the incoming hole carries momentum \mathbf{k}' and frequency ω' away from it. The interaction process transfers a momentum \mathbf{q} and a frequency ω'' between the two, so that the outgoing electron line carries momentum $\mathbf{k} + \mathbf{q}$ and frequency $\omega + \omega''$ away from it. Likewise, the outgoing hole carries momentum $\mathbf{k}' + \mathbf{q}$ and frequency $\omega' + \omega''$ into the interaction process. Regarding the band indices, the electron scatters from band c to band a , whereas the hole scatters from band d to band b .

By contrast, the Fourier transform of the independent-particle correlation function L_0 ,

$$L_0(1, 2; 3, 4) \equiv \sum_{\substack{\mathbf{k}, \mathbf{k}' \\ a, b, c, d}} \phi_{\mathbf{k}, a}(\mathbf{r}_1) \phi_{\mathbf{k}', d}(\mathbf{r}_4) \phi_{\mathbf{k}', b}^*(\mathbf{r}_2) \phi_{\mathbf{k}, c}^*(\mathbf{r}_3) \int \frac{d\omega}{2\pi} \int \frac{d\omega'}{2\pi} \\ \times e^{-i\omega(t_1-t_3)} e^{-i\omega'(t_4-t_2)} \tilde{L}_{0; \mathbf{k}; a, c}(\omega, \omega'), \quad (3.85)$$

can only depend on two crystal momenta and two time differences, as it is the product of two separate one-particle Green's functions:

$$\tilde{L}_{0; \mathbf{k}; a, c}(\omega, \omega') = \tilde{G}_{\mathbf{k}, a, c}(\omega) \tilde{G}_{\mathbf{k}', d, b}(\omega'). \quad (3.86)$$

In Fourier space, the BSE becomes an integro-matrix equation:

$$\begin{aligned}
\tilde{L}_{\mathbf{k}+\mathbf{q},a;\mathbf{k},c}^{\omega,\omega',\omega''}(\omega,\omega',\omega'') &= \tilde{L}_{0;\mathbf{k};a,c}(\omega,\omega')\delta_{\mathbf{q},0}2\pi\delta(\omega'') \\
&+ \sum_{\mathbf{q}'} \int \frac{d\omega'''}{2\pi} \tilde{L}_{0;\mathbf{k}+\mathbf{q};a,\bar{e}}(\omega+\omega'',\omega'+\omega''') \\
&\times \tilde{K}_{\mathbf{k}+\mathbf{q},\bar{e};\mathbf{k}+\mathbf{q}',\bar{g}}^{(2)}(\omega+\omega''',\omega'+\omega''',\omega''-\omega''') \\
&\times \tilde{L}_{\mathbf{k}+\mathbf{q}',\bar{g};\mathbf{k},c}(\omega,\omega',\omega'''),
\end{aligned} \tag{3.87}$$

which is graphically illustrated in Fig. 3.10. As before, a bar over a band index indicates that it is being summed over.

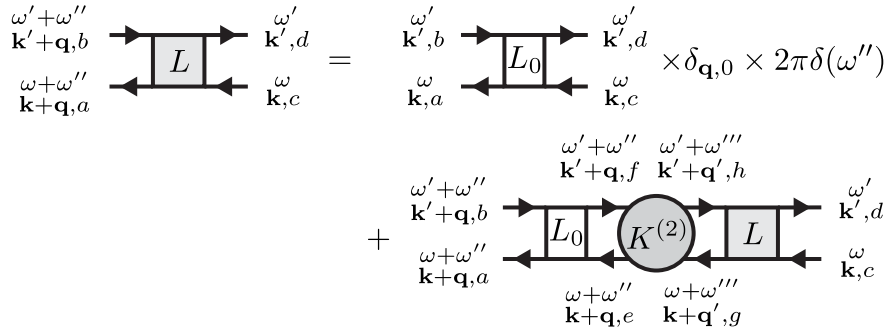


Figure 3.10: **Diagrammatic representation of the Bethe-Salpeter equation in Fourier space.**

The full Bethe-Salpeter equation features quantities that depend on three different frequencies. Thus it is impossible to solve exactly and hence further approximations are required to obtain a practically useful equation for the two-particle correlation function L . The most common approximation nowadays [109, 110] is to approximate the two-particle-irreducible interaction kernel, usually by employing the GW approximation for the one-particle-irreducible self-energy and neglecting the functional derivative of the screened Coulomb interaction:

$$\Sigma_{\text{Coul.}}(1,2) \approx iG(1,2)W(1,2) - iG(\bar{3},\bar{3}^+)v(1,\bar{3})\delta(1,2), \quad \frac{\delta W(1,2)}{\delta G(3,4)} \approx 0. \tag{3.88}$$

This approximation leads to a particularly simple form of the interaction kernel:

$$K^{(2)}(1, 2; 3, 4) = \frac{\Sigma_{\text{Coul.}}(1, 2)}{\delta G(3, 4)} \approx iW(1, 2)\delta(1, 3)\delta(3, 4) - iv(1, 3)\delta(1, 2)\delta(3, 4). \quad (3.89)$$

When the BSE is applied to study the correlated propagation of an electron and a hole, the two terms retained in this approximation have a simple physical interpretation: the first term describes the *screened, electrostatic attraction* between the electron and the hole, while the second term represents an *unscreened, “exchange-like” repulsion* between them. Despite its apparent simplicity, this approximation still captures the most important effects of electronic correlation and in many cases leads to good predictions [109, 110].

The simple structure of the interaction kernel becomes even more apparent in Fourier space, in which it reads:

$$\tilde{K}_{\substack{\mathbf{k}+\mathbf{q},a;\mathbf{k},c \\ \mathbf{k}'+\mathbf{q},b;\mathbf{k}',d}}^{(2)}(\omega, \omega', \omega'') \approx i\tilde{W}_{\substack{\mathbf{k}+\mathbf{q},a;\mathbf{k},c \\ \mathbf{k}'+\mathbf{q},b;\mathbf{k}',d}}(\omega'') - iv_{\substack{\mathbf{k}+\mathbf{q},a;\mathbf{k},c \\ \mathbf{k}'+\mathbf{q},b;\mathbf{k}',d}} \equiv \tilde{K}_{\substack{\mathbf{k}+\mathbf{q},a;\mathbf{k},c \\ \mathbf{k}'+\mathbf{q},b;\mathbf{k}',d}}^{(2)}(\omega''). \quad (3.90)$$

The matrix elements of the unscreened Coulomb interaction were defined in Eq. 3.52 and the matrix elements and Fourier components of $W(1, 2)$ are defined as

$$\begin{aligned} \tilde{W}_{\substack{\mathbf{k}+\mathbf{q},a;\mathbf{k},c \\ \mathbf{k}'+\mathbf{q},b;\mathbf{k}',d}}(\omega) &\equiv \int dt e^{i\omega t} \int d^3r_1 \int d^3r_2 \phi_{\mathbf{k}+\mathbf{q},a}^*(\mathbf{r}_1)\phi_{\mathbf{k}',d}^*(\mathbf{r}_2) \\ &\times \phi_{\mathbf{k}'+\mathbf{q},b}(\mathbf{r}_2)\phi_{\mathbf{k},c}(\mathbf{r}_1)W(\mathbf{r}_1, t; \mathbf{r}_2, 0). \end{aligned} \quad (3.91)$$

Still, this approximation is not sufficient to simplify the BSE to the point where it can be solved easily, as it still involves a convolution in frequency space. To resolve this issue, it is common to approximate the interaction kernel as being static, i.e.,

$$\tilde{K}_{\substack{\mathbf{k}+\mathbf{q},a;\mathbf{k},c \\ \mathbf{k}'+\mathbf{q},b;\mathbf{k}',d}}^{(2)}(\omega'') \approx i\tilde{W}_{\substack{\mathbf{k}+\mathbf{q},a;\mathbf{k},c \\ \mathbf{k}'+\mathbf{q},b;\mathbf{k}',d}}(0) - iv_{\substack{\mathbf{k}+\mathbf{q},a;\mathbf{k},c \\ \mathbf{k}'+\mathbf{q},b;\mathbf{k}',d}} \equiv \tilde{K}_{\substack{\mathbf{k}+\mathbf{q},a;\mathbf{k},c \\ \mathbf{k}'+\mathbf{q},b;\mathbf{k}',d}}^{(2)}. \quad (3.92)$$

The mathematical and physical justification for this approximation lies in the fact that the only frequency dependence of $\tilde{K}^{(2)}$ is due to the frequency dependence of the screened Coulomb interaction \tilde{W} . The spectral decomposition of the latter shows that

it has an isolated pole at the *plasma frequency*, which typically possesses by far the largest spectral weight and it is therefore often a reasonable approximation to describe the entire frequency dependence of \tilde{W} with a simple pole at the plasma frequency only [109, 110]. Note that typical plasma frequencies in solids are on the order of ~ 25 eV [109], which is much larger than typical frequencies we want to solve the BSE for. The latter fall into the range of 0-4 eV, as it covers both the typical crystal vibration frequencies in solids (0-200 meV) as well as the frequency range of visible light (~ 1.6 -3.3 eV). It is then often a reasonable approximation to neglect the frequency dependence of \tilde{W} , which renders the interaction kernel *static*.

In this approximation of a static interaction kernel, the BSE becomes:

$$\begin{aligned} \tilde{L}_{\mathbf{k}+\mathbf{q},a;\mathbf{k},c;\mathbf{k}'+\mathbf{q},b;\mathbf{k}',d}(\omega,\omega',\omega'') &= \tilde{L}_{0,\mathbf{k};a,c;\mathbf{k}';b,d}(\omega,\omega')\delta_{\mathbf{q},0}2\pi\delta(\omega'') \\ &+ \sum_{\mathbf{q}'} \tilde{L}_{0,\mathbf{k}+\mathbf{q};a,\bar{e};\mathbf{k}'+\mathbf{q};b,\bar{f}}(\omega+\omega'',\omega'+\omega'')\tilde{K}_{\mathbf{k}+\mathbf{q},\bar{e};\mathbf{k}+\mathbf{q}',\bar{g};\mathbf{k}'+\mathbf{q},\bar{f};\mathbf{k}'+\mathbf{q}',\bar{h}}^{(2)} \\ &\times \int \frac{d\omega'''}{2\pi} \tilde{L}_{\mathbf{k}+\mathbf{q}',\bar{g};\mathbf{k},c;\mathbf{k}'+\mathbf{q}',\bar{h};\mathbf{k}',d}(\omega,\omega',\omega'''), \end{aligned} \quad (3.93)$$

which does not feature a convolution in frequency space anymore. The full three-frequency two-particle correlation function can still not be obtained easily, however. But as we will see in the next chapters, this is not necessary for the theoretical approaches discussed in this thesis though.

For the latter, it will be sufficient to have knowledge of the two-particle correlation function with two different time arguments only, which, after some simplification, reads:¹⁷

$$\begin{aligned} L(\mathbf{r}_1, t_1; \mathbf{r}_2, t_1^+; \mathbf{r}_3, t_2^+; \mathbf{r}_4, t_2) &= \sum_{\substack{\mathbf{k}, \mathbf{k}', \mathbf{q} \\ a, b, c, d}} \phi_{\mathbf{k}+\mathbf{q},a}(\mathbf{r}_1)\phi_{\mathbf{k}',d}(\mathbf{r}_4)\phi_{\mathbf{k}'+\mathbf{q},b}^*(\mathbf{r}_2)\phi_{\mathbf{k},c}^*(\mathbf{r}_3) \int \frac{d\omega}{2\pi} e^{-i\omega(t_1-t_2)} \\ &\times \int \frac{d\omega'}{2\pi} \int \frac{d\omega''}{2\pi} \tilde{L}_{\mathbf{k}+\mathbf{q},a;\mathbf{k},c;\mathbf{k}'+\mathbf{q},b;\mathbf{k}',d}(\omega+\omega',\omega',\omega''). \end{aligned} \quad (3.94)$$

¹⁷ $t_{1,2}^+ \equiv t_{1,2} + 0^+$, where 0^+ is a positive infinitesimal, included to resolve the equal time ordering of the fermion field operators.

Due to time translation invariance, it can only depend on one time difference and its Fourier transform can therefore depend on one frequency only:

$$\tilde{L}_{\substack{\mathbf{k}+\mathbf{q},a;\mathbf{k},c \\ \mathbf{k}'+\mathbf{q},b;\mathbf{k}',d}}(\omega) \equiv \int \frac{d\omega'}{2\pi} \int \frac{d\omega''}{2\pi} \tilde{L}_{\substack{\mathbf{k}+\mathbf{q},a;\mathbf{k},c \\ \mathbf{k}'+\mathbf{q},b;\mathbf{k}',d}}(\omega + \omega', \omega', \omega''). \quad (3.95)$$

Replacing $\omega \rightarrow \omega + \omega'$ in Eq. 3.93 and integrating over ω' and ω'' , the different frequency components decouple and the BSE becomes an algebraic equation, local in frequency space:

$$\tilde{L}_{\substack{\mathbf{k}+\mathbf{q},a;\mathbf{k},c \\ \mathbf{k}'+\mathbf{q},b;\mathbf{k}',d}}(\omega) = \tilde{L}_{0;\substack{\mathbf{k};a,c \\ \mathbf{k}';b,d}}(\omega) \delta_{\mathbf{q},\mathbf{0}} + \sum_{\mathbf{q}'} \tilde{L}_{0;\substack{\mathbf{k}+\mathbf{q};a,\bar{e} \\ \mathbf{k}'+\mathbf{q};b,\bar{f}}}(\omega) \tilde{K}_{\substack{\mathbf{k}+\mathbf{q},\bar{e};\mathbf{k}+\mathbf{q}',\bar{g} \\ \mathbf{k}'+\mathbf{q},\bar{f};\mathbf{k}'+\mathbf{q}',\bar{h}}}^{(2)} \tilde{L}_{\substack{\mathbf{k}+\mathbf{q}',\bar{g};\mathbf{k},c \\ \mathbf{k}'+\mathbf{q}',\bar{h};\mathbf{k}',d}}(\omega), \quad (3.96)$$

with the one-frequency independent-particle correlation function

$$\tilde{L}_{0;\substack{\mathbf{k};a,c \\ \mathbf{k}';b,d}}(\omega) \equiv \int \frac{d\omega'}{2\pi} \tilde{L}_{0;\substack{\mathbf{k};a,c \\ \mathbf{k}';b,d}}(\omega + \omega', \omega'). \quad (3.97)$$

Eq. 3.96 can, in principle, be solved for the matrix inverse of \tilde{L} :¹⁸

$$\tilde{L}_{\substack{\mathbf{k}+\mathbf{q},a;\mathbf{k},c \\ \mathbf{k}'+\mathbf{q},b;\mathbf{k}',d}}^{-1}(\omega) = \tilde{L}_{0;\substack{\mathbf{k};a,c \\ \mathbf{k}';b,d}}^{-1}(\omega) \delta_{\mathbf{q},\mathbf{0}} - \tilde{K}_{\substack{\mathbf{k}+\mathbf{q},a;\mathbf{k},c \\ \mathbf{k}'+\mathbf{q},b;\mathbf{k}',d}}^{(2)}. \quad (3.98)$$

The most important approach in practice, however, is to employ the quasi-particle approximation to the one-particle Green's function [109, 110]. The independent-particle

¹⁸The matrix inverses are understood as

$$\sum_{\mathbf{q}',e,f} \tilde{L}_{\substack{\mathbf{k}+\mathbf{q},a;\mathbf{k}+\mathbf{q}',e \\ \mathbf{k}'+\mathbf{q},b;\mathbf{k}'+\mathbf{q}',f}}^{-1}(\omega) \tilde{L}_{\substack{\mathbf{k}+\mathbf{q}',e;\mathbf{k},c \\ \mathbf{k}'+\mathbf{q}',f;\mathbf{k}',d}}(\omega) = \delta_{\mathbf{q},\mathbf{0}} \delta_{a,c} \delta_{b,d},$$

$$\sum_{e,f} \tilde{L}_{0;\substack{\mathbf{k};a,e \\ \mathbf{k}';b,f}}^{-1}(\omega) \tilde{L}_{0;\substack{\mathbf{k};e,c \\ \mathbf{k}';f,d}}(\omega) = \delta_{a,c} \delta_{b,d}.$$

two-particle correlation function then becomes:

$$\begin{aligned}
\tilde{L}_{0;\mathbf{k};a,c;\mathbf{k}';b,d}(\omega) &\stackrel{\text{QPA}}{\approx} \delta_{a,c}\delta_{b,d} \int \frac{d\omega'}{2\pi} G_{\mathbf{k},c}^{(\text{QP})}(\omega + \omega') G_{\mathbf{k}',d}^{(\text{QP})}(\omega') \\
&= i Z_{\mathbf{k},c}^{(\text{QP})} Z_{\mathbf{k}',d}^{(\text{QP})} \delta_{a,c}\delta_{b,d} \left\{ \frac{(f_{\mathbf{k},c} - f_{\mathbf{k}',d})(\omega - \varepsilon_{\mathbf{k},c}^{(\text{QP})} + \varepsilon_{\mathbf{k}',d}^{(\text{QP})})}{(\omega - \varepsilon_{\mathbf{k},c}^{(\text{QP})} + \varepsilon_{\mathbf{k}',d}^{(\text{QP})})^2 + (\gamma_{\mathbf{k},c}^{(\text{QP})} + \gamma_{\mathbf{k}',d}^{(\text{QP})})^2/4} \right. \\
&\quad \left. + \frac{i [f_{\mathbf{k},c}(1 - f_{\mathbf{k}',d}) + f_{\mathbf{k}',d}(1 - f_{\mathbf{k},c})](\gamma_{\mathbf{k},c}^{(\text{QP})} + \gamma_{\mathbf{k}',d}^{(\text{QP})})}{2 (\omega - \varepsilon_{\mathbf{k},c}^{(\text{QP})} + \varepsilon_{\mathbf{k}',d}^{(\text{QP})})^2 + (\gamma_{\mathbf{k},c}^{(\text{QP})} + \gamma_{\mathbf{k}',d}^{(\text{QP})})^2/4} \right\}. \tag{3.99}
\end{aligned}$$

Furthermore, the quasi-particle weight factors $Z_{\mathbf{k},a}^{(\text{QP})}$ can in many cases be well approximated with 1, while the decay widths are usually neglected as well:

$$\tilde{L}_{0;\mathbf{k};a,c;\mathbf{k}';b,d}^{(\text{QP})}(\omega) \approx i \delta_{a,c}\delta_{b,d} \frac{f_{\mathbf{k},c} - f_{\mathbf{k}',d}}{\omega - \varepsilon_{\mathbf{k},c}^{(\text{QP})} + \varepsilon_{\mathbf{k}',d}^{(\text{QP})}}, \tag{3.100}$$

when Eq. 3.98 takes on the simplified form

$$i(f_{\mathbf{k},c} - f_{\mathbf{k}',d}) \tilde{L}_{\mathbf{k}+\mathbf{q},a;\mathbf{k},c;\mathbf{k}'+\mathbf{q},b;\mathbf{k}',d}^{-1}(\omega) = \omega - H_{\mathbf{k}+\mathbf{q},a;\mathbf{k},c;\mathbf{k}'+\mathbf{q},b;\mathbf{k}',d}^{(2p.)}, \tag{3.101}$$

where the effective two-particle Hamiltonian is defined as (also compare Ref. 110)

$$H_{\mathbf{k}+\mathbf{q},a;\mathbf{k},c;\mathbf{k}'+\mathbf{q},b;\mathbf{k}',d}^{(2p.)} \equiv \delta_{a,c}\delta_{b,d} \left(\varepsilon_{\mathbf{k},c}^{(\text{QP})} - \varepsilon_{\mathbf{k}',d}^{(\text{QP})} \right) \delta_{\mathbf{q},\mathbf{0}} + i(f_{\mathbf{k},c} - f_{\mathbf{k}',d}) \tilde{K}_{\mathbf{k}+\mathbf{q},a;\mathbf{k},c;\mathbf{k}'+\mathbf{q},b;\mathbf{k}',d}^{(2)}. \tag{3.102}$$

This Hamiltonian can be interpreted as describing a system of two particles with dispersions $+\varepsilon_{\mathbf{k},c}^{(\text{QP})}$ and $-\varepsilon_{\mathbf{k}',d}^{(\text{QP})}$ which interact with each other via a static, two-particle interaction $\tilde{K}^{(2)}$ that transfers crystal momentum \mathbf{q} between them and furthermore scatters them to different bands (“species” in the context of particle physics). In the approximation to the kernel given in Eq. 3.92, the effective two-particle Hamiltonian simply reads

$$\begin{aligned}
H_{\mathbf{k}+\mathbf{q},a;\mathbf{k},c;\mathbf{k}'+\mathbf{q},b;\mathbf{k}',d}^{(2p.)} &= \delta_{a,c}\delta_{b,d} \left(\varepsilon_{\mathbf{k},c}^{(\text{QP})} - \varepsilon_{\mathbf{k}',d}^{(\text{QP})} \right) \delta_{\mathbf{q},\mathbf{0}} \\
&\quad - (f_{\mathbf{k},c} - f_{\mathbf{k}',d}) \tilde{W}_{\mathbf{k}+\mathbf{q},a;\mathbf{k},c;\mathbf{k}'+\mathbf{q},b;\mathbf{k}',d} + (f_{\mathbf{k},c} - f_{\mathbf{k}',d}) v_{\mathbf{k}+\mathbf{q},a;\mathbf{k},c;\mathbf{k}'+\mathbf{q},b;\mathbf{k}',d}. \tag{3.103}
\end{aligned}$$

For the two particles being one electron and one hole, the two-particle interaction potential is the sum of a screened, attractive part \tilde{W} and an unscreened, repulsive part v and hence the spectrum of $H^{(2p.)}$ can potentially feature bound states.

In order to find the two-particle correlation function $\tilde{L}(\omega)$ at a fixed frequency ω , one first diagonalizes $H^{(2p.)}$, possibly only partially depending on the range of interest of ω . We denote its eigenvalues and eigenvectors by ε_S and $A^S(\mathbf{q})_{\mathbf{k},a}$, respectively. The latter are eigenvectors of $H^{(2p.)}$ in the sense that

$$\sum_{\substack{\mathbf{k},\mathbf{k}' \\ c,d}} H_{\substack{\mathbf{k}+\mathbf{q},a;\mathbf{k},c \\ \mathbf{k}'+\mathbf{q},b;\mathbf{k}',d}}^{(2p.)} A_{\mathbf{k},c}^S = \varepsilon_S A_{\substack{\mathbf{k}+\mathbf{q},a \\ \mathbf{k}'+\mathbf{q},b}}^S. \quad (3.104)$$

In term of these eigenvalues and -vectors, the two-particle correlation function can be written as

$$\tilde{L}_{\substack{\mathbf{k}+\mathbf{q},a;\mathbf{k},c \\ \mathbf{k}'+\mathbf{q},b;\mathbf{k}',d}}(\omega) = i(f_{\mathbf{k},c} - f_{\mathbf{k}',d}) \sum_{S,S'} \frac{A_{\substack{\mathbf{k}+\mathbf{q},a \\ \mathbf{k}'+\mathbf{q},b}}^S N_{S,S'}^{-1} A_{\mathbf{k},c}^{S',*}}{\omega - \varepsilon_S + i\eta}, \quad (3.105)$$

where the overlap matrix N is defined as

$$N_{S,S'} \equiv \sum_{\substack{\mathbf{k},\mathbf{k}' \\ a,b}} A_{\mathbf{k},a}^{S,*} A_{\mathbf{k}',b}^{S'}. \quad (3.106)$$

Note that the effective two-particle Hamiltonian is in general not hermitian [110] and as a result its eigenvectors are not necessarily mutually orthogonal. In this case, the overlap matrix is non-trivial and needs to be included. As first pointed out by I. Tamm [121] and S .Dancoff [122], in systems with a sizable energy gap, the coupling matrix elements between electronic transitions of positive and negative energy can be neglected. In this so-called *Tamm-Dancoff approximation*, the two-particle Hamiltonian becomes hermitian and the overlap matrix becomes the identity matrix and can hence be omitted. This approximation is well-justified for semi-conductors and insulators, in which the positive- and negative-energy transitions are separated by twice the electronic band gap. The latter is typically much larger than the usual order of magnitude of the Coulomb matrix elements between these transitions [109].

Nowadays the Tamm-Dancoff approximation is regularly and successfully employed in calculations of the optical absorption spectrum of semi-conductors and insulators [109, 110], for which it reduces the computational cost of solving the BSE enormously. For (semi-)metallic systems, however, the lack of a band gap casts doubt on the applicability of the Tamm-Dancoff approximation. Since it is one of the central points of this work to use the BSE also for a better description of the screening of the electron-nuclei interaction in (semi-)metallic systems, we retain the more general form of the two-particle correlation function, given in Eq. 3.105.

This concludes our review and discussion of the electronic correlation functions that will be needed throughout this thesis. In the next chapter, we will move on to study the electron-nuclei system on a level of theory that goes beyond the clamped nuclei approximation.

Chapter 4

Phonons

In this chapter we discuss the treatment of the coupled electron-nuclei system beyond the clamped nuclei approximation of the previous chapter. To this end, we will now restore the nuclei kinetic energy part in the full electron-nuclei Hamiltonian of Eq. 2.14 and introduce the *adiabatic, Born-Oppenheimer approximation (BOA)*, which essentially consists of neglecting only certain matrix elements of the nuclei kinetic energy operator, instead of neglecting the entire operator as in the CNA.

After presenting a brief review of the BOA, the physical motivation behind it, and how it leads to a purely nucleonic problem, we will treat the latter in the *harmonic approximation (HA)*, in which the effective potential for the nuclei is approximated by a quadratic potential. This will allow us to introduce the notion of *phonons*. However, contrary to many popular treatments of phonons [105, 123–125], we will all the time stick to an entirely quantum mechanical description and will treat the nuclei entirely within the operator and state formalism of quantum mechanics.

To obtain the eigenstates of the phonon Hamiltonian, it will be necessary to calculate the effective coupling constants between the nuclei, traditionally known as *force constants*. The interaction between different nuclei is given by the sum of the nuclei-nuclei Coulomb repulsion and the indirect Coulomb attraction mediated by the electronic system. The latter is particularly hard to calculate as the screening of the Coulomb interaction needs to be described properly. The approach that is applied most often nowadays is the calculation of the force constants via a DFT-based approach, known

as *density functional perturbation theory (DFPT)*. However, as already discussed in the last chapter, DF(P)T is in some cases not able to correctly capture the response of the electronic system to a lattice distortion.

We therefore derive a *novel and concrete theoretical approach using many-body perturbation theory (MBPT)* that allows the calculation of force constants *beyond the approximations employed in DFPT*. While an implementation of this approach is beyond the scope of this thesis, our concrete expressions will allow a timely test of the proposed method. For the calculations presented later in this thesis, we instead used the currently available implementations of DFPT. Finally, we show how and in which approximation the DFPT approach can be recovered from our newly developed MBPT-based formalism.

4.1 The adiabatic, Born-Oppenheimer approximation

While the clamped nuclei approximation is able to capture the mostly electronic part of the excited states of the matter Hamiltonian, it cannot describe the excitations that are mostly nucleonic in nature. These excited states correspond to movements of the nuclei around their equilibrium position, i.e., to vibrations of the lattice in the case of a solid-state system. For typical systems of interest, such as semi-conductors and insulators, these vibrational excitations are of much lower energy than the lowest lying electronic excitations. Typical vibration energies in a solid are on the order of 0-0.2 eV, whereas typical electronic excitation energies in semi-conductors start from ~ 1 eV [85].

Instead of neglecting the vibrational excitations altogether then, as done in the CNA, we can make use of the information that the two kinds of excitations are energetically separated by a gap of a relative size of one order of magnitude and *neglect the vibration-induced coupling between electronic states*. This comprises the *adiabatic, Born-Oppenheimer approximation (BOA)*.

Note that this approximation is in general questionable in case of (semi-)metals or systems with small electronic gaps as the vibrational and electronic excitations are no longer energetically separated by a sizable gap and neglecting the coupling between the

two can no longer be well motivated *a priori* on physical grounds. Indeed, it has been shown that in the case of graphene, a semi-metallic system, the Born-Oppenheimer approximation fails to capture some effects, such as changes in the vibrational frequencies when the density of electrons is changed [28]. As a large part of this work also deals with the application of the developed theoretical and computational methods to graphene, we want to point out that, contrary to most works that use the Born-Oppenheimer approximation, we do *not* consider it to be the final approximation for the treatment of the electron-nuclear system, but rather we view it as an *intermediate step in its perturbative treatment* that provides a *better starting point* than the clamped nuclei approximation, even for the case of graphene or other (semi-)metallic systems.

In order to be more precise and introduce the BOA in mathematical terms, we return again to the full electron-nuclei Hamiltonian, which is given by the sum of the CNA Hamiltonian and the kinetic energy operator for the nuclei:

$$\hat{\mathcal{H}}_M = \hat{\mathcal{H}}_{\text{CNA}} + \sum_I \frac{\hat{\mathbf{P}}_I^2}{2M_I}. \quad (4.1)$$

We can express the full matter Hamiltonian in the complete basis of the electron-nuclei system provided by the eigenstates of the CNA Hamiltonian (see Eq. 3.3):

$$\begin{aligned} \hat{\mathcal{H}}_M = & \sum_{\nu} \sum_{\{\mathbf{R}_I\}} V_{\nu}(\{\mathbf{R}_I\}) |\nu, \{\mathbf{R}_I\}\rangle \langle \nu, \{\mathbf{R}_I\}| \\ & + \sum_{\nu, \nu'} \sum_{\{\mathbf{R}_I\}, \{\mathbf{R}'_I\}} T_{\nu, \nu'}(\{\mathbf{R}_I\}, \{\mathbf{R}'_I\}) |\nu, \{\mathbf{R}_I\}\rangle \langle \nu', \{\mathbf{R}'_I\}|, \end{aligned} \quad (4.2)$$

where we defined the matrix elements of the nuclear kinetic energy operator as

$$T_{\nu, \nu'}(\{\mathbf{R}_I\}, \{\mathbf{R}'_I\}) \equiv \langle \nu, \{\mathbf{R}_I\} | \sum_I \frac{\hat{\mathbf{P}}_I^2}{2M_I} | \nu', \{\mathbf{R}'_I\} \rangle \quad (4.3)$$

and the $V_{\nu}(\{\mathbf{R}_I\})$ are the eigenvalues of the CNA Hamiltonian as defined in Eq. 3.5. While the CNA consists of neglecting *all* matrix elements $T_{\nu, \nu'}(\{\mathbf{R}_I\}, \{\mathbf{R}'_I\})$ entirely, in the BOA, we merely neglect the subset of them that corresponds to the coupling of

electronic and nuclei excitations.

To start with, we directly evaluate the matrix elements by inserting the tensor product form of the states $|\nu, \{\mathbf{R}_I\}\rangle$ (see Eq. 3.3):

$$T_{\nu,\nu'}(\{\mathbf{R}_I\}, \{\mathbf{R}'_I\}) = {}_e\langle\nu(\{\mathbf{R}_I\})|\nu'(\{\mathbf{R}'_I\})\rangle_e \times {}_n\langle\{\mathbf{R}_I\}|\sum_I \frac{\hat{\mathbf{P}}_I^2}{2M_I}|\{\mathbf{R}'_I\}\rangle_n. \quad (4.4)$$

The second factor can be evaluated in a position space basis and reads

$${}_n\langle\{\mathbf{R}_I\}|\sum_I \frac{\hat{\mathbf{P}}_I^2}{2M_I}|\{\mathbf{R}'_I\}\rangle_n = \sum_I \frac{1}{2M_I}[-\nabla_I'^2\delta^{(3)}(\mathbf{R}_I - \mathbf{R}'_I)] \times \prod_{J\neq I} \delta^{(3)}(\mathbf{R}_J - \mathbf{R}'_J), \quad (4.5)$$

where the prime on ∇_I' refers to the derivative with respect to \mathbf{R}'_I . Applying the usual rules for the treatment of the derivatives of distributions and products, the nuclear kinetic energy term in the Hamiltonian can be written as the sum of three contributions:

$$\begin{aligned} & \sum_{\nu,\nu'} \sum_{\{\mathbf{R}_I\},\{\mathbf{R}'_I\}} T_{\nu,\nu'}(\{\mathbf{R}_I\}, \{\mathbf{R}'_I\}) |\nu, \{\mathbf{R}_I\}\rangle \langle\nu', \{\mathbf{R}'_I\}| \\ &= \sum_{\nu,\nu'} \sum_{\{\mathbf{R}_I\},\{\mathbf{R}'_I\}} |\nu, \{\mathbf{R}_I\}\rangle \delta_{\{\mathbf{R}_I\},\{\mathbf{R}'_I\}} \\ & \times \left\{ \sum_I \frac{-1}{2M_I} \left[({}_e\langle\nu(\{\mathbf{R}_I\})|\nabla_I'^2|\nu'(\{\mathbf{R}'_I\})\rangle_e) \langle\nu', \{\mathbf{R}'_I\}| \right. \right. \\ & \quad \left. \left. + 2({}_e\langle\nu(\{\mathbf{R}_I\})|\nabla_I'|\nu'(\{\mathbf{R}'_I\})\rangle_e) \cdot (\nabla_I'\langle\nu', \{\mathbf{R}'_I\}|) \right. \right. \\ & \quad \left. \left. + ({}_e\langle\nu(\{\mathbf{R}_I\})|\nu'(\{\mathbf{R}'_I\})\rangle_e) (\nabla_I'^2\langle\nu', \{\mathbf{R}'_I\}|) \right] \right\}, \end{aligned} \quad (4.6)$$

where $\delta_{\{\mathbf{R}_I\},\{\mathbf{R}'_I\}} \equiv \prod_I \delta^{(3)}(\mathbf{R}_I - \mathbf{R}'_I)$. To make the notation cleaner, we introduce the abbreviations

$$(\mathbf{P}_{\text{eff},I})_{\nu,\nu'}(\{\mathbf{R}_I\}) \equiv {}_e\langle\nu(\{\mathbf{R}_I\})|[-i\nabla_I|\nu'(\{\mathbf{R}_I\})\rangle_e], \quad (4.7)$$

$$\Delta V_{\nu,\nu'}(\{\mathbf{R}_I\}) \equiv \sum_I \frac{1}{2M_I} {}_e\langle\nu(\{\mathbf{R}_I\})|[-\nabla_I^2|\nu'(\{\mathbf{R}_I\})\rangle_e]. \quad (4.8)$$

It is important to note that both of these quantities are just *numbers* that depend on the electronic quantum numbers ν and ν' and the nuclear configuration $\{\mathbf{R}_I\}$. Also note that for $\nu = \nu'$ we have $(\mathbf{P}_{\text{eff},I})_{\nu,\nu}(\{\mathbf{R}_I\}) = 0$, as follows from the normalization of the states $|\nu(\{\mathbf{R}_I\})\rangle_e$ (see also Ref. 92). With these abbreviations, the full matter Hamiltonian becomes the sum of four terms:

$$\begin{aligned}
\hat{\mathcal{H}}_M = & \sum_{\nu, \{\mathbf{R}_I\}} |\nu, \{\mathbf{R}_I\}\rangle \left[V_\nu(\{\mathbf{R}_I\}) + \Delta V_{\nu,\nu}(\{\mathbf{R}_I\}) \right] \langle \nu, \{\mathbf{R}_I\} | \\
& + \sum_{\nu, \{\mathbf{R}_I\}} |\nu, \{\mathbf{R}_I\}\rangle \left[\sum_I \left(-\frac{\nabla_I^2}{2M_I} \right) \right] \langle \nu, \{\mathbf{R}_I\} | \\
& + \sum_{\substack{\nu, \nu', \{\mathbf{R}_I\} \\ \nu \neq \nu'}} |\nu, \{\mathbf{R}_I\}\rangle \left[\Delta V_{\nu,\nu'}(\{\mathbf{R}_I\}) \right] \langle \nu', \{\mathbf{R}_I\} | \\
& + \sum_{\substack{\nu, \nu', \{\mathbf{R}_I\} \\ \nu \neq \nu'}} |\nu, \{\mathbf{R}_I\}\rangle \left[\sum_I \frac{1}{M_I} (\mathbf{P}_{\text{eff},I})_{\nu,\nu'}(\{\mathbf{R}_I\}) \cdot (-i\nabla_I) \right] \langle \nu', \{\mathbf{R}_I\} |.
\end{aligned} \tag{4.9}$$

The first of these terms is the matter Hamiltonian in the CNA with the eigenvalues shifted by $\Delta V_{\nu,\nu}(\{\mathbf{R}_I\})$. The term in the second line describes a coupling between states of different nuclear configuration but involving the same electronic state. By contrast, the third term describes a coupling between different electronic states with the same nuclear configuration. Finally, the last line contains all terms involving both a coupling between electronic states and nuclear configurations.

As discussed and motivated in the introduction to this section, the *adiabatic approximation* consists of neglecting all couplings between different electronic states. This approximation is also often called the *Born-Oppenheimer approximation (BOA)* after M. Born and R. Oppenheimer, who introduced it in 1927 as part of their work on the rotational and vibrational spectra of molecules [126]. This approximation has its physical justification in the picture that the electronic part of many systems adjusts itself *instantaneously* to a change of the nuclei positions. In Fourier space, i.e., in terms of energies, this corresponds to the fact that electronic excitation frequencies and decay rates are sizably larger than the vibrational frequencies, as mentioned at the beginning

of this section.

As for the full matter Hamiltonian as written in Eq. 4.9, the BOA consists of neglecting the terms in the third and fourth line. However, it is also common to neglect the slight shift to the CNA eigenvalues provided by $\Delta V_{\nu,\nu}(\{\mathbf{R}_I\})$, as it is typically very small due to the smallness of the spatial gradient of the state $|\nu, \{\mathbf{R}_I\}\rangle$ and the smallness of the inverse nuclei masses [92].¹ We then define the electron-nuclei Hamiltonian in the BOA as

$$\hat{\mathcal{H}}_{\text{BOA}} \equiv \sum_{\nu, \{\mathbf{R}_I\}} |\nu, \{\mathbf{R}_I\}\rangle \left[\sum_I \left(-\frac{\nabla_I^2}{2M_I} \right) + V_\nu(\{\mathbf{R}_I\}) \right] \langle \nu, \{\mathbf{R}_I\}|. \quad (4.10)$$

To find the eigenstates and the spectrum of $\hat{\mathcal{H}}_{\text{BOA}}$, we note that the BOA Hamiltonian is diagonal in the quantum number ν and hence we can label its eigenstates with the quantum number ν and write it as a superposition of states $|\nu, \{\mathbf{R}_I\}\rangle$ of different $\{\mathbf{R}_I\}$ but same ν :

$$|\alpha, \nu\rangle = \sum_{\{\mathbf{R}_I\}} A_\nu^\alpha(\{\mathbf{R}_I\}) |\nu, \{\mathbf{R}_I\}\rangle, \quad (4.11)$$

where α labels the different eigenstates of $\hat{\mathcal{H}}_{\text{BOA}}$ to the same electronic quantum number ν . Application of the BOA Hamiltonian to $|\alpha, \nu\rangle$ then yields

$$\hat{\mathcal{H}}_{\text{BOA}} |\alpha, \nu\rangle = \sum_{\{\mathbf{R}_I\}} \left\{ \left[\sum_I \left(-\frac{\nabla_I^2}{2M_I} \right) + V_\nu(\{\mathbf{R}_I\}) \right] A_\nu^\alpha(\{\mathbf{R}_I\}) \right\} |\nu, \{\mathbf{R}_I\}\rangle \quad (4.12)$$

from where it follows that the Schrödinger equation

$$\hat{\mathcal{H}}_{\text{BOA}} |\alpha, \nu\rangle = E_\alpha(\nu) |\alpha, \nu\rangle \quad (4.13)$$

is equivalent to an infinite set of independent differential equations for the coefficient

¹Some works, e.g., Ref. 92, distinguish between the adiabatic and the *frozen phonon* approximations. The former consists of only neglecting terms which involve different electronic quantum numbers, while the latter further neglects terms diagonal in the electronic quantum number but off-diagonal in the nuclear configurations. For our purposes, however, this distinction is not important.

functions $A_\nu^\alpha(\{\mathbf{R}_I\})$, one for each electron quantum number ν :

$$\left[\sum_I \left(-\frac{\nabla_I^2}{2M_I} \right) + V_\nu(\{\mathbf{R}_I\}) \right] A_\nu^\alpha(\{\mathbf{R}_I\}) = E_\alpha(\nu) A_\nu^\alpha(\{\mathbf{R}_I\}). \quad (4.14)$$

This equation has the form of a many-body Schrödinger equation in nuclear space, expressed in the eigenbasis of the position operators. If we identify a state $|\alpha(\nu)\rangle_n$ via $A_\nu^\alpha(\{\mathbf{R}_I\}) \equiv {}_n\langle \{\mathbf{R}_I\} | \alpha(\nu) \rangle_n$, we can re-write Eq. 4.14 as an abstract Schrödinger equation in the nuclear Hilbert space:

$$\hat{H}_n(\nu) |a(\nu)\rangle_n = E_\alpha(\nu) |a(\nu)\rangle_n, \quad (4.15)$$

where we introduced the purely nucleonic Hamiltonian

$$\hat{H}_n(\nu) \equiv \sum_I \frac{\hat{\mathbf{P}}_I^2}{2M_I} + V_\nu(\{\hat{\mathbf{R}}_I\}), \quad (4.16)$$

with the potential function V_ν now being evaluated at the set of position *operators*, $\{\hat{\mathbf{R}}_I\}$. This Hamiltonian acts in the nuclear subspace of the full electron-nuclei Hilbert space only, and depends on the electrons only parametrically through the appearance of the quantum number ν . The BOA thus leads to a similar simplification as the clamped nuclei approximation does for the electronic subsystem (compare Eq. 3.8), where we similarly arrived at a family of independent Schrödinger equations for the electrons that depend on the nuclei only parametrically. We will denote the ground state of the BOA Hamiltonian by $|0_{\text{BOA}}\rangle \equiv \sum_{\{\mathbf{R}_I\}} A_0^{\alpha=0}(\{\mathbf{R}_I\}) [|0(\{\mathbf{R}_I\})\rangle_e \otimes |\{\mathbf{R}_I\}\rangle_n]$, while its energy can be written as $E_{0,\text{BOA}} \equiv E_{0,\text{CNA}} + E_{0,\text{ZP}}$ where $E_{0,\text{CNA}}$ is the ground state energy of the Hamiltonian in the clamped nuclei approximation.

The potential operator $V_\nu(\{\hat{\mathbf{R}}_I\})$ effectively couples *all* nuclei through their electrostatic interaction with electrons and between each other and hence the nuclear Hamiltonians $\hat{H}_n(\nu)$ describe *collective* excitations of the nuclei. The potential also contains arbitrarily high powers of the position operators $\hat{\mathbf{R}}_I$ and thus the many-particle Schrödinger equation for the nuclei is not easy to solve or to simplify on general grounds. However, for the purpose of describing only low-energy excitations from the ground

state, we can focus on the $\nu = 0$ -Hamiltonian only, for which the function $V_{\nu=0}(\{\mathbf{R}_I\})$ has, for a solid-state system, a pronounced minimum at a configuration $\{\mathbf{R}_I^{(0)}\}$. In a first approximation then, we can expand the function $V_0(\{\mathbf{R}_I\})$ into a Taylor series around $\{\mathbf{R}_I^{(0)}\}$.

4.2 The harmonic approximation

For many systems, the terms of third or higher order in the Taylor expansion of $V_0(\{\mathbf{R}_I\})$ typically have small expansion coefficients and the expansion can in a first approximation be terminated after the quadratic order. We will focus on the potential provided by the electrons in their ground state $\nu = 0$ only, as this yields the lowest-energy excitations. The eigenstates of the nuclei Hamiltonian in this approximation will later be used to study the fully interacting electron-nuclei system in perturbation theory.

The $\nu = 0$ -potential for the nuclei is given by

$$V_0(\{\hat{\mathbf{R}}_I\}) = {}_e\langle 0(\{\hat{\mathbf{R}}_I\}) | \left[\sum_i \frac{\hat{\mathbf{p}}_i^2}{2m} + \frac{1}{2} \sum_{\substack{i,j \\ i \neq j}} \frac{e^2}{|\hat{\mathbf{r}}_i - \hat{\mathbf{r}}_j|} + \sum_{i,I} \frac{-Z_I e^2}{|\hat{\mathbf{r}}_i - \hat{\mathbf{R}}_I|} \right] | 0(\{\hat{\mathbf{R}}_I\}) \rangle_e + \frac{1}{2} \sum_{\substack{I,J \\ I \neq J}} \frac{Z_I Z_J e^2}{|\hat{\mathbf{R}}_I - \hat{\mathbf{R}}_J|}. \quad (4.17)$$

It depends on the $\hat{\mathbf{R}}_I$ through *both* the electronic Hamiltonian $\hat{H}_e(\{\hat{\mathbf{R}}_I\})$ and the electronic ground state $|0(\{\hat{\mathbf{R}}_I\})\rangle_e$. With the function $V_0\{\mathbf{R}_I\}$ having a stable minimum at the equilibrium nuclear configuration $\{\mathbf{R}_I^{(0)}\}$, we expand the potential up to second order in the nuclei positions:

$$V_0(\{\mathbf{R}_I\}) \simeq V_0(\{\mathbf{R}_I^{(0)}\}) + \sum_{I,i} \frac{\partial V_0}{\partial R_{I,i}^{(0)}}(\{\mathbf{R}_I^{(0)}\})(R_{I,i} - R_{I,i}^{(0)}) + \frac{1}{2} \sum_{\substack{I,J \\ i,j}} \frac{\partial^2 V_0}{\partial R_{I,i}^{(0)} \partial R_{J,j}^{(0)}}(\{\mathbf{R}_I^{(0)}\})(R_{I,i} - R_{I,i}^{(0)})(R_{J,j} - R_{J,j}^{(0)}), \quad (4.18)$$

where the index i runs over the three cartesian directions and the linear term vanishes on account of $\{\mathbf{R}_I^{(0)}\}$ being the location of a minimum of $V_0(\{\mathbf{R}_I\})$. We will call this approximation the *harmonic approximation (HA)* since such a potential describes a system of coupled harmonic oscillators, that is, coupled vibrations of the nuclei around their equilibrium positions, which result in lattice vibrations in case of a solid. As the latter are responsible for transporting sound through a solid, the eigenstates of the corresponding Hamiltonian are traditionally called *phonons*. The approximation of replacing the full potential with a harmonic one is a very good one for many solids, in which anharmonic effects, i.e., phonon-phonon scattering, are often very small [105]. They can then be treated perturbatively [127], which, however, is beyond the scope of this thesis and will not be discussed much further.

Denoting the second derivatives of V_0 , the so-called *force constants*, by $C_{I,J}$, the nuclear Hamiltonian in the harmonic approximation reads

$$\hat{H}_{\text{HA}} = V_0(\{\mathbf{R}_I^{(0)}\}) + \frac{1}{2} \sum_{\substack{I,J \\ i,j}} C_{I,J} \hat{u}_{I,i} \hat{u}_{J,j} \equiv E_{0,\text{CNA}} + \hat{H}_{\text{ph}}, \quad (4.19)$$

where we split off the ground state energy of the electron-nuclei system in the CNA and simplified the notation by introducing the *displacement operators*

$$\hat{\mathbf{u}}_I \equiv \hat{\mathbf{R}}_I - \mathbf{R}_I^{(0)}. \quad (4.20)$$

Note that the $\hat{\mathbf{u}}_I$, still obey the canonical commutation relations with the momentum operators $\hat{\mathbf{P}}_I$:

$$\left[\hat{u}_{I,i}, \hat{u}_{J,j} \right] = \left[\hat{P}_{I,i}, \hat{P}_{J,j} \right] = 0, \quad \left[\hat{u}_{I,i}, \hat{P}_{J,j} \right] = i\delta_{I,J}\delta_{i,j}. \quad (4.21)$$

As noted in the previous chapter, for solid-state systems, each vector describing the position of a specific nucleus in the equilibrium configuration $\{\mathbf{R}_I^{(0)}\}$ is given by the sum of a lattice vector \mathbf{R}_n and a vector $\boldsymbol{\tau}_\alpha$ describing the position of the nucleus within the unit cell of the crystal. We will then label the nuclei by a tuple (n, α) , i.e., we write $\mathbf{R}_I^{(0)} \equiv \mathbf{R}_{n,\alpha}^{(0)} \equiv \mathbf{R}_n + \boldsymbol{\tau}_\alpha$. Due to the discrete translation symmetry of the crystal lattice,

the force constants can only depend on the differences $\mathbf{R}_I^{(0)} - \mathbf{R}_J^{(0)} = \mathbf{R}_{n,\alpha}^{(0)} - \mathbf{R}_{m,\beta}^{(0)}$. They thus remain invariant if both $\mathbf{R}_I^{(0)}$ and $\mathbf{R}_J^{(0)}$ are shifted by the same lattice vector, that is,

$$C_{I,J} \equiv C_{(n,\alpha),(m,\beta)} = C_{(n-m,\alpha),(0,\beta)} \equiv C_{\alpha,\beta}(\mathbf{R}_n - \mathbf{R}_m), \quad (4.22)$$

where in the intermediate step $n - m$ is a short-hand notation for $\mathbf{R}_n - \mathbf{R}_m$. In terms of the index tuples (n, α) , the phonon Hamiltonian then reads

$$\hat{H}_{\text{ph}} = \sum_{n,\alpha} \frac{\hat{\mathbf{P}}_{(n,\alpha)}^2}{2M_\alpha} + \frac{1}{2} \sum_{n,m} \sum_{\substack{\alpha,\beta \\ i,j}} C_{\alpha,\beta}(\mathbf{R}_n) \hat{u}_{(n+m,\alpha),i} \hat{u}_{(m,\beta),j}. \quad (4.23)$$

The force constants are defined on the regular grid of lattice points \mathbf{R}_n and can therefore be interpreted as the coefficients of a Fourier series

$$D_{\alpha,\beta}(\mathbf{q}) \equiv \frac{1}{\sqrt{M_\alpha M_\beta}} \sum_n e^{-i\mathbf{q}\cdot\mathbf{R}_n} C_{\alpha,\beta}(\mathbf{R}_n), \quad (4.24)$$

where $D(\mathbf{q})$ is called the *dynamical matrix* and depends on the vector \mathbf{q} , which, due to the periodicity of the Fourier series, can be restricted to the first Brillouin zone. The inverse transformation is given by

$$C_{\alpha,\beta}(\mathbf{R}_n) = \sqrt{M_\alpha M_\beta} \frac{1}{N} \sum_{\mathbf{q}} e^{i\mathbf{q}\cdot\mathbf{R}_n} D_{\alpha,\beta}(\mathbf{q}), \quad (4.25)$$

where N is the number of unit cells in a system with periodic boundary conditions. By introducing the *normal mode* displacement and momentum operators via

$$\hat{u}_{\mathbf{q}}^{\alpha,i} \equiv \frac{1}{\sqrt{N}} \sum_n e^{-i\mathbf{q}\cdot\mathbf{R}_n} \hat{u}_{(n,\alpha),i}, \quad \hat{P}_{\mathbf{q}}^{\alpha,i} \equiv \frac{1}{\sqrt{N}} \sum_n e^{-i\mathbf{q}\cdot\mathbf{R}_n} \hat{P}_{(n,\alpha),i}, \quad (4.26)$$

the phonon Hamiltonian can be written in the form

$$\hat{H}_{\text{ph}} = \sum_{\mathbf{q}} \left\{ \sum_{\alpha,i} \frac{\hat{P}_{-\mathbf{q}}^{\alpha,i} \hat{P}_{+\mathbf{q}}^{\alpha,i}}{2M_\alpha} + \frac{1}{2} \sum_{\substack{\alpha,\beta \\ i,j}} \hat{u}_{-\mathbf{q}}^{\alpha,i} \sqrt{M_\alpha} D_{\alpha,\beta}(\mathbf{q}) \sqrt{M_\beta} \hat{u}_{+\mathbf{q}}^{\beta,j} \right\}. \quad (4.27)$$

The normal mode position and momentum operators satisfy the commutation relations

$$\left[\hat{u}_{\mathbf{q}}^{\alpha,i}, \hat{u}_{\mathbf{q}'}^{\beta,j} \right] = \left[\hat{P}_{\mathbf{q}}^{\alpha,i}, \hat{P}_{\mathbf{q}'}^{\beta,j} \right] = 0, \quad \left[\hat{u}_{\mathbf{q}}^{\alpha,i}, \hat{P}_{\mathbf{q}'}^{\beta,j} \right] = \delta_{\alpha,\beta} \delta_{i,j} \delta_{\mathbf{q},-\mathbf{q}'}. \quad (4.28)$$

We also note that $(\hat{u}_{\mathbf{q}}^{\alpha,i})^\dagger = \hat{u}_{-\mathbf{q}}^{\alpha,i}$ and $(\hat{P}_{\mathbf{q}}^{\alpha,i})^\dagger = \hat{P}_{-\mathbf{q}}^{\alpha,i}$.

While the different normal modes, labeled by \mathbf{q} , are now decoupled, the different coordinate degrees of freedom of each normal mode are still coupled via the dynamical matrix. To decouple them, one can diagonalize the matrix $D(\mathbf{q})$:

$$\sum_{\beta,j} D_{\alpha,\beta}(\mathbf{q}) v_{\mathbf{q},\lambda}^{\beta,j} = \omega_{\mathbf{q},\lambda}^2 v_{\mathbf{q},\lambda}^{\alpha,i}, \quad (4.29)$$

where λ labels the different eigenvectors. In a system with N_{at} atoms in the unit cell, $D(\mathbf{q})$ is a hermitian $(3N_{\text{at}}) \times (3N_{\text{at}})$ -matrix. Hence there are $3N_{\text{at}}$ mutually orthogonal eigenvectors $v_{\mathbf{q},\lambda}^{\alpha,i}$ and the index λ is said to label the different *phonon branches*. Assuming time-reversal symmetry, we have $v_{-\mathbf{q},\lambda}^{\alpha,i} = (v_{\mathbf{q},\lambda}^{\alpha,i})^*$ and the hermiticity of $D(\mathbf{q})$ implies that its eigenvalues $\omega_{\mathbf{q},\lambda}^2$ are real. The fact that the equilibrium configuration $\{\mathbf{R}_I^{(0)}\}$ is a *stable* minimum furthermore implies $\omega_{\mathbf{q},\lambda}^2 \geq 0$, i.e., the *phonon frequencies* $\omega_{\mathbf{q},\lambda}$ in a stable system are real.

The normal mode position and momentum operators can in a next step be expanded in the basis of eigenvectors of $D(\mathbf{q})$:

$$\hat{u}_{\mathbf{q}}^{\alpha,i} \equiv \frac{M_0}{M_\alpha} \sum_{\lambda} v_{\mathbf{q},\lambda}^{\alpha,i} \hat{u}_{\mathbf{q},\lambda}, \quad \hat{P}_{\mathbf{q}}^{\alpha,i} \equiv \frac{M_\alpha}{M_0} \sum_{\lambda} v_{\mathbf{q},\lambda}^{\alpha,i} \hat{P}_{\mathbf{q},\lambda}, \quad (4.30)$$

where M_0 is a fixed, arbitrary reference mass, introduced for later convenience. In terms of the operators $\hat{u}_{\mathbf{q},\lambda}$ and $\hat{P}_{\mathbf{q},\lambda}$, the Hamiltonian becomes

$$\hat{H}_{\text{ph}} = \sum_{\mathbf{q},\lambda} \left\{ \frac{\hat{P}_{-\mathbf{q},\lambda} \hat{P}_{+\mathbf{q},\lambda}}{2M_0} + \frac{1}{2} M_0 \omega_{\mathbf{q},\lambda}^2 \hat{u}_{-\mathbf{q},\lambda} \hat{u}_{+\mathbf{q},\lambda} \right\} \quad (4.31)$$

and thus describes a set of independent harmonic oscillators.

To find the spectrum and eigenvectors of \hat{H}_{ph} , the familiar algebraic method of creation and annihilation operators can be applied. We thus define the phonon creation

and annihilation operators as

$$\begin{aligned}\hat{b}_{\mathbf{q},\lambda} &\equiv \sqrt{\frac{M_0\omega_{\mathbf{q},\lambda}}{2}} \left[\hat{u}_{\mathbf{q},\lambda} + i \frac{1}{M_0\omega_{\mathbf{q},\lambda}} \hat{P}_{\mathbf{q},\lambda} \right], \\ \hat{b}_{\mathbf{q},\lambda}^\dagger &= \sqrt{\frac{M_0\omega_{\mathbf{q},\lambda}}{2}} \left[\hat{u}_{-\mathbf{q},\lambda} - i \frac{1}{M_0\omega_{\mathbf{q},\lambda}} \hat{P}_{-\mathbf{q},\lambda} \right],\end{aligned}\tag{4.32}$$

which obey the commutation relations

$$\left[\hat{b}_{\mathbf{q},\lambda}, \hat{b}_{\mathbf{q}',\lambda'} \right] = \left[\hat{b}_{\mathbf{q},\lambda}^\dagger, \hat{b}_{\mathbf{q}',\lambda'}^\dagger \right] = 0, \quad \left[\hat{b}_{\mathbf{q},\lambda}, \hat{b}_{\mathbf{q}',\lambda'}^\dagger \right] = \delta_{\mathbf{q},\mathbf{q}'} \delta_{\lambda,\lambda'}.\tag{4.33}$$

In terms of these operators, the phonon Hamiltonian factorizes and takes on the well-known form

$$\hat{H}_{\text{ph}} = \sum_{\mathbf{q},\lambda} \omega_{\mathbf{q},\lambda} \left(\hat{b}_{\mathbf{q},\lambda}^\dagger \hat{b}_{\mathbf{q},\lambda} + \frac{1}{2} \right).\tag{4.34}$$

The eigenstates of the Hamiltonian for each normal mode can be labeled by a non-negative integer $n \in \mathbb{N}_0$:

$$\hat{H}_{\text{ph}} |n, \mathbf{q}, \lambda\rangle_n = \omega_{\mathbf{q},\lambda} \left(n + \frac{1}{2} \right) |n, \mathbf{q}, \lambda\rangle_n,\tag{4.35}$$

where the states $|n, \mathbf{q}, \lambda\rangle_n$ are defined as

$$|n, \mathbf{q}, \lambda\rangle_n \equiv \frac{1}{\sqrt{n!}} \left(\hat{b}_{\mathbf{q},\lambda}^\dagger \right)^n |0, \mathbf{q}, \lambda\rangle_n,\tag{4.36}$$

with the energetically lowest eigenstate being determined by the equation

$$\hat{b}_{\mathbf{q},\lambda} |0, \mathbf{q}, \lambda\rangle_n = 0.\tag{4.37}$$

The spectrum of the nuclear Hamiltonian in the harmonic approximation is thus entirely determined from knowledge of the phonon frequencies $\omega_{\mathbf{q},\lambda}$. As these are directly experimentally accessible, for example, via Raman spectroscopy or inelastic neutron or X-ray scattering, it is thus of great interest to have a reliable theoretical method available that allows their calculation. The main challenge lies in the calculation of

the dynamical matrix or, equivalently, the force constants. From their definition as the second derivatives of the effective potential for the nuclei, Eq. 4.17, they are given by the sum of an electronic and a nuclear contribution:

$$C_{\alpha,\beta}^{i,j}(\mathbf{R}_n) = C_{\alpha,\beta}^{(\text{el})}(\mathbf{R}_n) + C_{\alpha,\beta}^{(\text{nuc})}(\mathbf{R}_n), \quad (4.38)$$

where the latter is straightforward to calculate and reads

$$C_{\alpha,\beta}^{(\text{nuc})}(\mathbf{R}_n) = (1 - \delta_{n,0}\delta_{\alpha,\beta}) \left[\frac{\delta_{i,j}}{|\mathbf{R}_n + \boldsymbol{\tau}_\alpha - \boldsymbol{\tau}_\beta|^3} - \frac{3(\mathbf{R}_n + \boldsymbol{\tau}_\alpha - \boldsymbol{\tau}_\beta)_i(\mathbf{R}_n + \boldsymbol{\tau}_\alpha - \boldsymbol{\tau}_\beta)_j}{|\mathbf{R}_n + \boldsymbol{\tau}_\alpha - \boldsymbol{\tau}_\beta|^5} \right] \\ - \delta_{n,0}\delta_{\alpha,\beta} \sum_{\substack{m \neq n \\ \gamma \neq \beta}} \left[\frac{\delta_{i,j}}{|\mathbf{R}_m + \boldsymbol{\tau}_\gamma - \boldsymbol{\tau}_\beta|^3} - \frac{3(\mathbf{R}_m + \boldsymbol{\tau}_\gamma - \boldsymbol{\tau}_\beta)_i(\mathbf{R}_m + \boldsymbol{\tau}_\gamma - \boldsymbol{\tau}_\beta)_j}{|\mathbf{R}_m + \boldsymbol{\tau}_\gamma - \boldsymbol{\tau}_\beta|^5} \right]. \quad (4.39)$$

The electronic part of the force constants can be obtained by applying the Hellmann-Feynman theorem [128, 129] to simplify the first derivative of the electronic part of the potential:

$$\frac{\partial}{\partial R_{n,\alpha,i}} V_0^{(\text{el})}(\{\mathbf{R}_I\}) = \frac{\partial}{\partial R_{n,\alpha,i}} {}_e\langle 0(\{\mathbf{R}_I\}) | \hat{H}_e(\{\mathbf{R}_I\}) | 0(\{\mathbf{R}_I\}) \rangle_e \\ \stackrel{\text{H.-F.}}{=} {}_e\langle 0(\{\mathbf{R}_I\}) | \frac{\partial \hat{H}_e}{\partial R_{n,\alpha,i}}(\{\mathbf{R}_I\}) | 0(\{\mathbf{R}_I\}) \rangle_e \quad (4.40) \\ = \int d^3r \frac{\partial V_{\text{lat}}}{\partial R_{n,\alpha,i}}(\mathbf{r}; \{\mathbf{R}_I\}) n(\mathbf{r}; \{\mathbf{R}_I\}).$$

The electronic part of the force constants is then given by

$$C_{\alpha,\beta}^{(\text{el})}(\mathbf{R}_n) = \int d^3r \left[\frac{\partial^2 V_{\text{lat}}(\mathbf{r})}{\partial R_{n,\alpha,i}^{(0)} \partial R_{0,\beta,j}^{(0)}} n(\mathbf{r}) + \frac{\partial V_{\text{lat}}(\mathbf{r})}{\partial R_{n,\alpha,i}^{(0)}} \frac{\partial n(\mathbf{r})}{\partial R_{0,\beta,j}^{(0)}} \right], \quad (4.41)$$

where the electron density in the equilibrium nuclear configuration has been denoted by $n(\mathbf{r}) \equiv n(\mathbf{r}; \{\mathbf{R}_I^{(0)}\})$. While the derivatives of the lattice potential do not pose any theoretical or computational problems [130], the ground state electronic charge density $n(\mathbf{r}; \{\mathbf{R}_I^{(0)}\})$ and its first derivative with respect to the displacement of a nucleus can

only be calculated in some approximation. In the remainder of this chapter we will therefore discuss two approaches for their calculation and their comparison.

Firstly, we will review an approach by Baroni *et al.* [130] based on an extension of DFT called *density functional perturbation theory (DFPT)*. After briefly describing the basic approach, we will apply it to the case of graphene. Even though it works very well for many materials, it gives inaccurate results for systems with strong electronic correlation effects and in (semi-)metallic systems in which so-called *Kohn anomalies* are present [68], of which graphene is one example.

To overcome the shortcomings of DFPT, we propose a *novel theoretical approach based on many-body perturbation theory (MBPT)* for the calculation of force constants and hence of phonon frequencies. Note that the main focus of this thesis is still the study of Raman spectroscopy and as such a computational application of our new approach is beyond its scope. Nevertheless, we will still work out a concrete expression for the dynamical matrix that goes beyond the approximations present in DFPT. On the one hand, this will allow an easy and timely implementation, which will be the subject of future work. On the other hand, it permits a discussion of the underlying physics that is not captured in DFPT. Regarding to the latter, we will also analytically establish a link between the common DFPT approach and our new MBPT approach and show in which approximation the latter reduces to the former.

4.3 Phonons in density functional perturbation theory

One efficient, and for many systems very accurate way, of calculating force constants is based on density functional theory. In Section 3.2, we reviewed how the exact ground state electron density could be well approximated by an electron density calculated self-consistently within Kohn-Sham density functional theory:

$$n(\mathbf{r}) = {}_e\langle 0 | \hat{\psi}^\dagger(\mathbf{r}) \hat{\psi}(\mathbf{r}) | 0 \rangle_e \rightarrow n_{\text{KS}}(\mathbf{r}) = {}_e\langle 0_{\text{KS}} | \hat{\psi}^\dagger(\mathbf{r}) \hat{\psi}(\mathbf{r}) | 0_{\text{KS}} \rangle_e. \quad (4.42)$$

In the *density functional perturbation theory* approach to the calculation of force constants, pioneered by Baroni *et al.* [130], this approximation is applied to the *derivative* of the electron density as well:

$$\frac{\partial n(\mathbf{r})}{\partial R_{0,\beta,j}^{(0)}} \rightarrow \frac{\partial n_{\text{KS}}(\mathbf{r})}{\partial R_{0,\beta,j}^{(0)}}. \quad (4.43)$$

While the exact density does usually not differ much from the density of the Kohn-Sham system, its *change* under nuclei displacements can be very much different for some systems, such as graphene, as the failure of this approximation for some phonon modes reveals [53]. Nevertheless, this approach yields a very good result for many systems, including most phonon modes of graphene [130, 131] and is computationally very efficient. Before discussing its shortcomings and a theoretical approach to overcome them, we will thus firstly briefly review the DFPT approach.

According to Eq. 4.41, the electronic part of the force constants is entirely defined by the zeroth and first derivative of the charge density. For the auxiliary Kohn-Sham system of DFT, the ground state charge density is given by

$$n_{\text{KS}}(\mathbf{r}) = \sum_{(\mathbf{k},n) \in \mathcal{O}} |\phi_{\mathbf{k},n}(\mathbf{r})|^2, \quad (4.44)$$

where \mathcal{O} denotes the set of indices of all occupied states, with the KS states being filled up from lowest to highest energy until $\int d^3r n_{\text{KS}}(\mathbf{r}) = N_{\text{el}}$. The derivative with respect to $A \equiv R_{0,\beta,j}^{(0)}$ is then given by

$$\partial_A n_{\text{KS}}(\mathbf{r}) = 2 \operatorname{Re} \sum_{(\mathbf{k},n) \in \mathcal{O}} \phi_{\mathbf{k},n}^*(\mathbf{r}) \left(\partial_A \phi_{\mathbf{k},n}(\mathbf{r}) \right), \quad (4.45)$$

i.e., it can be computed from the change of the KS orbitals $\phi_{\mathbf{k},n}(\mathbf{r}) = {}_e \langle \mathbf{r} | \mathbf{k}, n \rangle_e$. The derivative of the KS orbitals, in turn, can be obtained by taking the derivative on both sides of the one-particle Schrödinger equation:

$$\left(\hat{H}_{\text{KS}} - \varepsilon_{\mathbf{k},n} \right) \left(\partial_A | \mathbf{k}, n \rangle_e \right) = - \left(\partial_A \hat{H}_{\text{KS}} - \partial_A \varepsilon_{\mathbf{k},n} \right) | \mathbf{k}, n \rangle_e, \quad (4.46)$$

where we inserted the derivative of the KS Hamiltonian, $\partial_A \hat{H}_{\text{KS}} = \partial_A \hat{V}_{\text{scf}}$, and the derivative of the KS eigenvalue $\varepsilon_{\mathbf{k},n}$ as given by

$$\left(\partial_A \hat{V}_{\text{scf}}\right)[n_{\text{KS}}, \partial_A n_{\text{KS}}] = \partial_A \hat{V}_{\text{lat}} + \int d^3r \frac{\delta \hat{V}_{\text{Hxc}}[n_{\text{KS}}]}{\delta n_{\text{KS}}(\mathbf{r})} \left(\partial_A n_{\text{KS}}(\mathbf{r})\right), \quad (4.47)$$

$$\partial_A \varepsilon_{\mathbf{k},n} = {}_e \langle \mathbf{k}, n | \partial_A \hat{V}_{\text{scf}} | \mathbf{k}, n \rangle_e. \quad (4.48)$$

The standard perturbation theory approach to the problem consists of solving Eq. 4.46 by inserting the complete set of eigenstates of \hat{H}_{KS} and obtain the expansion coefficients of $\partial_A |\mathbf{k}, n\rangle_e$ in the basis $\{|\mathbf{k}, n\rangle_e\}$. However, this procedure involves a summation over many states, which is computationally undesirable. In the DFPT approach, by contrast, the set of equations 4.45, 4.46, and 4.47 is instead treated as a coupled set of equations for which a *self-consistent solution* for $\partial_A n_{\text{KS}}(\mathbf{r})$ and $\partial_A \hat{V}_{\text{scf}}$ is to be found.

It is noteworthy that the whole procedure of self-consistently solving the coupled set of equations *only involves occupied states*, which is a small and computationally manageable set of states compared to the full set of intermediate states that needs to be inserted in the traditional perturbation theory approach. In particular, to obtain the derivative of the states, Eq. 4.46 only needs to be solved for $\partial_A |\mathbf{k}, n\rangle_e$ for $(\mathbf{k}, n) \in \mathcal{O}$.² The self-consistent DFPT algorithm is graphically summarized in Fig. 4.1. Having obtained the self-consistent derivative of the Kohn-Sham electron density, it can then be inserted into Eq. 4.41 to obtain the electronic part of the force constants. In practice, one usually directly calculates the Fourier-transformed force constants, i.e., the dynamical matrix, for a desired wave vector \mathbf{q} , as in this way, one needs to only consider the change of the charge density for one specific linear combination of nuclei displacements. This method thus has a major computational advantage over so-called *frozen phonon* methods in which the force constants are calculated by evaluating the first derivatives

²On a technical note, solving Eq. 4.46 for $\partial_A |\mathbf{k}, n\rangle_e$ involves inverting the operator $\hat{H}_{\text{KS}} - \varepsilon_{\mathbf{k},n}$, which appears to cause a problem when acting on the $|\mathbf{k}, n\rangle_e$ -component of the right-hand side. However, it is straightforward to show from the conventional perturbation theory expression [92, 130] that $\partial_A n_{\text{KS}}(\mathbf{r})$ stays invariant when the perturbation operator $\partial_A \hat{V}_{\text{scf}}$ is replaced by $\hat{P}_{\text{non-occ.}} \partial_A \hat{V}_{\text{scf}}$, where $\hat{P}_{\text{non-occ.}}$ is a projection operator that projects into the subspace of non-occupied states, as the contribution of occupied states vanishes identically. For the purpose of obtaining $\partial_A n_{\text{KS}}(\mathbf{r})$, it is then permissible to replace $(\partial_A \hat{H}_{\text{KS}} - \partial_A \varepsilon_{\mathbf{k},n})$ by $\hat{P}_{\text{non-occ.}} (\partial_A \hat{H}_{\text{KS}} - \partial_A \varepsilon_{\mathbf{k},n})$, when the singularity of the inverse of $\hat{H}_{\text{KS}} - \varepsilon_{\mathbf{k},n}$ for $(\mathbf{k}, n) \in \mathcal{O}$ does not matter, since it is never applied to an occupied state.

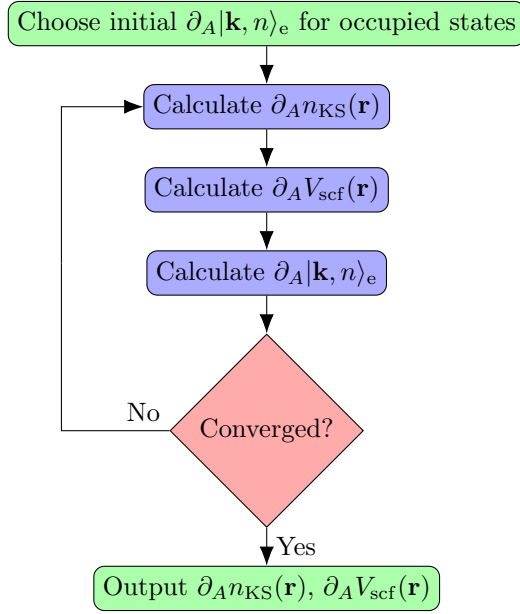


Figure 4.1: **Self-consistency cycle in density functional perturbation theory.**

of the forces on an atom in the unit cell. While the forces can be calculated via the Hellmann-Feynman theorem [128, 129], their first derivatives are calculated with finite difference methods in the frozen phonon approach, which hence requires multiple computations.

To give an example for the application of the DFPT method, we show the DFPT phonon dispersion of graphene in Fig. 4.2a. Note that we follow the historically rooted spectroscopic custom to give the phonon frequencies and energies in units of cm^{-1} , i.e., in terms of the inverse wave length of a corresponding light wave:

$$\frac{1}{\lambda} = \frac{\omega}{2\pi c} = \frac{E}{2\pi\hbar c}. \quad (4.49)$$

For practical uses we also note that the conversion between the most often used units for phonon frequencies can most easily be done by keeping in mind that

$$8 \text{ cm}^{-1} \hat{=} 1.51 \text{ THz} \hat{=} 1 \text{ meV}. \quad (4.50)$$

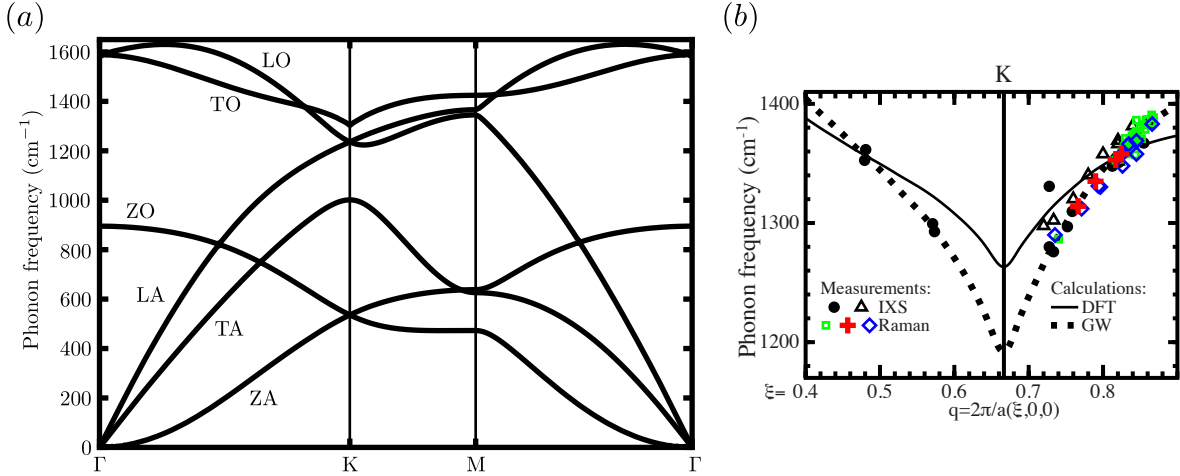


Figure 4.2: **Phonon dispersion of graphene in DFPT and example of a Kohn anomaly.** (a) Phonon dispersion of graphene along the high-symmetry-line Γ - K - M - Γ of the first Brillouin zone (see Fig. 7.1 for a sketch of the first BZ). The calculation was done using the DFPT method within the LDA. (see Ref. 67 for numerical details and convergence parameters). (b) Zoom-in into the *Kohn anomaly* of the TO branch of the phonon dispersion near $\mathbf{q} = \mathbf{K}$. Symbols denote experimental data obtained from inelastic X-ray scattering (IXS) on graphite⁴ and Raman spectroscopy.⁵ Lines represent the results of a calculation by Lazzeri *et al.* [53] using the DFPT method (full line) and a method based on finite differences of KS energies corrected within the GW approximation (dashed line). (Figure of panel (b) reprinted with permission from Lazzeri, M. *et al.*, *Phys. Rev. B* **78**, 081406 (2008). Copyright 2008 by the American Physical Society.)

Since graphene features two atoms in the unit cell (compare sketch in Fig. 7.1), the dynamical matrix is of size 6×6 , and hence there are six phonon branches: two out-of-plane ones, in which the nuclei move perpendicular to the graphene sheet and of which one is optically active (ZO) and one is not (ZA), and four in-plane ones, of which two are optically active (LO, TO) and two are not (LA, TA). An illustration of the vibration patterns for the two degenerate in-plane optical branches at $\mathbf{q} = \Gamma$, and the highest optical branch at $\mathbf{q} = \mathbf{K}$ is shown in Fig. 4.3. The modes are often denoted by the representation of the point group of the respective wave vectors they transform in, using the *Mulliken notation*³ [132]. In this notation, the doubly degenerate in-plane

³In the Mulliken notation, *A* and *B* denote a one-dimensional representation with the mode behav-

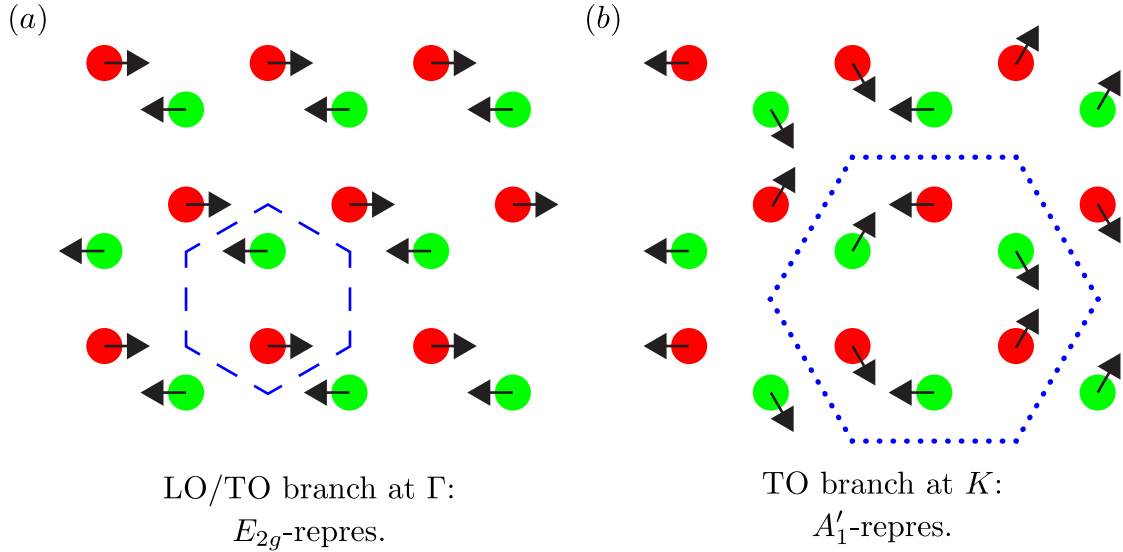


Figure 4.3: **Illustration of the vibration patterns of two phonon modes of graphene.** Patterns of the nuclei vibrations according to the highest optical phonon branches at Γ (panel (a)) and K (panel (b)). The red and green dots mark the nuclei positions in equilibrium (compare Fig. 7.1), while the arrows denote the displacements of the nuclei according to the respective eigenvector of the dynamical matrix. The dashed lines in panel (a) trace the Wigner-Seitz cell of the graphene lattice, while the dotted lines in panel (b) mark a supercell of six atoms, as the wave length of the lattice vibrations for $\mathbf{q} = \mathbf{K}$ is three times the lattice constant. Note that both the dashed and the dotted hexagons also represent the respective unit cells of the vibration patterns. (Figure inspired by Ref. 53.)

optical mode at the Γ -point is denoted by E_{2g} , while the non-degenerate highest optical branch at the K -point is characterized by the symbol A_1' .

The vibrational band structure shown in Fig. 4.2a is, as a whole, in very good agreement with the experimentally obtained dispersion from both inelastic X-ray scattering

ing in either an even or odd way under rotations, respectively, while E and T denote doubly and triply degenerate modes, respectively. A subscript 1 is used for modes that are even under reflections with respect to a C_2 axis, while 2 is used for modes that are odd under this operation. For crystals with inversion symmetry, a subscript of g or u is attached if the mode transforms in an even (*gerade*) or odd (*ungerade*) way under spatial inversion, respectively. Likewise, in crystals with horizontal mirror plane symmetry, a single prime ($'$) is used to label modes that are even under reflections at this plane, while a double prime ($''$) is used for modes that are odd under such reflections.

(IXS) on graphite⁴ [62, 133, 134] and Raman spectroscopy⁵ [61, 135] and also agrees well with previous calculations on the same level of theory [53, 56, 136]. However, both the DFPT and DFT-based frozen phonon methods have problems in accurately describing the phonon frequencies near certain points in the first Brillouin zone, at which the phonon dispersion features anomalies in the form of kinks. For graphene these kinks appear in the highest optical branches at Γ and K , where the phonon dispersion becomes non-analytic. These anomalies have first been discussed by W. Kohn in 1959 [68] and are nowadays known as *Kohn anomalies*.

The non-analyticity of the phonon dispersion is a sign of the long-range nature of the force constants, which decay only very slowly as a function of $|\mathbf{R}_n|$. This directly follows from the fact that the dynamical matrix depends on \mathbf{q} through a sum of the analytical functions $\exp(-i\mathbf{q} \cdot \mathbf{R}_n)$, weighted by the force constants $C_{(\alpha,i),(\beta,j)}(\mathbf{R}_n)$. A sum of a finite number of analytical functions is again analytic and hence a non-analytic behavior can only result from summing an *infinite* number of functions, for which it is necessary that the force constants decay very slowly with $|\mathbf{R}_n|$, i.e., that they are long-range in nature. As seen from the zoom-in into the TO branch in the region around K shown in Fig. 4.2, the DFPT approach has problems reproducing the experimentally observed behavior around the K point. While the Kohn anomaly does appear in the DFPT dispersion, it appears much less pronounced compared to the one observed in experiment. The failure of DFPT to correctly reproduce the strength of the anomaly is directly related to the problem of overscreening of the Coulomb interaction in DFT by the use of exchange-correlation functionals inspired by the free electron gas. Due to the overestimation of the screening capabilities of the electronic system, the change of the lattice potential due to the displacement of one atom is underestimated and as a result the response of the electronic system to this perturbation is underestimated as well. In

⁴Due to the generally very small X-ray scattering cross sections for monolayer materials, no IXS data is available for graphene. Instead, the theoretical phonon dispersion of graphene is usually compared to IXS data for bulk *graphite*, which has a sizable IXS cross section. The dispersions of the in-plane phonon branches (LA,TA,LO,TO) of graphene and graphite are very similar with the exception of the Kohn anomalies in the highest optical branch at Γ and K , where the larger screening effects of graphite weaken the anomalies compared to the case of graphene.

⁵The phonon dispersion of graphene can be obtained from Raman spectroscopy only in the region around the K point and only for the highest optical branch, using the so-called *double resonant* model [60, 61]. See also Ref. 67 for an introductory, conceptual explanation.

particular, the perturbation and the response of the electronic system both appear to be much more short-ranged. Since it is the response of the electronic system that is responsible for the electronic part of the force constants, the force constants appear to be of shorter range in DFPT than they are in reality.

For many materials, in particular insulators and semi-conductors, this problem of DFPT is of little consequence, as the electrons tend to be localized and thus electrons very far away from a local perturbation of the lattice potential will not be strongly affected by it in any case. As a result, the force constants in these kinds of systems are in general of a short-range nature. Therefore, DFPT is a very accurate way to calculate phonon frequencies in these kinds of systems and has been applied successfully to a wide variety of them [130]. For metals and semi-metals such as graphene, however, in which the electrons are very much delocalized, electrons at a large distance from a local perturbation *can* in general be affected by it. Nevertheless, the strong metallic screening of the perturbation in these systems still leads to force constants that are rather short-range in general. However, as first pointed out by W. Kohn [68], for perturbations of a certain wave vector, this screening can be very much decreased and as a result the force constants become much more long-ranged, which in turn leads to the non-analytic behavior in the phonon dispersion, as discussed above.

The failure of DFPT to correctly capture the strength of the Kohn anomalies is thus entirely related to the response of the electronic system to the perturbation potential due to the displacement of a nucleus. As reviewed above, in the harmonic approximation, this response is captured in the derivative of the electron density with respect to a nuclear displacement. In the DFPT approach, the derivative of the *exact* electron density is replaced by the derivative of the *Kohn-Sham* electron density. While the two electron densities are in many cases very similar *themselves*, as the KS auxiliary system is set up with this goal in mind, their *derivatives*, in general, are not. In the following section we will therefore propose a *new approach based on many-body perturbation theory (MBPT)* that allows a calculation of the derivative of the *exact* electron density within perturbation theory, using the Kohn-Sham DFT system only as a starting point.

4.4 Phonons from many-body perturbation theory

The new theoretical approach we propose for the calculation of phonon frequencies focuses on a calculation of the electronic part of the force constants within many-body perturbation theory. The calculation of the electronic part of the force constants, defined in Eq. 4.41, requires the computation of the first and second derivatives of the lattice potential with respect to nuclear displacements as well as knowledge of the exact electronic charge density and its first derivative with respect to nuclei displacements. As stated earlier, the computation of derivatives of the lattice potential does not present any larger computational or theoretical problems and can easily be done in reciprocal space [130]. Instead, the main aim of this section is to present an approach based on the formalism of many-particle electronic Green's functions [87, 91, 110] for the computation of the zeroth and first derivative of the *exact* electron density.

We start with the exact electron density, which can be written in terms of the exact electronic ground state $|0\rangle \equiv |0(\{\mathbf{R}_I^{(0)}\})\rangle_e$ and the electron field operators:

$$n(\mathbf{r}_1) = \langle 0 | \hat{\psi}^\dagger(\mathbf{r}_1) \hat{\psi}(\mathbf{r}_1) | 0 \rangle. \quad (4.51)$$

It can equally well be expressed in terms of the exact one-particle Green's function G as

$$n(\mathbf{r}_1) = (-i)G(\mathbf{r}_1, t_1; \mathbf{r}_1, t_1^+), \quad (4.52)$$

where G was defined in Eq. 3.37. As before, $t_1^+ \equiv t_1 + 0^+$, with 0^+ being a positive infinitesimal, while the additional minus sign arises from the standard definition of the time-ordering symbol for fermionic operators.

The computation of the exact charge density is thus reduced to the calculation of the exact one-particle Green's function, which we sketched in Section 3.3.1. It requires, in principle, a self-consistent solution of Dyson's equation, in which the irreducible self-energy can either be approximated by a few selected terms or subseries (as done, for example, in the GW approximation) or calculated via a self-consistent scheme of integro-differential equations first derived by Hedin [117]. Still, for practical purposes and for many materials [92, 109, 110], the exact electron density $n(\mathbf{r})$ can be well

approximated by the unperturbed Kohn-Sham electron density $n_{\text{KS}}(\mathbf{r})$, which avoids the need to solve Dyson's equation or the Hedin scheme self-consistently. However, in case the KS charge density is not a good approximation for the exact charge density, the latter can also be taken from other reference systems. Examples where KS-DFT does not yield a good approximation for the true ground state charge density are some highly correlated materials, such as TiSe_2 [108], where a more accurate estimation for the charge density can often be obtained via more complicated (hybrid) xc-functions.

However, as discussed at the end of the previous section, the *derivative* of the exact charge density is *not* always well approximated by the derivative of the Kohn-Sham charge density, especially in (semi-)metallic systems. Therefore, a better description of phonon frequencies requires a more accurate calculation of the derivative of the charge density on a level of theory that goes *beyond* that offered by density functional perturbation theory. With the charge density being directly related to the exact one-particle Green's function, we focus on obtaining a practically useful yet accurate expression for the derivative of G . Our starting point will be Dyson's equation for the one-particle Green's function, Eq. 3.54:

$$G(1, 2) = G_0(1, 2) + G_0(1, \bar{3})\Sigma(\bar{3}, \bar{4})G(\bar{4}, 2). \quad (4.53)$$

As before, we make use of the short-hand notation $1 \equiv (\mathbf{r}_1, t_1)$, etc., and understand a bar over an index to imply its being integrated over (see Eq. 3.55). Note that the irreducible self-energy is a functional of both the exact one-particle Green's function $G(1, 2)$ and the Kohn-Sham charge density $n_{\text{KS}}(\mathbf{r})$: $\Sigma(1, 2) = \Sigma[G, n_{\text{KS}}](1, 2)$.

To obtain the derivative of G with respect to the i th cartesian component of the displacement of the α th atom in the n th unit cell, $\mathbf{R}_{n,\alpha,i}^{(0)}$, we take the derivative on both sides of Dyson's equation:

$$\begin{aligned} \partial_A G(1, 2) &= \partial_A G_0(1, 2) + [\partial_A G_0(1, \bar{3})]\Sigma(\bar{3}, \bar{4})G(\bar{4}, 2) \\ &+ G_0(1, \bar{3}) \left\{ \frac{\delta \Sigma(\bar{3}, \bar{4})}{\delta G(\bar{5}, \bar{6})} [\partial_A G(\bar{5}, \bar{6})] + \frac{\delta \Sigma(\bar{3}, \bar{4})}{\delta n_{\text{KS}}(\bar{\mathbf{r}}_5)} [\partial_A n_{\text{KS}}(\bar{\mathbf{r}}_5)] \right\} G(\bar{4}, 2) \quad (4.54) \\ &+ G_0(1, \bar{3})\Sigma(\bar{3}, \bar{4})[\partial_A G(\bar{4}, 2)], \end{aligned}$$

where we use the abbreviation $\partial_A \equiv \partial/\partial R_{n,\alpha,i}^{(0)}$. According to Eq. 3.56, the irreducible self-energy is given by the sum of two parts, each of which is a functional of only G or n_{KS} but not the other. The functional derivatives of $\Sigma(1, 2)$ are therefore straightforward to evaluate:

$$\frac{\delta\Sigma(3, 4)}{\delta G(5, 6)} = \frac{\delta\Sigma_{\text{Coul.}}(3, 4)}{\delta G(5, 6)} = K^{(2)}(3, 4; 5, 6) \quad (4.55)$$

$$\frac{\delta\Sigma(3, 4)}{\delta n_{\text{KS}}(\mathbf{r}_5)} = \frac{\delta\Sigma_{-\text{Hxc}}(3, 4)}{\delta n_{\text{KS}}(\mathbf{r}_5)} = - \left\{ \frac{\delta V_{\text{H}}(\mathbf{r}_3)}{\delta n_{\text{KS}}(\mathbf{r}_5)} + \frac{\delta V_{\text{xc}}(\mathbf{r}_3)}{\delta n_{\text{KS}}(\mathbf{r}_5)} \right\} \delta(3, 4). \quad (4.56)$$

In the first line, we identified the two-particle-irreducible interaction kernel $K^{(2)}(3, 4; 5, 6)$ (see the discussion surrounding Eq. 3.78). The contribution of the second line can be combined with the derivative of the KS charge density:

$$\frac{\delta\Sigma(3, 4)}{\delta n_{\text{KS}}(\bar{\mathbf{r}}_5)} [\partial_A n_{\text{KS}}(\bar{\mathbf{r}}_5)] = -[\partial_A V_{\text{Hxc}}(\mathbf{r}_3)] \delta(3, 4). \quad (4.57)$$

Rearranging terms, Eq. 4.54 reads:

$$\begin{aligned} \left\{ \delta(1, \bar{4}) - G_0(1, \bar{3})\Sigma(\bar{3}, \bar{4}) \right\} [\partial_A G(\bar{4}, 2)] &= [\partial_A G_0(1, \bar{3})] \left\{ \delta(\bar{3}, 2) + \Sigma(\bar{3}, \bar{4})G(\bar{4}, 2) \right\} \\ &+ G_0(1, \bar{3}) \left\{ K^{(2)}(\bar{3}, \bar{4}; \bar{5}, \bar{6}) [\partial_A G(\bar{5}, \bar{6})] \right. \\ &\quad \left. - [\partial_A V_{\text{Hxc}}(\bar{\mathbf{r}}_3)] \delta(\bar{3}, \bar{4}) \right\} G(\bar{4}, 2). \end{aligned} \quad (4.58)$$

The first two terms in curly braces can be simplified using Dyson's equation. Multiplying the latter from the right with G^{-1} or from the left with G_0^{-1} yields the two identities

$$\delta(1, 4) - G_0(1, \bar{3})\Sigma(\bar{3}, 4) = G_0(1, \bar{3})G^{-1}(\bar{3}, 4), \quad (4.59)$$

$$\delta(3, 2) + \Sigma(3, \bar{4})G(\bar{4}, 2) = G_0^{-1}(3, \bar{4})G(\bar{4}, 2). \quad (4.60)$$

Further defining the two useful two-point functions

$$g(1, 2) \equiv G^{-1}(1, \bar{3})[\partial_A G(\bar{3}, \bar{4})]G^{-1}(\bar{4}, 2) \quad (4.61)$$

$$g^{(0)}(1, 2) \equiv G_0^{-1}(1, \bar{3})[\partial_A G_0(\bar{3}, \bar{4})]G_0^{-1}(\bar{4}, 2), \quad (4.62)$$

we find that $g(1, 2)$ obeys an integral equation:

$$g(1, 2) = g^{(0)}(1, 2) - [\partial_A V_{\text{Hxc}}(\mathbf{r}_1)]\delta(1, 2) + K^{(2)}(1, 2; \bar{3}, \bar{4})G(\bar{3}, \bar{5})g(\bar{5}, \bar{6})G(\bar{6}, \bar{4}). \quad (4.63)$$

As will become clear in the next chapter, the two-point functions $g(1, 2)$ and $g^{(0)}(1, 2)$ can be interpreted as the *static, screened electron-nuclei coupling*, with the screening described *exactly* ($g(1, 2)$) or on the level of *DFPT* ($g^{(0)}(1, 2)$). The DFPT electron-nuclei coupling $g^{(0)}(1, 2)$ can be evaluated in terms of $\partial_A G_0^{-1}$ by noting that the definition of the inverse Kohn-Sham Green's function, $G_0^{-1}(1, \bar{3})G_0(\bar{3}, 2) = \delta(1, 2)$, implies that the derivatives of G_0 and G_0^{-1} are related by⁶

$$\partial_A G_0^{-1}(1, 2) = -G_0^{-1}(1, \bar{3})[\partial_A G_0(\bar{3}, \bar{4})]G_0^{-1}(\bar{4}, 2). \quad (4.64)$$

It is easily verified that the inverse KS Green's function is explicitly given by

$$G_0^{-1}(1, 2) = \delta(1, 2) \left\{ i \frac{\partial}{\partial t_2} + \frac{\nabla_2^2}{2m} - V_{\text{scf}}(\mathbf{r}_2) \right\}, \quad (4.65)$$

from which the DFPT electron-nuclei coupling is immediately obtained as

$$g^{(0)}(1, 2) = -\partial_A G_0^{-1}(1, 2) = \delta(1, 2) \partial_A V_{\text{scf}}(\mathbf{r}_2) = \delta(1, 2) \left\{ \partial_A V_{\text{lat}}(\mathbf{r}_2) + \partial_A V_{\text{Hxc}}(\mathbf{r}_2) \right\} \quad (4.66)$$

by noting that the only explicit dependence of G_0^{-1} on the nuclei positions is through the self-consistent potential, which is composed of the lattice potential and the sum of the local Hartree (H) and exchange-correlation (xc) potentials. Defining the *bare*

⁶Alternatively, this relation follows from a generalization of the chain rule for derivatives.

electron-nuclei coupling as

$$g^{(b)}(1, 2) \equiv \delta(1, 2) \partial_A V_{\text{lat}}(\mathbf{r}_2), \quad (4.67)$$

we find that Eq. 4.63 takes on the form

$$\left\{ \delta(1, \bar{5}) \delta(2, \bar{6}) - K^{(2)}(1, 2; \bar{3}, \bar{4}) L_0(\bar{3}, \bar{4}; \bar{5}, \bar{6}) \right\} g(\bar{5}, \bar{6}) = g^{(b)}(1, 2) \quad (4.68)$$

where we identified the independent-particle two-particle correlation function $L_0(3, 4; 5, 6) \equiv G(3, 5)G(6, 4)$, introduced in Section 3.3.2. Multiplying this equation from the left with the *exact* two-particle correlation function L and using the Bethe-Salpeter equation in the form

$$L(1, 2; 4, 3) - L(1, 2; \bar{5}, \bar{6}) K^{(2)}(\bar{5}, \bar{6}; \bar{7}, \bar{8}) L_0(\bar{7}, \bar{8}; 3, 4) = L_0(1, 2; 3, 4), \quad (4.69)$$

we arrive at

$$g(1, 2) = L_0^{-1}(1, 2; \bar{3}, \bar{4}) L(\bar{3}, \bar{4}; \bar{5}, \bar{6}) g^{(b)}(\bar{5}, \bar{6}), \quad (4.70)$$

where we also multiplied by the inverse of the independent-particle correlation function, $L_0^{-1}(1, 2; 3, 4) = G^{-1}(1, 3)G^{-1}(4, 2)$. In the next chapter, we will see how this expression can indeed be interpreted as the static, screened electron-nuclei coupling and also derive its non-static version diagrammatically. For the purpose of the present discussion, however, it is sufficient to obtain the derivative of the exact charge density from it. Substituting our definition of $g(1, 2)$, we obtain the derivative of the exact one-particle Green's function as

$$\partial_A G(1, 2) = L(1, 2; \bar{3}, \bar{4}) g^{(b)}(\bar{3}, \bar{4}), \quad (4.71)$$

from which the derivative of the exact charge density follows as

$$\partial_A n(\mathbf{r}_1) = (-i) \partial_A G(1, 1^+) = (-i) L(1, 1^+; \bar{2}^+, \bar{2}) [\partial_A V_{\text{lat}}(\bar{\mathbf{r}}_2)]. \quad (4.72)$$

In the last expression, we introduced another positive infinitesimal shift to t_2 in order to fix the time-ordering of the equal-time two-particle correlation function, such that the ordering of the two electron field operators at equal times follows that of the lattice

potential part of the Hamiltonian ($\sim \hat{\psi}^\dagger V_{\text{lat}} \hat{\psi}$).

Putting everything together, we have derived the following expression for the *exact* electronic part of the force constants from many-body perturbation theory:

$$C_{\alpha,\beta}^{(\text{el})}(\mathbf{R}_n) = \int d^3r \frac{\partial^2 V_{\text{lat}}}{\partial R_{n,\alpha,i}^{(0)} R_{0,\beta,j}^{(0)}}(\mathbf{r}) (-i) G(\mathbf{r}, t; \mathbf{r}, t^+) \\ + \int d^3r \int d^3r' \int_{-\infty}^{+\infty} dt' \frac{\partial V_{\text{lat}}}{\partial R_{n,\alpha,i}^{(0)}}(\mathbf{r}) (-i) L(\mathbf{r}, t; \mathbf{r}, t^+; \mathbf{r}', t^+; \mathbf{r}', t') \frac{\partial V_{\text{lat}}}{\partial R_{0,\beta,j}^{(0)}}(\mathbf{r}'). \quad (4.73)$$

We can obtain a more practically useful expression for it and the electronic part of the dynamical matrix by expanding the exact one-particle Green's function and the two-particle correlation function in the basis of Kohn-Sham states and performing a Fourier decomposition, as defined in Eqs. 3.45 and 3.84. We also define the matrix elements of the derivatives of the lattice potential between KS states via

$$g_{a,b}^{(\text{b});(n,\alpha,i)} \equiv \int d^3r \phi_{\mathbf{k}',a}^*(\mathbf{r}) \frac{\partial V_{\text{lat}}(\mathbf{r})}{\partial R_{n,\alpha,i}^{(0)}} \phi_{\mathbf{k},b}(\mathbf{r}), \quad (4.74)$$

$$g_{a,b}^{(\text{b});(2);(n,\alpha),(m,\beta)} \equiv \int d^3r \phi_{\mathbf{k}',a}^*(\mathbf{r}) \frac{\partial^2 V_{\text{lat}}(\mathbf{r})}{\partial R_{n,\alpha,i}^{(0)} R_{m,\beta,j}^{(0)}} \phi_{\mathbf{k},b}(\mathbf{r}), \quad (4.75)$$

with $\phi_{\mathbf{k},a}(\mathbf{r})$ being a one-particle KS wave function. Making use of Bloch' theorem, Eq. 3.36, we can write these matrix elements in terms of the matrix elements involving the $n = 0$ unit cell only:

$$g_{a,b}^{(\text{b});(n,\alpha,i)} = \frac{1}{\sqrt{N}} e^{i(\mathbf{k}-\mathbf{k}') \cdot \mathbf{R}_n} g_{a,b}^{(\text{b});(\alpha,i)}, \quad (4.76)$$

$$g_{a,b}^{(\text{b});(2);(n,\alpha),(m,\beta)} = \delta_{n,m} e^{i(\mathbf{k}-\mathbf{k}') \cdot \mathbf{R}_n} g_{a,b}^{(\text{b});(2);(\alpha,\beta)}_{i,j}, \quad (4.77)$$

where the “reduced” matrix elements are defined in terms of the lattice periodic part,

$\chi_{\mathbf{k},a}(\mathbf{r})$, of the KS wave function only:

$$g_{a,b}^{(b);(\alpha,i)} \equiv \frac{1}{\sqrt{N}} \int d^3r e^{-i(\mathbf{k}'-\mathbf{k})\cdot\mathbf{r}} \chi_{\mathbf{k}',a}^*(\mathbf{r}) \frac{\partial V_{\text{lat}}(\mathbf{r})}{\partial R_{0,\alpha,i}^{(0)}} \chi_{\mathbf{k},b}(\mathbf{r}), \quad (4.78)$$

$$g_{a,b}^{(b);(2);(\alpha,\beta)} \equiv \frac{1}{N} \int d^3r e^{-i(\mathbf{k}'-\mathbf{k})\cdot\mathbf{r}} \chi_{\mathbf{k}',a}^*(\mathbf{r}) \frac{\partial^2 V_{\text{lat}}(\mathbf{r})}{\partial R_{0,\alpha,i}^{(0)} \partial R_{0,\beta,j}^{(0)}} \chi_{\mathbf{k},b}(\mathbf{r}). \quad (4.79)$$

The particular dependence of the matrix elements on the lattice vector \mathbf{R}_n makes it particularly easy to evaluate the lattice Fourier transform that leads to the dynamical matrix. After further algebraic simplifications, the electronic part of the dynamical matrix, defined by letting $C \rightarrow C^{(\text{el})}$ in Eq. 4.24, takes on the form:

$$D_{i,j}^{(\text{el})}(\mathbf{q}) = \frac{1}{\sqrt{M_\alpha M_\beta}} (-i) \sum_{\substack{\mathbf{k},\mathbf{k}' \\ a,b,c,d}} \left(g_{a,b}^{(b);(\alpha,i)} \right)^* \tilde{L}_{\substack{\mathbf{k}'+\mathbf{q},a;\mathbf{k}+\mathbf{q},c \\ \mathbf{k}',b;\mathbf{k},d}}(0) g_{c,d}^{(b);(\beta,j)} \\ + \frac{1}{\sqrt{M_\alpha M_\beta}} \sum_{\mathbf{k},a,b} g_{a,b}^{(b);(2);(\alpha,\beta)} \int \frac{d\omega}{2\pi i} e^{i\omega 0^+} \tilde{G}_{\mathbf{k},a,b}(\omega). \quad (4.80)$$

This expresses the exact dynamical matrix in terms of the KS matrix elements of the first and second derivatives of the lattice potential and of the exact one-particle Green's function and two-particle correlation function. The matrix elements of the derivatives of the lattice potential can most conveniently be calculated in a plane-wave basis [130]. The correlation functions G and L can, in principle, be obtained from Dyson's equation and the Bethe-Salpeter equation, as discussed in Section 3.3. However, since the exact solution of these equations is still computationally unfeasible for many solid-state systems, our suggested practical approach consists of solving the BSE in the approximations discussed in Section 3.3.2, i.e., deriving the interaction kernel from the self-energy in the GW approximation, neglecting the functional derivative of the screened Coulomb interaction, and treating the latter as being static. Under these approximations, the two-particle correlation function is given by Eq. 3.105. Furthermore, as discussed earlier, the exact charge density itself, which appears in the second term of Eq. 4.80, can often be well approximated with the Kohn-Sham charge density. Within these approximations, we find a practically useful expression for the electronic part of the dynamical

matrix:⁷

$$\begin{aligned}
D_{\alpha,\beta}^{(\text{el})}(\mathbf{q}) = & \frac{1}{\sqrt{M_\alpha M_\beta}} \sum_{\substack{\mathbf{k}, \mathbf{k}' \\ a, b, c, d}} \left(g_{\mathbf{k}'+\mathbf{q}, \mathbf{k}'}^{(\text{b});(\alpha, i)} \right)^* \sum_{S, S'} \frac{A_{\mathbf{k}'+\mathbf{q}, a}^S N_{S, S'}^{-1} A_{\mathbf{k}+\mathbf{q}, c}^{S', *}}{-\varepsilon_S + i\eta} g_{\mathbf{k}+\mathbf{q}, \mathbf{k}}^{(\text{b});(\beta, j)} \\
& + \frac{1}{\sqrt{M_\alpha M_\beta}} \sum_{(\mathbf{k}, a) \in \mathcal{O}} g_{\mathbf{k}, \mathbf{k}}^{(\text{b});(2);(\alpha, \beta)}_{a, a},
\end{aligned} \tag{4.81}$$

where, as before, \mathcal{O} denotes the set of all tuples (\mathbf{k}, a) specifying a state $|\mathbf{k}, a\rangle$ that is occupied in the KS ground state $|\emptyset\rangle$. Introducing the (bare) *bilinear exciton-nuclei coupling*

$$g_{\mathbf{q}, S}^{(\text{b});(\alpha, i)} \equiv \sum_{\substack{\mathbf{k}, a, b \\ \mathbf{k}, b}} A_{\mathbf{k}+\mathbf{q}, a}^{S, *} g_{\mathbf{k}+\mathbf{q}, \mathbf{k}}^{(\text{b});(\alpha, i)}_{a, b}, \tag{4.82}$$

our proposed expression for the electronic part of the dynamical matrix takes on the compact form

$$D_{\alpha,\beta}^{(\text{el})}(\mathbf{q}) = \frac{1}{\sqrt{M_\alpha M_\beta}} \left\{ \sum_{S, S'} \frac{\left(g_{\mathbf{q}, S}^{(\text{b});(\alpha, i)} \right)^* N_{S, S'}^{-1} g_{\mathbf{q}, S'}^{(\text{b});(\beta, j)}}{-\varepsilon_S + i\eta} + \sum_{(\mathbf{k}, a) \in \mathcal{O}} g_{\mathbf{k}, \mathbf{k}}^{(\text{b});(2);(\alpha, \beta)}_{a, a} \right\}. \tag{4.83}$$

This expression is one of the central results presented in this thesis.

We can summarize our proposed approach for the calculation of phonon frequencies as follows:

1. Calculation of a set of Kohn-Sham states and eigenvalues in density functional theory.
2. Correction of the KS eigenvalues on the level of the GW approximation.
3. Computation of the static two-particle interaction kernel, solving the static ($\omega = 0$) Bethe-Salpeter equation for both the eigenstates and eigenvalues, and calculation of the overlap matrix.

⁷To make the expression more compact, we absorbed the occupation factor $(f_{\mathbf{k}+\mathbf{q}, c} - f_{\mathbf{k}, d})$ appearing in Eq. 3.105 into the eigenvectors $A_{\mathbf{k}+\mathbf{q}, c}^S_{\mathbf{k}, d}$.

4. Calculation of the matrix elements of the first and second derivatives of the lattice potential in the KS basis and computation of the bilinear exciton-nuclei coupling.
5. Construction of the electronic part of the dynamical matrix according to Eq. 4.83, addition of the nuclear part, and subsequent diagonalization.

So far, this approach has not been tested in practice due to the lack of an implementation that allows both the evaluation of electron-nuclei matrix elements and solving of the BSE for finite excitation wave vectors \mathbf{q} . Its concrete implementation in a computer code is beyond the scope of this thesis, but will be the subject of further research.

4.5 Physical interpretation and relation between different approximations for force constants

To conclude this chapter, we discuss the differences between our, in principle exact, MBPT approach and other approaches, in particular DFPT. Other common approximations for the electronic part of the force constants that we will discuss are the random phase approximation (RPA) and a Hartree-Fock-based approximation (HFA).

In order to be able to compare the different approaches and approximations for the computation of the electronic part of the force constants with one another, it is simplest to formulate them in the same language, for which the language of many-body perturbation theory suggests itself. The first term appearing in the general expression for the electronic part of the force constants, Eq. 4.41, involves the charge density itself. It will usually not vary much from approach to approach, assuming that every approach for the electronic structure calculation is at least sensible enough to yield a good approximation of the charge density when it is applied self-consistently. The second term, which involves the first derivative of the charge density with respect to nuclear displacements, is what varies substantially from approach to approach, as already discussed at the end of Section 4.3.

To start with, we consider the derivative of the charge density within DFPT and

re-write it in the MBPT formalism:

$$\partial_A n_{\text{KS}}(\mathbf{r}_1) = (-i)\partial_A G_0(1, 1^+) = (-i)G_0(1, \bar{3})[\partial_A G_0^{-1}(\bar{3}, \bar{4})]G_0(\bar{4}, 1^+), \quad (4.84)$$

where again $\partial_A \equiv \partial/\partial R_{n,\alpha,i}^{(0)}$. Introducing the independent-particle two-particle correlation function on the Kohn-Sham level,

$$L_0^{(\text{KS})}(1, 2; 3, 4) \equiv G_0(1, 3)G_0(4, 2) \quad (4.85)$$

and making use of Eq. 4.66, the derivative of the KS charge density reads

$$\partial_A n_{\text{KS}}(\mathbf{r}_1) = (-i)L_0^{(\text{KS})}(1, 1^+; \bar{2}^+, \bar{2})[\partial_A V_{\text{scf}}(\bar{\mathbf{r}}_2)]. \quad (4.86)$$

The electronic part of the force constants in DFPT is then given by

$$\begin{aligned} C_{\alpha,\beta}^{(\text{el})}(\mathbf{R}_n) \Big|_{\text{DFPT}} &= \int d^3r \frac{\partial^2 V_{\text{lat}}}{\partial R_{n,\alpha,i}^{(0)} \partial R_{0,\beta,j}^{(0)}}(\mathbf{r}) (-i)G_0(\mathbf{r}, t; \mathbf{r}, t^+) \\ &+ \int d^3r \int d^3r' \int_{-\infty}^{+\infty} dt' \frac{\partial V_{\text{lat}}}{\partial R_{n,\alpha,i}^{(0)}}(\mathbf{r}) \\ &\times (-i)L_0^{(\text{KS})}(\mathbf{r}, t; \mathbf{r}, t^+; \mathbf{r}', t'^+; \mathbf{r}', t') \frac{\partial V_{\text{scf}}}{\partial R_{0,\beta,j}^{(0)}}(\mathbf{r}'). \end{aligned} \quad (4.87)$$

Note that the second term involves both the derivative of the lattice potential and the derivative of the self-consistent potential. As will be discussed in the next chapter, the latter can be interpreted as a screened electron-phonon coupling, while the former corresponds to the unscreened or bare electron-phonon coupling. Diagrammatically, the calculation of the force constants in DFPT then involves the product of a vertex for the bare electron-nuclei interaction, the independent-particle two-particle correlation function, and a vertex for the screened electron-nuclei interaction.⁸ This fact is often ignored in the literature, where both vertices are often treated as being screened, as done for instance in the work by Lazzeri *et al.* [53] on the phonon dispersion of graphene, which we will briefly discuss further in the next chapter.

⁸This fact also been noticed and pointed out independently by F. Giustino [131].

To make the approximations implicit in the DFPT description more transparent, we express the derivative of the self-consistent potential in a different way. Letting $V_{\text{scf}}(1, 2) \equiv \delta(1, 2)V_{\text{scf}}(\mathbf{r}_2)$ and similarly for the lattice and Hartree+xc potential, we have:

$$\begin{aligned}\partial_A V_{\text{scf}}(1, 2) &= \partial_A V_{\text{lat}}(1, 2) + \frac{\delta V_{\text{Hxc}}(1, 2)}{\delta n_{\text{KS}}(\bar{\mathbf{r}}_3)} [\partial_A n_{\text{KS}}(\bar{\mathbf{r}}_3)] \\ &= \partial_A V_{\text{lat}}(1, 2) + \frac{\delta V_{\text{Hxc}}(1, 2)}{\delta G_0(\bar{3}, \bar{4}^+)} \delta(\bar{3}, \bar{4}) [\partial_A G_0(\bar{3}, \bar{4}^+)].\end{aligned}\quad (4.88)$$

We can cast this equation in a more familiar form by defining the two-particle irreducible interaction kernel in KS-DFPT via

$$K^{(2);(\text{KS})}(1, 2; 3, 4) \equiv \frac{\delta V_{\text{Hxc}}(1, 2)}{\delta G_0(3, 4^+)} \delta(3, 4). \quad (4.89)$$

Inserting the explicit expression for the Hartree+xc potential (see Eq. 3.30), one finds:

$$K^{(2);(\text{KS})}(1, 2; 3, 4) = -i\delta(1, 2)\delta(3, 4)[v(1, 3) - \Delta v_{\text{xc}}(1, 3)], \quad (4.90)$$

where

$$\Delta v_{\text{xc}}(1, 2) \equiv -\frac{\delta V_{\text{xc}}[n_{\text{KS}}](\mathbf{r}_1)}{\delta n_{\text{KS}}(\mathbf{r}_2)} \delta(t_1 - t_2) \quad (4.91)$$

and we included a minus sign in the last definition to emphasize the fact that the exchange-correlation potential is mostly attractive. With these definitions and using Eq. 4.86, the derivative of the self-consistent potential is found to obey the integral equation

$$\partial_A V_{\text{scf}}(1, 2) = \partial_A V_{\text{lat}}(1, 2) + K^{(2);(\text{KS})}(1, 2; \bar{3}, \bar{4}) L_0^{(\text{KS})}(\bar{3}, \bar{4}; \bar{5}, \bar{6}) [\partial_A V_{\text{scf}}(\bar{5}, \bar{6})]. \quad (4.92)$$

If we further define the exact two-particle correlation function on the KS-DFT level via the Bethe-Salpeter equation

$$L^{(\text{KS})}(1, 2; 3, 4) \equiv L_0^{(\text{KS})}(1, 2; 3, 4) + L_0^{(\text{KS})}(1, 2; \bar{5}, \bar{6}) K^{(2);(\text{KS})}(\bar{5}, \bar{6}; \bar{7}, \bar{8}) L^{(\text{KS})}(\bar{7}, \bar{8}; 3, 4), \quad (4.93)$$

we can solve Eq. 4.92 using the same algebraic manipulations as used in the exact MBPT case:

$$\partial_A V_{\text{scf}}(1, 2) = (L_0^{(\text{KS})})^{-1}(1, 2; \bar{3}, \bar{4})L^{(\text{KS})}(\bar{3}, \bar{4}; \bar{5}, \bar{6})[\partial_A V_{\text{lat}}(\bar{5}, \bar{6})]. \quad (4.94)$$

Putting everything together, the electronic part of the force constants in KS-DFPT can be written in the form

$$\begin{aligned} C_{\alpha,\beta}^{(\text{el})}(\mathbf{R}_n) \Big|_{\text{DFPT}}^{i,j} &= \int d^3r \frac{\partial^2 V_{\text{lat}}}{\partial R_{n,\alpha,i}^{(0)} R_{0,\beta,j}^{(0)}}(\mathbf{r})(-i)G_0(\mathbf{r}, t; \mathbf{r}, t^+) \\ &+ \int d^3r \int d^3r' \int_{-\infty}^{+\infty} dt' \frac{\partial V_{\text{lat}}}{\partial R_{n,\alpha,i}^{(0)}}(\mathbf{r}) \\ &\times (-i)L^{(\text{KS})}(\mathbf{r}, t; \mathbf{r}, t^+; \mathbf{r}', t'^+; \mathbf{r}', t') \frac{\partial V_{\text{lat}}}{\partial R_{0,\beta,j}^{(0)}}(\mathbf{r}'). \end{aligned} \quad (4.95)$$

This expression has the same structure as the exact one obtained from MBPT (compare Eq. 4.73). The only difference is the replacement of the one-particle Green's function and the two-particle correlation function by their counterparts from KS-DFT. The most important aspect of the approximations implicit in the DFPT approach is the approximation to the two-particle-irreducible interaction kernel (compare Eq. 4.90). It is this quantity which governs the screening of the electron-nuclei interaction.

To better understand the DFPT approximation to the kernel, it should be compared to other approximations, four of which are listed in Table 4.1.

Approach/Approximation	$K^{(2)}(1, 2; 3, 4)$
RPA	$-i\delta(1, 2)\delta(3, 4)v(1, 3)$
HFA	$-i\delta(1, 2)\delta(3, 4)v(1, 3) + i\delta(1, 3)\delta(2, 4)v(1, 2)$
MBPT (GWA, $\delta W/\delta G=0$)	$-i\delta(1, 2)\delta(3, 4)v(1, 3) + i\delta(1, 3)\delta(2, 4)W(1, 2)$
DFPT	$-i\delta(1, 2)\delta(3, 4)[v(1, 3) - \Delta v_{\text{xc}}(1, 3)]$

Table 4.1: **Different approximations for the two-particle-irreducible interaction kernel.**

In the *random phase approximation* (RPA), the interaction kernel is derived from

an electron self-energy on the level of the Hartree approximation:

$$\text{RPA} \longleftrightarrow \Sigma_{\text{Coul.}}(1, 2) \stackrel{\text{Hartree}}{\simeq} -i\delta(1, 2)v(1, \bar{3})G(\bar{3}, \bar{3}^+). \quad (4.96)$$

It corresponds to the simplest non-trivial two-particle-irreducible interaction kernel, consisting of the unscreened Coulomb interaction only. Physically, the screening of the electron-nuclei interaction in the RPA is taken into account by describing the irreducible polarizability of the material on the level of electron-hole pairs, whose dipole moments serve as a screening medium. While the interaction between the induced electron-hole pairs is included in the self-consistent Bethe-Salpeter equation, the electron and hole are treated as not interacting with each other.

Going beyond the RPA, the next-to-leading-order approximation to the irreducible interaction kernel is derived from the *Hartree-Fock approximation (HFA)* to the electron self-energy:

$$\text{HFA} \longleftrightarrow \Sigma_{\text{Coul.}}(1, 2) \stackrel{\text{Hartree-Fock}}{\simeq} -i\delta(1, 2)v(1, \bar{3})G(\bar{3}, \bar{3}^+) + iv(1, 2)G(1, 2). \quad (4.97)$$

It remedies the problem of the overscreening present in the RPA by taking into account the interaction between the electron and the hole in the induced electron-hole pairs. In a real space picture, this reduces the spatial extend of the approximate dipoles formed by the electron-hole pairs, thus reducing the polarizability of the material. This leads to a significant reduction of the screening of the effective electron-nuclei interaction and thereby greatly increases the electronic contribution to the force constants. The HFA approximation to the interaction kernel treats the electron-hole interaction as unscreened however. The electron and hole are thus described as being bound too close together, which reduces the size of their dipole moment and thus the screening of the effective electron-nuclei interaction too much.

In our proposed *MBPT approach* to the calculation of the force constants, this problem is addressed by including the screening of the electron-hole interaction perturbatively as the two-particle interaction kernel is derived from the electron self-energy

in the GW approximation:

$$\text{MBPT} \longleftrightarrow \Sigma_{\text{Coul.}}(1, 2) \stackrel{\text{GWA}}{\simeq} -i\delta(1, 2)v(1, \bar{3})G(\bar{3}, \bar{3}^+) + iW(1, 2)G(1, 2). \quad (4.98)$$

This approach thus includes a screening of the electron-hole interaction on the level of the RPA. It therefore does not lead to an overbinding of the induced electron-hole pairs or, equivalently, an underestimation of their dipole moments and of the polarizability of the material. As a result, the electron-nuclei interaction is expected to be much less screened than in the HFA and captured more accurately.

The *DFPT approach*, finally, resembles a conceptually very much different point of view. Rather than attempting to better describe the magnitude of the induced electron-hole dipole moments, it replaces the bare Coulomb interaction simply by an effective, weaker interaction, by subtracting an xc-contribution $\Delta v_{\text{xc}}(1, 2)$ from it. In the self-energy/interaction kernel language, we have seen that it makes use of an irreducible interaction kernel derived from an electron self-energy of the form

$$\text{DFPT} \longleftrightarrow \Sigma_{\text{Coul.}}(1, 2) \stackrel{\text{DFT}}{\simeq} -i\delta(1, 2)[v(1, \bar{3}) - \Delta v_{\text{xc}}(1, \bar{3})]G(\bar{3}, \bar{3}^+). \quad (4.99)$$

The irreducible polarizability of the material, i.e., the induced electron-hole dipoles, is thus described on the same level as in the RPA. However, the coupling between the different electron-hole dipoles is not given by the standard Coulomb interaction, but rather by an effective, weaker one. As such, the effective electron-nuclei interaction appears less screened than in the RPA. Compared to our proposed MBPT approach, however, this screening is expected to still be overestimated, based on related calculations of the electron-nuclei coupling by Lazzeri *et al.* [53]. There, the authors used finite difference methods to calculate the derivative of the diagonal KS matrix elements of the *non-self-consistently* calculated electron self-energy to obtain a better estimate for the screened electron-nuclei interaction. However, the non-self-consistency of the calculations by Lazzeri *et al.* *cannot* capture the entire series of terms considered and exactly summed in our MBPT approach, but instead is expected to correspond to the first few leading-order terms appearing in our proposed method only. An analytic proof for this statement will be the subject of further research, as will be the concrete implementation

and comparison of our ansatz.

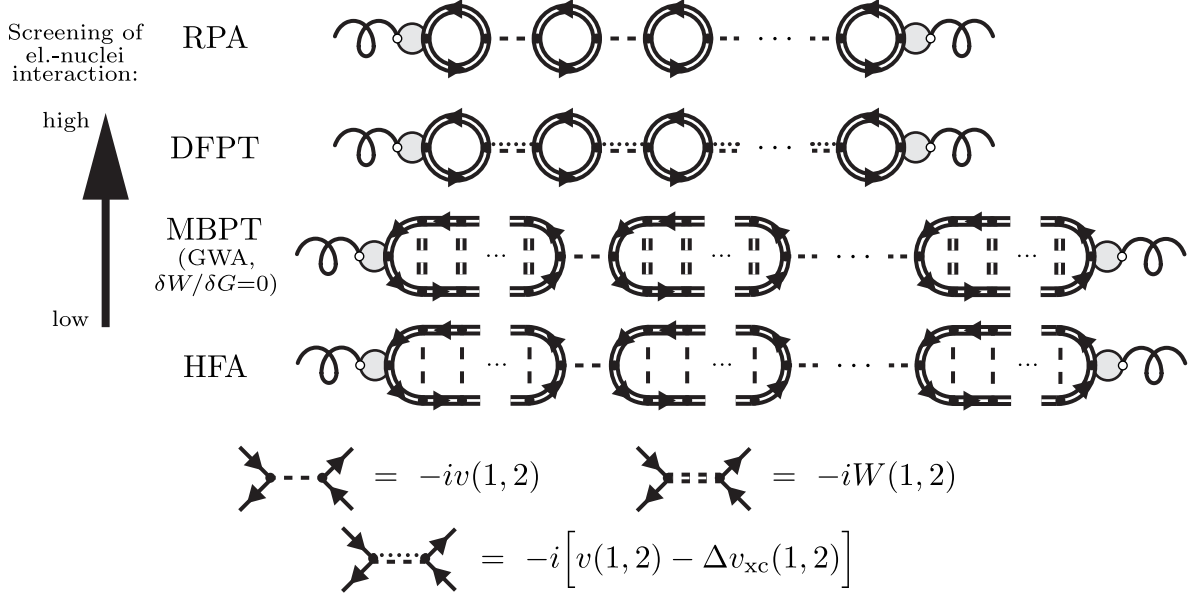


Figure 4.4: **Different approximations for the electronic part of the force constants.** Typical diagrammatic contributions to the perturbation series for the electronic part of the force constants that is quadratic in the first derivative of the lattice potential in different approximations. From top to bottom: random phase approximation (RPA), density functional perturbation theory (DFPT), many-body perturbation theory (MBPT) on the level of the GW approximation with $\delta W(1,2)/\delta G(3,4) = 0$, and Hartree-Fock approximation (HFA). From top to bottom, the screening of the effective electron-nuclei interaction decreases, which leads to a larger electronic contribution to the force constants. The vertex involving the curly (gluon-type) line represents the matrix element corresponding to the first derivative of the lattice potential (the bare electron-nuclei coupling). Dashed and double-dashed lines represent the unscreened and screened Coulomb interaction, respectively, while dotted-dashed lines denote the difference of the unscreened Coulomb interaction and a xc-correction $\Delta v_{xc}(1,2)$ as defined in the text.

We graphically summarize the above discussion in Fig. 4.4, where, for each method or approximation, we show a typical term in the perturbation series for the electronic part of the force constants quadratic in the first derivative of the lattice potential. From top to bottom, the screening of the electron-nuclei coupling decreases.

This concludes our comparison of the different approaches to the calculation of phonon frequencies and with that also the discussion of the description of the matter system in the Born-Oppenheimer approximation. In the next chapter, we will move on and go beyond the BOA and discuss the coupling between electrons and phonons.

Chapter 5

Electron-Phonon Interaction

In the previous two chapters we dealt with the problem of finding the eigenstates of the full matter Hamiltonian (see Eq. 2.14) by approximating it in two different ways: firstly in the “clamped nuclei approximation” (CNA), in which the nuclei are treated as being completely static and as providing an effective potential for the electrons, and secondly in the “adiabatic, Born-Oppenheimer approximation” (BOA), which treats the nuclei as moving within an effective potential generated by the electrons described in the CNA. In both cases, the approximative Hamiltonian could still not be diagonalized exactly, but instead required a further perturbative or approximative treatment, provided by Kohn-Sham density functional theory and the harmonic approximation respectively. In the case of the electrons, we were able to obtain a full basis of the one-particle Hilbert space in the form of the KS states, while for the nuclei, the harmonic approximation gave rise to the notion of phonon states, which, likewise, provide a basis of the nuclear part of the Hilbert space. By combining the two bases, we thus have a complete basis of the full electron-nuclei Hilbert space.

While the approximative electron and nuclei Hamiltonians are, by construction, diagonal in the KS and phonon basis, respectively, the full matter Hamiltonian (Eq. 2.14) is not. Nevertheless, many systems, most prominently a large number of semi-conducting materials [85], are well approximated in this way and the off-diagonal elements of the full Hamiltonian are comparatively small and can be treated in perturbation theory. In this chapter, we will discuss the perturbative treatment of the fully interacting

electron-nuclei system using the KS and phonon states as a starting point.

In a first step, we express the *full electron-nuclei Hamiltonian in the KS and phonon basis*. This is most conveniently done within the occupation number formalism using creation and annihilation operators. We briefly discuss the electron, the phonon, and the electron-phonon interaction part of the Hamiltonian before summarizing the Feynman rules for a perturbative treatment of the theory.

The second section deals with a description of the screening of the electron-phonon coupling. As we will see in the following chapter, whenever a factor for the electron-phonon coupling appears in perturbation theory, it is accompanied by an entire subseries of terms that has the physical interpretation of describing the *screening of the electron-phonon interaction*. It is then convenient to consider the screened electron-phonon coupling as a building block for the terms in the perturbation series, similar to how the non-interacting Green's function is replaced by the exact Green's function in a skeleton expansion (compare Section 3.3). We show how the subseries describing the screening can be summed up exactly and expressed in terms of quantities introduced in the previous two chapters. In this way, we provide a practical approach for the calculation of the screened electron-phonon coupling beyond the commonly used approximation of density functional perturbation theory. Such an approach is needed in materials such as graphene, where DFPT has been shown to severely underestimate the coupling of the electronic system to certain phonon modes [53]. Since the electron-phonon coupling plays an important role in the perturbative description of various physical processes, such as the scattering of charge carriers in charge transport and in Raman scattering, it is thus vital for a wide variety of calculations that a method be developed that goes beyond DFPT. The theoretical developments presented here provide such a method and pave the way for the implementation of a more accurate computational approach to the calculation of the screened electron-phonon coupling, which, however, is beyond the scope of this thesis.

Finally, the last section of this chapter contains a *discussion of the exact one-phonon Green's function*. This object plays an important role in our novel theoretical approach to one-phonon-induced Raman scattering. It also contains information on the eigenvalues of the full matter Hamiltonian. After a brief review of its spectral or *Lehmann*

representation, we will discuss the calculation of the exact one-phonon Green's function in perturbation theory. The perturbative approach in particular allows the correction of phonon frequencies whilst taking non-adiabatic effects into account. The latter can potentially play an important role in (semi-)metallic systems, as has been demonstrated most prominently for graphene [28].

5.1 Electron-phonon interaction Hamiltonian and Feynman rules

We start setting up the perturbative approach for the fully interacting electron-nuclei system from the full matter Hamiltonian¹

$$\hat{\mathcal{H}}_M = \sum_i \frac{\hat{\mathbf{p}}_i^2}{2m} + \frac{1}{2} \sum_{\substack{i,j \\ i \neq j}} \frac{e^2}{|\hat{\mathbf{r}}_i - \hat{\mathbf{r}}_j|} + \sum_I \frac{\hat{\mathbf{P}}_I^2}{2M_I} + \frac{1}{2} \sum_{\substack{I,J \\ I \neq J}} \frac{Z_I Z_J e^2}{|\hat{\mathbf{R}}_I - \hat{\mathbf{R}}_J|} + \sum_{i,I} \frac{-Z_I e^2}{|\hat{\mathbf{r}}_i - \hat{\mathbf{R}}_I|.} \quad (5.1)$$

To treat this system in perturbation theory, we seek to write it in the form $\hat{\mathcal{H}}_M = \hat{\mathcal{H}}_0 + \hat{\mathcal{H}}_1$, where $\hat{\mathcal{H}}_0$ describes a system of non-interacting (quasi-)particles or collective excitations and $\hat{\mathcal{H}}_1$ contains all the interactions among them. More concretely, we will take $\hat{\mathcal{H}}_0$ to be given by the sum of a Hamiltonian describing a system of non-interacting Kohn-Sham electrons and a Hamiltonian describing non-interacting phonons in the harmonic approximation. The interaction Hamiltonian $\hat{\mathcal{H}}_1$ can then be obtained by taking the difference of the full Hamiltonian $\hat{\mathcal{H}}_M$ and the non-interacting Hamiltonian $\hat{\mathcal{H}}_0$.

In order to identify the concrete parts of $\hat{\mathcal{H}}_M$ that are included in $\hat{\mathcal{H}}_0$ and $\hat{\mathcal{H}}_1$, we first separate it into a purely electronic part, a purely nuclei part, and a part containing all the electron-nuclei interaction:

$$\hat{\mathcal{H}}_M \equiv \hat{\mathcal{H}}_{\text{el}} + \hat{\mathcal{H}}_{\text{nuc}} + \hat{\mathcal{H}}_{\text{el-nuc}}, \quad (5.2)$$

¹As before, letters in calligraphic font denote operators in the full electron-nuclei Hilbert space, while operators acting in only the electronic or nuclear subspace will be denoted by non-calligraphic symbols.

with the three parts being defined as

$$\hat{\mathcal{H}}_{\text{el}} \equiv \sum_i \frac{\hat{\mathbf{P}}_i^2}{2m} + \frac{1}{2} \sum_{\substack{i,j \\ i \neq j}} \frac{e^2}{|\hat{\mathbf{r}}_i - \hat{\mathbf{r}}_j|} + \sum_{i,I} \frac{-Z_I e^2}{|\hat{\mathbf{r}}_i - \mathbf{R}_I^{(0)}|} + \frac{1}{2} \sum_{\substack{I,J \\ I \neq J}} \frac{Z_I Z_J e^2}{|\mathbf{R}_I^{(0)} - \mathbf{R}_J^{(0)}|} \quad (5.3)$$

$$\hat{\mathcal{H}}_{\text{nuc}} \equiv \sum_I \frac{\hat{\mathbf{P}}_I^2}{2M_I} + \frac{1}{2} \sum_{\substack{I,J \\ I \neq J}} \left[\frac{Z_I Z_J e^2}{|\hat{\mathbf{R}}_I - \hat{\mathbf{R}}_J|} - \frac{Z_I Z_J e^2}{|\mathbf{R}_I^{(0)} - \mathbf{R}_J^{(0)}|} \right] \quad (5.4)$$

$$\hat{\mathcal{H}}_{\text{el-nuc}} \equiv \sum_{i,I} \left[\frac{-Z_I e^2}{|\hat{\mathbf{r}}_i - \hat{\mathbf{R}}_I|} - \frac{-Z_I e^2}{|\hat{\mathbf{r}}_i - \mathbf{R}_I^{(0)}|} \right], \quad (5.5)$$

where the nuclei positions in equilibrium, $\mathbf{R}_I^{(0)}$, have been introduced in Chapter 3, but will also be defined later once more. The Hamiltonians in the first and second line only contain operators acting on the electronic or nuclear subspace only, while the third line contains the terms that couple the two subspaces. We can then conveniently set up the perturbative approach for each of the three terms separately, i.e., single out those terms of each of the three parts written above that are to be included in $\hat{\mathcal{H}}_0$ or $\hat{\mathcal{H}}_1$. This will be done over the course of the next three subsections.

5.1.1 Electronic Hamiltonian

The electronic Hamiltonian of Eq. 5.3 has the form $\hat{\mathcal{H}}_{\text{el}} = (\hat{H}_{\text{el}})_e \otimes \mathbb{1}_n$, where the operator \hat{H}_{el} acts only in the electronic subspace. \hat{H}_{el} can be written as the sum of a Hamiltonian describing a non-interacting Kohn-Sham system and a Hamiltonian describing the residual Coulomb interaction:

$$\hat{H}_{\text{el}} \equiv \hat{H}_{\text{KS}} + \hat{H}_{e-e}, \quad (5.6)$$

as discussed more extensively in Chapter 3. The two operators are defined as

$$\hat{H}_{\text{KS}} \equiv \sum_i \left[\frac{\hat{\mathbf{p}}_i^2}{2m} + V_{\text{lat}}(\hat{\mathbf{r}}_i; \{\mathbf{R}_I^{(0)}\}) + V_{\text{Hxc}}[n_{\text{KS}}](\hat{\mathbf{r}}_i) \right] + V_{\text{n-n}}(\{\mathbf{R}_I^{(0)}\}), \quad (5.7)$$

$$\hat{H}_{\text{e-e}} \equiv \frac{1}{2} \sum_{\substack{i,j \\ i \neq j}} \frac{e^2}{|\hat{\mathbf{r}}_i - \hat{\mathbf{r}}_j|} - \sum_i V_{\text{Hxc}}[n_{\text{KS}}](\hat{\mathbf{r}}_i), \quad (5.8)$$

where the one-particle potentials have partially been defined in Section 3.2, but for convenience are given here again:

$$V_{\text{lat}}(\mathbf{r}; \{\mathbf{R}_I\}) \equiv \sum_I \frac{-Z_I e^2}{|\mathbf{r} - \mathbf{R}_I|}, \quad (5.9)$$

$$V_{\text{Hxc}}[n](\mathbf{r}) \equiv V_{\text{H}}[n](\mathbf{r}) + V_{\text{xc}}[n](\mathbf{r}) \equiv e^2 \int d^3r' \frac{n(\mathbf{r}')}{|\mathbf{r} - \mathbf{r}'|} + \frac{\delta E_{\text{xc}}[n]}{\delta n(\mathbf{r})}, \quad (5.10)$$

$$V_{\text{n-n}}(\{\mathbf{R}_I\}) \equiv \frac{1}{2} \sum_{\substack{I,J \\ I \neq J}} \frac{Z_I Z_J e^2}{|\mathbf{R}_I - \mathbf{R}_J|}. \quad (5.11)$$

The ground state $|\emptyset\rangle$ of the Kohn-Sham Hamiltonian \hat{H}_{KS} defines the Kohn-Sham charge density

$$n_{\text{KS}}(\mathbf{r}) \equiv \langle \emptyset | \hat{\psi}^\dagger(\mathbf{r}) \hat{\psi}(\mathbf{r}) | \emptyset \rangle \quad (5.12)$$

where $\hat{\psi}(\mathbf{r})$ is the electron field operator. Finally, the set of nuclei positions $\{\mathbf{R}_I^{(0)}\}$ is defined as the location of the minimum of the function

$$V_0(\{\mathbf{R}_I\}) \equiv \langle 0(\{\mathbf{R}_I\}) | \hat{H}_e(\{\mathbf{R}_I\}) | 0(\{\mathbf{R}_I\}) \rangle + V_{\text{n-n}}(\{\mathbf{R}_I\}), \quad (5.13)$$

with the state $|0(\{\mathbf{R}_I\})\rangle$ being defined as the ground state of the Hamiltonian

$$\hat{H}_e(\{\mathbf{R}_I\}) \equiv \sum_i \frac{\hat{\mathbf{p}}_i^2}{2m} + \sum_i V_{\text{lat}}(\hat{\mathbf{r}}_i; \{\mathbf{R}_I\}) + \frac{1}{2} \sum_{\substack{i,j \\ i \neq j}} \frac{e^2}{|\hat{\mathbf{r}}_i - \hat{\mathbf{r}}_j|}. \quad (5.14)$$

5.1.2 Phonon Hamiltonian

The Hamiltonian $\hat{\mathcal{H}}_{\text{nuc}}$, defined in Eq. 5.4, acts in the nuclear subspace only: $\hat{\mathcal{H}}_{\text{nuc}} = \mathbb{1}_e \otimes (\hat{H}_{\text{nuc}})_n$. We write it as the sum of a Hamiltonian for non-interacting phonons and a term containing the phonon-phonon interaction terms:

$$\hat{H}_{\text{nuc}} \equiv \hat{H}_{\text{ph}} + \hat{H}_{\text{ph,int}}. \quad (5.15)$$

The non-interacting phonon Hamiltonian is given as

$$\hat{H}_{\text{ph}} \equiv \sum_I \frac{\hat{\mathbf{P}}_I^2}{2M_I} + \frac{1}{2} \sum_{\substack{I,J \\ i,j}} C_{I,J}{}_{i,j} (\hat{R}_{I,i} - R_{I,i}^{(0)}) (\hat{R}_{J,j} - R_{J,j}^{(0)}), \quad (5.16)$$

with the force constants

$$C_{I,J}{}_{i,j} \equiv \left(\frac{\partial^2}{\partial R_{I,i} \partial R_{J,j}} V_0(\{\mathbf{R}_I\}) \right) \Big|_{\{\mathbf{R}_I\}=\{\mathbf{R}_I^{(0)}\}}, \quad (5.17)$$

as discussed in Section 4.2. To obtain the inter-phonon interaction Hamiltonian $\hat{H}_{\text{ph,int}}$, we expand the inter-nuclei Coulomb interaction $V_{\text{n-n}}(\{\mathbf{R}_I\})$ around $\{\mathbf{R}_I^{(0)}\}$:

$$V_{\text{n-n}}(\{\mathbf{R}_I\}) = \sum_{n \geq 0} \frac{1}{n!} \sum_{\substack{I_1, \dots, I_n \\ i_1, \dots, i_n}} C_{I_1, \dots, I_n}^{(\text{nuc});(n)}{}_{i_1, \dots, i_n} (\hat{R}_{I_1, i_1} - R_{I_1, i_1}^{(0)}) \dots (\hat{R}_{I_n, i_n} - R_{I_n, i_n}^{(0)}). \quad (5.18)$$

The expansion coefficients $C^{(n)}$ are given by the n th partial derivative of the left hand-side with respect to the nuclei positions, evaluated at $\{\mathbf{R}_I^{(0)}\}$:

$$C_{I_1, \dots, I_n}^{(\text{nuc});(n)}{}_{i_1, \dots, i_n} \equiv \left(\frac{\partial^n}{\partial R_{I_1, i_1} \dots \partial R_{I_n, i_n}} V_{\text{n-n}}(\{\mathbf{R}_I\}) \right) \Big|_{\{\mathbf{R}_I\}=\{\mathbf{R}_I^{(0)}\}}. \quad (5.19)$$

Subtracting the force constants term from the expansion of $V_{\text{n-n}}(\{\mathbf{R}_I\})$, one finds:

$$\begin{aligned}\hat{H}_{\text{ph,int}} &\equiv \sum_{n \geq 3} \frac{1}{n!} \sum_{\substack{I_1, \dots, I_n \\ i_1, \dots, i_n}} C_{I_1, \dots, I_n}^{(\text{nuc});(n)} (\hat{R}_{I_1, i_1} - R_{I_1, i_1}^{(0)}) \dots (\hat{R}_{I_n, i_n} - R_{I_n, i_n}^{(0)}) \\ &\quad - \sum_{I, i} F_{I, i}^{(\text{el})} (\hat{R}_{I, i} - R_{I, i}^{(0)}) - \frac{1}{2} \sum_{\substack{I, J \\ i, j}} C_{I, J}^{(\text{el})} (\hat{R}_{I, i} - R_{I, i}^{(0)}) (\hat{R}_{J, j} - R_{J, j}^{(0)}), \quad (5.20) \\ &\equiv \hat{H}_{\text{ph-ph}} + \hat{H}_{\text{ph,ad.}}\end{aligned}$$

where

$$C_{I, J}^{(\text{el})} \equiv \left(\frac{\partial^2}{\partial R_{I, i} \partial R_{J, j}} V_0^{(\text{el})}(\{\mathbf{R}_I\}) \right) \Big|_{\{\mathbf{R}_I\} = \{\mathbf{R}_I^{(0)}\}} \quad (5.21)$$

denotes the electronic part of the force constants derived from the electronic part of the potential

$$V_0^{(\text{el})}(\{\mathbf{R}_I\}) \equiv \langle 0(\{\mathbf{R}_I\}) | \hat{H}_e(\{\mathbf{R}_I\}) | 0(\{\mathbf{R}_I\}) \rangle \quad (5.22)$$

and

$$F_{I, i}^{(\text{el})} \equiv \left(\frac{\partial}{\partial R_{I, i}} V_0^{(\text{el})}(\{\mathbf{R}_I\}) \right) \Big|_{\{\mathbf{R}_I\} = \{\mathbf{R}_I^{(0)}\}} = - \left(\frac{\partial}{\partial R_{I, i}} V_{\text{n-n}}(\{\mathbf{R}_I\}) \right) \Big|_{\{\mathbf{R}_I\} = \{\mathbf{R}_I^{(0)}\}} \quad (5.23)$$

denotes the electronic part of the i th cartesian component of the force on atom I in equilibrium. The Hamiltonian $\hat{H}_{\text{ph,int}}$ contains a part $\hat{H}_{\text{ph-ph}}$ that accounts for direct phonon-phonon interaction, i.e., anharmonic effects,² as well as two correction terms, included in $\hat{H}_{\text{ph,ad.}}$, that play the same role the V_{Hxc} -term does for the electronic system.

5.1.3 Electron-phonon interaction Hamiltonian

Finally, we turn to the electron-nuclei interaction Hamiltonian $\hat{\mathcal{H}}_{\text{el-nuc}}$, given in Eq. 5.5. Expanding it around the equilibrium nuclear configuration $\{\mathbf{R}_I^{(0)}\}$, it can be written as

²Note that the Hamiltonian $\hat{H}_{\text{ph-ph}}$ does *not* include a term that accounts for *indirect* phonon-phonon interaction mediated by electrons. In the treatment presented here, these terms appear in higher orders in perturbation theory in the electron-phonon interaction, but may still be of equal importance for the study of anharmonic effects.

the sum of electron- n -phonon interaction Hamiltonians

$$\hat{\mathcal{H}}_{\text{el-nuc}} \equiv \sum_{n \geq 1} \hat{\mathcal{H}}_{\text{el-ph}}^{(n)}, \quad (5.24)$$

with the latter being given by

$$\hat{\mathcal{H}}_{\text{el-ph}}^{(n)} \equiv \frac{1}{n!} \sum_{\substack{I_1, \dots, I_n \\ i_1, \dots, i_n}} \left[\sum_i V_{\text{lat}; i_1, \dots, i_n}^{(n)}(\hat{\mathbf{r}}_i) \right] (\hat{R}_{I_1, i_1} - R_{I_1, i_1}^{(0)}) \dots (\hat{R}_{I_n, i_n} - R_{I_n, i_n}^{(0)}). \quad (5.25)$$

Here, we defined the expansion coefficients as the n th derivative of the equilibrium potential function V_{lat} :

$$V_{\text{lat}; i_1, \dots, i_n}^{(n)}(\mathbf{r}) \equiv \left(\frac{\partial^n}{\partial R_{I_1, i_1} \dots \partial R_{I_n, i_n}} V_{\text{lat}}(\mathbf{r}; \{\mathbf{R}_I\}) \right) \Big|_{\{\mathbf{R}_I\} = \{\mathbf{R}_I^{(0)}\}}. \quad (5.26)$$

5.1.4 Feynman rules for perturbation theory

Having discussed the individual parts of the matter Hamiltonian in the first three subsections, we can now turn to a perturbative treatment of the interacting electron-phonon system. The standard way to do this is to pass to the interaction picture with respect to an exactly diagonalizable Hamiltonian. In our case, we can split the total Hamiltonian into two parts:

$$\begin{aligned} \hat{\mathcal{H}}_{\text{M}} &\equiv \left(\hat{\mathcal{H}}_{\text{KS}} + \hat{\mathcal{H}}_{\text{ph}} \right) + \left(\hat{\mathcal{H}}_{\text{e-e}} + \hat{\mathcal{H}}_{\text{ph-ph}} + \hat{\mathcal{H}}_{\text{ph,ad.}} + \sum_{n=1}^{\infty} \hat{\mathcal{H}}_{\text{el-ph}}^{(n)} \right) \\ &\equiv \hat{\mathcal{H}}_0 + \hat{\mathcal{H}}_1. \end{aligned} \quad (5.27)$$

The Hamiltonian $\hat{\mathcal{H}}_0$ is defined as the sum of the non-interacting Kohn-Sham and phonon Hamiltonians. In terms of the creation and annihilation operators for the KS electrons and phonons, introduced in Chapters 3 and 4, it takes on the form

$$\hat{\mathcal{H}}_0 = \sum_{\mathbf{k}, n} \varepsilon_{\mathbf{k}, n} \hat{c}_{\mathbf{k}, n}^\dagger \hat{c}_{\mathbf{k}, n} + V_{\text{n-n}}(\{\mathbf{R}_I^{(0)}\}) + \sum_{\mathbf{q}, \lambda} \omega_{\mathbf{q}, \lambda} \left(\hat{b}_{\mathbf{q}, \lambda}^\dagger \hat{b}_{\mathbf{q}, \lambda} + \frac{1}{2} \right). \quad (5.28)$$

We will denote its ground state by $|\emptyset\rangle \equiv |\emptyset\rangle_e \otimes |0_{\text{ph}}\rangle_n$, where $|\emptyset\rangle_e$ denotes the ground state of the KS Hamiltonian \hat{H}_{KS} and $|0_{\text{ph}}\rangle_n$ is the ground state of the phonon Hamiltonian \hat{H}_{ph} , i.e., a state of zero phonons.

The interaction Hamiltonian is then given by the rest of the terms in $\hat{\mathcal{H}}_{\text{M}}$. For the content presented in the remainder of this thesis, which will mostly concern the description of one-phonon-induced Raman scattering and non-adiabatic corrections to the phonon frequencies, we can focus on the electron-one- and -two-phonon interaction terms only:

$$\hat{\mathcal{H}}_1 = \hat{\mathcal{H}}_{e-e} + \hat{\mathcal{H}}_{\text{ph,ad.}} + \hat{\mathcal{H}}_{\text{el-ph}}^{(1)} + \hat{\mathcal{H}}_{\text{el-ph}}^{(2)} + \text{other terms.} \quad (5.29)$$

Note that it is important to retain the adiabatic “counterterm” Hamiltonian $\hat{\mathcal{H}}_{\text{ph,ad.}}$ in the perturbation Hamiltonian, in order to ensure that the fully interacting theory predicts the adiabatic phonon frequencies in the adiabatic limit. We will revisit this point in the last section of this chapter as well as in Section 7.1.

As already noted during our treatment of electrons and phonons in Chapters 3 and 4, respectively, the residual inter-electron Coulomb interaction is a very important perturbation and needs to be considered explicitly as well. This especially is true in the context of processes involving interactions between electrons and phonons. The electrostatic, i.e., Coulombic, origin of the latter and the non-negligible polarizability of the electronic system make it necessary to include higher-order terms involving electron-electron interaction in the perturbation series. A proper description of the screened electron-phonon interaction is important, as it enters many physical observables, such as temperature-dependent absorption spectra [137] and Raman spectra [56]. As shown in a first study of the electron-phonon coupling in graphene using *ab initio*, finite-difference methods, the magnitude of the electron-phonon coupling very much depends on the level of theory on which the screening is described [53].

In order to account for the important role of electron-electron interaction for the description of the screened electron-phonon coupling, we use a “nested” form of perturbation theory in the interaction picture. In this way, we can account for the difference in strength and importance of the various terms in the complete interaction Hamiltonian $\hat{\mathcal{H}}_1$. Instead of directly splitting up the full Hamiltonian into an exactly diagonalizable

part and a residual part containing all interactions, we include the electron-electron interaction in the “unperturbed” Hamiltonian:

$$\begin{aligned}\hat{\mathcal{H}}_M &\equiv \left(\hat{\mathcal{H}}_{\text{KS}} + \hat{\mathcal{H}}_{e-e} + \hat{\mathcal{H}}_{\text{ph}} \right) + \left(\hat{\mathcal{H}}_{\text{ph-ph}} + \hat{\mathcal{H}}_{\text{ph,ad.}} + \sum_{n=1}^{\infty} \hat{\mathcal{H}}_{\text{el-ph}}^{(n)} \right) \\ &\equiv \hat{\mathcal{H}}_0 + \hat{\mathcal{H}}_1,\end{aligned}\quad (5.30)$$

i.e., $\hat{\mathcal{H}}_0$ is now defined as the sum of the *full* electronic Hamiltonian $\hat{\mathcal{H}}_{\text{el}}$ and the phonon Hamiltonian in the harmonic approximation. We will denote its ground state by $|0\rangle \equiv |0\rangle_e \otimes |0_{\text{ph}}\rangle_n$, where $|0\rangle_e$ is the ground state of the full electronic Hamiltonian \hat{H}_{el} .

To pass to the (“first”) interaction picture, we define the interaction picture electron field operator and nuclei displacement operators as:³

$$\hat{\psi}_I(\mathbf{r}, t) \equiv e^{+i\hat{\mathcal{H}}_0 t} \hat{\psi}(\mathbf{r}) e^{-i\hat{\mathcal{H}}_0 t} = e^{+i\hat{H}_{\text{el}} t} \hat{\psi}(\mathbf{r}) e^{-i\hat{H}_{\text{el}} t}, \quad (5.31)$$

$$\hat{\mathbf{u}}_{n,\alpha,I}(t) \equiv e^{+i\hat{\mathcal{H}}_0 t} \hat{\mathbf{u}}_{n,\alpha} e^{-i\hat{\mathcal{H}}_0 t} = e^{+i\hat{H}_{\text{ph}} t} \hat{\mathbf{u}}_{n,\alpha} e^{-i\hat{H}_{\text{ph}} t}. \quad (5.32)$$

Note that the electron field operator in the “first” interaction picture can equally well be regarded as the electron field operator in the Heisenberg picture with respect to the Hamiltonian \hat{H}_{el} , as used in Section 3.3. In terms of the Kohn-Sham electron and phonon creation and annihilation operators, the electron field and nuclei displacement operators read:

$$\hat{\psi}_I(\mathbf{r}, t) = \sum_{\mathbf{k},n} \phi_{\mathbf{k},n}(\mathbf{r}) \hat{c}_{\mathbf{k},n,I}(t), \quad \hat{\mathbf{u}}_{n,\alpha,I}(t) = \sum_{\mathbf{q},\lambda} \boldsymbol{\xi}_{\mathbf{q},\lambda}^{\alpha}(\mathbf{R}_n) \hat{B}_{\mathbf{q},\lambda,I}(t), \quad (5.33)$$

with the one-particle KS wave function $\phi_{\mathbf{k},n}(\mathbf{r}) = N^{-1/2} \exp(i\mathbf{k} \cdot \mathbf{r}) \chi_{\mathbf{k},n}(\mathbf{r})$ with lattice-periodic part $\chi_{\mathbf{k},n}(\mathbf{r})$ and the phonon “wave function” and mode operators

$$\boldsymbol{\xi}_{\mathbf{q},\lambda}^{\alpha}(\mathbf{R}_n) \equiv \frac{1}{\sqrt{N}} e^{i\mathbf{q} \cdot \mathbf{R}_n} \sqrt{\frac{1}{2M_{\alpha}\omega_{\mathbf{q},\lambda}}} \mathbf{v}_{\mathbf{q},\lambda}^{\alpha}, \quad \hat{B}_{\mathbf{q},\lambda} \equiv \hat{b}_{\mathbf{q},\lambda} + \hat{b}_{-\mathbf{q},\lambda}^{\dagger}, \quad (5.34)$$

³We again label the atoms by a tuple (n, α) to distinguish the different unit cells (n) and atoms in the unit cell (α) .

where $\mathbf{v}_{\mathbf{q},\lambda}^\alpha$ denotes the eigenvectors of the (unperturbed) dynamical matrix (compare Eq. 4.29).

We also define *non-interacting*⁴ electron and phonon Green's functions as⁵

$$G(1, 2) \equiv -i\langle 0|\mathcal{T}\{\hat{\psi}_I(1)\hat{\psi}_I^\dagger(2)\}|0\rangle \quad (5.35)$$

$$D_{A,B}(t_1, t_2) \equiv -i\langle 0|\mathcal{T}\{\hat{u}_{A,I}(t_1)\hat{u}_{B,I}^\dagger(t_2)\}|0\rangle. \quad (5.36)$$

To avoid a cluttering of these and similar expressions with too many indices, we use the short-hand notations $1 \equiv (\mathbf{r}_1, t_1)$, $2 \equiv (\mathbf{r}_1, t_1)$, etc. and $A \equiv (n, \alpha, i)$, $B \equiv (m, \beta, j)$, etc. We also want to point out that in our perturbation scheme, the “non-interacting” electron Green's function still includes *all* effects of the inter-electron Coulomb interaction, as the corresponding Hamiltonian \hat{H}_{e-e} is included in the “free” Hamiltonian $\hat{\mathcal{H}}_0$. The Green's function G is the same as the “exact” Green's function discussed in Chapter 3. It can be treated by passing to a “second” interaction picture by taking \hat{H}_{e-e} as the interaction Hamiltonian. This “second-layer” perturbative treatment has already been discussed in Section 3.3 and we can simply re-use all of the content of this section. Besides the non-interacting Green's functions, we will also make use of the *exact* Green's functions, defined as

$$\mathcal{G}(1, 2) \equiv -i\langle \Omega|\mathcal{T}\{\hat{\psi}(1)\hat{\psi}^\dagger(2)\}|\Omega\rangle \quad (5.37)$$

$$\mathcal{D}_{A,B}(t_1, t_2) \equiv -i\langle \Omega|\mathcal{T}\{\hat{u}_A(t_1)\hat{u}_B^\dagger(t_2)\}|\Omega\rangle, \quad (5.38)$$

in which all operators are understood to be in the Heisenberg picture with respect to the full Hamiltonian $\hat{\mathcal{H}}_M$. The ground state of the latter was already introduced in Section 2.4 and is denoted as $|\Omega\rangle$.

The last ingredient needed for a perturbative treatment of the electron-phonon

⁴“Non-interacting” here is understood to refer to the non-interacting nature with respect to $\hat{\mathcal{H}}_1$, i.e., the electron-phonon interaction.

⁵The displacement operator \hat{u}_A is hermitian, i.e., $\hat{u}_A = \hat{u}_A^\dagger$, and hence the phonon Green's function could also be defined without adjoining the second operator in the correlation function. However, to make the expression look comparable to the one for the electron Green's function, we explicitly include the adjoint symbol in the definition.

system is the interaction Hamiltonian $\hat{\mathcal{H}}_1$ in the interaction picture, which reads:

$$\begin{aligned}
\hat{\mathcal{H}}_{1,I}(t_1) = & - \sum_A F_A^{(\text{el})} \hat{u}_{A;I}(t_1) - \frac{1}{2} \sum_{A,B} C_{A,B}^{(\text{el})} \hat{u}_{A;I}(t_1) \hat{u}_{B;I}(t_1) \\
& + \sum_A \int d^3 r_1 g_A^{(\text{b})}(\mathbf{r}_1) \hat{\psi}_I^\dagger(1) \hat{\psi}_I(1) \hat{u}_{A;I}(t_1) \\
& + \sum_{A,B} \int d^3 r_1 g_{A,B}^{(\text{b});(2)}(\mathbf{r}_1) \hat{\psi}_I^\dagger(1) \hat{\psi}_I(1) \hat{u}_{A;I}(t_1) \hat{u}_{B;I}(t_1) \\
& + \text{ other terms.}
\end{aligned} \tag{5.39}$$

Here, we set $g_A^{(\text{b})}(\mathbf{r}_1) \equiv \partial V_{\text{lat}}(\mathbf{r}_1; \{\mathbf{R}_I^{(0)}\}) / \partial R_A^{(0)}$ and $g_{A,B}^{(\text{b});(2)}(\mathbf{r}_1) \equiv \partial^2 V_{\text{lat}}(\mathbf{r}_1; \{\mathbf{R}_I^{(0)}\}) / (\partial R_A^{(0)} \partial R_B^{(0)})$ to reflect the notation for the static, unscreened electron-phonon coupling from the previous chapter. To organize our perturbation theory calculations, we will again make use of Feynman diagrams. With each of the terms in the interaction Hamiltonian we associate a vertex diagram, while each Green's function will be represented by a straight or wiggly line. We summarize the Feynman rules for the interacting electron-phonon system together with the Feynman rules for the perturbative treatment of the purely electronic system in Table 5.1. The definition of part of the electronic quantities appearing in the table has been given in Section 3.3 and remains unaltered in our “nested” perturbative approach.

5.2 Screened electron-phonon coupling

As a first application of the diagrammatic, perturbative approach, we will derive an expression for the screened electron-phonon coupling on a level of theory beyond the one offered by the commonly applied density functional perturbation theory. As mentioned in the introduction to this chapter, such a development is necessary if one wants to obtain a correct quantitative description of the effective electron-phonon coupling that can be used for the calculation of Raman spectra or electronic band energy corrections in (semi-)metallic systems, such as graphene. So far, most of the efforts to improve the DFPT description of the electron-phonon coupling in graphene have been focused on an approach in which the intra-electron-band electron-phonon coupling is obtained from

Electrons	Phonons	Electron-Phonon
$= iG_0(1, 2)$	$= iD_{A,B}(t_1, t_2)$	$= -ig_A^{(b)}(\mathbf{r}_1)$
$= -iv(1, 2)$	$= iF_A^{(\text{el})}$	$= -ig_{A,B}^{(b);(2)}(\mathbf{r}_1)$
$= iv^{(\text{Hxc})}(\mathbf{r}_1)$	$= iC_{A,B}^{(\text{el})}$	\vdots
$= iG(1, 2)$	$= -iC_{A,B,C}^{(\text{nuc});(3)}$	$= -ig_A(1, 2; t_3)$
$= -iW(1, 2)$	\vdots	
$= i\mathcal{G}(1, 2)$	$= i\mathcal{D}_{A,B}(t_1, t_2)$	
$= i^2\mathcal{L}_0(1, 2; 3, 4)$	$= -i\Pi_{A,B}(t_1, t_2)$	
$= (-i)^2\mathcal{K}^{(2)}(1, 2; 3, 4)$		
$= i^2\mathcal{L}(1, 2; 3, 4)$		

Table 5.1: Feynman rules for the basic building blocks of the interacting electron-phonon system and some derived quantities (separated by horizontal lines).

a computation of the derivative of the electronic band energies with respect to nuclei displacements via the finite difference method [53, 56, 57]. To go beyond the level of DFPT, previous studies featured calculations of the electron self-energy on the level of the G_0W_0 approximation. This approach leads to estimations of the electron-phonon coupling strength that are larger than those obtained with DFPT but lower than those obtained in the Hartree-Fock approximation, which hints at this approach offering an improved description of the screening of the bare electron-phonon coupling.

From a theoretical and conceptual point of view, however, the results obtained with this method cannot be considered too reliable, due to the non-self-consistent nature of a G_0W_0 calculation. As we have already seen in Sections 4.4 and 4.5, a correct theoretical description of the screening of the electron-nuclei interaction appearing in the force constants requires a self-consistent treatment of Dyson's equation. This is hardly surprising as the one-particle KS wave functions are not corrected in the G_0W_0 method and as such the change of the exact wave functions induced by a nuclei displacement is not considered. By using the derivative of the corrected band energies to estimate the electron-phonon coupling, the calculated electron-phonon coupling will be given by the sum of the DFPT electron-phonon coupling (stemming from the derivative of the KS band energy) and the derivative of the electronic self-energy calculated on the G_0W_0 level. The derivative of the latter, however, only contains the derivative of the KS Green's function, i.e., the electron-phonon coupling on the DFPT level:

$$\begin{aligned} \partial_A \Sigma_{G_0W_0}(1, 2) &= i[\partial_A G_0(1, 2)]W_0(1, 2) + \mathcal{O}\left(\frac{\delta W_0(1, 2)}{\delta G_0(3, 4)}\right) \\ &= iW_0(1, 2)L_0(1, 2; \bar{3}, \bar{4})g^{(0)}(\bar{3}, \bar{4}) + \mathcal{O}\left(\frac{\delta W_0(1, 2)}{\delta G_0(3, 4)}\right). \end{aligned} \quad (5.40)$$

We see that the only additional term generated by the derivative of the G_0W_0 self-energy is the leading-order term appearing in the ladder approximation used in the Bethe-Salpeter equation, multiplied by the DFPT electron-phonon coupling. This approach therefore creates a mixture of the DFPT and MBPT approaches and it is thus not clear whether the results obtained with this method are actually reliable in general.

To remedy the theoretical problems associated with this approach, it is important to go beyond the G_0W_0 approximation and treat Dyson's equation self-consistently,

as partially discussed in the previous chapter. However, the methods employed there were entirely static and in the form given there are not directly relatable to a formal perturbative approach. In this section, we will therefore derive an expression for the screened electron-phonon coupling using the methods of diagrammatic, time-dependent perturbation theory. Our derivations will be less detailed than for the case of the force constants in the preceding chapter, as many of the concepts and techniques have been utilized before. Likewise, the discussion of the physics underlying our approach will also be kept brief, as it mimics the one of the physics behind the method we developed for the force constants.

To start with, we give a diagrammatic definition of the screened electron-phonon coupling. By “screened electron-phonon coupling”, we refer to a part of a Feynman diagram that does not fall into two pieces if a single phonon line, a single electron line, and a single hole line are cut. With this definition, it is clear that such a piece of a diagram is to be represented by a type of diagram shown in the bottom line of the right column of Table 5.1. Mathematically, this definition translates to

$$\begin{aligned}
(-i)g_A(1, 2; t_3) &\equiv (-i)\mathcal{G}^{-1}(1, \bar{4})(-i)\mathcal{G}^{-1}(\bar{5}, 2)(-i)\mathcal{D}_{A,\bar{B}}^{-1}(t_3, \bar{t}_6) \\
&\times \langle \Omega | \mathcal{T} \left\{ \hat{\psi}(\bar{4}) \hat{\psi}^\dagger(\bar{5}) \hat{u}_{\bar{B}}(\bar{t}_6) \right\} | \Omega \rangle_{\text{con.}},
\end{aligned} \tag{5.41}$$

where the subscript “con.” refers to the *connected part* of the correlation function, i.e., the sum of all terms in the corresponding perturbation series that are represented by fully connected Feynman diagrams.⁶ Note that in a diagrammatic skeleton expansion of the connected Green’s function in the second line, each contributing diagram will “end” in one exact phonon Green’s function and two exact electron Green’s function, which are canceled by the three factors of the first line. This then leaves behind an *amputated* version of the diagram, which can be identified with the screened electron-phonon coupling as defined with the diagrammatic criterion given above.

To generate the exact diagrammatic series for the screened electron-phonon cou-

⁶Formally, this corresponds to the definition $\langle \Omega | \mathcal{T} \{ \hat{\psi}(1) \hat{\psi}^\dagger(2) \hat{u}_A(t_3) \} | \Omega \rangle_{\text{con.}} \equiv \langle \Omega | \mathcal{T} \{ \hat{\psi}(1) \hat{\psi}^\dagger(2) \hat{u}_A(t_3) \} | \Omega \rangle - \langle \Omega | \mathcal{T} \{ \hat{\psi}(1) \hat{\psi}^\dagger(2) \} | \Omega \rangle \langle \Omega | \hat{u}_A(t_3) | \Omega \rangle$, as the second term is the only term in the perturbation series represented by a disconnected Feynman diagram that does not vanish trivially.

pling, we proceed in a similar way as we did in Section 3.3 for the one- and two-particle electron Green's functions and make use of a skeleton expansion once again. As the screened electron-phonon coupling vertex by definition connects to exactly one electron and one hole line, its diagrammatic series takes on a similar form as the one leading to the Bethe-Salpeter equation, discussed in Section 3.3.2, and is shown in Fig. 5.1. Here,

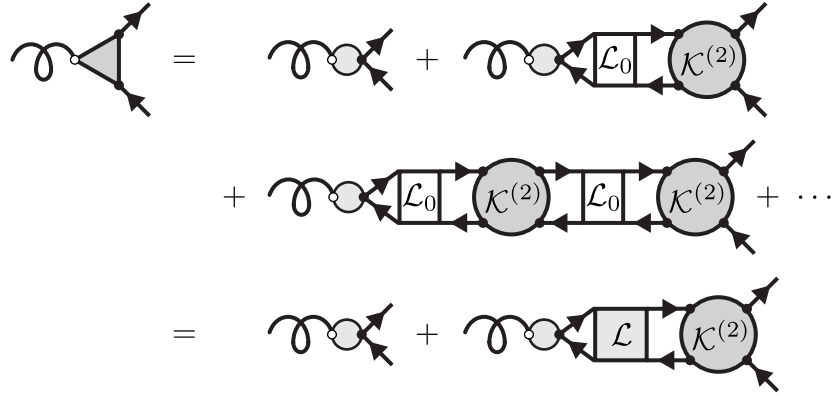


Figure 5.1: **Diagrammatic representation of the perturbation series for the screened electron-phonon coupling.**

we introduced the exact two-particle correlation function \mathcal{L} and its independent-particle counterpart \mathcal{L}_0 in the electron-phonon system, which are defined as

$$\begin{aligned} \mathcal{L}(1, 2; 3, 4) \equiv & (-i)^2 \langle \Omega | \mathcal{T} \left\{ \hat{\psi}(1) \hat{\psi}(4) \hat{\psi}^\dagger(2) \hat{\psi}^\dagger(3) \right\} | \Omega \rangle \\ & + (-i)^2 \langle \Omega | \mathcal{T} \left\{ \hat{\psi}(1) \hat{\psi}^\dagger(2) \right\} | \Omega \rangle \langle \Omega | \mathcal{T} \left\{ \hat{\psi}(4) \hat{\psi}^\dagger(3) \right\} | \Omega \rangle, \end{aligned} \quad (5.42)$$

$$\mathcal{L}_0(1, 2; 3, 4) \equiv (-i)^2 \langle \Omega | \mathcal{T} \left\{ \hat{\psi}(1) \hat{\psi}^\dagger(3) \right\} | \Omega \rangle \langle \Omega | \mathcal{T} \left\{ \hat{\psi}(4) \hat{\psi}^\dagger(2) \right\} | \Omega \rangle, \quad (5.43)$$

in analogy with their purely electronically interacting versions L and L_0 defined in Eq. 3.76. The field operators are here again understood to be in the Heisenberg picture, i.e., they evolve with the full Hamiltonian $\hat{\mathcal{H}}_M$. We also define a new two-particle-irreducible interaction kernel $\mathcal{K}^{(2)}$ as shown in Fig. 5.2. The new exact two-particle-irreducible interaction kernel now also contains contributions from the electron-phonon coupling Hamiltonians. The exact two-particle correlation functions \mathcal{L}_0 and \mathcal{L} including

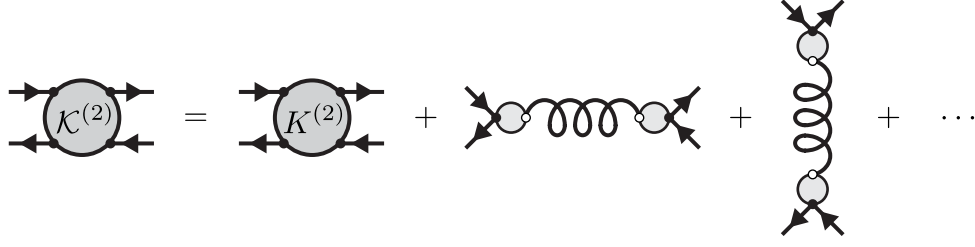


Figure 5.2: **Diagrammatic expansion of the two-particle interaction kernel in the interacting electron-phonon system.**

electron-phonon interaction effects are again related by a Bethe-Salpeter equation:

$$\mathcal{L}(1, 2; 3, 4) = \mathcal{L}_0(1, 2; 3, 4) + \mathcal{L}(1, 2; \bar{5}, \bar{6})\mathcal{K}^{(2)}(\bar{5}, \bar{6}; \bar{7}, \bar{8})\mathcal{L}(\bar{7}, \bar{8}; 3, 4). \quad (5.44)$$

The diagrammatic series for the exact, screened electron-phonon coupling can be summed exactly by identifying the diagrammatic version of the BSE for \mathcal{L} as shown in the second line of Fig. 5.1 and can hence be calculated from

$$g_A(1, 2; t_3) = \delta(1, 2)\delta(t_1 - t_3)g_A^{(b)}(\mathbf{r}_1) + \mathcal{K}^{(2)}(1, 2; \bar{4}, \bar{5})\mathcal{L}(\bar{4}, \bar{5}; (\bar{\mathbf{r}}_3, t_3^+), (\bar{\mathbf{r}}_3, t_3))g_A^{(b)}(\bar{\mathbf{r}}_3). \quad (5.45)$$

For practical calculations, it is most convenient to work in Fourier space and expand g_A in the basis of KS states and the BOA phonon “wave functions”:

$$\begin{aligned} g_A(1, 2; t_3) &\equiv g_{n,\alpha,i}((\mathbf{r}_1, t_1), (\mathbf{r}_2, t_2); t_3) \\ &\equiv \sum_{\mathbf{k}, a, b} \sum_{\mathbf{q}, \lambda} \phi_{\mathbf{q}+\mathbf{k}, a}(\mathbf{r}_1) \phi_{\mathbf{k}, b}^*(\mathbf{r}_2) \xi_{\mathbf{q}, \lambda}^{*\alpha, i}(\mathbf{R}_n) \\ &\quad \times \int \frac{d\omega}{2\pi} \int \frac{d\omega'}{2\pi} e^{-\omega(t_1-t_2)} e^{-\omega'(t_1-t_3)} \tilde{g}_{\mathbf{k}+\mathbf{q}, \mathbf{k}}^{a, b}(\omega, \omega'). \end{aligned} \quad (5.46)$$

Note that due to time-translation invariance and crystal momentum conservation, the expansion coefficients \tilde{g} can only depend on two time differences, i.e., two frequencies, and two momenta. Likewise, we expand the unscreened electron-phonon coupling as

$$g_{n,\alpha,i}^{(b)}(\mathbf{r}_1) \equiv \sum_{\mathbf{k}, a, b} \sum_{\mathbf{q}, \lambda} \phi_{\mathbf{q}+\mathbf{k}, a}(\mathbf{r}_1) \phi_{\mathbf{k}, b}^*(\mathbf{r}_1) \xi_{\mathbf{q}, \lambda}^{*\alpha, i}(\mathbf{R}_n) g_{\mathbf{k}+\mathbf{q}, \mathbf{k}}^{(b); \mathbf{q}, \lambda}{}_{a, b}. \quad (5.47)$$

Together with the Fourier space decomposition of \mathcal{L} and $\mathcal{K}^{(2)}$, as given in Eq. 3.84, this allows us to write Eq. 5.45 in Fourier space:

$$\begin{aligned} \tilde{g}_{\mathbf{k}+\mathbf{q},\mathbf{k}}^{\mathbf{q},\lambda}_{a,b}(\omega, \omega') &= g_{\mathbf{k}+\mathbf{q},\mathbf{k}}^{(b);\mathbf{q},\lambda}_{a,b} + \sum_{\mathbf{k}',\mathbf{k}''} \int \frac{d\omega''}{2\pi} \int \frac{d\omega'''}{2\pi} \tilde{\mathcal{K}}_{\mathbf{k}+\mathbf{q},a;\mathbf{k}''+\mathbf{q},\bar{c}}^{(2)}(\omega' + \omega''', \omega''', \omega - \omega''') \\ &\quad \times \tilde{\mathcal{L}}_{\mathbf{k}''+\mathbf{q},\bar{c};\mathbf{k}'+\mathbf{q},\bar{e}}(\omega' + \omega'', \omega'', \omega''' - \omega'') g_{\mathbf{k}'+\mathbf{q},\mathbf{k}'}^{(b);\mathbf{q},\lambda}_{\bar{e},\bar{f}}, \end{aligned} \quad (5.48)$$

where overlined band indices are understood to be summed over. The momentum and frequency flows in this equation are illustrated in Fig. 5.3.

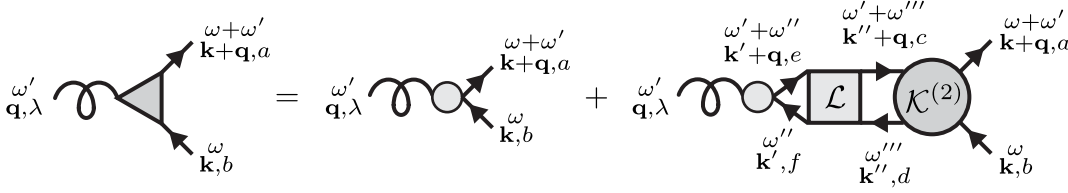


Figure 5.3: **Diagrammatic representation of the screened electron-phonon coupling in Fourier space.**

To turn this expression into a practically useful one, the interaction kernel and the two-particle correlation function need to be approximated. As has been shown in the literature [53] and already discussed at length in the preceding chapter, a better approximation of the inter-electron Coulomb interaction-based kernel $K^{(2)}$ will most likely already be sufficient to better describe the screening of the electron-phonon interaction as compared to, for example, DFPT. For the purpose of gaining a better description of the screening of the bare electron-phonon interaction by the electronic system, it is therefore in a first approximation sufficient to approximate the exact kernel $\mathcal{K}^{(2)}$ by its purely electronic version $K^{(2)}$ that consists of the inter-electron Coulomb interaction only. In this approximation, the exact BSE including the electron-phonon coupling, Eq. 5.45, reduces to the BSE with the electronic part of the kernel, $K^{(2)}$, only. In consequence, we have $\mathcal{L} = L$, where L is the solution of Eq. 3.83. To arrive at a closed expression, we also approximate the kernel $K^{(2)}$ on the level of the GW approximation, neglecting the functional derivative of the screened Coulomb interaction, and

furthermore pass to the static limit for the kernel:

$$\begin{aligned} \tilde{\mathcal{K}}_{\substack{\mathbf{k}+\mathbf{q},a;\mathbf{k},c \\ \mathbf{k}'+\mathbf{q},b;\mathbf{k}',d}}^{(2)}(\omega, \omega', \omega'') &\approx \tilde{K}_{\substack{\mathbf{k}+\mathbf{q},a;\mathbf{k},c \\ \mathbf{k}'+\mathbf{q},b;\mathbf{k}',d}}^{(2)}(\omega, \omega', \omega'') \approx i\tilde{W}_{\substack{\mathbf{k}+\mathbf{q},a;\mathbf{k},c \\ \mathbf{k}'+\mathbf{q},b;\mathbf{k}',d}}(0) - iv_{\substack{\mathbf{k}+\mathbf{q},a;\mathbf{k},c \\ \mathbf{k}'+\mathbf{q},b;\mathbf{k}',d}} \\ &\equiv \tilde{K}_{\substack{\mathbf{k}+\mathbf{q},a;\mathbf{k},c \\ \mathbf{k}'+\mathbf{q},b;\mathbf{k}',d}}^{(2)}, \end{aligned} \quad (5.49)$$

where the matrix elements and Fourier components of the bare and screened Coulomb interaction v and W have been defined in Eqs. 3.49 and 3.91, respectively. The frequency integrations in Eq. 5.48 then only act on the two-particle correlation function, which reduces the expression to an algebraic equation that depends on one frequency, ω' , only:

$$\tilde{g}_{\substack{\mathbf{k}+\mathbf{q},\mathbf{k} \\ a,b}}^{\mathbf{q},\lambda}(\omega') = g_{\substack{\mathbf{k}+\mathbf{q},\mathbf{k} \\ a,b}}^{(b);\mathbf{q},\lambda} + \sum_{\mathbf{k}',\mathbf{k}''} \tilde{K}_{\substack{\mathbf{k}+\mathbf{q},a;\mathbf{k}''+\mathbf{q},\bar{c} \\ \mathbf{k},b;\mathbf{k}'',\bar{d}}}^{(2)} \tilde{L}_{\substack{\mathbf{k}''+\mathbf{q},\bar{c};\mathbf{k}'+\mathbf{q},\bar{e} \\ \mathbf{k}'',\bar{d};\mathbf{k}',f}}(\omega') g_{\substack{\mathbf{k}'+\mathbf{q},\mathbf{k}' \\ \bar{e},f}}^{(b);\mathbf{q},\lambda}, \quad (5.50)$$

where the one-frequency Fourier component of L has been defined in Eq. 3.95. In the approximation of a static kernel, the BSE for L can be solved exactly and L can be written in the form given in Eq. 3.105, which depends only on the eigenvalues ε_S and eigenvectors $A_{\mathbf{k}+\mathbf{q},a;\mathbf{k},b}^S$ of the effective two-particle Hamiltonian and the overlap matrix $N_{S,S'}$ of the latter. In order to simplify the notation, we introduce the *exciton-independent-particle coupling*

$$\Xi_{\substack{\mathbf{k}+\mathbf{q},\mathbf{k} \\ a,b}}^S \equiv \sum_{\mathbf{k}',c,d} i\tilde{K}_{\substack{\mathbf{k}+\mathbf{q},a;\mathbf{k}'+\mathbf{q},c \\ \mathbf{k},b;\mathbf{k}',d}}^{(2)} A_{\substack{\mathbf{k}'+\mathbf{q},c \\ \mathbf{k}',d}}^S \quad (5.51)$$

and the (bare) *bilinear exciton-phonon coupling*

$$g_{\mathbf{q},S}^{(b);\mathbf{q},\lambda} \equiv \sum_{\mathbf{k},a,b} A_{\substack{\mathbf{k}+\mathbf{q},a \\ \mathbf{k},b}}^{S,*} g_{\substack{\mathbf{k}+\mathbf{q},\mathbf{k} \\ a,b}}^{(b);\mathbf{q},\lambda}. \quad (5.52)$$

Note that the bare electron-phonon coupling matrix elements in the KS basis are related to the previously defined “reduced” electron-nuclei coupling matrix elements (compare

Eq. 4.78) via

$$\begin{aligned}
g_{\mathbf{k}+\mathbf{q},\mathbf{k}}^{(b);\mathbf{q},\lambda}_{a,b} &= \sum_{\alpha,i} \sqrt{\frac{1}{2M_\alpha\omega_{\mathbf{q},\lambda}}} v_{\mathbf{q},\lambda}^{\alpha,i} g_{\mathbf{k}+\mathbf{q},\mathbf{k}}^{(b);(\alpha,i)}_{a,b} \\
&= \sum_{\alpha,i} \sqrt{\frac{1}{2NM_\alpha\omega_{\mathbf{q},\lambda}}} v_{\mathbf{q},\lambda}^{\alpha,i} \int d^3r e^{-i\mathbf{q}\cdot\mathbf{r}} \chi_{\mathbf{k}+\mathbf{q},a}^*(\mathbf{r}) \frac{\partial V_{\text{lat}}(\mathbf{r})}{\partial R_{0,\alpha,i}^{(0)}} \chi_{\mathbf{k},b}^*(\mathbf{r}).
\end{aligned} \tag{5.53}$$

We then arrive at the following compact, closed-form expression for the screened electron-phonon coupling:

$$\tilde{g}_{\mathbf{k}+\mathbf{q},\mathbf{k}}^{\mathbf{q},\lambda}_{a,b}(\omega') = g_{\mathbf{k}+\mathbf{q},\mathbf{k}}^{(b);\mathbf{q},\lambda}_{a,b} + \sum_{S,S'} \frac{\Xi_{\mathbf{k}+\mathbf{q},\mathbf{k}}^S N_{S,S'}^{-1} g_{\mathbf{q},S'}^{(b);\mathbf{q},\lambda}}{\omega' - \varepsilon_S + i\eta}. \tag{5.54}$$

This equation is another central result presented in this thesis.

To summarize, we propose the following algorithm for an improved calculation of the screened electron-phonon coupling:

1. Calculation of a set of Kohn-Sham states and eigenvalues in density functional theory.
2. Correction of the KS eigenvalues on the level of the GW approximation.
3. Computation of the static two-particle interaction kernel, solving the Bethe-Salpeter equation for both the eigenstates and eigenvalues, and calculation of the overlap matrix.
4. Calculation of the matrix elements of the first derivative of the lattice potential in the KS basis and computation of the bilinear exciton-phonon coupling and the exciton-independent particle coupling.
5. Computation of the screened electron-phonon matrix elements according to Eq. 5.54.

Like our proposed novel approach for the calculation of phonon frequencies using many-body perturbation theory, this approach is yet to be implemented and tested, since, as of now, no existing *ab initio* code features both a solver for the BSE at finite-wave vector excitations and also allows for the computation of the bare electron-phonon interaction matrix elements. The concrete implementation of our proposed methods to calculate both phonon frequencies and the screened electron-phonon coupling will thus be the focus of future efforts, but is beyond the scope of this thesis.

Instead, we would like to conclude this section by establishing the link of our proposed approach to the frequently used method of DFPT. As discussed in Section 4.3, the self-consistent DFPT algorithm generates, amongst other quantities, the derivative of the self-consistent potential, $\partial_A V_{\text{scf}}(\mathbf{r})$, which is often taken as an approximation for the electron-phonon coupling in the static limit [130, 131]. By “static limit”, we refer to the $\omega' \rightarrow 0$ limit of the frequency-dependent, screened electron-phonon coupling. Note that passing to the $\omega' \rightarrow 0$ limit is equivalent to integrating over t_3 without any exponential factor:

$$\tilde{g}_A(1, 2; \omega') \equiv \int_{-\infty}^{+\infty} dt_3 e^{i\omega' t_3} g_A(1, 2; t_3) \xrightarrow{\omega' \rightarrow 0} \int_{-\infty}^{+\infty} dt_3 g_A(1, 2; t_3) \equiv g_A(1, 2), \quad (5.55)$$

which is easily seen to be consistent with our previous definition of the Fourier components of g_A in Eq. 5.46. Integrating both sides of Eq. 5.45 over t_3 , one obtains an equation for the static, screened electron-phonon coupling:

$$g_A(1, 2) = \delta(1, 2) g_A^{(b)}(\mathbf{r}_1) + \mathcal{K}^{(2)}(1, 2; \bar{3}, \bar{4}) \mathcal{L}(\bar{3}, \bar{4}; \bar{5}^+, \bar{5}) g_A^{(b)}(\bar{\mathbf{r}}_5). \quad (5.56)$$

As discussed before in Section 4.5, the approximations employed in DFPT are equivalent to approximating the two-particle-irreducible interaction kernel as

$$\mathcal{K}^{(2)}(1, 2; 3, 4) \stackrel{\text{DFPT}}{\simeq} K^{(2); \text{KS}}(1, 2; 3, 4) \equiv -\delta(1, 2) \delta(3, 4) [v(1, 3) - \Delta v_{\text{xc}}(1, 3)], \quad (5.57)$$

where $\Delta v_{\text{xc}}(1, 3)$ has been defined in Eq. 4.91 as the negative, instantaneous functional derivative of the exchange-correlation potential with respect to the KS charge density.

Within this approximation, the BSE for \mathcal{L} is solved by the KS two-particle correlation function $L^{(\text{KS})}$, i.e., the static electron-phonon coupling within DFPT obeys Eq. 5.56 with the replacements $\mathcal{K}^{(2)} \rightarrow K^{(2);\text{KS}}$ and $\mathcal{L} \rightarrow L^{(\text{KS})}$. However, as shown in Section 4.5, a combination of Eqs. 4.92 and 4.94 shows that this equation is solved by $g_A(1, 2) = \delta(1, 2)\partial_A V_{\text{scf}}(\mathbf{r}_2)$.

We have thus shown that in the limit of approximating the two-particle-irreducible interaction kernel with its KS-DFT-derived equivalent, the derivative of the self-consistent potential of KS-DFT indeed provides an approximation for the static electron-phonon coupling. In the same way, different approximations to the two-particle-irreducible interaction kernel yield different approximations to the electron-phonon coupling. The entire discussion about the physical interpretation and drawbacks of various approximations presented in Section 4.5 applies equally well to the case of the screened electron-phonon coupling and we will therefore not discuss the physical interpretation of our improved approach here again.

This concludes our treatment of the screened electron-phonon coupling, for which we presented a novel approach that is expected to yield a much more realistic estimation of the strength of the effective electron-phonon coupling, which enters various observable quantities, such as phonon frequencies beyond the adiabatic approximation and Raman scattering rates. In the final section of this chapter, we will turn to a discussion of the exact phonon Green's function, which is another ingredient needed for our treatment of Raman scattering.

5.3 Phonons beyond the adiabatic, Born-Oppenheimer approximation

The one-phonon Green's function plays an important role for the theoretical description of Raman scattering. As mentioned in the introduction to this thesis, the Raman spectrum features sharp peaks at energies corresponding to matter excitation energies, the lowest of which typically correspond to excitations of lattice vibrations, i.e., phonons. The position of the Raman peaks therefore corresponds to the exact phonon frequencies, which are closely related to the Fourier-transformed one-phonon Green's function.

More generally, the latter also contains information about a large set of excited states of the full matter Hamiltonian, which are needed for the calculation of Raman scattering rates within our developed theoretical approach.

In a first step, we will briefly review the *spectral* or *Lehmann representation* of the one-phonon Green's function, before discussing the calculation of the exact one-phonon Green's function within perturbation theory, based on Dyson's equation and the concept of the phonon self-energy. For the latter, we will suggest an approximation that leads to a natural extension of our approach for the calculation of phonon frequencies to the non-adiabatic regime. This is important for (semi-)metallic systems, where the adiabatic approximation is in general not justified. Indeed, as has been shown for graphene [28], the phonon frequencies in these systems are strongly influenced by non-adiabatic effects, as electronic excitations in low- or zero-gap systems can resonantly couple to lattice vibrations. We will revisit this important point once more in Chapter 7, where the phenomenon of “magneto-phonon resonances” will be discussed.

To begin with, we expand the exact phonon Green's function $\mathcal{D}_{A,B}(t_1, t_2)$ in the basis of phonon “wave functions”:

$$\mathcal{D}_{A,B}(t_1, t_2) \equiv \mathcal{D}_{(n,\alpha,i),(m,\beta,j)}(t_1, t_2) \equiv \sum_{\mathbf{q},\lambda,\lambda'} \xi_{\mathbf{q},\lambda}^{\alpha,i}(\mathbf{R}_n) \xi_{\mathbf{q},\lambda'}^{\beta,j;*}(\mathbf{R}_m) \mathcal{D}_{\mathbf{q},\lambda,\lambda'}(t_1, t_2), \quad (5.58)$$

where

$$\mathcal{D}_{\mathbf{q},\lambda,\lambda'}(t_1, t_2) \equiv -i \langle \Omega | \mathcal{T} \{ \hat{B}_{\mathbf{q},\lambda}(t_1) \hat{B}_{\mathbf{q},\lambda'}^\dagger(t_2) \} | \Omega \rangle \equiv \int \frac{d\omega}{2\pi} e^{-i\omega(t_1-t_2)} \tilde{\mathcal{D}}_{\mathbf{q},\lambda,\lambda'}(\omega) \quad (5.59)$$

is the Green's function for the mode operators $\hat{B}_{\mathbf{q},\lambda} \equiv \hat{b}_{\mathbf{q},\lambda} + \hat{b}_{-\mathbf{q},\lambda}^\dagger$, whose time-dependent versions are understood to be in the Heisenberg picture. With the last equality, we also defined the Fourier components of $\mathcal{D}_{\mathbf{q},\lambda,\lambda'}(t_1, t_2)$, which, due to time-translation invariance, can only depend on the time difference $t_1 - t_2$. Also note that, in the absence of “spontaneous symmetry breaking”, the exact ground state $|\Omega\rangle$ of $\hat{\mathcal{H}}_M$ has the same crystal symmetries as the ground state $|0\rangle$ of $\hat{\mathcal{H}}_0$ since the interaction Hamiltonian $\hat{\mathcal{H}}_1$ only contains terms that respect the symmetries of the crystal, fixed by the equilibrium

nuclear configuration $\{\mathbf{R}_I^{(0)}\}$. We therefore take the phonon Green's function to be diagonal in the wave vector \mathbf{q} , but note that it will in general *not* be diagonal in the space of the phonon branches, labeled by λ .

By inserting a complete set of states $\{|\alpha\rangle\}$ of the full matter Hamiltonian $\hat{\mathcal{H}}_M$, the phonon Green's function in mode space can be written in the form:

$$\begin{aligned} \mathcal{D}_{\mathbf{q},\lambda,\lambda'}(t_1, t_2) = & -i \sum_{\alpha} \left\{ \Theta(t_1 - t_2) e^{-i(E_{\alpha} - E_0)(t_1 - t_2)} \langle \Omega | \hat{B}_{\mathbf{q},\lambda} | \alpha \rangle \langle \alpha | \hat{B}_{\mathbf{q},\lambda'}^{\dagger} | \Omega \rangle \right. \\ & \left. + \Theta(t_2 - t_1) e^{-i(E_{\alpha} - E_0)(t_2 - t_1)} \langle \Omega | \hat{B}_{\mathbf{q},\lambda'}^{\dagger} | \alpha \rangle \langle \alpha | \hat{B}_{\mathbf{q},\lambda} | \Omega \rangle \right\}. \end{aligned} \quad (5.60)$$

Here, Θ denotes the Heaviside step function and E_{α}, E_0 are the energies of the states $|\alpha\rangle, |\Omega\rangle$, respectively. In Fourier space, this expression reads:

$$\tilde{\mathcal{D}}_{\mathbf{q},\lambda,\lambda'}(\omega) = \sum_{\alpha} \left\{ \frac{\langle \Omega | \hat{B}_{\mathbf{q},\lambda} | \alpha \rangle \langle \alpha | \hat{B}_{\mathbf{q},\lambda'}^{\dagger} | \Omega \rangle}{\omega - \Delta E_{\alpha} + i\eta} - \frac{\langle \Omega | \hat{B}_{\mathbf{q},\lambda'}^{\dagger} | \alpha \rangle \langle \alpha | \hat{B}_{\mathbf{q},\lambda} | \Omega \rangle}{\omega + \Delta E_{\alpha} - i\eta} \right\}, \quad (5.61)$$

where $\eta \equiv 0^+$ is a positive infinitesimal, which is needed to make the Fourier transformation of the step function well-defined, and $\Delta E_{\alpha} \equiv E_{\alpha} - E_0$ is the short notation for the excitation energies of $\hat{\mathcal{H}}_M$ which we already introduced at the end of Section 2.4. Eq. 5.61 is known as the *spectral* or *Lehmann representation* of the phonon Green's function, after H. Lehmann, who introduced it in his 1954 paper on renormalization constants of quantum fields [138].⁷

The spectral composition can be written in an alternative way by introducing the *retarded* and *advanced spectral functions*

$$\mathcal{A}_{\mathbf{q},\lambda,\lambda'}^{(R)}(\omega) \equiv \sum_{\alpha} \langle \Omega | \hat{B}_{\mathbf{q},\lambda} | \alpha \rangle \langle \alpha | \hat{B}_{\mathbf{q},\lambda'}^{\dagger} | \Omega \rangle \delta(\omega - \Delta E_{\alpha}) \quad (5.62)$$

$$\mathcal{A}_{\mathbf{q},\lambda,\lambda'}^{(A)}(\omega) \equiv \sum_{\alpha} \langle \Omega | \hat{B}_{\mathbf{q},\lambda'}^{\dagger} | \alpha \rangle \langle \alpha | \hat{B}_{\mathbf{q},\lambda} | \Omega \rangle \delta(\omega - \Delta E_{\alpha}), \quad (5.63)$$

which will also play a role in our approach to one-phonon-induced Raman scattering pre-

⁷In the particle physics literature the spectral decomposition is also known as the *Källén-Lehmann* representation, as it was independently used by G. Källén in his 1952 work on renormalization constants in relativistic quantum electrodynamics [139]. In the context of condensed matter physics, the spectral representation is often associated with the name of Lehmann alone, however.

sented in the next chapter. In terms of the spectral functions, the Fourier-transformed Green's function reads⁸

$$\tilde{\mathcal{D}}_{\mathbf{q},\lambda,\lambda'}(\omega) = \int_0^\infty d\omega' \left\{ \frac{\mathcal{A}_{\mathbf{q},\lambda,\lambda'}^{(\text{R})}(\omega')}{\omega - \omega' + i\eta} - \frac{\mathcal{A}_{\mathbf{q},\lambda,\lambda'}^{(\text{A})}(\omega')}{\omega + \omega' - i\eta} \right\}. \quad (5.64)$$

In systems with time-reversal symmetry, on which we will focus exclusively, the retarded and advanced Green's functions are related to each other by complex conjugation:⁹ $\mathcal{A}^{(\text{A})}(\omega) = [\mathcal{A}^{(\text{R})}(\omega)]^*$. It then makes sense to speak of *the* spectral function $\mathcal{A}(\omega) \equiv \mathcal{A}^{(\text{R})}(\omega)$ and omit the superscripts R and A:

$$\tilde{\mathcal{D}}_{\mathbf{q},\lambda,\lambda'}(\omega) \stackrel{\text{TRS}}{=} \int_0^\infty d\omega' \left\{ \frac{\mathcal{A}_{\mathbf{q},\lambda,\lambda'}(\omega')}{\omega - \omega' + i\eta} - \frac{\mathcal{A}_{\mathbf{q},\lambda,\lambda'}^*(\omega')}{\omega + \omega' - i\eta} \right\}. \quad (5.65)$$

From the spectral decomposition, we see that the one-phonon Green's function has singularities at (± 1) times the excitation energies of the full Hamiltonian, with their residues being given by the matrix elements of the mode operators between the ground and excited states. The presence of singularities with matrix elements as their residues is a general feature of Fourier-transformed correlation functions and in the next chapter we will exploit it to obtain the matrix elements for Raman scattering. For now, however, we confine ourselves to a brief description of how to obtain an expression for the excitation energies ΔE_α from perturbation theory. The latter play an important role for the description of Raman scattering, since, as we have seen in Section 2.4, the Raman scattering rate features sharp peaks whenever the energy difference between the incoming and scattered light is equal to an excitation energy of the full matter

⁸Note that, since $\Delta E_\alpha > 0$ for all states $|\alpha\rangle$, the δ -function does not contribute to the integral for $\omega < 0$ and we can hence take the integral to start at 0.

⁹In time reversal-invariant systems, the Hamiltonian commutes with the *anti*-unitary time-reversal operator $\hat{\mathcal{T}}$: $[\hat{\mathcal{T}}, \hat{\mathcal{H}}_{\text{M}}] = 0$. The eigenstates of $\hat{\mathcal{H}}$ can then be chosen to be eigenstates of $\hat{\mathcal{T}}$ as well. As $\hat{\mathcal{T}}$ is anti-unitary, its eigenvalues have the form $e^{i\eta_\alpha}$ with a real phase η_α , i.e., the eigenstates $|\alpha\rangle$ of $\hat{\mathcal{H}}_{\text{M}}$ can be chosen such that $\hat{\mathcal{T}}|\alpha\rangle = e^{i\eta_\alpha}|\alpha\rangle$. We then have $\langle \Omega | \hat{B}_{\mathbf{q},\lambda} |\alpha\rangle \langle \alpha | \hat{B}_{\mathbf{q},\lambda'}^\dagger | \Omega \rangle = \langle \Omega | \hat{\mathcal{T}} \hat{B}_{\mathbf{q},\lambda} \hat{\mathcal{T}}^\dagger |\alpha\rangle \langle \alpha | \hat{\mathcal{T}} \hat{B}_{\mathbf{q},\lambda'}^\dagger \hat{\mathcal{T}}^\dagger | \Omega \rangle$. If one uses the *anti*-linearity of $\hat{\mathcal{T}}$ and the fact that $\hat{u}_{a,\alpha,i}$ and $\hat{P}_{a,\alpha,i}$ are even and odd under time-reversal, respectively, it follows from our definition of $\hat{B}_{\mathbf{q},\lambda}$ in terms of $\hat{u}_{a,\alpha,i}$ and $\hat{P}_{a,\alpha,i}$ that $\hat{\mathcal{T}} \hat{B}_{\mathbf{q},\lambda} \hat{\mathcal{T}}^\dagger = \hat{B}_{-q,\lambda} = \hat{B}_{q,\lambda}^\dagger$. In systems with time-reversal symmetry, we then have $\langle \Omega | \hat{B}_{\mathbf{q},\lambda} |\alpha\rangle \langle \alpha | \hat{B}_{\mathbf{q},\lambda'}^\dagger | \Omega \rangle = [\langle \Omega | \hat{B}_{\mathbf{q},\lambda'}^\dagger |\alpha\rangle \langle \alpha | \hat{B}_{\mathbf{q},\lambda} | \Omega \rangle]^*$.

Hamiltonian. Therefore, the positions of the peaks appearing in the Raman spectrum can be determined from the poles of the matter Green’s functions, i.e., the many-particle electron and phonon Green’s functions. In this work, we will confine ourselves to phonon-induced Raman scattering, i.e., to peaks appearing at excitation energies of $\hat{\mathcal{H}}_M$ which can “mostly” be associated with the excitation of phonons, as for many materials, these kinds of excitations dominate the Raman spectrum [85]. To make this notion of “mostly” more precise, we assume that the coupling of the electronic and phonon system can be considered a small perturbation only. In this case, to each elementary electronic or phonon excitation of the unperturbed system, there then exists a corresponding excitation of the fully interacting system whose excitation energy is close to that of the excitation energy of the unperturbed system, in the sense that their relative difference can be considered to be significantly smaller than one.

In order to find the singularities of the Fourier-transformed phonon Green’s function, we make use of its series expansion in time-dependent perturbation theory, similarly to our discussion of the one-particle electron Green’s function in Section 3.3.1. We first express the needed time-ordered correlation function in terms of interaction-picture operators and the ground state $|0\rangle$ of the non-interacting reference system described by $\hat{\mathcal{H}}_0$ as defined in Eq. 5.30:

$$\langle\Omega|\mathcal{T}\{\hat{u}_A(t_1)\hat{u}_B^\dagger(t_2)\}|\Omega\rangle = \frac{\langle 0|\mathcal{T}\left\{\hat{u}_{A,I}(t_1)\hat{u}_{B,I}^\dagger(t_2)\exp\left[-i\int_{-\infty}^{+\infty}dt\hat{\mathcal{H}}_{1,I}(t)\right]\right\}|0\rangle}{\langle 0|\mathcal{T}\left\{\exp\left[-i\int_{-\infty}^{+\infty}dt\hat{\mathcal{H}}_{1,I}(t)\right]\right\}|0\rangle}. \quad (5.66)$$

Just as for the electron Green’s function, we can expand the right-hand side in powers of the interaction Hamiltonian $\hat{\mathcal{H}}_1$ and organize the arising terms via Feynman diagrams, according to the rules given in Table 5.1. The perturbation series for the exact one-phonon Green’s function is then given by the sum of all fully connected Feynman diagrams with two “phonon endpoints”, represented by open circles.¹⁰

¹⁰As usual and as is well known [83, 87–89, 91, 115], the denominator on the right-hand side of Eq. 5.66 serves to cancel the terms arising from the sum of disconnected diagrams, which is known in the literature as the *linked cluster theorem*.

To organize this series of diagrams even further, we introduce the *one-particle-irreducible phonon self-energy* $\Pi_{A,B}(t_1, t_2)$ as i times the sum of all one-phonon -irreducible, fully connected diagrams, i.e., diagrams that do not fall into two pieces if a single phonon line is cut (also compare the definition of the electron self-energy in Section 3.3.1).¹¹ The perturbation series for $\mathcal{D}_{A,B}(t_1, t_2)$ then takes on the form of a geometric series, as shown in Fig. 5.4. This diagrammatic equation is equivalent to

$$\begin{aligned}
\text{Diagram 1} &= \text{Diagram 2} + \text{Diagram 3} \\
&+ \text{Diagram 4} + \dots \\
&= \text{Diagram 5} + \text{Diagram 6}
\end{aligned}$$

Figure 5.4: **Diagrammatic representation of Dyson’s equation for the one-phonon Green’s function.**

Dyson’s equation

$$\mathcal{D}_{A,B}(t_1, t_2) = D_{A,B}(t_1, t_2) + D_{A,\bar{C}}(t_1, \bar{t}_3) \Pi_{\bar{C},\bar{D}}(\bar{t}_3, \bar{t}_4) \mathcal{D}_{\bar{D},B}(\bar{t}_4, t_2), \quad (5.67)$$

where barred indices and time variables are summed or integrated over, respectively. Expanding the non-interacting phonon Green’s function D and the self-energy Π in the basis of phonon “wave functions” and defining their Fourier-transformed version analogously to Eq. 5.59, Dyson’s equation can easily be solved for the inverse Green’s function

$$2\sqrt{\omega_{\mathbf{q},\lambda}\omega_{\mathbf{q},\lambda'}} \tilde{D}_{\mathbf{q},\lambda,\lambda'}^{-1}(\omega) = \delta_{\lambda,\lambda'}(\omega^2 - \omega_{\mathbf{q},\lambda}^2) - 2\sqrt{\omega_{\mathbf{q},\lambda}\omega_{\mathbf{q},\lambda'}} \tilde{\Pi}_{\mathbf{q},\lambda,\lambda'}(\omega) l, \quad (5.68)$$

whose zeros define the poles of \mathcal{D} . Here, we made use of the fact that the Fourier-

¹¹Just as in the case of the electron self-energy, the factor of i is included in the definition of Π so that the sum of all such diagrams equals $(-i)\Pi_{A,B}(t_1, t_2)$. The factor $(-i)$ then cancels the factor of i stemming from the factor of $iD_{A,B}(t_1, t_2)$ associated with a single phonon line.

transformed and expanded non-interacting Green's function has the form

$$\tilde{D}_{\mathbf{q},\lambda,\lambda'}(\omega) = \delta_{\lambda,\lambda'} \frac{2\omega_{\mathbf{q},\lambda}}{\omega^2 - \omega_{\mathbf{q},\lambda}^2 + i\eta}, \quad (5.69)$$

as is easily shown from its definition.

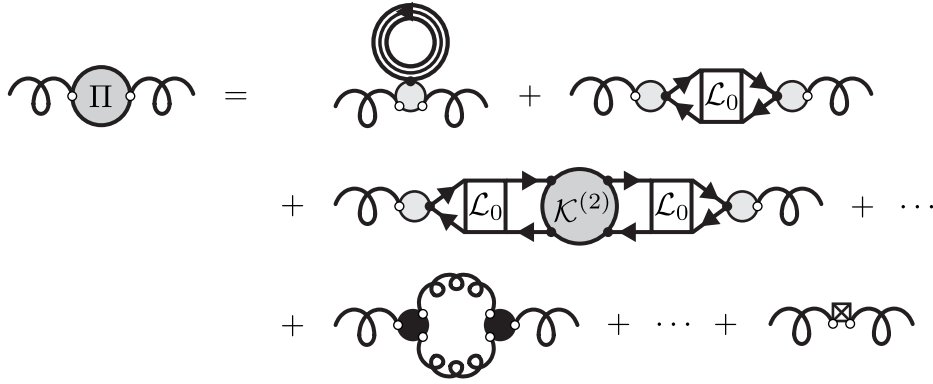


Figure 5.5: Examples of terms appearing in the diagrammatic expansion of the irreducible phonon self-energy.

The phonon self-energy Π , in turn, can be obtained from its diagrammatic definition. In Fig. 5.5, we show a few of the terms appearing in its perturbative expansion. The terms in the first two lines arise from electron-phonon interaction processes that also include electron-mediated anharmonic effects, while the first term of the third line is an example of a term that appears due to pure phonon-phonon interaction. Finally, the last diagram represents the static counterterm $-C_{A,B}^{(\text{el})}$, i.e., the electronic part of the force constants, in the adiabatic and harmonic approximations. It serves to cancel the contribution to the self-energy that is already included in the adiabatic and harmonic phonon frequencies $\omega_{\mathbf{q},\lambda}$ that serve as a starting point for the perturbative treatment. We will denote this counterterm contribution to the self-energy as $\tilde{\Pi}_{\mathbf{q},\lambda,\lambda'}^{(\text{ad.})}$. Explicitly, it

is given by

$$\begin{aligned}
\tilde{\Pi}_{\mathbf{q},\lambda,\lambda'}^{(\text{ad.})} &= - \sum_{A,B} \xi_{\mathbf{q},\lambda}^{A,*} C_{A,B}^{(\text{el})} \xi_{\mathbf{q},\lambda'}^B \\
&= - \frac{1}{N} \sum_{n,m} \frac{1}{2\sqrt{\omega_{\mathbf{q},\lambda}\omega_{\mathbf{q},\lambda'}}} \sum_{\substack{\alpha,\beta \\ i,j}} \frac{1}{\sqrt{M_\alpha M_\beta}} e^{-i\mathbf{q}\cdot(\mathbf{R}_n - \mathbf{R}_m)} \\
&\quad \times v_{\mathbf{q},\lambda}^{\alpha,i,*} \left[C_{\alpha,\beta}^{i,j}(\mathbf{R}_n - \mathbf{R}_m) - C_{\alpha,\beta}^{(\text{nuc})}(\mathbf{R}_n - \mathbf{R}_m) \right] v_{\mathbf{q},\lambda'}^{\beta,j},
\end{aligned} \tag{5.70}$$

where we replaced the electronic part of the force constants by the difference between the total force constants and the nuclear part, defined in Eq. 4.39. If we identify the (unperturbed) dynamical matrix and note that the $v_{\mathbf{q},\lambda}^{\alpha,i}$ are its mutually orthogonal and normalized eigenvectors to the eigenvalues $\omega_{\mathbf{q},\lambda}^2$, this expression simplifies considerably:

$$\tilde{\Pi}_{\mathbf{q},\lambda,\lambda'}^{(\text{ad.})} = -\delta_{\lambda,\lambda'} \frac{\omega_{\mathbf{q},\lambda}^2}{2\omega_{\mathbf{q},\lambda}} + \frac{1}{2\sqrt{\omega_{\mathbf{q},\lambda}\omega_{\mathbf{q},\lambda'}}} D_{\lambda,\lambda'}^{(\text{nuc})}(\mathbf{q}), \tag{5.71}$$

where we defined the mode-projected, nuclear part of the dynamical matrix as

$$D_{\lambda,\lambda'}^{(\text{nuc})}(\mathbf{q}) \equiv \sum_{\substack{\alpha,\beta \\ i,j}} v_{\mathbf{q},\lambda}^{\alpha,i,*} \frac{1}{\sqrt{M_\alpha M_\beta}} \left[\sum_n e^{-i\mathbf{q}\cdot\mathbf{R}_n} C_{\alpha,\beta}^{i,j}(\mathbf{R}_n) \right] v_{\mathbf{q},\lambda'}^{\beta,j}. \tag{5.72}$$

In terms of the *non-adiabatic* part of the self-energy, $\tilde{\Pi}^{(\text{NA})}(\omega) \equiv \tilde{\Pi}(\omega) - \tilde{\Pi}^{(\text{ad.})}$, Dyson's equation then reduces to

$$2\sqrt{\omega_{\mathbf{q},\lambda}\omega_{\mathbf{q},\lambda'}} \tilde{\mathcal{D}}_{\mathbf{q},\lambda,\lambda'}^{-1}(\omega) = \delta_{\lambda,\lambda'} \omega^2 - \left[D_{\lambda,\lambda'}^{(\text{nuc})}(\mathbf{q}) + 2\sqrt{\omega_{\mathbf{q},\lambda}\omega_{\mathbf{q},\lambda'}} \tilde{\Pi}_{\mathbf{q},\lambda,\lambda'}^{(\text{NA})}(\omega) \right]. \tag{5.73}$$

In a last step, we need to obtain an approximative expression for the non-adiabatic part of the self-energy. As seen from the diagrammatic expansion shown in Fig. 5.5, the non-adiabatic part of the self-energy consists of a sum of terms due to electron-phonon interaction and a sum of terms involving phonon-phonon interaction processes. These latter terms involve the third derivative of the nuclei-nuclei potential energy and hence are related to anharmonic effects. In a first approximation, we neglect those and focus

on the electronic part of the self-energy instead: $\Pi^{(\text{NA})} \approx \Pi^{(\text{el})}$. It is given by the series

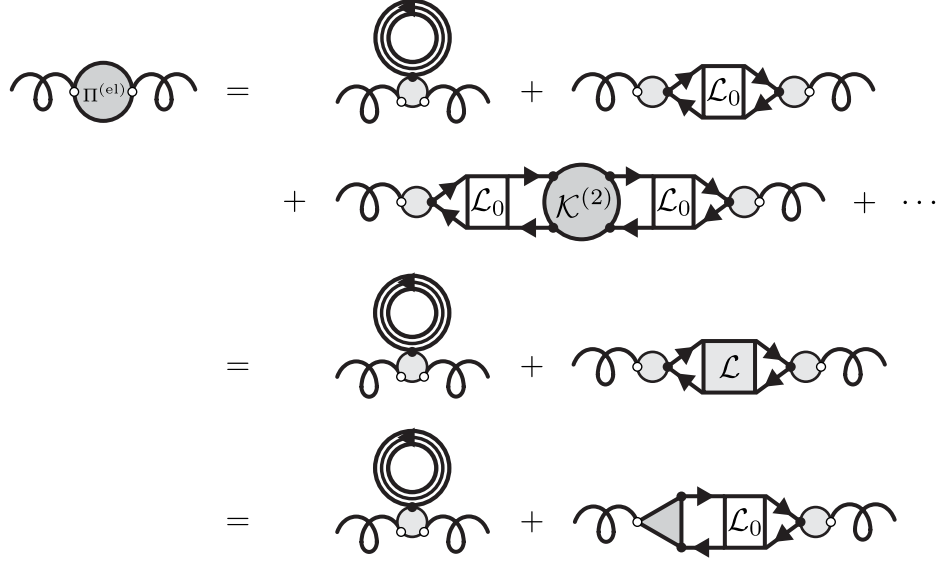


Figure 5.6: **Diagrammatic expansion of the electronic part of the irreducible phonon self-energy.**

of diagrams shown in Fig. 5.6 and can be summed exactly by making use of the Bethe-Salpeter equation for the two-particle correlation function. In real space, it is given by:

$$\begin{aligned}
\Pi_{A,B}^{(\text{el})}(t_1, t_2) &= \int d^3r_1 g_{A,B}^{(\text{b});(2)}(\mathbf{r}_1) (-i) \mathcal{G}((\mathbf{r}_1, t_1^+), (\mathbf{r}_1, t_1)) \delta(t_1 - t_2) \\
&\quad + \int d^3r_1 \int d^3r_2 g_A^{(\text{b})}(\mathbf{r}_1) (-i) \mathcal{L}((\mathbf{r}_1, t_1), (\mathbf{r}_1, t_1^+); (\mathbf{r}_2, t_2^+), (\mathbf{r}_2, t_2)) g_B^{(\text{b})}(\mathbf{r}_2) \\
&= \int d^3r_1 g_{A,B}^{(\text{b});(2)}(\mathbf{r}_1) (-i) \mathcal{G}((\mathbf{r}_1, t_1^+), (\mathbf{r}_1, t_1)) \delta(t_1 - t_2) \\
&\quad + \int d^3r_1 \int d^3r_2 g_A(\mathbf{r}_1) (-i) \mathcal{L}_0((\mathbf{r}_1, t_1), (\mathbf{r}_1, t_1^+); (\mathbf{r}_2, t_2^+), (\mathbf{r}_2, t_2)) g_B^{(\text{b})}(\mathbf{r}_2),
\end{aligned} \tag{5.74}$$

where in the last equality we traded the product of the *bare* electron-phonon coupling $g^{(\text{b})}$ and the *exact* two-particle correlation function \mathcal{L} for the product of the *screened* electron-phonon coupling g and the *independent-particle* two-particle correlation func-

tion \mathcal{L}_0 , as pointed out in the previous section. Also note that we included an additional minus sign due to the appearance of a closed fermion loop in both diagrams.

The electronic part of the phonon self-energy consists of two parts. The first one involves the second derivative of the lattice potential and the exact electron charge density in the interacting electron-phonon system. Since this term only gives a static contribution to the self-energy, its effect on the phonon frequencies should not differ much if the exact density is replaced by the one in the non-interacting electronic system, which, in turn, can be reasonably well approximated by the Kohn-Sham density, as argued in the previous chapter. The second part, by contrast, is dynamic and therefore can potentially have a big influence on the phonon frequencies in (semi-)metallic systems, where the non-interacting phonon and electron systems have similar excitation energies and thus can be in resonance with one another. To obtain a practically useful expression for this second part, we use the same approximation as for the description of the screened electron-phonon coupling in the previous section and let $\mathcal{K}^{(2)} \rightarrow K^{(2)}$ and $\mathcal{L}_{(0)} \rightarrow L_{(0)}$. This corresponds to neglecting the electron-phonon interaction contributions to the kernel or electron self-energy. As argued before, this should in general be a very good approximation for the purpose of describing the screening of the electron-phonon interaction. Note however, that *neglecting the electron-phonon coupling in the two-particle-irreducible interaction kernel means that dynamic, indirect phonon-phonon interaction effects are not included anymore*. The latter appear, for example, in contributions to the kernel that involve two internal phonon lines. These contributions can potentially give a sizable contribution to anharmonic effects on the phonon frequencies and lifetimes and thus our approximation leads to the complete omission of all anharmonic effects. If the inclusion of the latter is desirable or necessary, they can still be included perturbatively by including the respective diagrams just mentioned.

In our approximation then, the Fourier-transformed and mode-projected electronic part of the self-energy reads:

$$\tilde{\Pi}_{\mathbf{q},\lambda,\lambda'}^{(\text{el})}(\omega) = \frac{1}{2\sqrt{\omega_{\mathbf{q},\lambda}\omega_{\mathbf{q},\lambda'}}} \sum_{\substack{\alpha,\beta \\ i,j}} v_{\mathbf{q},\lambda}^{\alpha,i,*} D_{\alpha,\beta}^{(\text{el,dyn})}(\mathbf{q},\omega) v_{\mathbf{q},\lambda'}^{\beta,j}, \equiv \frac{1}{2\sqrt{\omega_{\mathbf{q},\lambda}\omega_{\mathbf{q},\lambda'}}} D_{\lambda,\lambda'}^{(\text{el,dyn})}(\mathbf{q},\omega) \quad (5.75)$$

where in the first step we defined the electronic part of a dynamic, effective dynamical

matrix as

$$\begin{aligned}
D_{\alpha,\beta}^{(\text{el,dyn})}(\mathbf{q}, \omega) &\equiv \frac{1}{\sqrt{M_\alpha M_\beta}} (-i) \sum_{\mathbf{k}, \mathbf{k}'} \sum_{a,b,c,d} \left(g_{\mathbf{k}'+\mathbf{q}, \mathbf{k}'}^{(\text{b});(\alpha,i)} \right)^* \tilde{L}_{\mathbf{k}'+\mathbf{q}, a; \mathbf{k}+\mathbf{q}, c}(\omega) g_{\mathbf{k}+\mathbf{q}, \mathbf{k}}^{(\text{b});(\beta,j)} \\
&+ \frac{1}{\sqrt{M_\alpha M_\beta}} \sum_{\mathbf{k}, a, b} g_{\mathbf{k}, \mathbf{k}}^{(\text{b});(2);(\alpha,\beta)} \int \frac{d\omega}{2\pi i} e^{i\omega 0^+} \tilde{G}_{\mathbf{k}, a, b}(\omega).
\end{aligned} \tag{5.76}$$

Here, we identified the “reduced”, bare, electron-nuclei coupling matrix elements, as defined in Eqs. 4.78 and 4.79. Inserting the eigenmode expansion of the two-particle correlation function and approximating the interacting electron charge density in the second line with the Kohn-Sham one, we arrive at the concrete expression

$$D_{\alpha,\beta}^{(\text{el,dyn})}(\mathbf{q}, \omega) = \frac{1}{\sqrt{M_\alpha M_\beta}} \left\{ \sum_{S, S'} \frac{\left(g_{\mathbf{q}, S}^{(\text{b});(\alpha,i)} \right)^* N_{S, S'}^{-1} g_{\mathbf{q}, S'}^{(\text{b});(\beta,j)}}{\omega - \varepsilon_S + i\eta} + \sum_{(\mathbf{k}, a) \in \mathcal{O}} g_{\mathbf{k}, \mathbf{k}}^{(\text{b});(2);(\alpha,\beta)} \right\}, \tag{5.77}$$

in which we identified the bilinear exciton-phonon coupling as defined in Eq. 4.82. If we finally define the dynamic, total, effective dynamical matrix as $D^{(\text{dyn})}(\mathbf{q}, \omega) \equiv D^{(\text{el,dyn})}(\mathbf{q}, \omega) + D^{(\text{nuc})}(\mathbf{q})$, we see that the problem of finding the zeros of Dyson’s equation, which now reads

$$2\sqrt{\omega_{\mathbf{q}, \lambda} \omega_{\mathbf{q}, \lambda'}} \tilde{D}_{\mathbf{q}, \lambda, \lambda'}^{-1}(\omega) = \delta_{\lambda, \lambda'} \omega^2 - D_{\lambda, \lambda'}^{(\text{dyn})}(\mathbf{q}, \omega), \tag{5.78}$$

is equivalent to solving a non-linear eigenvalue problem. Note that the dynamic, effective dynamical matrix reduces to the ordinary, static dynamical matrix in the static $\omega \rightarrow 0$ limit, as seen from a comparison of Eqs. 5.76 and 4.80. As seen in Section 3.3.2, the frequency ω appears in the two-particle correlation function only through its difference with an electronic excitation energy. In systems with a sizable electronic band gap, we can therefore neglect the frequency dependence of the effective dynamical matrix if we are only interested in low-energy solutions to Dyson’s equation, i.e., solutions ω that are much smaller than the smallest electronic excitation energy. This is typically the case for semi-conducting or insulating systems, but not for (semi-)metallic systems with small or vanishing band gaps, such as graphene, where the frequency dependence

of the effective dynamical matrix is usually not negligible.

So far, our treatment of phonons beyond the Born-Oppenheimer approximation was based on a perturbative approach, starting from a known set of phonon frequencies and eigenvectors, $\{\omega_{\mathbf{q},\lambda}, v_{\mathbf{q},\lambda}^{\alpha,i}\}$. However, in our final expression for Dyson's equation, the only remnant of this is the fact that both the exact phonon Green's function and the effective dynamical matrix have been projected on the phonon eigenmodes. Instead, one can equally well write it in a cartesian basis:

$$\tilde{D}_{\alpha,\beta}^{-1}(\mathbf{q}, \omega) = \delta_{\alpha,\beta} \delta_{i,j} \omega^2 - D_{\alpha,\beta}^{(\text{el,dyn})}(\mathbf{q}, \omega). \quad (5.79)$$

This allows a computation of phonon frequencies beyond the adiabatic, Born-Oppenheimer approximation without the need to first calculate the phonons of a reference system, such as the one within the BOA.

To conclude, our proposed approach for computing phonons, and in general any excitation energies of the matter Hamiltonian with a non-vanishing one-phonon contribution, can be summarized as follows:

1. Calculation of a set of Kohn-Sham states and eigenvalues in density functional theory.
2. Correction of the KS eigenvalues on the level of the GW approximation.
3. Computation of the static two-particle interaction kernel, solving the frequency-dependent Bethe-Salpeter equation for both the eigenstates and eigenvalues, and calculation of the overlap matrix.
4. Calculation of the matrix elements of the first and second derivatives of the lattice potential in the KS basis and computation of the bilinear exciton-phonon coupling.
5. Construction of the electronic part of the effective dynamical matrix according to Eq. 5.77, addition of the static, nuclear part, and solving the non-linear eigenvalue problem $\tilde{D}^{-1}(\mathbf{q}, \omega) = 0$.

Once again, as of now, no existing *ab initio* code features both a solver for the BSE at finite-wave vector excitations and also allows for the computation of the bare electron-phonon interaction matrix elements. The concrete implementation of our proposed way of calculating phonons beyond the Born-Oppenheimer approximation will be the subject of future efforts but is beyond the scope of this thesis.

Our novel and concrete approach for the calculation of phonons beyond the adiabatic, Born-Oppenheimer approximation combines both the inclusion of non-adiabatic effects and a description of the screening of the electron-phonon interaction on a level of theory beyond common modern approaches such as DFPT. It thus constitutes a significant advancement in the theory of phonons and electron-phonon interaction. So far, not many works have discussed approaches to this problem. The only other works of note that are concerned with the calculation of frequencies beyond the BOA are the works by Pisana *et al.* on graphene [28] and a recent work by Caruso *et al.* [140] on boron-doped diamond. The methods applied in these works, however, make use of either a semi-empirical analytical model for the electron-phonon coupling or use the DFPT-level electron-phonon coupling, respectively, and furthermore require a prior calculation of reference phonon frequencies.

In conclusion, this chapter dealt with a discussion of the perturbative treatment of the exact, full matter Hamiltonian. We applied the methods of time-dependent perturbation theory to obtain concrete expressions for a description of the screened electron-phonon coupling and for phonon frequencies beyond the adiabatic, Born-Oppenheimer approximation and beyond the currently often employed level of theory, such as DFPT. The latter has been shown to not yield satisfactory results in (semi-)metallic systems, such as graphene [53], in which Kohn anomalies exist and non-adiabatic effects are important. The theoretical approach we developed over the past two chapters goes beyond these limitations and our concrete expressions allow a timely implementation, which will be the subject of future research.

Now that we have reviewed and developed a way to find the energies of excitations of the full matter Hamiltonian with at least a partial phonon component, we are in a position to discuss and develop a concrete approach to the calculation of one-phonon-

induced Raman scattering rates, which will be the subject of the next chapter.

Chapter 6

One-Phonon Raman Spectroscopy

Parts of the content of this chapter have been published in the following publications:

- Reichardt, S. & Wirtz, L. Raman Spectroscopy of Graphene, *Optical Properties of Graphene*, chap. 3, 85–132 (World Scientific, Singapore, 2017)
- Miranda, H. P. C., Reichardt, S., Froehlicher, G., Molina-Sánchez, A., Berciaud, S. & Wirtz, L. Quantum interference effects in resonant Raman spectroscopy of single-and triple-layer MoTe₂ from first-principles. *Nano Lett.* **17**, 2381–2388 (2017)¹
- Reichardt, S. & Wirtz, L. Ab initio calculation of the G peak intensity of graphene: Laser-energy and Fermi-energy dependence and importance of quantum interference effects. *Phys. Rev. B* **95**, 195422 (2017)

¹Contributions of the author of this thesis to the cited work:

Provided key ideas for interpretation of the calculations in the form of the concepts of approximate angular momentum conservation, quantum interference effects, and visualization of the computational results; extensively discussed the results with the co-authors; co-wrote the manuscript.

In the preceding chapters we developed a general theory for inelastic light scattering and presented an approximation to it based on a generalization of Fermi's golden rule. As mentioned earlier, the latter approach allows an efficient computation of only parts of the Raman spectrum, by selecting the states for which the scattering matrix element is evaluated. In the present chapter, we will now focus on the contribution of one-phonon-like states to the inelastic scattering rate.

We will present a concrete approach that allows the computation of the needed scattering matrix element and permits the inclusion of *both* excitonic and non-adiabatic effects. Previous approaches only allowed the inclusion of one [75] or the other [50, 59], but not both at the same time. The means that enables us to overcome this limitation is the application of the Lehmann-Symanzik-Zimmermann reduction formula [80], which is widely applied in the field of particle physics but so far has not seen any use in condensed matter physics. Our approach thus constitutes a major advancement for both the practical and theoretical side of the description of Raman spectroscopy.

In addition to these theoretical developments, we show results of a first concrete computation for the case of graphene, which demonstrates the viability of the method, firstly in the simpler setting of negligible excitonic effects. A computational demonstration of the viability of the method for materials in which excitonic effects are relevant will be the subject of future work. However, already the case of graphene demonstrates the full power and flexibility of our approach, as it allows us to study the dependence of the Raman intensity on both the frequency of the incoming light and variations of the Fermi energy in great detail. Furthermore, it permits the identification of the dominant contributions to the scattering matrix element and demonstrate the importance of quantum interference effects, which were also a subject of experimental interest [81].

6.1 One-phonon Raman scattering in perturbation theory

We first focus on the theoretical description of one-phonon-induced Raman scattering at zero temperature and at macroscopically long observation times. In these limits, the Raman scattering rate was shown in Section 2.4 to be given by a generalization of

Fermi's golden rule that involves matrix elements of a time-ordered product of current density operators in the Heisenberg picture. In the first part of this section, we will see how these matrix elements appear as residues of poles of higher-order correlation functions, similarly to how the exact one-particle Green's functions have poles whose residues can be written as matrix elements of field operators. The relation between these kinds of matrix elements and higher-order correlation functions is described by the *Lehmann-Symanzik-Zimmermann (LSZ) reduction formula* [80]. Since it is practically unheard of in the domain of condensed matter physics, we shall briefly review its derivation in the context of the matrix elements needed for our description of Raman scattering. The derivation of the LSZ reduction formula reviewed here follows in spirit that of the books by Peskin and Schroeder [88] and Weinberg [83].

The remainder of this section will be devoted to the discussion of the needed higher-order correlation function and approximations to it that lead to a concrete approach for the calculation of the one-phonon-induced Raman scattering rate. The main theoretical result will be a concrete perturbative expression that allows the computation of the one-phonon Raman scattering matrix element including excitonic effects, a comprehensive description of the screening of the electron-phonon coupling, and dynamically treated phonons. As a first test case that avoids the added complexity arising from the presence of excitonic effects, we will apply the independent-particle version of our approach to graphene in the next section.

6.1.1 LSZ reduction formula

As seen in Chapter 2, we can compute the Raman scattering rate, which is directly proportional to the measured Raman intensity, from knowledge of the matrix elements

$$\tilde{J}_{\mathbf{k}_{\text{out}},\mathbf{k}_{\text{in}}}^{\alpha}(\omega) = \int_{-\infty}^{+\infty} dt e^{i\omega t} \langle \alpha | \mathcal{T} \left\{ \hat{J}_{\mathbf{k}_{\text{out}},\nu}(t) \hat{J}_{\mathbf{k}_{\text{in}},\mu}^{\dagger}(0) \right\} | \Omega \rangle, \quad (6.1)$$

where the spatially Fourier-transformed and projected current density operators have been defined in Eq. 2.35, $|\alpha\rangle$ is an eigenstate of the full matter Hamiltonian $\hat{\mathcal{H}}_M$ and

$|\Omega\rangle$ is its ground state.² Note that we omitted the subscript I on the current density operators, as with respect to the Hamiltonian $\hat{\mathcal{H}}_M$ they are in the *Heisenberg* picture.

For the purpose of the work presented in this chapter, i.e., one-phonon-induced Raman scattering, we will be interested in matrix elements involving states $|\alpha\rangle$ that are largely phononic in character. By this, we mean that we restrict ourselves to contributions from states for which the matrix elements $\langle\alpha|\hat{u}_A|\Omega\rangle$ are sizably different from zero. Note that in the non-interacting theory we would have $\langle\alpha|\hat{u}_A|0\rangle \neq 0$ if and only if $|\alpha\rangle = |\mathbf{q}, \lambda\rangle$, i.e., $|\alpha\rangle$ is a state with exactly one phonon. In the full, interacting theory, the non-interacting one-phonon states will mix with the other non-interacting states to form the eigenstates $|\alpha\rangle$ of the full matter Hamiltonian and the matrix elements $\langle\alpha|\hat{u}_A|0\rangle$ will be non-vanishing for an entire set or continuum of states that will be energetically close to the one-phonon states if the interactions can be considered small. For these kinds of states $|\alpha\rangle$, the needed matrix elements of a time-ordered product of current operators can be obtained from the higher-order correlation function

$$S_A(t', t; \mathbf{k}_{\text{out}}, \nu; \mathbf{k}_{\text{in}}, \mu) \equiv \langle\Omega|\mathcal{T}\left\{\hat{u}_A(t')\hat{J}_{\mathbf{k}_{\text{out}},\nu}(t)\hat{J}_{\mathbf{k}_{\text{in}},\mu}^\dagger(0)\right\}|\Omega\rangle, \quad (6.2)$$

where $A \equiv (n, \alpha, i)$ is the short-hand notation for the indices specifying a displacement of the α th atom in unit cell n in the i th cartesian direction. We will denote the Fourier transform of S_A with respect to t' by

$$\tilde{S}_A(\omega'; t; \Phi) \equiv \int_{-\infty}^{+\infty} dt' e^{i\omega't'} S_A(t'; t; \mathbf{k}_{\text{out}}, \nu; \mathbf{k}_{\text{in}}, \mu), \quad (6.3)$$

where we introduced the short-hand notation $\Phi \equiv (\mathbf{k}_{\text{out}}, \nu; \mathbf{k}_{\text{in}}, \mu)$ in order to avoid an overloading of the expressions with too many explicitly appearing quantities.

Our main subject of interest will be the singularities of \tilde{S} as a function of ω' . We have already seen in the previous chapter that correlation functions can exhibit singularities at exact excitation energies of the interacting system, the residues of which are related to certain matrix elements. Here, we will exploit this feature to extract the needed

²As in the previous two chapters, we make use of a calligraphic font to denote operators that act in more than one subspace of the complete Hilbert space. In this case, $\hat{\mathcal{H}}_M$ acts on both the electronic and the nuclear part of the Hilbert space. This operator was previously denoted by \hat{H}_M in the context of our discussion of the interacting light-matter system in Chapter 2.

matrix elements for Raman scattering. To compute the Fourier transform of S , we first divide the integration interval into three regions:

$$(-\infty, +\infty) = (-\infty, -T) \cup [-T, +T] \cup (+T, +\infty), \quad (6.4)$$

where T is an intermediate time chosen such that $-T < \min\{t, 0\} \leq \max\{t, 0\} < +T$. The Fourier integral then splits into three separate integrals, one over each of the three regions. For the purpose of finding the singularities of \tilde{S} as a function of ω' , the integral over the finite interval $[-T, +T]$ can be ignored as the integrand depends on ω' only through the analytic exponential function $\exp(i\omega't')$ and an integral over t' over the finite region $[-T, +T]$ will yield an analytic function of ω' . We then have

$$\begin{aligned} \tilde{S}_A(\omega'; t; \Phi) &= \int_{-\infty}^{-T} dt' e^{i\omega't'} S_A(t', t; \Phi) + \int_{+T}^{+\infty} dt' e^{i\omega't'} S_A(t', t; \Phi) \\ &+ \text{terms regular in } \omega'. \end{aligned} \quad (6.5)$$

The second term reads

$$\int_{+T}^{+\infty} dt' e^{i\omega't'} S_A(t', t; \Phi) = \int_{+T}^{+\infty} dt' e^{i\omega't'} \sum_{\alpha} \langle \Omega | \hat{u}_A(t') | \alpha \rangle \langle \alpha | \mathcal{T} \left\{ \hat{J}_{\mathbf{k}_{\text{out}}, \nu}(t) \hat{J}_{\mathbf{k}_{\text{in}}, \mu}^{\dagger}(0) \right\} | \Omega \rangle, \quad (6.6)$$

where we inserted a complete set of eigenstate of $\hat{\mathcal{H}}_M$ and included the time-ordering symbol only in the second factor since $t' > T > \max\{t, 0\}$ everywhere in the integration region. Inserting the definition of \hat{u}_A in the Heisenberg picture and letting $\omega' \rightarrow \omega' + i\eta$ with a positive infinitesimal η to ensure the convergence of the integral, we find

$$\int_{+T}^{+\infty} dt' e^{i\omega't'} S_A(t', t; \Phi) = \sum_{\alpha} i e^{i(\omega' - \Delta E_{\alpha} + i\eta)T} \langle \Omega | \hat{u}_A | \alpha \rangle \frac{\langle \alpha | \mathcal{T} \left\{ \hat{J}_{\mathbf{k}_{\text{out}}, \nu}(t) \hat{J}_{\mathbf{k}_{\text{in}}, \mu}^{\dagger}(0) \right\} | \Omega \rangle}{\omega' - \Delta E_{\alpha} + i\eta}, \quad (6.7)$$

with $\Delta E_{\alpha} \equiv E_{\alpha} - E_0$ denoting the excitation energies of the full matter Hamiltonian $\hat{\mathcal{H}}_M$. After similar manipulations for the integral over the $(-\infty, -T)$ -region, one finds

for \tilde{S}_A :

$$\begin{aligned} \tilde{S}_A(\omega'; t; \Phi) = \sum_{\alpha} \left\{ i e^{i(\omega' - \Delta E_{\alpha} + i\eta)T} \langle \Omega | \hat{u}_A | \alpha \rangle \frac{\langle \alpha | \mathcal{T} \left\{ \hat{J}_{\mathbf{k}_{\text{out}}, \nu}(t) \hat{J}_{\mathbf{k}_{\text{in}}, \mu}^{\dagger}(0) \right\} | \Omega \rangle}{\omega' - \Delta E_{\alpha} + i\eta} \right. \\ \left. - i e^{-i(\omega' + \Delta E_{\alpha} - i\eta)T} \langle \alpha | \hat{u}_A | \Omega \rangle \frac{\langle \Omega | \mathcal{T} \left\{ \hat{J}_{\mathbf{k}_{\text{out}}, \nu}(t) \hat{J}_{\mathbf{k}_{\text{in}}, \mu}^{\dagger}(0) \right\} | \alpha \rangle}{\omega' + \Delta E_{\alpha} - i\eta} \right\} \quad (6.8) \\ + \text{terms regular in } \omega'. \end{aligned}$$

We see that the Fourier transform of $S_A(t', t; \Phi)$ with respect to t' has poles at the excitation energies ΔE_{α} of the full matter Hamiltonian, whose residues are proportional to the matrix elements needed for Raman scattering. The latter can therefore be extracted by taking the appropriate limit:

$$\langle \alpha | \mathcal{T} \left\{ \hat{J}_{\mathbf{k}_{\text{out}}, \nu}(t) \hat{J}_{\mathbf{k}_{\text{in}}, \mu}^{\dagger}(0) \right\} | \Omega \rangle = \frac{-i}{\langle \Omega | \hat{u}_A | \alpha \rangle} \lim_{\omega' \rightarrow \Delta E_{\alpha} - i\eta} \left\{ (\omega' - \Delta E_{\alpha} + i\eta) \tilde{S}_A(\omega'; t; \Phi) \right\}. \quad (6.9)$$

By dividing by $\langle \Omega | \hat{u}_A | \alpha \rangle$ we implicitly assumed that this matrix element is non-vanishing, which is reasonable as we are only interested in those states $|\alpha\rangle$ that have a large one-phonon component, i.e., for which this matrix element is precisely sizably different from zero.

The fact that correlation functions have poles at exact excitation energies of the fully interacting system whose residues correspond to matrix elements for scattering processes has first been pointed out by H. Lehmann, K. Symanzik, and W. Zimmermann in their classic 1955 paper [80]. In the same paper, they also first derived the type of formula shown in Eq. 6.9, which relates a scattering matrix element to the residue of a pole in a many-particle correlation function. This formula is hence nowadays known as the *LSZ reduction formula* and is widely applied in particle physics [83, 88, 115], yet does not seem to be all too well-known in the context of condensed matter physics. For the purpose of formulating a correlation function-based theory of Raman scattering it is of great use, however.

After applying the LSZ reduction formula, the fully Fourier-transformed Raman

scattering matrix element reads:

$$\tilde{J}^\alpha(\omega; \Phi) \equiv \tilde{J}_{\nu, \mu}^{\alpha, \mathbf{k}_{\text{out}}, \mathbf{k}_{\text{in}}}(\omega) = \frac{-i}{\langle \Omega | \hat{u}_A | \alpha \rangle} \lim_{\omega' \rightarrow \Delta E_\alpha - i\eta} \left\{ (\omega' - \Delta E_\alpha + i\eta) \tilde{S}_A(\omega'; \omega; \Phi) \right\}, \quad (6.10)$$

where the fully Fourier-transformed correlation function is given by

$$\tilde{S}_A(\omega'; \omega; \Phi) \equiv \int_{-\infty}^{+\infty} dt e^{i\omega t} \int_{-\infty}^{+\infty} dt' e^{i\omega' t'} \langle \Omega | \mathcal{T} \left\{ \hat{u}_A(t') \hat{J}_{\mathbf{k}_{\text{out}}, \nu}(t) \hat{J}_{\mathbf{k}_{\text{in}}, \mu}^\dagger(0) \right\} | \Omega \rangle. \quad (6.11)$$

We have thus managed to reduce the calculation of the Raman scattering matrix element to the computation of a correlation function involving two current densities and a nuclei displacement. This is perfectly reasonable on conceptual grounds, as it links the probability amplitude for lattice vibration-induced inelastic light scattering to the correlation between two currents – one light-induced, one light-emitting – and the displacement of an atom. Mathematically, we note that the current density operators can be expressed in terms of electron field operators and nuclei displacement and momentum operators. Hence we have reduced the task of computing the one-phonon-induced Raman scattering matrix element to the task of computing a time-ordered correlation function of electron field and nuclei displacement operators. The latter can be calculated, for example, within perturbation theory. Before we discuss this perturbative calculation in more detail, however, we will first simplify our expression for the scattering matrix element and the scattering rate a bit further.

As will become clear from the diagrammatic representation of the perturbation series for $S_A(t', t; \Phi)$ presented in the next section, the “endpoint” of the diagram labeled by the displacement operator coordinates (A, t') is connected to the rest of the diagram by an exact one-phonon Green’s function, i.e., the exact correlation function has the general form

$$S_A(t', t; \Phi) = \sum_B \int_{-\infty}^{+\infty} dt'' i\mathcal{D}_{A,B}(t', t'') \mathcal{M}_B(t'', t; \Phi), \quad (6.12)$$

which defines the *reduced matrix element* $\mathcal{M}_B(t'', t; \Phi)$. Note that this definition is very

much reminiscent of our definition of the screened electron-phonon matrix element in Section 5.2. In fact, we could equally well have derived the screened electron-phonon coupling from an LSZ reduction formula-based approach.

Due to time-translation invariance, the exact one-phonon Green's function can only depend on the time difference $t' - t''$ and the time integral in Eq. 6.12 is actually a convolution in the time domain. In Fourier space, it thus becomes a simple product of Fourier transforms:

$$\tilde{S}_A(\omega'; \omega; \Phi) = \sum_B i\tilde{\mathcal{D}}_{A,B}(\omega')\tilde{\mathcal{M}}_B(\omega'; \omega; \Phi), \quad (6.13)$$

where

$$\tilde{\mathcal{M}}_B(\omega'; \omega; \Phi) \equiv \int_{-\infty}^{+\infty} dt e^{i\omega t} \int_{-\infty}^{+\infty} dt' e^{i\omega' t'} \mathcal{M}_B(t', t; \Phi) \quad (6.14)$$

is the fully Fourier-transformed reduced matrix element. Note that in a practical, diagrammatic calculation, it can be obtained from the diagrammatic expansion of \tilde{S}_A by simply omitting the factor associated with the one-phonon Green's function that ends in the point (the atom) labeled by A .³ Since the Fourier-transformed one-phonon Green's function has the Lehmann decomposition (compare Eq. 5.61)

$$\tilde{\mathcal{D}}_{A,B}(\omega') = \sum_{\beta} \left\{ \frac{\langle \Omega | \hat{u}_A | \beta \rangle \langle \beta | \hat{u}_B^\dagger | \Omega \rangle}{\omega' - \Delta E_{\beta} + i\eta} - \frac{\langle \Omega | \hat{u}_B^\dagger | \beta \rangle \langle \beta | \hat{u}_A | \Omega \rangle}{\omega' + \Delta E_{\beta} - i\eta} \right\}, \quad (6.15)$$

we can easily perform the limit operation of Eq. 6.10 by making use of the factorization of \tilde{S}_A given in Eq. 6.13. One then finds in the $\eta \rightarrow 0$ limit:

$$\tilde{J}^{\alpha}(\omega; \Phi) = \sum_B \langle \alpha | \hat{u}_B^\dagger | \Omega \rangle \tilde{\mathcal{M}}_B(\omega'; \omega; \Phi) \Big|_{\omega' = \Delta E_{\alpha}}. \quad (6.16)$$

Besides being very compact, this expression for the Raman scattering matrix element has an accessible physical interpretation: the reduced matrix element $\tilde{\mathcal{M}}_B = \tilde{\mathcal{M}}_{m,\beta,j}$ is the amplitude for generating a displacement of the atom (m, β) in direction j with the

³The omission of one of the “legs” of a diagram is also known as *amputating a diagram* in the particle physics literature [88] and the resulting diagram, drawn without the leg, is known as an *amputated diagram*.

Raman process, while the matrix element $\langle \alpha | \hat{u}_{m,\beta,j}^\dagger | \Omega \rangle$ gives the probability amplitude for this displacement to mediate a transition between the ground state $|\Omega\rangle$ and the excited state $|\alpha\rangle$ of $\hat{\mathcal{H}}_M$. This is what we mean when we call this process “phonon-induced Raman scattering”.

Finally, we return to our expression for the Raman scattering *rate*, derived over the course of Chapter 2 (compare Eq. 2.50):

$$\dot{P}_{\text{inel.}} = \sum_{\alpha} \Gamma_{\text{kin.}}(\omega_L, \omega_D) \left| \tilde{J}^{\alpha}(\omega_D; \Phi) \right|^2 \times 2\pi \delta(\omega_L - \omega_D - \Delta E_{\alpha}), \quad (6.17)$$

where we introduced the abbreviation

$$\Gamma_{\text{kin.}}(\omega_L, \omega_D) \equiv \frac{\omega_L \omega_D \Delta \Omega_L \Delta \omega_L \Delta \Omega_D \Delta \omega_D}{(2\pi)^4 c^6}. \quad (6.18)$$

for the product of kinematic prefactors and used the defining property of the δ -function to replace the frequency argument of \tilde{J}^{α} by the detector frequency ω_D , i.e., the frequency of the outgoing light for which the scattering rate should be calculated. Inserting the factorized expression for the scattering matrix element, the one-phonon-induced scattering rate reads:

$$\begin{aligned} \dot{P}_{\text{inel.};1\text{-ph}} &= \Gamma_{\text{kin.}}(\omega_L, \omega_D) \sum_{A,B} \tilde{\mathcal{M}}_A^*(\omega_L - \omega_D; \omega_D; \Phi) \tilde{\mathcal{M}}_B(\omega_L - \omega_D; \omega_D; \Phi) \\ &\times 2\pi \sum_{\alpha} \langle \Omega | \hat{u}_A | \alpha \rangle \langle \alpha | \hat{u}_B^\dagger | \Omega \rangle \delta(\omega_L - \omega_D - \Delta E_{\alpha}). \end{aligned} \quad (6.19)$$

We can write this in an even more illuminating way by inserting the mode expansion of the displacement operators, $\hat{u}_A = \sum_{\mathbf{q},\lambda} \xi_{\mathbf{q},\lambda}^A \hat{B}_{\mathbf{q},\lambda}$ and identifying the phonon spectral function $\mathcal{A}_{\mathbf{q},\lambda,\lambda'}(\omega)$:

$$\begin{aligned} \dot{P}_{\text{inel.};1\text{-ph}} &= \Gamma_{\text{kin.}}(\omega_L, \omega_D) \sum_{\mathbf{q},\lambda,\lambda'} \tilde{\mathcal{M}}_{\mathbf{q},\lambda}^*(\omega_L - \omega_D; \omega_D; \Phi) \\ &\times 2\pi \mathcal{A}_{\mathbf{q},\lambda,\lambda'}(\omega_L - \omega_D) \tilde{\mathcal{M}}_{\mathbf{q},\lambda'}(\omega_L - \omega_D; \omega_D; \Phi). \end{aligned} \quad (6.20)$$

Here, we defined the spatially Fourier-transformed and projected version of the reduced

matrix element as

$$\begin{aligned}
\tilde{\mathcal{M}}_{\mathbf{q},\lambda}(\omega';\omega;\Phi) &\equiv \sum_A \xi_{\mathbf{q},\lambda}^{A;*} \tilde{\mathcal{M}}_A(\omega;\omega';\Phi) \\
&= \sum_n \frac{1}{\sqrt{N}} e^{-i\mathbf{q}\cdot\mathbf{R}_n} \sum_{\alpha,i} \sqrt{\frac{1}{2M_\alpha\omega_{\mathbf{q},\lambda}}} v_{\mathbf{q},\lambda}^{\alpha,i;*} \tilde{\mathcal{M}}_{n,\alpha,i}(\omega;\omega';\Phi).
\end{aligned} \tag{6.21}$$

In Eq. 6.20, all different unperturbed phonon branches are still, in principle, coupled. In many systems, however, the spectral function can be approximated by its diagonal elements only, since the mixing of the unperturbed eigenvectors in the Green's function is mediated by non-adiabatic or anharmonic effects only. These either are very much negligible, or, in a first approximation, can be taken to modify the phonon frequencies only. Furthermore, even in systems in which non-adiabatic effects are relevant, such as in graphene, the mixing of the eigenmodes is often irrelevant for the one-phonon Raman spectrum. This is due to the fact that, as we will see in the next section, the only wave vector \mathbf{q} that gives a sizable contribution to the one-phonon Raman scattering rate is $\mathbf{q} = 0$, a high-symmetry point in the first Brillouin zone, at which mixing of the phonon modes is usually symmetry-prohibited.

Approximating the spectral function by its diagonal elements $\mathcal{A}_{\mathbf{q},\lambda,\lambda}(\omega)$ only, the expression for the Raman scattering rate takes on the form of the ordinary version of Fermi's golden rule:

$$\dot{P}_{\text{inel};1\text{-ph}} \approx \Gamma_{\text{kin.}}(\omega_L, \omega_D) \sum_{\mathbf{q},\lambda} \left| \tilde{\mathcal{M}}_{\mathbf{q},\lambda}(\omega_L - \omega_D; \omega_D; \Phi) \right|^2 \times 2\pi \mathcal{A}_{\mathbf{q},\lambda,\lambda}(\omega_L - \omega_D). \tag{6.22}$$

Note that from the definition of the spectral function, it follows that its diagonal elements are real and positive and furthermore vanish for negative ω . We can then make use of Eq. 5.65, which links the one-phonon Green's function to its spectral function, to obtain the spectral function from the negative imaginary part of the time-ordered

Green's function:

$$\begin{aligned}\mathcal{A}_{\mathbf{q},\lambda,\lambda}(\omega) &= -\frac{1}{\pi}\text{Im}\tilde{\mathcal{D}}_{\mathbf{q},\lambda,\lambda}(\omega) \\ &= \frac{1}{\pi}\frac{-\text{Im}\tilde{\Pi}_{\mathbf{q},\lambda,\lambda}(\omega)}{\left((2\omega_{\mathbf{q},\lambda})^{-1}(\omega^2 - \omega_{\mathbf{q},\lambda}^2) - \text{Re}\tilde{\Pi}_{\mathbf{q},\lambda,\lambda}(\omega)\right)^2 + \left(\text{Im}\tilde{\Pi}_{\mathbf{q},\lambda,\lambda}(\omega)\right)^2},\end{aligned}\quad (6.23)$$

where we made use of Dyson's equation to establish a link between the spectral function and the phonon self-energy. For frequencies $\omega = \omega_{\text{L}} - \omega_{\text{D}}$ close to the unperturbed phonon frequencies $\omega_{\mathbf{q},\lambda}$, the expression in the numerator and denominator can be approximated by the first non-trivial terms of their Taylor series. This corresponds to the *quasi-particle approximation (QPA)*, which we have already introduced in Section 3.3.1 in the context of the one-electron Green's function. In the QPA, the spectral function is approximated by

$$\mathcal{A}_{\mathbf{q},\lambda,\lambda}(\omega) \stackrel{\text{QPA}}{\approx} \frac{Z_{\mathbf{q},\lambda}^{(\text{QP})}}{\pi} \frac{\gamma_{\mathbf{q},\lambda}^{(\text{QP})}/2}{\left(\omega - \omega_{\mathbf{q},\lambda}^{(\text{QP})}\right)^2 + \left(\gamma_{\mathbf{q},\lambda}^{(\text{QP})}/2\right)^2}, \quad (6.24)$$

where the phonon *quasi-particle weight*, *frequency*, and *decay width* are defined by

$$Z_{\mathbf{q},\lambda}^{(\text{QP})} \equiv 1 \left/ \left(1 - \left. \frac{\partial \tilde{\Pi}_{\mathbf{q},\lambda,\lambda}(\omega)}{\partial \omega} \right|_{\omega=\omega_{\mathbf{q},\lambda}} \right) \right. \quad (6.25)$$

$$\omega_{\mathbf{q},\lambda}^{(\text{QP})} \equiv \omega_{\mathbf{q},\lambda} + \text{Re} \left(Z_{\mathbf{q},\lambda}^{(\text{QP})} \tilde{\Pi}_{\mathbf{q},\lambda,\lambda}(\omega) \Big|_{\omega=\omega_{\mathbf{q},\lambda}} \right) \quad (6.26)$$

$$\gamma_{\mathbf{q},\lambda}^{(\text{QP})} \equiv -2 \text{Im} \left(Z_{\mathbf{q},\lambda}^{(\text{QP})} \tilde{\Pi}_{\mathbf{q},\lambda,\lambda}(\omega) \Big|_{\omega=\omega_{\mathbf{q},\lambda}} \right). \quad (6.27)$$

We thus see that according to Eq. 6.22 and within the quasi-particle approximation, the one-phonon Raman spectrum is given by the sum of single Lorentzian peaks centered on the quasi-phonon frequencies, whose full width at half maximum (FWHM) is given by the quasi-phonon decay width. The height of one of the Lorentzian Raman peaks, which corresponds to the recorded intensity in experiment, is proportional to the product of the kinetic factor Γ_{kin} and the square of the reduced matrix element $\tilde{\mathcal{M}}$, which are

the only two factors that depend on the frequency of the incident light, ω_L , and on the frequency ω_D , at which the Raman spectrum is probed. The only non-trivial task remaining is then the calculation of the reduced matrix element, which will be discussed over the course of the remainder of this section.

6.1.2 Reduced scattering matrix element

In order to calculate the reduced Raman scattering matrix element $\tilde{\mathcal{M}}_{\mathbf{q},\lambda}(\omega'; \omega; \Phi)$, we can trace its definition all the way back to the Fourier transform of the current-current-nuclei displacement correlation function $S_A(t, t'; \Phi)$. Explicitly, the latter is given by

$$S_A(t, t'; \mathbf{k}_{\text{out}}, \nu; \mathbf{k}_{\text{in}}, \mu) = \int d^3r_1 e^{-i\mathbf{k}_{\text{out}} \cdot \mathbf{r}_1} \int d^3r_2 e^{+i\mathbf{k}_{\text{in}} \cdot \mathbf{r}_2} \sum_i (\epsilon_{\mathbf{k}_{\text{out}}, \nu}^i)^* \sum_j \epsilon_{\mathbf{k}_{\text{in}}, \mu}^j \quad (6.28)$$

$$\times \langle \Omega | \mathcal{T} \left\{ \hat{u}_A(t') \hat{J}_i(\mathbf{r}_1, t) \hat{J}_j(\mathbf{r}_2, 0) \right\} | \Omega \rangle.$$

We can reduce this expression to a more familiar-looking correlation function by expressing the current density operator, defined in Eq. 2.17, in terms of electron field operators and nuclear displacement and momentum operators:

$$\hat{\mathbf{J}}(\mathbf{r}) = \frac{-e}{m} \hat{\psi}^\dagger(\mathbf{r}) (-i\nabla) \hat{\psi}(\mathbf{r}) + \sum_{n,\alpha} \frac{Z_\alpha e}{M_\alpha} \delta^{(3)}(\mathbf{r} - \mathbf{R}_n - \boldsymbol{\tau}_\alpha - \hat{\mathbf{u}}_{n,\alpha}) \hat{\mathbf{P}}_{n,\alpha}. \quad (6.29)$$

Under the assumption that the matrix elements of the nuclei operators in this expression are at most on the same order of magnitude than the matrix elements of the operators in the first term, the second term will be relatively smaller by a factor of $m/M_\alpha \ll 1$. Therefore, we choose to neglect the nuclei contribution to the total current density and take the current density operator to be given in terms of electron fields only. The

needed correlation function then reads:

$$\begin{aligned}
S_A(t, t'; \mathbf{k}_{\text{out}}, \nu; \mathbf{k}_{\text{in}}, \mu) &= \int d^3 r_1 e^{-i\mathbf{k}_{\text{out}} \cdot \mathbf{r}_1} \int d^3 r_2 e^{+i\mathbf{k}_{\text{in}} \cdot \mathbf{r}_2} \sum_i (\epsilon_{\mathbf{k}_{\text{out}}, \nu}^i)^* \sum_j \epsilon_{\mathbf{k}_{\text{in}}, \mu}^j \\
&\times \frac{e^2}{m^2} \lim_{\mathbf{r}'_1 \rightarrow \mathbf{r}_1} (-i) \frac{\partial}{\partial r'_{1,i}} \lim_{\mathbf{r}'_2 \rightarrow \mathbf{r}_2} (-i) \frac{\partial}{\partial r'_{2,j}} \\
&\times \langle \Omega | \mathcal{T} \left\{ \hat{u}_A(t') \hat{\psi}^\dagger(\mathbf{r}_1, t) \hat{\psi}(\mathbf{r}'_1, t) \hat{\psi}^\dagger(\mathbf{r}_2, 0) \hat{\psi}(\mathbf{r}'_2, 0) \right\} | \Omega \rangle,
\end{aligned} \tag{6.30}$$

where we introduced two limiting operations in order to be able to pull the derivative operators out of the actual correlation function.

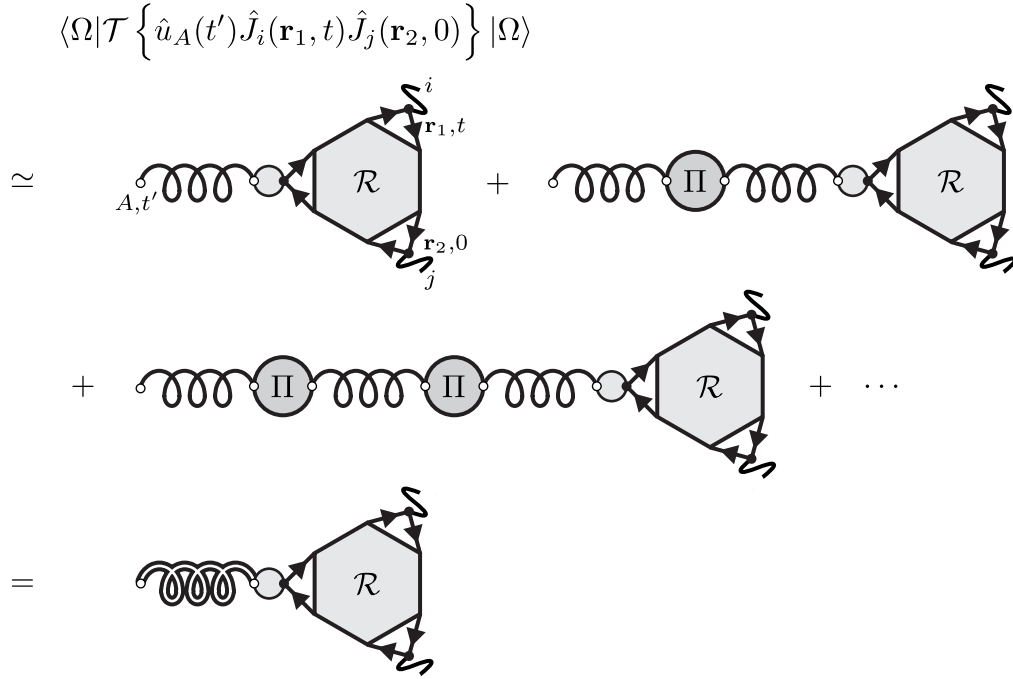


Figure 6.1: **Leading-order expansion of the correlation function needed for Raman scattering.** Wavy lines represent the derivative and limit operations, originally stemming from the electron-light coupling. The hexagon, labeled by \mathcal{R} , denotes the three-particle electronic correlation function as defined in the text.

To leading order in the electron-phonon coupling, the correlation function has the diagrammatic expansion shown in Fig. 6.1. We can sum the “phonon leg” of the diagram exactly, using Dyson’s equation. Mathematically, the leading-order, diagrammatic

expansion corresponds to the factorization approximation

$$\begin{aligned}
& \langle \Omega | \mathcal{T} \left\{ \hat{u}_A(t') \hat{\psi}^\dagger(\mathbf{r}_1, t) \hat{\psi}(\mathbf{r}'_1, t) \hat{\psi}^\dagger(\mathbf{r}_2, 0) \hat{\psi}(\mathbf{r}'_2, 0) \right\} | \Omega \rangle \\
& \simeq \int_{-\infty}^{+\infty} dt'' \int d^3 r_3 (-i) g_A^{(b)}(\mathbf{r}_3) \langle \Omega | \mathcal{T} \left\{ \hat{u}_A(t') \hat{u}_B^\dagger(t'') \right\} | \Omega \rangle \\
& \times \langle \Omega | \mathcal{T} \left\{ \hat{\psi}^\dagger(\mathbf{r}_3, t'') \hat{\psi}(\mathbf{r}_3, t'') \hat{\psi}^\dagger(\mathbf{r}_1, t) \hat{\psi}(\mathbf{r}'_1, t) \hat{\psi}^\dagger(\mathbf{r}_2, 0) \hat{\psi}(\mathbf{r}'_2, 0) \right\} | \Omega \rangle_{\text{con.}},
\end{aligned} \tag{6.31}$$

where the subscript “con.” again refers to the fully connected part of the correlation function as represented by Feynman diagrams. As mentioned in the previous section, it has the algebraic structure $\sum_B \int dt'' i \mathcal{D}_{A,B}(t', t'') \times \mathcal{M}_B(t'', t)$. Defining the three-particle correlation function as

$$\mathcal{R}(1, 1'; 2, 2'; 3, 3') \equiv (-i)^3 \langle \Omega | \mathcal{T} \left\{ \hat{\psi}^\dagger(1) \hat{\psi}(1') \hat{\psi}^\dagger(2) \hat{\psi}(2') \hat{\psi}^\dagger(3) \hat{\psi}(3') \right\} | \Omega \rangle_{\text{con.}}, \tag{6.32}$$

we can identify the reduced matrix element \mathcal{M} , whose fully Fourier-transformed version reads:

$$\begin{aligned}
& \tilde{\mathcal{M}}_{\mathbf{q}, \lambda}(\omega'; \omega; (\mathbf{k}_{\text{out}}, \nu); (\mathbf{k}_{\text{in}}, \mu)) \\
& = (-1) \sum_n \frac{1}{\sqrt{N}} e^{-i\mathbf{q} \cdot \mathbf{R}_n} \int d^3 r_1 e^{-i\mathbf{k}_{\text{out}} \cdot \mathbf{r}_1} \int d^3 r_2 e^{+i\mathbf{k}_{\text{in}} \cdot \mathbf{r}_2} \\
& \times \sum_{\alpha, k} \sqrt{\frac{1}{2M_\alpha \omega_{\mathbf{q}, \lambda}}} v_{\mathbf{q}, \lambda}^{\alpha, k; *} \sum_i (\epsilon_{\mathbf{k}_{\text{out}}, \nu}^i)^* \sum_j \epsilon_{\mathbf{k}_{\text{in}}, \mu}^j \\
& \times \lim_{\mathbf{r}'_1 \rightarrow \mathbf{r}_1} \frac{-e}{m} (-i) \frac{\partial}{\partial r'_{1,i}} \lim_{\mathbf{r}'_2 \rightarrow \mathbf{r}_2} \frac{-e}{m} (-i) \frac{\partial}{\partial r'_{2,j}} \int d^3 r_3 g_{n, \alpha, k}^{(b)}(\mathbf{r}_3) \\
& \times \int_{-\infty}^{+\infty} dt e^{i\omega t} \int_{-\infty}^{+\infty} dt' e^{i\omega' t'} \mathcal{R}((\mathbf{r}_3, t^+), (\mathbf{r}_3, t'); (\mathbf{r}_1, t^+), (\mathbf{r}'_1, t); (\mathbf{r}_2, 0^+), (\mathbf{r}'_2, 0)).
\end{aligned} \tag{6.33}$$

This formula for the reduced matrix element in Fourier space has a very simple and intuitive algebraic structure: The first line contains the spatial and lattice Fourier transforms, while the second line constitutes a projection on the polarization and eigenvectors of the final state (quasi-)particles, two photons and one phonon. The third line corresponds to the bare coupling of the three (quasi-)particles to the electronic system.

Finally, the last line contains the correlation of the electronic system that mediates the Raman process, described by the Fourier-transformed three-particle correlation function. In the language of condensed matter physics, it describes both excitonic effects, i.e., possible intermediate states of bound electron-hole pairs (*excitons*), and the screening of the electron-phonon interaction. Note that both effects can mathematically be described in the same way and hence, for the purpose of deriving a concrete expression for the reduced Raman matrix element, we will not distinguish between these two concepts for the time being.

To find a concrete expression for the reduced matrix element, we expand the three-

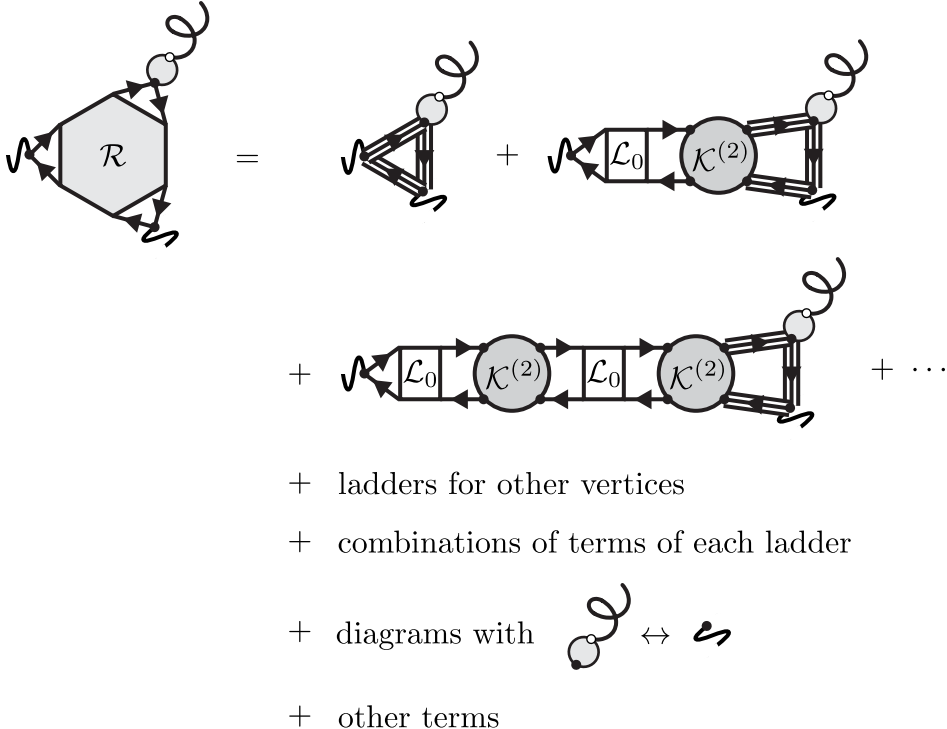


Figure 6.2: **Diagrammatic approximation for the reduced matrix element for one-phonon-induced Raman scattering.**

particle correlation function in a perturbation series. In terms of Feynman diagrams, we obtain the expansion shown in Fig. 6.2. The leading-order term simply consists of the bare electron-light and electron-phonon couplings and the independent-particle

three-particle correlation function:

$$\mathcal{R}_0(1, 1'; 2, 2'; 3, 3') \equiv - [\mathcal{G}(1, 2')\mathcal{G}(2, 3')\mathcal{G}(3, 1') + \mathcal{G}(1, 3')\mathcal{G}(3, 2')\mathcal{G}(2, 1')], \quad (6.34)$$

where the minus sign arises due to the anti-commuting nature of the electron field operators or, equivalently, due to the presence of a closed fermion loop. Note that these two terms are the only independent-particle-like contributions that yield fully connected diagrams when $(1, 2, 3) \rightarrow (1', 2', 3')$. Also note that the only difference between the diagrams for \mathcal{M} representing the two terms in \mathcal{R}_0 is the exchange of an electron-light vertex and an electron-phonon vertex. This is equivalent to changing the orientation of the arrows of the independent-particle Green's function in the fermion loop and leaving the order of the vertices unchanged. In Fig. 6.2, we chose to only show one of the two terms for each possible diagram and include all diagrams involving the other one in the fifth line under “diagrams with $\dots \leftrightarrow \dots$ ”.

The next-to-leading-order terms involve the two-particle-irreducible interaction kernel $\mathcal{K}^{(2)}$ and an independent-particle two-particle correlation function \mathcal{L}_0 . This diagrammatic piece can be inserted separately for each of the three vertices. In the next-to-next-to-leading-order, a second factor of $\mathcal{K}^{(2)}\mathcal{L}_0$ appears, which can be attached either to the same vertex, as shown in the second line, or to a different vertex, as indicated in the fourth line. This procedure is then continued for each vertex or “leg” of the diagram, leading to a sum of terms for each leg that has the form of a ladder with increasingly more rungs. This kind of diagrammatic structure has been discussed already in the context of the screened electron-phonon coupling in Section 5.2, where we showed how a closed expression in the approximation of a static two-particle interaction kernel can be obtained. For the electron-light coupling, we can similarly define a “screened” version, which in this case, however, is more appropriately interpreted as including the effects of bound electron-hole pairs. Diagrammatically, we define it by the series of diagrams shown in Fig. 6.3. Mathematically, we first introduce the bare electron-light coupling as

$$d_i^{(b)}(\mathbf{r}_1) \equiv \frac{-e}{m} \left(-i \frac{\partial}{\partial r_{1,i}} \right), \quad (6.35)$$

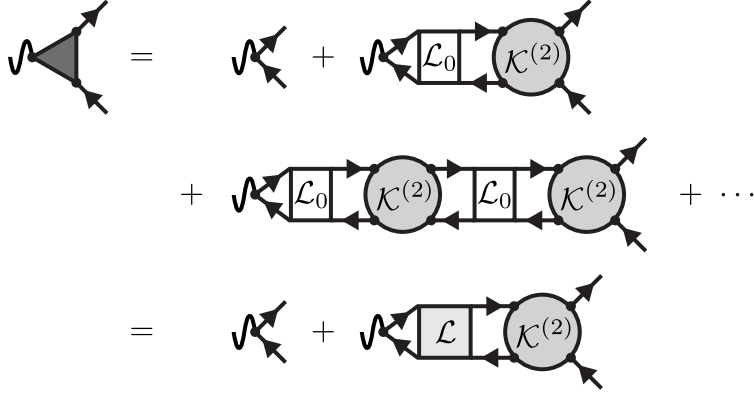


Figure 6.3: **Diagrammatic representation of corrections to the electron-light coupling matrix element that capture excitonic effects.**

with the understanding that the derivative acts on the left-most space-time coordinate of one of the connecting one-electron Green’s functions. This then allows us to compute the “screened” electron-light coupling from

$$d_i(1, 2; 3) = \delta(1, 2)\delta(1, 3)d_i^{(b)}(\mathbf{r}_1) + \mathcal{K}^{(2)}(1, 2; \bar{4}, \bar{5})\mathcal{L}(\bar{4}, \bar{5}; 3^+, 3)d_i^{(b)}(\mathbf{r}_3). \quad (6.36)$$

For later use, we also define the KS matrix elements of the *bare electron-photon coupling*, which we, in turn, define as the electron-light coupling, Fourier-transformed with respect to the last coordinate and projected on the photon polarization vector:

$$\begin{aligned} d_{\mathbf{k}', \mathbf{k}}^{(b); (\mathbf{k}_{\text{in}}, \mu)}_{a, b} &\equiv \frac{-e}{m} \boldsymbol{\epsilon}_{\mathbf{k}_{\text{in}}, \mu} \cdot \int d^3r e^{i\mathbf{k}_{\text{in}} \cdot \mathbf{r}} \phi_{\mathbf{k}', a}^*(\mathbf{r}) (-i\nabla) \phi_{\mathbf{k}, b}(\mathbf{r}). \\ &= \delta_{\mathbf{k}_{\text{in}}^{(\text{BZ})} + \mathbf{k}, \mathbf{k}'} \frac{(-e)}{m} \boldsymbol{\epsilon}_{\mathbf{k}_{\text{in}}, \mu} \cdot \int_{\text{u.c.}} d^3r e^{i(\mathbf{k}_{\text{in}} + \mathbf{k} - \mathbf{k}') \cdot \mathbf{r}} \chi_{\mathbf{k}', a}^*(\mathbf{r}) (\mathbf{k} - i\nabla) \chi_{\mathbf{k}, b}(\mathbf{r}), \end{aligned} \quad (6.37)$$

where we exploited the invariance of the lattice periodic part of the KS wave function, $\chi_{\mathbf{k}, a}(\mathbf{r})$, to extract a crystal momentum-conserving Kronecker- δ and to limit the integration to one unit cell only. $\mathbf{k}_{\text{in}}^{(\text{BZ})}$ is the part of the light wave vector \mathbf{k}_{in} which falls into the first Brillouin zone.⁴ Within the approximations for the BSE that we used during

⁴Note that any wave vector \mathbf{q} can always uniquely be decomposed as $\mathbf{q} = \mathbf{q}^{(\text{BZ})} + \mathbf{G}_{\mathbf{q}}$, with $\mathbf{q}^{(\text{BZ})}$ lying in the first Brillouin zone and $\mathbf{G}_{\mathbf{q}}$ being a reciprocal lattice vector.

the last two chapters, i.e., $\mathcal{K}^{(2)} \rightarrow K^{(2)}$ and a static kernel, the KS matrix elements of the “screened” *electron-photon coupling* are then given in closed form by

$$\tilde{d}_{\mathbf{k}+\mathbf{k}_{\text{in}},\mathbf{k}}^{(\mathbf{k}_{\text{in}},\mu)}(\omega) = d_{\mathbf{k}+\mathbf{k}_{\text{in}},\mathbf{k}}^{(\mathbf{k}_{\text{in}},\mu)} + \sum_{S,S'} \frac{\Xi_{\mathbf{k}+\mathbf{k}_{\text{in}},\mathbf{k}}^S N_{S,S'}^{-1} d_{\mathbf{k}_{\text{in}},S'}^{(\mathbf{k}_{\text{in}},\mu)}}{\omega - \varepsilon_S + i\eta}. \quad (6.38)$$

Here, the exciton-independent-particle coupling $\Xi_{\mathbf{k}+\mathbf{k}_{\text{in}},\mathbf{k}}^S$ has previously been defined in Eq. 5.51 and we introduced the (bare) *bilinear exciton-photon coupling* via

$$d_{\mathbf{k}_{\text{in}},S}^{(\mathbf{k}_{\text{in}},\mu)} \equiv \sum_{\mathbf{k},a,b} A_{\mathbf{k}+\mathbf{k}_{\text{in}},a}^{S,*} d_{\mathbf{k}+\mathbf{k}_{\text{in}},\mathbf{k}}^{(\mathbf{k}_{\text{in}},\mu)}. \quad (6.39)$$

Together with Eq. 5.54, this expression allows the computation of the reduced Raman matrix element in the approximation that only the ladder-like structures on the legs are retained. The terms in the diagrammatic expansion that are omitted in this approximation involve the three-particle-irreducible interaction kernel $K^{(3)}(1, 2; 3, 4; 5, 6)$, which is given by the sum of all diagrams that cannot be split into two by cutting three pairs of electron lines. While it can be shown diagrammatically that the two-particle interaction kernel is related to the Coulombic part of the one-particle self-energy via $K^{(2)}(1, 2; 3, 4) = \delta\Sigma_{\text{Coul.}}(1, 2)/\delta G(3, 4)$ (see, for example, Ref. 91), this proof can be generalized to the three-particle interaction kernel to show that $K^{(3)}(1, 2; 3, 4; 5, 6) = \delta^2\Sigma_{\text{Coul.}}(1, 2)/(\delta G(3, 4)\delta G(5, 6))$. In the approximation for the two-particle interaction kernel that we have been using throughout this thesis, i.e., $K^{(2)} \sim iW - iv$, with $\delta W(1, 2)/\delta G(3, 4) \approx 0$, we need to set $K^{(3)}(1, 2; 3, 4; 5, 6) = \delta K^{(2)}(1, 2; 3, 4)/\delta G(5, 6) \approx 0$ for consistency. In this ladder-like approximation then, the reduced matrix element can be represented diagrammatically as shown in Fig. 6.4. It should be pointed out that a complete expression for the three-particle correlation function has also been derived independently by Saunders and Young using functional methods [141]. However, the approach presented here allows the derivation of concrete expressions for the computation of Raman scattering rates including excitonic effects and using modern and general *ab initio* computational methods, while the cited work confined itself to a discussion of a rough analytical model for the independent-particle case.

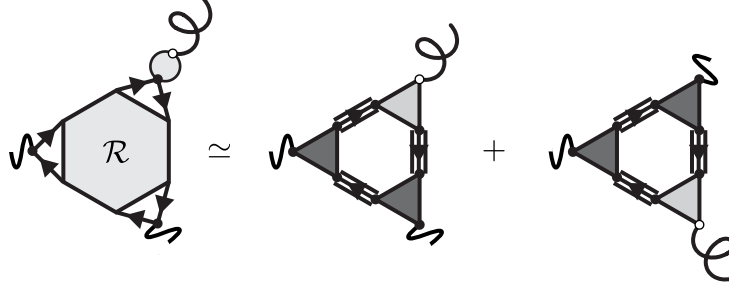


Figure 6.4: **Partially summed diagrammatic expression for the reduced matrix element for one-phonon-induced Raman scattering.**

Explicitly, the reduced Raman matrix element in our suggested ladder-like approximation reads:

$$\begin{aligned}
& \tilde{\mathcal{M}}_{\mathbf{q},\lambda}(\omega'; \omega; (\mathbf{k}_{\text{out}}, \nu); (\mathbf{k}_{\text{in}}, \mu)) \\
& \simeq \left[\int_{-\infty}^{+\infty} dt e^{i\omega t} \int d^3r e^{i\mathbf{k}_{\text{in}} \cdot \mathbf{r}} \sum_i \boldsymbol{\epsilon}_{\mathbf{k}_{\text{in}},\mu}^i d_i(\bar{1}, \bar{2}; (\mathbf{r}, t)) \right] \\
& \times \left[\int d^3r' e^{-i\mathbf{k}_{\text{out}} \cdot \mathbf{r}'} \sum_j \boldsymbol{\epsilon}_{\mathbf{k}_{\text{out}},\nu}^{j;*} d_j(\bar{3}, \bar{4}; (\mathbf{r}', 0)) \right] \\
& \times \left[\int_{-\infty}^{+\infty} dt' e^{i\omega' t'} \sum_n \frac{1}{\sqrt{N}} e^{-i\mathbf{q} \cdot \mathbf{R}_n} \sum_{\alpha,k} v_{\mathbf{q},\lambda}^{\alpha,k;*} g_{n,\alpha,k}(\bar{5}, \bar{6}; t') \right] \\
& \times \mathcal{R}_0(\bar{1}, \bar{6}; \bar{3}, \bar{2}; \bar{5}, \bar{4}).
\end{aligned} \tag{6.40}$$

To turn this expression into one that is more useful for computational purposes, we express it in the KS basis. For this, we need the Fourier transform of the independent-particle three-particle correlation function:

$$\tilde{\mathcal{R}}_0(\omega_1; \omega_2; \omega_3)_{\substack{\mathbf{k}_1;a,b \\ \mathbf{k}_2;c,d \\ \mathbf{k}_3;e,f}} \equiv \tilde{\mathcal{G}}(\omega_1)_{\mathbf{k}_1,a,b} \tilde{\mathcal{G}}(\omega_2)_{\mathbf{k}_2,c,d} \tilde{\mathcal{G}}(\omega_3)_{\mathbf{k}_3,e,f}. \tag{6.41}$$

We will also employ the so-called *dipole approximation* for the electron-photon matrix elements. For the typical case of visible light, with wave lengths much larger than the dimensions of the unit cell, $|\mathbf{k}_{\text{in}}|$ and $|\mathbf{k}_{\text{out}}|$ are much smaller than the typical exten-

sion of the first Brillouin zone. For the purpose of evaluating the electron-light matrix elements given in Eq. 6.37, we can then let $\mathbf{k}_{\text{in}} \rightarrow \mathbf{0}$, when the reduced matrix element ceases to explicitly depend on \mathbf{k}_{in} and \mathbf{k}_{out} . Due to overall crystal momentum conservation, the reduced matrix element can then only be non-zero for $\mathbf{q} = \mathbf{0}$, which we could call the “one-phonon Raman selection rule”. The dipole approximation has the main practical advantage that it eliminates the \mathbf{q} -integration over the first Brillouin zone, as only the BZ center phonons have to be considered explicitly. Within the dipole approximation and after some simplifications, the reduced matrix element $\tilde{\mathcal{M}}_{\mu,\nu,\lambda}(\omega'; \omega) \equiv \tilde{\mathcal{M}}_{\mathbf{q}=\mathbf{0},\lambda}(\omega'; \omega; (\mathbf{k}_{\text{out}} = \mathbf{0}, \nu); (\mathbf{k}_{\text{in}} = \mathbf{0}, \mu))$ can then be written as

$$\begin{aligned} \tilde{\mathcal{M}}_{\mu,\nu,\lambda}(\omega'; \omega) = \sum_{\mathbf{k}} \int \frac{d\omega''}{2\pi} \left\{ \tilde{d}_{\mathbf{k},\mathbf{k}}^{\mathbf{k}_{\text{in}}=\mathbf{0},\mu}(\omega) \tilde{d}_{\mathbf{k},\mathbf{k}}^{\mathbf{k}_{\text{out}}=\mathbf{0},\nu,*}(\omega - \omega') \tilde{g}_{\mathbf{k},\mathbf{k}}^{\mathbf{q}=\mathbf{0},\lambda,*}(\omega') \right. \\ \times \tilde{\mathcal{G}}_{\mathbf{k},d,a}(\omega'' + \omega) \tilde{\mathcal{G}}_{\mathbf{k},f,c}(\omega'' + \omega') \tilde{\mathcal{G}}_{\mathbf{k},b,e}(\omega'') \\ \left. + \tilde{d}_{\mathbf{k},\mathbf{k}}^{\mathbf{k}_{\text{in}}=\mathbf{0},\mu}(\omega) \tilde{g}_{\mathbf{k},\mathbf{k}}^{\mathbf{q}=\mathbf{0},\lambda,*}(\omega') \tilde{d}_{\mathbf{k},\mathbf{k}}^{\mathbf{k}_{\text{out}}=\mathbf{0},\nu,*}(\omega - \omega') \right. \\ \left. \times \tilde{\mathcal{G}}_{\mathbf{k},d,a}(\omega'' + \omega) \tilde{\mathcal{G}}_{\mathbf{k},f,c}(\omega'' + \omega - \omega') \tilde{\mathcal{G}}_{\mathbf{k},b,e}(\omega'') \right\}. \end{aligned} \quad (6.42)$$

Note that the index structure in this equation is that of a trace of a product of matrices in band space. It then makes sense to introduce matrices $\mathbf{d}_{\mathbf{k}}^{\mu}(\omega)$, $\mathbf{g}_{\mathbf{k}}^{\lambda}(\omega')$, and $\mathbf{G}_{\mathbf{k}}(\omega)$ for the electron-photon coupling, the electron-phonon coupling, and the electron Green’s function, respectively, according to:

$$(\mathbf{d}_{\mathbf{k}}^{\mu}(\omega))_{ab} \equiv \tilde{d}_{\mathbf{k},\mathbf{k}}^{\mathbf{k}_{\text{in}}=\mathbf{0},\mu}(\omega), \quad (\mathbf{g}_{\mathbf{k}}^{\lambda}(\omega'))_{ab} \equiv \tilde{g}_{\mathbf{k},\mathbf{k}}^{\mathbf{q}=\mathbf{0},\lambda}(\omega'), \quad (\mathbf{G}_{\mathbf{k}}(\omega))_{ab} \equiv \tilde{\mathcal{G}}_{\mathbf{k},a,b}(\omega). \quad (6.43)$$

The expression for the reduced matrix element then takes on a much simpler form:

$$\begin{aligned}
& \tilde{\mathcal{M}}_{\mu,\nu,\lambda}(\omega'; \omega) \\
&= \sum_{\mathbf{k}} \int \frac{d\omega''}{2\pi} \left\{ \text{tr} \left[\mathbf{G}_{\mathbf{k}}(\omega'' + \omega) \mathbf{d}_{\mathbf{k}}^{\mu}(\omega) \mathbf{G}_{\mathbf{k}}(\omega'') \mathbf{g}_{\mathbf{k}}^{\lambda;\dagger}(\omega') \mathbf{G}_{\mathbf{k}}(\omega'' + \omega') \mathbf{d}_{\mathbf{k}}^{\nu;\dagger}(\omega - \omega') \right] \right. \\
&\quad \left. + \text{tr} \left[\mathbf{G}_{\mathbf{k}}(\omega'' + \omega) \mathbf{d}_{\mathbf{k}}^{\mu}(\omega) \mathbf{G}_{\mathbf{k}}(\omega'') \mathbf{d}_{\mathbf{k}}^{\nu;\dagger}(\omega - \omega') \mathbf{G}_{\mathbf{k}}(\omega'' + \omega - \omega') \mathbf{g}_{\mathbf{k}}^{\lambda;\dagger}(\omega') \right] \right\}.
\end{aligned} \tag{6.44}$$

Note that the integral over ω'' concerns only the three one-electron Green's functions. Within the quasi-particle approximation,

$$\tilde{\mathcal{G}}_{\mathbf{k},a,b}(\omega) \stackrel{\text{QPA}}{\approx} \frac{\delta_{a,b} Z_{\mathbf{k},a}^{(\text{QP})}}{\omega - \varepsilon_{\mathbf{k},a}^{(\text{QP})} + \frac{i}{2} \gamma_{\mathbf{k},a}^{(\text{QP})}} = \frac{f_{\mathbf{k},a} \delta_{a,b} Z_{\mathbf{k},a}^{(\text{QP})}}{\omega - \varepsilon_{\mathbf{k},a}^{(\text{QP})} - \frac{i}{2} \left| \gamma_{\mathbf{k},a}^{(\text{QP})} \right|} + \frac{(1 - f_{\mathbf{k},a}) \delta_{a,b} Z_{\mathbf{k},a}^{(\text{QP})}}{\omega - \varepsilon_{\mathbf{k},a}^{(\text{QP})} + \frac{i}{2} \left| \gamma_{\mathbf{k},a}^{(\text{QP})} \right|}, \tag{6.45}$$

it can be evaluated exactly using the residue theorem for each of the poles:^{5,6}

$$\begin{aligned}
& (-i)(Z_{\mathbf{k},a}^{(\text{QP})} Z_{\mathbf{k},b}^{(\text{QP})} Z_{\mathbf{k},c}^{(\text{QP})})^{-1} \tilde{\mathcal{R}}_{0;\mathbf{k};a,b,c}^{(\text{QP})}(\omega_1, \omega_2) \\
& \equiv (Z_{\mathbf{k},a}^{(\text{QP})} Z_{\mathbf{k},b}^{(\text{QP})} Z_{\mathbf{k},c}^{(\text{QP})})^{-1} \int \frac{d\omega''}{2\pi i} \mathcal{G}_{\mathbf{k},a,a}^{(\text{QP})}(\omega) \mathcal{G}_{\mathbf{k},b,b}^{(\text{QP})}(\omega - \omega_1) \mathcal{G}_{\mathbf{k},c,c}^{(\text{QP})}(\omega - \omega_2) \\
& = - \frac{f_a f_b \bar{f}_c}{[-\omega_2 - \Delta\varepsilon_{c,a}^{(\text{QP})} + \frac{i}{2}\bar{\gamma}_{c,a}^{(\text{QP})}][-\omega_2 + \omega_1 - \Delta\varepsilon_{c,b}^{(\text{QP})} + \frac{i}{2}\bar{\gamma}_{c,b}^{(\text{QP})}]} \\
& \quad - \frac{f_a \bar{f}_b f_c}{[-\omega_1 - \Delta\varepsilon_{b,a}^{(\text{QP})} + \frac{i}{2}\bar{\gamma}_{b,a}^{(\text{QP})}][-\omega_1 + \omega_2 - \Delta\varepsilon_{b,c}^{(\text{QP})} + \frac{i}{2}\bar{\gamma}_{b,c}^{(\text{QP})}]} \\
& \quad - \frac{\bar{f}_a f_b f_c}{[\omega_1 - \Delta\varepsilon_{a,b}^{(\text{QP})} + \frac{i}{2}\bar{\gamma}_{a,b}^{(\text{QP})}][\omega_2 - \Delta\varepsilon_{a,c}^{(\text{QP})} + \frac{i}{2}\bar{\gamma}_{a,c}^{(\text{QP})}]} \\
& \quad + \frac{f_a \bar{f}_b \bar{f}_c}{[\omega_2 - \Delta\varepsilon_{a,c}^{(\text{QP})} + \frac{i}{2}\bar{\gamma}_{a,c}^{(\text{QP})}][\omega_2 - \omega_1 - \Delta\varepsilon_{b,c}^{(\text{QP})} + \frac{i}{2}\bar{\gamma}_{b,c}^{(\text{QP})}]} \\
& \quad + \frac{\bar{f}_a f_b \bar{f}_c}{[\omega_1 - \Delta\varepsilon_{a,b}^{(\text{QP})} + \frac{i}{2}\bar{\gamma}_{a,b}^{(\text{QP})}][\omega_1 - \omega_2 - \Delta\varepsilon_{c,b}^{(\text{QP})} + \frac{i}{2}\bar{\gamma}_{c,b}^{(\text{QP})}]} \\
& \quad + \frac{f_a \bar{f}_b \bar{f}_c}{[-\omega_1 - \Delta\varepsilon_{b,a}^{(\text{QP})} + \frac{i}{2}\bar{\gamma}_{b,a}^{(\text{QP})}][-\omega_2 - \Delta\varepsilon_{c,a}^{(\text{QP})} + \frac{i}{2}\bar{\gamma}_{c,a}^{(\text{QP})}]} .
\end{aligned} \tag{6.46}$$

Here, $f_a \equiv f_{\mathbf{k},a}$ and $\bar{f}_a \equiv 1 - f_a$ are abbreviations for the occupation numbers of state $|\mathbf{k}, a\rangle$, $\Delta\varepsilon_{a,b}^{(\text{QP})} \equiv \varepsilon_{\mathbf{k},a}^{(\text{QP})} - \varepsilon_{\mathbf{k},b}^{(\text{QP})}$ denotes the excitation energy for an excitation from state $|\mathbf{k}, b\rangle$ to state $|\mathbf{k}, a\rangle$, and $\bar{\gamma}_{a,b}^{(\text{QP})} \equiv \gamma_{\mathbf{k},a}^{(\text{QP})} + \gamma_{\mathbf{k},b}^{(\text{QP})}$ is defined as the total decay width of the states $|\mathbf{k}, a\rangle$ and $|\mathbf{k}, b\rangle$.

In terms of the quasi-independent-particle three-particle correlation function, the

⁵For the application of the residue theorem, the integration path has to be completed to form a closed contour, i.e., in this case a semi-circle in either the lower or upper half-plane. The product of the three Green's functions yields a total of eight terms, two of which involve either three occupied or three empty states. In these two cases, the imaginary parts of the pole of each of the three Green's functions have the same sign and closing the contour in the opposite half of the complex plane leads to a vanishing of these two contributions. The other six terms each feature one pole in one half of the complex plane and two in the other. The contour is then best chosen to include only the single pole and in the case of this procedure leading to a clockwise contour, an additional minus sign has to be included.

⁶In case the quasi-particle approximation cannot be justified, the integration over ω'' can still be carried out by writing the electron Green's function in terms of its (non-diagonal) spectral function, which, however, we will not pursue here in detail.

reduced Raman scattering matrix element takes on the final form:

$$\begin{aligned} \tilde{\mathcal{M}}_{\mu,\nu,\lambda}(\omega';\omega) = i \sum_{\substack{\mathbf{k} \\ a,b,c}} \left\{ (\mathbf{d}_{\mathbf{k}}^{\mu}(\omega))_{ab} (\mathbf{g}_{\mathbf{k}}^{\lambda;\dagger}(\omega'))_{bc} (\mathbf{d}_{\mathbf{k}}^{\nu;\dagger}(\omega - \omega'))_{ca} \tilde{\mathcal{R}}_{0;\mathbf{k};a,b,c}^{(\text{QP})}(\omega, \omega - \omega') \right. \\ \left. + (\mathbf{d}_{\mathbf{k}}^{\mu}(\omega))_{ab} (\mathbf{d}_{\mathbf{k}}^{\nu;\dagger}(\omega - \omega'))_{bc} (\mathbf{g}_{\mathbf{k}}^{\lambda;\dagger}(\omega'))_{ca} \tilde{\mathcal{R}}_{0;\mathbf{k};a,b,c}^{(\text{QP})}(\omega, \omega') \right\}. \end{aligned} \quad (6.47)$$

This concludes the technical treatment of the calculation of the reduced Raman matrix element.

Note that despite the apparent independent-particle nature of the last line, it fully includes excitonic effects via the frequency-dependent “screened” electron-photon coupling (compare Eq. 6.38) as well as a description of the screening of the electron-phonon coupling on a level beyond the currently state-of-the-art DFPT via the computation of the screening on the MBPT level as given in Eq. 5.54. Our diagrammatic approach allowed the separation of these two effects from the “actual” correlated Raman process, described by the independent-particle three-particle correlation function. We can summarize our suggested approach for the calculation of Raman scattering rates *including excitonic effects and a dynamical treatment of phonons* as follows:

1. Calculation of a set of Kohn-Sham states and eigenvalues in density functional theory.
2. Correction of the KS eigenvalues on the level of the GW approximation and calculation of the quasi-particle weight if desired or required.
3. Computation of the static two-particle interaction kernel, solving the Bethe-Salpeter equation for both the eigenstates and eigenvalues, and calculation of the overlap matrix and the exciton-independent-particle coupling.
4. Calculation of the bare electron-photon matrix elements and computation of the bilinear exciton-photon coupling.

5. Inclusion of excitonic effects via computation of the “screened” electron-photon matrix elements according to Eq. 6.38.
6. Calculation of the matrix elements of the first and second derivatives of the lattice potential in the KS basis and computation of the bilinear exciton-phonon coupling.
7. Construction of the electronic part of the dynamical matrix according to Eq. 4.83, addition of the nuclear part, and subsequent diagonalization.
8. Computation of the screened electron-phonon matrix elements according to Eq. 5.54.
9. Computation of the Fourier-transformed independent-particle three-particle correlation function via Eq. 6.46.
10. Calculation of the reduced matrix element according to Eq. 6.47 for the desired ranges of $\omega = \omega_L$ and $\omega' = \omega_L - \omega_D$.

This algorithm is computationally very expensive and for many systems of current interest not all of the steps are necessary. In many cases, several of the above steps can be skipped or replaced by approximative approaches. For example, in low-dimensional, semi-conducting materials, such as some transition metal dichalcogenides, excitonic effects are known to be relevant whereas phonon frequencies and the electron-phonon coupling are rather accurately described already on the level of DFPT [50]. In this case, the screened electron-phonon coupling can be replaced by the one calculated with DFPT and does not need to be computed via our computationally expensive approach. In other cases, for instance in (semi-)metallic systems, such as graphene, excitonic effects do not play any role, but the electron-phonon coupling is not described very accurately by DFPT [108]. Then the calculation of the excitonic effects in the above algorithm can be skipped, but the MBPT calculation of the electron-phonon coupling may be kept. *Our suggested approach therefore also has the practical advantage that it is highly modular and different effects can be selectively included in the calculation.*

A concrete implementation of the parts of our scheme that involve the use of the solutions of the Bethe-Salpeter equation is still work in progress. However, as a first

test, we apply our suggested computational scheme to graphene, where excitonic effects are negligible for frequencies of visible light [142]. Furthermore, the simplicity of the band structure of graphene allows us to illustrate the full power and flexibility of our approach in one of the most simple settings.

6.2 Application to graphene: laser and Fermi energy dependence of the Raman scattering rate and importance of quantum interference effects

As mentioned in the introduction to this thesis, the Raman spectrum of graphene has been the subject of considerable attention over the past few years. Particular efforts have been devoted to study the two-phonon-induced contribution to the Raman spectrum, which, for the most part, results in a broadened peak around a particular frequency difference $\omega_L - \omega_D$, to which a continuum of pairs of phonons contribute. The two-phonon part of the Raman spectrum has been discussed in several works [56, 57, 60, 62, 67] and can nowadays be considered to be reasonably well understood from the resonant behavior of the scattering matrix element as a function of the phonon and light frequencies.

By contrast, the one-phonon-induced part of the Raman spectrum features only one Lorentzian-shaped peak, the so-called *G*-peak, in agreement with the quasi-particle approximation discussed in the preceding section. Note that out of the six phonon branches of graphene, four branches at $\mathbf{q} = \mathbf{0}$ are rendered Raman-inactive by crystal symmetries. The remaining two branches are degenerate and hence the one-phonon Raman spectrum features only one peak at the corresponding phonon frequency. While the position and width of the peak are determined entirely by the frequency and decay width of the phonon, the height of the peak, corresponding to the measured Raman intensity and being proportional to the scattering rate, is given by the interaction of two photons and one phonon with the system of electronic transitions. Naively, one would expect that the only relevant transitions are those in resonance with the light, i.e., laser, frequency as the latter is the driving force of the Raman process. Hence one

would expect that all other transitions play a rather negligible role in the scattering process. However, as we shall see in this section, quantum effects render this simplistic picture false and non-resonant transitions also play a crucial role.

This point has been first discussed by Basko [55], who, for his calculation, used an analytical, low-energy, and tight-binding-based model for the description of the electronic band structure and the electron-photon and electron-light coupling. However, the low-energy nature of the model does not allow one to study the one-phonon process in detail over a wider range of light frequencies, which has also been the focus of some experimental work [143]. Our general, first principles approach allows us to overcome this problem and look at both the dependence of the G -peak intensity on the laser frequency as well as the importance of quantum effects and the contributions of the different electronic transitions. Furthermore, it also allows us to study the dependence of the Raman intensity on the Fermi level, which has recently been investigated experimentally [81].

6.2.1 Theoretical details

Before we discuss the results of our calculation according to the theoretical approach developed in Section 6.1.2, we briefly summarize the further approximations employed for the specific case of graphene and the computational details of the numerical calculation over the course of the next two sections.

The calculations of the reduced matrix elements for one-phonon Raman scattering in graphene have been done without the inclusion of excitonic effects, i.e., by approximating the “screened” electron-light coupling d_i by its bare version: $d_i \approx d_i^{(b)}$. For the low- to mid-level frequency regime of visible light, excitonic effects on the optical properties were previously shown to be negligible [142]. Only when the laser frequency approaches the transition energy of the van Hove singularity in the density of states, i.e.,⁷ at around $\omega_L \approx 4.1$ eV, do excitonic effects start to play a role. However, while excitonic effects might affect the quantitative results for the upper end of the laser energy range we will study, the qualitative picture and conceptual understanding of the

⁷The van Hove singularity arises due to the flat shape of the $\pi^{(*)}$ bands around the M -point, compare Fig. 3.2.

G -peak process are not affected by them.

The screened electron-phonon coupling matrix elements were calculated on the level of DFPT. As mentioned in previous chapters and demonstrated by Lazzeri *et al.* [53], DFPT overestimates the screening of the electron-phonon coupling and thus underestimates its magnitude, in particular for phonons with momenta near the Γ - and K -points of the first Brillouin zone. Within the dipole approximation and due to selection rules, however, the only phonons that contribute to the one-phonon Raman spectrum are the two degenerate branches at the Γ -point. Since the underestimation of the electron-phonon coupling matrix elements is due to their sensitivity on \mathbf{q} only, it can be corrected by a simple rescaling of the matrix elements. In our discussions below, however, we will exclusively compare the calculated Raman intensities to a calculated reference value (for example, at a fixed value of the laser frequency or Fermi energy). In these ratios, the rescaling factor would always cancel and we will therefore not include it in our calculations.

Finally, the one-particle Green's functions appearing in the independent-particle three-particle correlation function have been approximated by the KS Green's functions. As such, the band energies are also not corrected for electron-electron interaction effects. In graphene, these effects were shown to mainly lead to a stretching of the π - and π^* -bands [52, 144]. This will change the quantitative results, but does not impact the qualitative discussion below.

Before we go into more detail on the concrete numerical calculation, we want to point out two features of the reduced matrix element that play important roles in the discussion of the results. Firstly, the total matrix element can be viewed as an integration of \mathbf{k} -dependent matrix elements over the first Brillouin zone: $\mathcal{M} = \sum_{\mathbf{k}} \mathcal{M}_{\mathbf{k}}$. The modulus of the total matrix element is then squared to obtain the Raman scattering rate. As each matrix element $\mathcal{M}_{\mathbf{k}}$ is a complex number carrying a \mathbf{k} -dependent phase, the different matrix elements $\mathcal{M}_{\mathbf{k}}$ can interfere with each other in both a destructive or constructive way, leading to a reduction or even extinction of the Raman intensity or an enhancement of it, respectively. Since the *coherent* summation of the matrix elements over all \mathbf{k} -points is a characteristic of quantum mechanics, we refer to these interference effects as *quantum interference effects* in the following.

Secondly, we address the question of whether the naïve notion of only those electronic transitions that are in resonance with the incoming light being relevant for an accurate description is correct. For this, we write the \mathbf{k} -dependent matrix element as the sum of three terms:

$$\mathcal{M}_{\mathbf{k}} = \mathcal{M}_{\mathbf{k}}^{(\text{aDR})} + \mathcal{M}_{\mathbf{k}}^{(\text{SR})} + \mathcal{M}_{\mathbf{k}}^{(\text{NR})}, \quad (6.48)$$

where the superscripts refer to, in order, the *almost double-resonant*, the *single-resonant*, and the *non-resonant* part of the matrix element. By “resonant”, we refer to the resonance of an electronic transition with the incoming or scattered light. As such, we define the aDR contribution to $\mathcal{M}_{\mathbf{k}}$ as

$$\mathcal{M}_{\mathbf{k}}^{(\text{aDR})} \equiv \frac{(\mathbf{d}^{\nu;\dagger})_{\pi,\pi^*} (\mathbf{g}_{\mathbf{k}}^{\lambda;\dagger})_{\pi^*,\pi^*} (\mathbf{d}_{\mathbf{k}}^{\mu})_{\pi^*,\pi}}{[\omega_{\text{L}} - \Delta\varepsilon_{\mathbf{k};\pi^*,\pi} + \frac{i}{2}\bar{\gamma}_{\mathbf{k};\pi^*,\pi}][\omega_{\text{D}} - \Delta\varepsilon_{\mathbf{k};\pi^*,\pi} + \frac{i}{2}\bar{\gamma}_{\mathbf{k};\pi^*,\pi}]}, \quad (6.49)$$

where we assumed zero doping for simplicity. This amplitude has a simple interpretation: An electron from the occupied π -band is excited to the π^* -band by the incoming light. There, it is subsequently scattered to an intermediate π^* -band state via emission of a phonon, before it finally radiatively recombines with the hole in the π -band it left behind. Note that the factors in the denominator become minimal when the π -to- π^* transition energy equals the frequency of the incoming light ω_{L} or the frequency of the outgoing light ω_{D} . For laser energies ω_{L} that are much larger than the phonon energy, we have $\omega_{\text{L}} \approx \omega_{\text{D}}$ and this expression describes a double-resonant behavior. The SR term, on the other hand, is defined as

$$\mathcal{M}_{\mathbf{k}}^{(\text{SR})} \equiv \sum_{s=\pi,\pi^*} \left\{ \frac{(\mathbf{d}^{\nu;\dagger})_{\pi,\pi^*} (\mathbf{d}_{\mathbf{k}}^{\mu})_{\pi^*,s} (\mathbf{g}_{\mathbf{k}}^{\lambda;\dagger})_{s,\pi}}{[\omega_{\text{D}} - \Delta\varepsilon_{\mathbf{k};\pi^*,\pi} + \frac{i}{2}\bar{\gamma}_{\mathbf{k};\pi^*,\pi}][\omega_{\text{D}} - \omega_{\text{L}} - \Delta\varepsilon_{\mathbf{k};s,\pi} + \frac{i}{2}\bar{\gamma}_{\mathbf{k};s,\pi}]} + \frac{(\mathbf{g}_{\mathbf{k}}^{\lambda;\dagger})_{\pi,s} (\mathbf{d}^{\nu;\dagger})_{s,\pi^*} (\mathbf{d}_{\mathbf{k}}^{\mu})_{\pi^*,\pi}}{[\omega_{\text{L}} - \omega_{\text{D}} - \Delta\varepsilon_{\mathbf{k};s,\pi} + \frac{i}{2}\bar{\gamma}_{\mathbf{k};s,\pi}][\omega_{\text{L}} - \Delta\varepsilon_{\mathbf{k};\pi^*,\pi} + \frac{i}{2}\bar{\gamma}_{\mathbf{k};\pi^*,\pi}]} \right\}. \quad (6.50)$$

Here, one of the factors involves the difference between the in- and outgoing light frequencies, i.e., approximately the phonon frequency, and hence it can become only single-resonant. We summarily include all other terms appearing in $\mathcal{M}_{\mathbf{k}}$ in $\mathcal{M}_{\mathbf{k}}^{(\text{NR})}$.

Note that these contain terms that go resonant when the transition energy matches $\omega_L - \omega_D$, i.e., roughly the phonon energy. However, the number of states that can be in resonance with the light is much higher than the number of states that can be in resonance with an energy $\omega_L - \omega_D$ close to the phonon energy (compare the density of states shown in the inset of Fig. 6.5 further below) and we hence do not include them in the single-resonant category. We will make use of this categorization of terms in our later discussion of the importance of the contributions of non-resonant transitions to the Raman scattering rate.

6.2.2 Computational details

Having discussed the theoretical concepts that are needed for the further discussion, we now give the details of our numerical calculations.

The initial self-consistent DFT calculation has been done using the PWSCF code included in the `Quantum ESPRESSO` suite [145], making use of an ultrasoft pseudopotential to describe the influence of core electrons. We employ the generalized gradient approximation to the exchange-correlation potential in the parametrization of Perdew, Burke, and Ernzerhof (PBE) [104], include plane-wave components up to an energy cutoff of 80 Ry, and use a regular $60 \times 60 \times 1$ \mathbf{k} -point mesh to sample the first Brillouin zone for \mathbf{k} -space integrations. The chosen values lead to converged results for a vacuum spacing of 14 Å, which separates periodic copies of the graphene sheet in the direction perpendicular to the sheet. The in-plane lattice constant of 2.46 Å was obtained from a prior structure relaxation calculation. Finally, the electronic occupations were smeared out with a Fermi-Dirac distribution using a thermal broadening of 0.002 Ry $\hat{=} 315$ K, which is necessary due to the semi-metallic nature of graphene.

As mentioned before, only optical, Raman-active phonons from the Γ -point of the first BZ contribute to the Raman scattering matrix element in the dipole approximation. Out of the three optically active phonon branches of graphene at Γ , only the doubly-degenerate E_{2g} phonon can participate in the one-phonon Raman process, as the horizontal mirror plane symmetry forbids the partaking of the out-of-plane B_{2g} phonon branch.⁸ We fix the phonon frequency of the doubly-degenerate, in-plane opti-

⁸We refer to the different phonon modes by the Mulliken symbol of the representation of the

cal phonon at $1581 \text{ cm}^{-1} \hat{=} 196 \text{ meV}$. This value has been obtained from experiments [23] on pristine, freestanding graphene and is in excellent agreement with *ab initio* calculations on the DFPT level, as presented in Section 4.3. It should be noted that the frequency of the E_{2g} phonon depends on the Fermi level, as changes of the electronic occupations can suppress resonance effects in the non-adiabatic part of the phonon self-energy. Typical experimentally achievable chemical potentials lead to shifts on the order of a few cm^{-1} , i.e., on the order of 1-2 meV [28]. However, for the Fermi energy-dependent calculations of the Raman intensity, we ignore this slight shift, since the phonon frequency only enters through the denominator of the electronic Green's functions, which in turn are dominated by the energy scale of the light (1-4 eV for visible light, in our case).

The calculation of the reduced scattering matrix elements has been implemented in a self-made Python code that is not restricted to the calculation of graphene, but is kept completely general, requiring only the electronic band structure, the electron-light and electron-phonon couplings, and the phonon and light frequencies as input. For this first application of our approach, the electronic decay widths were approximated with a constant value of 100 meV for all states. For the numerical integration over the first BZ appearing in the expression of the one-phonon Raman matrix element, we note that a very fine sampling in \mathbf{k} -space is required to obtain converged results. The reason for this lies in the importance of resolving resonances between electronic transitions and the incoming and outgoing photons accurately, which is only possible if the electronic transition energies are available on a very fine \mathbf{k} -point grid. To this end, we chose to interpolate the electronic band energies using maximally localized Wannier functions [146–149]. Likewise, we interpolate the electron-light coupling matrix elements in the dipole approximation and the static, DFPT-level electron-phonon coupling matrix elements. In practice, we first obtained the band energies and Bloch wave functions on a coarse $12 \times 12 \times 1$ \mathbf{k} -point grid using the PWSCF code and then used a modified form of the EPW code [150, 151] to obtain the electronic Hamiltonian and the electron-light and electron-phonon coupling Hamiltonians in a basis of localized Wannier functions on a corresponding coarse grid in real space. From there, we Fourier transformed the

symmetry group in which the eigenvectors transform; also see Footnote 3 of Chapter 4.

electronic Hamiltonian back to reciprocal space onto a very fine mesh of $480 \times 480 \times 1$ \mathbf{k} -points, which leads to converged results for the Raman matrix element. After diagonalizing the Hamiltonian at each \mathbf{k} -point, we use the Bloch functions in the basis of Wannier functions to calculate the interpolated electron-light and electron-phonon coupling matrix elements from the respective Fourier-transformed interaction Hamiltonians. For graphene, we only consider the Wannier functions corresponding to localized p_z -orbitals in the calculation, as these make up the π - and π^* -bands, in which the Fermi level of pristine graphene lies and which are optically decoupled from the neighboring σ -bands by parity selection rules.

Finally, it should be pointed out that our choice to *not* calculate the interpolated quantities with the EPW code but instead use a self-made interface and code allows for greater flexibility and control, for instance in the choice of light and phonon polarization vectors, and furthermore allows the interpolation to non-uniform grids and \mathbf{k} -point paths.

6.2.3 Laser energy dependence

Now that we specified the further theoretical approximations and computational details for the case of graphene, we finally move on to a discussion of various results obtained with our perturbative approach. We start with a discussion of the dependence of the one-phonon Raman intensity on the frequency of the incoming photon. Since in experiment, the incoming photon is normally provided by a laser, we will use the terms “incoming-photon energy” and “laser frequency” interchangeably. Experimentally, one finds a strong dependence of the Raman intensity on the laser frequency, which is found to scale like ω_L^4 in the range $1.8 < \omega_L < 2.8$ eV [143]. Contrary to the case of optical absorption, however, this behavior can *not* be understood in terms of the joint density of states (JDOS) alone. Our perturbative approach allows us to give an explanation for the observed strong behavior. In Fig. 6.5a we show the calculated intensity of the Raman G -peak, I_G , as a function of the laser frequency ω_L . The Raman intensity strongly peaks at a laser energy corresponding to the van Hove singularity in the JDOS at 4.1 eV, which is connected to the flat shape of the transition energy band structure at the M -point (see inset of Fig. 6.5a). While this behavior is generally expected for optical spectra, at

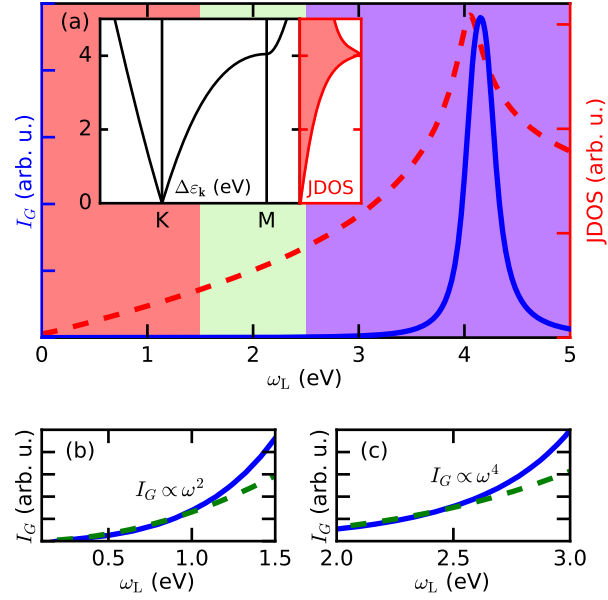


Figure 6.5: **Laser-energy dependence of the intensity of the Raman G -peak.** (a) Intensity I_G as a function of laser frequency ω_L (blue, full line) and joint density of states (JDOS) as a function of transition energy (red, dashed line). The shaded regions correspond to the three different ω_L -regimes discussed in the text. Inset: Transition energy $\Delta\varepsilon_{\mathbf{k}} = \varepsilon_{\mathbf{k},\pi^*} - \varepsilon_{\mathbf{k},\pi}$ on part of the high-symmetry line Γ - K - M - Γ . The right panel show the JDOS. (b,c) Zoom-in into the low- (red-shaded) and mid-range (green-shaded) ω_L -regime of panel (a). The green dashed lines depict an ω_L^2 - (panel (b)) and ω_L^4 -behavior (panel (c)). (Figure reprinted with permission from Reichardt, S. *et al.*, *Phys. Rev. B* **95**, 195422 (2017). Copyright 2017 by the American Physical Society.)

low- and mid-range energies, the Raman intensity is suppressed, however, even though there is still a sizable number of optically active transitions available, as seen from the non-vanishing JDOS. This behavior is in contrast to the case of optical absorption, which shows sizable, finite intensity, whenever dipole-allowed electronic transitions are available. Indeed, within the approximation of \mathbf{k} -point- and state-independent electron-light coupling matrix elements, the independent-particle optical absorption spectrum is directly proportional to $\text{JDOS}(\omega_L)/\omega_L$, i.e., it is constant for graphene in the low- to mid-level energy regime, while the Raman intensity is not (see Fig. 6.5b and c). The more complex behavior of the latter can be better understood if we distinguish between three different energy regimes (compare colored shades in Fig. 6.5a) and consider each of them in turn.

In the first regime up to a laser energy of 1.5 eV, we find that the Raman intensity follows an ω_L^2 -behavior (see Fig. 6.5). This prediction is in agreement with an earlier analytical calculation by Basko [55], who used a tight-binding model in the low-energy, Dirac electron approximation. Compared to the case of higher laser energy, however, the intensity is strongly suppressed. This relative suppression can be understood in terms of approximate angular momentum conservation, a concept that can be applied to any material with degenerate phonon branches and approximately circularly symmetric bands in some energy regime, such as, for instance, MoTe_2 [50]. As seen in the inset of Fig. 6.5a, the transition energy band structure is in a very good approximation circularly symmetric in the low-energy regime (compare the “Dirac cone” around the K -point in \mathbf{k} -space). This continuous in-plane rotation symmetry implies the conservation of the z -component of the angular momentum. As a consequence, the initial and final states must carry the same total angular momentum. As the state of the electronic system is the same in the initial and final state, its contribution to the total angular momentum of these states can be ignored. A (circularly polarized) photon coming in or going out perpendicular to the graphene flake (i.e., along the z -axis) contributes $\pm\hbar$ of angular momentum, while the doubly degenerate E_{2g} phonon transforms as a vector under in-plane rotations and hence also carries an angular momentum of $\pm\hbar$ if its polarization vectors are chosen to describe circular polarization. The final state, which consists of one photon and one phonon thus can have a total angular momentum

of $+2\hbar$, $0\hbar$, or $-2\hbar$, which differs from the total angular momentum of the initial state, consisting of one photon, as it has angular momentum $\pm 1\hbar$. Therefore, for a perfectly circularly symmetric band structure, this process would be disallowed. This explains why, in the low-energy regime, where the electronic band structure of graphene only weakly deviates from the circular, conic shape, the Raman G -peak intensity is relatively suppressed. Only the presence of weak trigonal warping effects that break the full rotation symmetry leads to a non-vanishing signal.

These trigonal warping effects get stronger the higher the excitation energy. In the second energy regime ($1.5 \lesssim \omega_L \lesssim 2.5$ eV), the band structure already is strongly trigonally warped and strongly deviates from its circularly symmetric shape at lower energies. The continuous rotation symmetry is hence broken down to the discrete 120° rotation symmetry of the graphene lattice. This discrete rotation symmetry implies that angular momentum is no longer exactly conserved but only up to integer multiples of $3\hbar$. As a result, an initial state with a total angular momentum of $\pm 1\hbar$ can scatter to a final state with total angular momentum $\mp 2\hbar$. In terms of (exact) selection rules, this means that incoming light with circular polarization σ^\pm undergoing the one-phonon Raman process is scattered with opposite polarization (σ^\mp) under the emission of one phonon of polarization σ^\mp . By taking appropriate linear combinations, we arrive at the well-known selection rules for cartesian polarizations [152]:

$$\mathbf{R}(x) = \begin{pmatrix} 0 & c \\ c & 0 \end{pmatrix}, \quad \mathbf{R}(y) = \begin{pmatrix} c & 0 \\ 0 & -c \end{pmatrix}, \quad (6.51)$$

with $c \in \mathbb{R}$ being the Raman matrix element, which can be shown to be real. Here, the argument in parenthesis refers to the cartesian polarization of the E_{2g} -phonon. The rows (columns) refer to the cartesian components of the polarization of the incoming (outgoing) light, so that the Raman matrix element can be obtained via $\sum_{i=x,y} (\mathbf{v}_{\text{ph}}^*)_i \boldsymbol{\epsilon}_{\text{out}}^* \cdot \mathbf{R}(i) \cdot \boldsymbol{\epsilon}_{\text{in}}$.⁹ We verified that the results of our calculations respect these selections rules up to a relative factor on the order of 10^{-6} .

⁹ $\mathbf{v}_{\text{ph}} = \mathbf{v}_{\mathbf{q}=\mathbf{0},\lambda=\text{LO,TO}}^{\alpha=A}$ in the notation of the past chapters, where the two atoms in the unit cell of graphene are conventionally labeled $\alpha = A, B$. Note that for the doubly degenerate optical phonon mode at Γ , we have $\mathbf{v}_{\mathbf{q}=\mathbf{0},\lambda=\text{LO,TO}}^{\alpha=B} = -\mathbf{v}_{\mathbf{q}=\mathbf{0},\lambda=\text{LO,TO}}^{\alpha=A}$ (also compare Fig. 4.3).

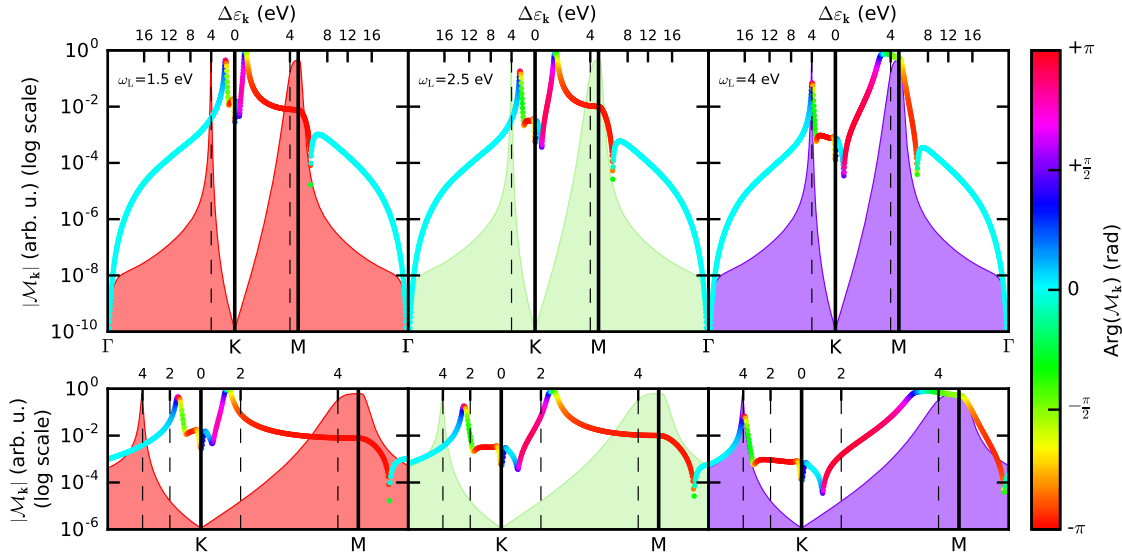


Figure 6.6: **k-point dependence of the contributions to the Raman matrix element.** Upper panels: Absolute value (in logarithmic scale) and phase (color-encoded) of the \mathbf{k} -point-dependent contribution $\mathcal{M}_{\mathbf{k}}$ to the total Raman matrix element on the high-symmetry line Γ - K - M - Γ for $\omega_L = 1.5, 2.5,$ and 4 eV (in order from left to right). The top horizontal axis gives the corresponding electronic transition energy $\Delta\varepsilon_{\mathbf{k}}$. The shaded area represents the JDOS evaluated at the value of $\Delta\varepsilon_{\mathbf{k}}$ of the respective \mathbf{k} -point. Lower panels: Zoom-in into the section of the path between K and M . (Figure reprinted with permission from Reichardt, S. *et al.*, *Phys. Rev. B* **95**, 195422 (2017). Copyright 2017 by the American Physical Society.)

As seen in Fig. 6.5c, our calculations reproduce the observed (see Ref. 143) ω_L^4 -behavior of the G -peak intensity in the mid-energy range quite well. However, when compared to higher excitation energies ($\gtrsim 2.5$ eV), the intensity is still very small, despite the presence of strong trigonal warping effects. To understand this behavior, we focus on the interplay of the contributions of the different \mathbf{k} -points to the total Raman matrix element $\mathcal{M} = \sum_{\mathbf{k}} \mathcal{M}_{\mathbf{k}}$. To this end, we visualize the \mathbf{k} -point dependence of the individual contributions to the total matrix element on the high-symmetry line Γ - K - M - Γ , as shown in Fig. 6.6 for three different values of ω_L . The absolute value of $\mathcal{M}_{\mathbf{k}}$ is given in a logarithmic scale on the vertical axis, while its phase is represented by color using a cyclic color scale. For further orientation, the electronic transition energy $\Delta\varepsilon_{\mathbf{k}}$

is displayed on the top horizontal axis. This is possible in graphene, where there is only one relevant electronic band transition and hence there is a well-defined mapping from \mathbf{k} -points to electronic transition energies. Finally, we can exploit the relative simplicity of the electronic band structure of graphene even further by plotting the joint density of states as a function of \mathbf{k} as a shaded area. For this, we evaluate the JDOS at the electronic transition energy of each \mathbf{k} -point. In this way, we are able to represent the relative weight of each \mathbf{k} -point on the high-symmetry line in the total matrix element when a full 2D integration over the first BZ is performed.

In Fig. 6.6 we can clearly identify the resonant states from the local maxima of $|\mathcal{M}_{\mathbf{k}}|$ (also see the zoom-in shown in the lower panels). For both $\omega_L = 1.5$ and 2.5 eV, we see that the resonant states are sharply centered around one point on each side of K . The phase, meanwhile, undergoes a continuous change of π when passing over this “resonance peak”. As a consequence, contributions from \mathbf{k} -points on opposite sides of the resonance peak cancel each other (see, for example, the blue and yellow dots in the first two panels of Fig. 6.6). This phase change of π across the resonance peak is typical for a driven system and indeed is well-known from the classic example of a driven and damped harmonic oscillator. However, this characteristic behavior is particularly important in the case of Raman scattering, as the total Raman matrix element is the sum of the contributions from different \mathbf{k} -points and a relative phase of π between two of these contributions leads to destructive interference, as exemplified by the states to both sides of the resonance peak. Besides the destructive interference of the states around the resonant \mathbf{k} -point to both sides of K , it should be noted that the “inner” flanks (i.e., towards K) of the two resonance peaks also carry opposite phase and similar weight and magnitude and hence also cancel each other. These opposite phases of the matrix elements around the K -point is an effect of the approximate full rotational symmetry in the vicinity of the K -point. A final point worthy of note concerns the contribution of the non-resonant states near the van Hove singularity at the M -point. While the amplitude of these contributions is smaller by two orders of magnitude compared to the contributions of the resonant states, the corresponding \mathbf{k} -points are broadly spread along the K - M -part of the high-symmetry line. This can be seen from the flat, red part of the curve in the first two panels of Fig. 6.6, which furthermore implies that

these states are all in phase and have a similar amplitude. In addition, the fact that the JDOS peaks at the M -point further implies that these states enter with a large weight in a full 2D-integration over the first BZ. As a consequence, the contribution from the region around the van Hove singularity at the M -point is far from negligible, even though it is non-resonant. However, this contribution is to a large part canceled by the contribution from the non-resonant states from the bulk of the Brillouin zone (represented by the cyan parts of the curve in the Γ - K - and M - Γ -directions in the first two panels of Fig. 6.6), which have opposite phase. We will demonstrate this statement more conclusively in Section 6.2.5.

While so far we have seen that in the low- to mid-energy regime the total Raman matrix element is strongly governed by destructive quantum interference effects, for higher laser energies, i.e., $\omega_L \gtrsim 2.5$ eV, this picture changes significantly (compare third panel of Fig. 6.6). While the flanks of the two resonance peaks still destructively interfere with each other (see blue and yellow parts of the curve), the resonance peak on the K - M -section becomes very broad along the high-symmetry line and these contributions are all largely in phase (cyan to green part of the curve). Combined with the high JDOS at the corresponding electronic transition energies, these resonant contributions dominate the total Raman matrix element for higher laser energies. While in the low-energy case, the contribution of the non-resonant states near the van Hove singularity was canceled by the non-resonant states from the bulk of the first BZ, here, the states near the Hove singularity become resonant and due to their large number, their contribution to the total matrix element cannot be canceled anymore by the non-resonant states from the bulk of the first BZ. Ultimately, this behavior is thus a consequence of the flatness of the transition energy band structure near the transition energies corresponding to the laser energy.

We can summarize the laser energy dependence of the one-phonon Raman intensity in graphene as follows: For low laser energies, the G -peak intensity is suppressed by an effective selection rule due to angular momentum conservation associated with the continuous rotation symmetry for low excitation energies. With increasing excitation energy the intensity still remains low, but in this regime the reason is to be found in destructive quantum interference effects, i.e., separate cancellations between the con-

tributions of both the resonant and non-resonant states. At even higher laser energies ($\omega_L \gtrsim 2.5$ eV), the resonant, in-phase contributions along the K - M -direction eventually dominate the Raman matrix element due to their increased weight in the 2D integration over the first BZ, caused by the presence of a van Hove singularity at M . Finally, it should be pointed out that the resonant states, in fact, do *not*, in general, dominate the Raman matrix element, as one would naïvely expect, but the sum of all non-resonant states also plays an important role for the Raman process. Only when the laser energy approaches the transition energy at which the JDOS peaks does the picture of the resonant states dominating the Raman matrix element actually hold.

6.2.4 Fermi energy dependence

With the conclusion of our analysis of the ω_L -dependence of the Raman G -peak intensity, we now move on to study its dependence on the Fermi level ε_F . To this end, we varied the Fermi level from -3 to +3 eV relative to that of pristine graphene. We use the rigid band approximation, i.e., we do not renormalize the electronic bands with ε_F , but we do include the effect of the change of ε_F on the electronic occupations by incorporating them in the electronic Green's functions, via changing the occupation factors f_a , etc., in Eq. 6.46. For each value of ε_F and for several different values of ω_L , we calculate the Raman G -peak intensity. The calculated intensities, for each value of ω_L normalized to the respective intensity for pristine graphene, are depicted in Fig. 6.7a. We represent the different laser energies by color, ranging from red for $\omega_L = 1.5$ eV to violet for $\omega_L = 4$ eV. For both positive (corresponding to electron or n -type doping) and negative (hole or p -type) values of ε_F , we find a strong increase of I_G , when ε_F approaches a critical value. As seen in Fig. 6.7b, this value matches the energy of the electronic state at a \mathbf{k} -point along the K - M -direction that is in resonance with the average of the incoming and outgoing light, $(\omega_{\text{in}} + \omega_{\text{out}})/2$ (compare colored full and dashed lines). The strong increase that we find in our calculation has been observed in experiment [81], although so far only for one fixed laser energy. Our calculations go beyond this limitation and predict a strong variation of the strength of the relative increase of I_G with laser energy (compare the peak heights of the red and violet curves in Fig. 6.7a). We also find that the electron-hole asymmetry of the critical value of

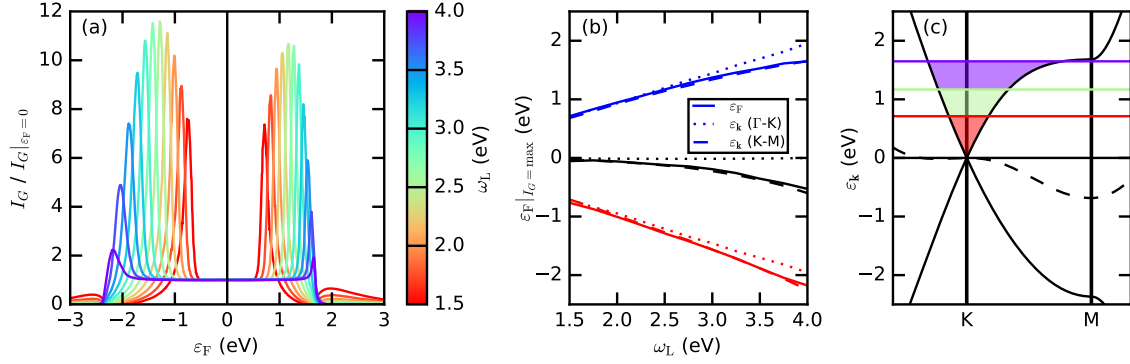


Figure 6.7: Fermi energy dependence of the intensity of the Raman G -peak. (a) Intensity of the G -peak as a function of Fermi energy ϵ_F and laser energy ω_L (color-encoded). All curves are normalized to the intensity at the Fermi energy of pristine graphene, separately for each value of ω_L . (b) Fermi energy at which I_G becomes maximal for both electron (full blue line) and hole doping (full red line). The colored dashed (dotted) lines represent the conduction (blue lines) and valence (red lines) energy at the \mathbf{k} -point along the K - M (Γ - K)-direction which is in resonance with $(\omega_{\text{in}} + \omega_{\text{out}})/2$. The black lines represent the sum of the respective blue and red lines, i.e., the electron-hole asymmetry. (c) Electronic band structure of graphene around the Fermi level of pristine graphene on part of the high-symmetry line Γ - K - M - Γ . The dashed line depicts the electron-hole asymmetry of the band structure. The red, green, and violet lines represent the positive Fermi level that maximizes the Raman intensity for laser energies of 1.5, 2.5, and 4 eV, respectively. The shaded areas mark those \mathbf{k} -points that do not contribute to the Raman amplitude due to the Pauli exclusion principle. (Figure reprinted with permission from Reichardt, S. *et al.*, *Phys. Rev. B* **95**, 195422 (2017). Copyright 2017 by the American Physical Society.)

ε_F at which the intensity increase occurs increases with laser energy (full black line in Fig. 6.7b). This behavior can be understood from the increasing electron-hole asymmetry of the resonant \mathbf{k} -points in the K - M -direction (dashed black line in Fig. 6.7b).

A conceptual explanation for this sharp increase of I_G at a certain critical value of ε_F had already been suggested in the original paper by Chen *et al.* [81]. There, the authors attributed the observed behavior to the blocking of destructive quantum interference effects due to the Pauli exclusion principle. When the Fermi level is increased, increasingly more electronic states in the π^* -band become occupied and these states are then no longer available for electronic transitions. Likewise, when the Fermi level is lowered, electronic states in the π -band become empty and can no longer partake in any optical transition (“Pauli blocking”). In Fig. 6.7c, this concept is illustrated for three different laser energies and the associated positive value of ε_F that leads to a maximum of I_G . The shaded regions underneath the horizontal, colored lines mark those \mathbf{k} -points which do not contribute to the total Raman matrix element due to Pauli blocking. At the depicted critical values of ε_F , a large part of the destructive quantum interference effects are suppressed and the G -peak intensity increases as a result. As seen from Fig. 6.7b, the magnitude of this increase depends on the laser energy. To understand this dependence on ω_L , we consider the two most extreme values of ω_L considered in our calculation ($\omega_L = 1.5$ and 4 eV) in more detail.

In the case of $\omega_L = 1.5$ eV, we can see from Fig. 6.7a that, on either side of the charge neutrality point, I_G goes through a sequence of maxima and minima: At first, I_G sharply increases, then drops to a minimum, before going through another small maximum which finally trails off for even larger values of ε_F . We can understand this behavior in terms of the concept of quantum interference discussed in the previous section for the mid-range energy regime. There, we stated that the total matrix element in this regime is suppressed because of two effects: firstly, almost-resonant contributions from \mathbf{k} -points around the resonance points (flanks of the resonance peaks in Fig. 6.6) cancel each other to a large degree and secondly, non-resonant contributions from \mathbf{k} -points near the van Hove singularity are mostly canceled by the sum of non-resonant contributions from within the bulk of the first BZ. When the Fermi level is now increased away from the charge neutrality point at K , more and more \mathbf{k} -points around K do not contribute

anymore because of Pauli blocking. The first transitions to be blocked are the ones on the “inner” flanks of the resonance peaks (as viewed from K), depicted in Fig. 6.6. The suppressive effect of the cancelation between the inner and outer flanks of the two resonance peaks is thus switched off, as the electronic states of the inner flanks do no longer contribute to the total matrix element. With the contributions of each outer flank being mostly in phase and not canceled anymore, the intensity of the G -peak reaches a maximum once the Fermi level is tuned such that all contributions from the inner flanks are blocked, i.e., when the Fermi level reaches the transition energy at which the resonance peak in Fig. 6.6 occurs. For a laser energy of $\omega_L = 1.5$ eV and electron doping this occurs at a Fermi energy of $\varepsilon_F = 0.71$ eV. When ε_F is now tuned towards even higher values, i.e., across the resonance peak, the contributions from the constructively interfering outer flank become more and more Pauli blocked and as a result the G -peak intensity decreases again. Once all almost-resonant electronic transitions on the outer flank of the resonance peak have been blocked, the intensity of the G -peak reaches a minimum (see dip in red curve in Fig. 6.7a at around $\varepsilon_F = 1.55$ eV). At this point, all almost-resonant contributions are suppressed by the Pauli principle and the only contributions to the total Raman matrix element stem from the non-resonant transitions near the van Hove singularity and from the bulk of the first BZ, which almost cancel each other. A further increase of ε_F then leads to the Pauli blocking of the transitions near the van Hove singularity, leaving the non-resonant, but in-phase states from the bulk of the first BZ unopposed and as a result the G -peak intensity as a function of ε_F goes through a second, albeit smaller, maximum (see small bump in red curve in Fig. 6.7a at around $\varepsilon_F = 1.97$ eV). Finally, an even further increase of the Fermi level only leads to an increasing suppression of the in-phase contributions from the bulk of the first BZ and in consequence I_G simply trails off with increasing ε_F .

By contrast, the behavior of I_G under changes of the Fermi level is much simpler for higher laser energies and becomes also less strong. Considering the case $\omega_L = 4$ eV explicitly, we see that when ε_F is increased away from the charge neutrality point, I_G shows almost no response over a large range of ε_F values. Only when the Fermi energy approaches a value of approximately $\varepsilon_F = 1.65$ eV does the intensity go through a slight maximum, before it quickly reduces to zero when ε_F is increased

even more. This is again consistent with our observation detailed in the previous section that for higher laser energies, the G -peak is mostly carried by resonant electronic transitions, with quantum interference effects only playing a minor role. This explains why, when the Fermi level is first increased, the G -peak intensity remains almost entirely unaffected, as only non-resonant transitions around the K -point become blocked. It is only when ε_F approaches the resonant states near M when I_G does show a sizable response, when once more the destructive quantum interference effects from the inner flank are suppressed. However, compared to the case of lower laser energy, the response of I_G is now significantly weaker. This can be related to the fact that for $\omega_L = 4$ eV, the resonance peak in \mathbf{k} -space is broad and mostly in phase (see broad plateau near M in the right-most panel in Fig. 6.6). In contrast to this, at lower laser energy, the resonance peaks in \mathbf{k} -space are very narrow and hence destructive interference effects between the flanks of the peaks play a much bigger role. After the G -peak intensity for $\omega_L = 4$ eV reached a maximum when the Fermi energy is tuned to a value of approximately $\varepsilon_F = 1.65$ eV, any further increase of ε_F only results in a blocking of more and more resonant transitions. This leads to a sharp decrease of I_G , as seen in the violet curve in Fig. 6.7. After all of the resonant transitions have been Pauli-blocked, i.e., the entire resonance peak in \mathbf{k} -space does no longer contribute, the value of I_G relative to that of pristine graphene remains insensitive to any further change of ε_F , which confirms our previous finding that non-resonant states from the bulk of the first BZ only play a minor role at higher laser energies.

To summarize this section, we found that our *ab initio* calculations confirm the suggestion of Chen *et al.* that the blocking of destructive quantum interference effects by shifting the Fermi level is the driving mechanism behind the observed strong increase of the G -peak intensity for certain critical values of the Fermi energy. In addition, we went beyond the case of fixed ω_L and calculated the *combined* dependence of I_G on both ε_F and ω_L . In this context, we demonstrated that the relative increase of I_G at the critical values of ε_F strongly depends on the laser energy, since quantum interference effects play a less important role for higher values of ω_L , as already established in the previous section. Furthermore, we also predict that for small values of ω_L , the intensity of the G -peak will resurge when ε_F approaches the van Hove singularity, even after all

resonant states have been Pauli-blocked.

6.2.5 Relevant states for the G -peak process

In the last part of this section, we will address the question of which electronic transitions are relevant for the G -peak process, i.e., which electronic states need to be taken into account in a theoretical description, a question first raised by Basko [55], who investigated it by means of a tight-binding model in the low-energy regime. However, as has become clear in the preceding two sections, the influence of quantum interference effects and of non-resonant states strongly depends on the laser energy. Hence it is not surprising that the states that need to be considered for a correct description of the G -peak intensity also vary with ω_L .

In order to approach this question from a quantitative side, we calculated the G -peak intensity for different values of ω_L and with increasingly more electronic transitions, starting with the ones that are in resonance with the incoming and/or outgoing light. More precisely, we select the included electronic states by introducing a transition energy window width ε_{cut} . We include only those electronic transitions whose transition energy obeys

$$\left| \Delta\varepsilon_{\mathbf{k}} - \frac{\omega_{\text{in}} + \omega_{\text{out}}}{2} \right| < \varepsilon_{\text{cut}}. \quad (6.52)$$

In order for a transition to be included, its transition energy needs to lie in a window of width $2\varepsilon_{\text{cut}}$ around the average resonance frequency $(\omega_{\text{in}} + \omega_{\text{out}})/2$. This criterion is illustrated in the inset of Fig. 6.8a. We calculate the G -peak intensity with only the states within a specified energy window. The graph of the corresponding function $I_G(\varepsilon_{\text{cut}})$ for different values of the laser energy (color-encoded) is depicted in Fig. 6.8a. For each value of ω_L , we normalized the respective curve to the value of I_G obtained by considering all electronic transitions.

The behavior we observe is consistent with the points discussed in the previous two sections. When ε_{cut} is first increased from zero, by definition, the first states that are included are the ones that are in resonance with the incoming and/or the outgoing light. These states contribute with a large amplitude to the total Raman matrix element. As a result, all curves in Fig. 6.8a feature a strong peak near $\varepsilon_{\text{cut}} = 0$. As ε_{cut} is increased

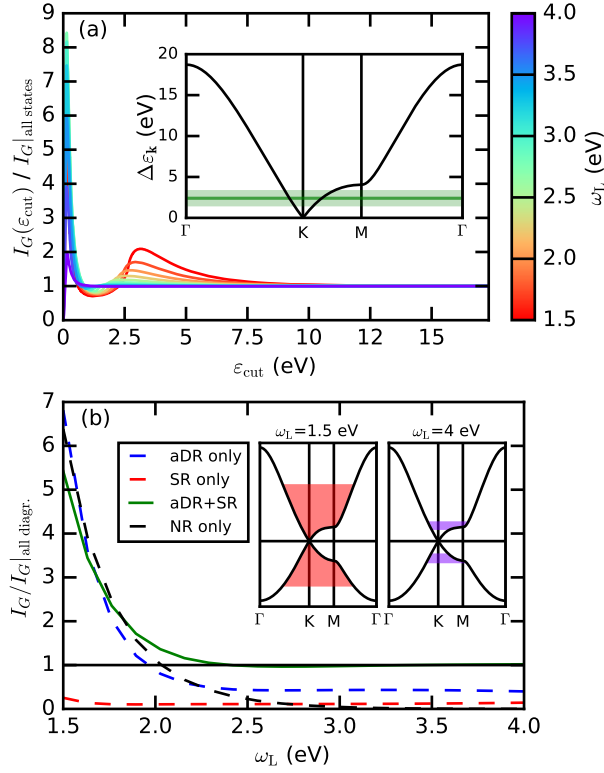


Figure 6.8: **Relevant electronic states for the G -peak process.** (a) G -peak intensity as a function of transition energy window width ε_{cut} (see main text for description). All lines are normalized to the intensity calculated with all states included. The laser energy is color-encoded. Inset: Illustration of the transition energy window width. The thin, dark-shaded region highlights the energy window in which the electronic states are in resonance with the in- or outgoing light for $\omega_L = 2.5$ eV for an electronic broadening of $2\gamma_{\mathbf{k}}$. The broad, light-shaded region marks the electronic states which are included at $\varepsilon_{\text{cut}} = 1$ eV. (b) Intensity of the Raman G -peak as a function of laser energy with certain (non-)resonant contributions only. All curves are normalized with respect to the intensity from the full calculation, including all contributions. The dashed blue, red, and black lines represent the values of I_G obtained with only the almost double-resonant (“aDR”), the single-resonant (“SR”), and the non-resonant (“NR”) terms, respectively. The full green line depicts the result obtained by taking into account the sum of the aDR and SR contributions. Inset: Graphical representation of the relevant electronic states (as defined in the text) for $\omega_L = 1.5$ (left panel) and 4 eV (right panel). (Figure reprinted with permission from Reichardt, S. *et al.*, *Phys. Rev. B* **95**, 195422 (2017). Copyright 2017 by the American Physical Society.)

further, the next states to be included stem from the flanks of the resonance peaks in \mathbf{k} -space (compare also Fig. 6.6). Since these states have partially opposite phase compared to the fully resonant ones, they destructively interfere in part with the latter and hence the intensity as a function of ε_{cut} decreases at first when these states are included in the calculation.

The behavior of I_G for higher values of ε_{cut} after this first drop depends on the laser-energy. For lower values of ω_L , $I_G(\varepsilon_{\text{cut}})$ increases once more when ε_{cut} is increased even further (see red to green curves in Fig. 6.8a). The reasons for this secondary maximum is to be found in the inclusion of the states near the van Hove singularity, which, as established in the previous sections, are all in phase and hence interfere constructively. Indeed, the point of steepest ascend in the red to green curves corresponds precisely to those values of ε_{cut} at which the energy window first includes the M -point. When the energy window is extended beyond this point, the destructively interfering states from the bulk of the first BZ are starting to be included and as a result I_G decreases once more. After a sufficient amount of these non-resonant transitions is included in the calculations, $I_G(\varepsilon_{\text{cut}})$ finally converges to the value of I_G obtained by taking all states into account.

For higher values of ω_L , however, $I_G(\varepsilon_{\text{cut}})$ does not change anymore after the inclusion of the resonant states (see blue to violet curves in Fig. 6.8a). Indeed, $I_G(\varepsilon_{\text{cut}})$ converges straight to the value of I_G obtained from a full calculation. This is yet another proof of the fact that non-resonant states do not play any noticeable role in this laser energy regime.

This last statement can further be elaborated upon by considering the resonant and non-resonant terms separately and calculating the G -peak intensity with only some of them. As mentioned at the end of Section 6.2.1, the total matrix element can be written as the sum of an almost double-resonant (aDR), a single-resonant (SR), and a non-resonant contribution (NR). Each of them is understood to already be summed over \mathbf{k} -points. A calculation of I_G with only one of these three contributions as a function of ω_L leads to the dashed lines in Fig. 6.8b, where the values of I_G are always normalized to the full calculation with all three contributions. Evidently, a calculation with only the aDR (blue line) or the NR terms (black line) severely overestimates the Raman

intensity in the low-laser energy regime, while it underestimates it for higher values of ω_L . This shows that the often-employed and -suggested textbook approximation of only retaining the aDR terms (see, for example, the book by Yu and Cardona [85]) fails in graphene. On the other hand, if the calculation is done with only the SR contribution, one always underestimates the G -peak intensity.

More interesting, however, is the result of a calculation with both the aDR and SR contributions only, that is, we include all terms that feature a resonance with either the incoming or outgoing light (full green line in Fig. 6.8b). The resulting curve confirms the previously made statements about the laser energy dependence of the importance of resonant transitions. For higher laser energies ($\omega_L \gtrsim 2.5$ eV), the resonant contributions to the total Raman matrix element are indeed the dominant ones and a calculation that takes only these terms into account yields very good results in this ω_L -regime.

On a final note, we can visualize the electronic states that need to be taken into account for an accurate quantitative description for different values of ω_L . To identify the necessary states, we go back to our results for $I_G(\varepsilon_{\text{cut}})$ and start from a calculation including all states, i.e., ε_{cut} equals the full π -band width. We then gradually lower the cutoff ε_{cut} until $I_G(\varepsilon_{\text{cut}})$ differs from the full result by more than 2%. This way, we obtain a minimum transition energy window width around the resonant states needed to achieve 2% accuracy. Given this minimum value of ε_{cut} , we can visualize the corresponding \mathbf{k} -points within the corresponding energy window in a band structure plot, as shown for $\omega_L = 1.5$ and 4 eV in the inset of Fig. 6.8b. From this representation, it immediately becomes clear that the relevant states for the G -peak process for lower values of the laser energy come from a large part of the first Brillouin zone. This is in agreement with Basko's finding, who obtained the same result using an analytical approach in the low-energy limit [55]. Our method, however, allows us to go beyond the low-energy limit and investigate also the mid- and high- ω_L -regime. In particular, we find that for larger values of ω_L , this picture changes qualitatively, as the relevant states are localized in a broad band of width 2 eV around the resonance energy. However, we want to stress that in no laser energy regime is it sensible to approximate the Raman scattering matrix element with an expression that only considers the resonant electronic transitions (i.e., in a narrow energy band of \pm the electronic decay width

around the resonance energy).

6.2.6 Summary of the results for graphene

In this section we focused on illustrating both the flexibility and power of our approach by analyzing the processes underlying the G -peak in the Raman spectrum of graphene and calculating the laser and Fermi energy dependence of its intensity. Our results compare very favorably to experimental observations and go beyond them by predicting and explaining the dependence of the G -peak intensity on a *combined* variation of *both* the laser and Fermi energy. In particular, we explicitly demonstrated the importance of quantum interference effects for the Raman scattering amplitude.

This concludes the application of our newly developed method to graphene. In the next section, we will summarize in what way the developed analysis techniques and the concept of quantum interference can be applied to other materials as well. However, we will not present any detailed results, but rather confine ourselves to a brief summary of the published results only.

6.3 Application to other 2D materials: triple-layer MoTe_2 and single-layer MoS_2

In the final section of this chapter, we will address the application of both the developed analysis techniques and our computational approach to other materials, choosing triple-layer MoTe_2 and MoS_2 as examples. Our coverage of these two topics will be kept short, however, as the main results have already been disseminated elsewhere [50, 153] or will be in the near future [82].¹⁰

¹⁰All computations with the method of the static first derivative of the transverse dielectric susceptibility referenced in this section were carried out by H. Miranda, who also participated equally in all discussions summarized in this section.

6.3.1 Triple-layer MoTe₂

The importance of quantum interference effects that we demonstrated for graphene is something that is not restricted to graphene alone, but also applies to many other materials. Another class of materials in which they sizably influence the Raman scattering rate is the family of single- and multi-layer transition metal dichalcogenides. To give one concrete example, we briefly review the case of triple-layer MoTe₂ in this section.

A single layer of MoTe₂ possesses three phonon modes which are active in one-phonon Raman scattering: one doubly degenerate in-plane one and one non-degenerate out-of-plane one. When passing from a monolayer to a trilayer crystal, the number of phonon modes triples and each monolayer mode exists in three copies that weakly interact with each other due to the interlayer van der Waals interaction, resulting in a splitting of each set of three copies into *Davydov triplets*. For the modes that are Raman-active in the single-layer crystal, each Davydov triplet now contains two Raman-active modes and one Raman-inactive one.

Recently, the laser frequency-dependent Raman intensity for triple-layer MoTe₂ has been measured experimentally [72, 154, 155]. It was observed that the in-plane modes remain silent for light frequencies not much bigger than the band gap, while the out-of-plane modes are bright right away. Secondly, the ratio of the intensity associated with the two Raman-active members of the out-of-plane Davydov triplet become inverted above a certain excitation frequency. This behavior *cannot* be understood within simple models, such as the bond polarizability model [69–71], which can only describe Raman scattering in the non-resonant regime, i.e., for excitation energies below the band gap energy.

To explain the observed behavior, we calculated the Raman scattering rate using the approach of the first derivative of the transverse dielectric susceptibility, which we mentioned as a possible alternative method for the calculation of Raman scattering rates in Chapter 1. We note that this approach can be proven to be completely equivalent to our perturbative method if in the latter the limit $\omega_D \rightarrow \omega_L$ is taken.¹¹ We then

¹¹The most simple and straightforward proof starts from the Bethe-Salpeter equation for the two-particle correlation function in real space. Taking derivatives with respect to a nuclei displacement on both sides, further elementary algebraic manipulations lead to an expression that matches our ladder-like approximation derived from perturbation theory up to a term that involves the functional

applied the same analysis techniques as shown for graphene above to the results of our calculation.

Firstly, the difference in behavior between the non-degenerate out-of plane mode and the doubly degenerate in-plane mode can be understood from the fact that the MoTe₂ band structure is also approximately invariant under arbitrary in-plane rotations near the location of the band gap, similar to the band structure of graphene. As discussed for the case of graphene, the approximate continuous rotation symmetry renders a doubly degenerate in-plane phonon mode silent, while the out-of-plane mode is not affected by this. Thus, the different behavior of the in- and out-of-plane phonon modes for excitation energies near the band gap can be understood by applying the same symmetry principles that we pointed out for graphene.

The second experimental observation of an intensity inversion of the two Raman-active members of the out-of-plane Davydov triplet cannot be explained in terms of symmetry principles alone, however, as the modes transform in the same way under crystal symmetry operations. Instead, we applied the same \mathbf{k} -point-resolved analysis technique we developed and used for our graphene calculation. In this way, we were able to provide an explanation of the observed behavior based on quantum interference effects. However, since we have already illustrated the use of approximate symmetry principles and of our \mathbf{k} -point-resolved analysis technique for the case of graphene, we will not go into any further detail here, but instead refer the reader to Ref. 50 for the details.

6.3.2 Single-layer MoS₂

Finally, we would like to briefly mention ongoing work on the application of our perturbative method to single-layer MoS₂ [82]. Here, the main focus will be on a comparison of our perturbative method to the method of the static derivative of the transverse

derivative of the two-particle interaction kernel with respect to the one-electron Green's function. This latter term corresponds to the terms involving the three-particle-irreducible interaction kernel that we neglected in our approach (see the paragraph before Eq. 6.40 for further discussion of this point). An alternative proof starts from the BSE in Fourier space and in the basis of the KS states, as outlined within certain approximations in Ref. 153. However, this method of proving the equivalence of the two approaches is much more cumbersome, as one also needs to take into account the change of the basis functions, i.e., the change of the KS states.

dielectric susceptibility. As mentioned above, the analytical proof is straightforward, yet the numerical verification of the equivalence of the two methods is still very much important to ensure the validity of the perturbative method in a practical setting.

Similarly to MoTe₂, a single layer of MoS₂ features two main Raman-active modes, an in-plane, doubly degenerate mode E' and a non-degenerate out-of-plane mode A' . We calculated the Raman scattering rate using both approaches: the static, first derivative of the transverse dielectric susceptibility with respect to a nuclear displacement pattern according to the phonon mode in question and our perturbative method described earlier. Both calculations were done on the independent-particle level using KS-DFT wave functions, eigenvalues, and KS electron-light matrix elements. The static derivative of the susceptibility with respect to nuclear displacements was computed using the method of finite differences [50, 75]. In the case of the perturbative method, the static electron-phonon coupling computed on the level of DFPT was used for the screened electron-phonon coupling, to ensure a consistent treatment of the change of the charge density under nuclei displacements. We also evaluated the perturbative expressions for $\omega_L = \omega_D$ to reflect the static nuclear displacements of the derivative method.

In Fig. 6.9 we show the results of a first preliminary calculation with our perturbative method for single-layer MoS₂ and compare it to the results of a calculation with the static first derivative method. The red and blue lines represent the Raman scattering rate involving the E' and A' modes, respectively, as obtained with the perturbative method. The colored dots represent the corresponding results obtained with the static, first derivative method. The results for the out-of-plane mode are in excellent agreement with one another. However, the results for the in-plane mode still show some quantitative differences, even though the qualitative behavior is in very good agreement.

One possible source for this discrepancy in the results for the in-plane mode could be the polar nature of MoS₂. For polar materials, a displacement of an atom induces an internal polarization, which in turn modifies the effective screened electron-phonon coupling. In the method of static first derivatives of the transverse dielectric susceptibility, the polar nature is already taken into account due to the self-consistent nature of the two DFT calculations used for the finite difference calculations. In the perturbative

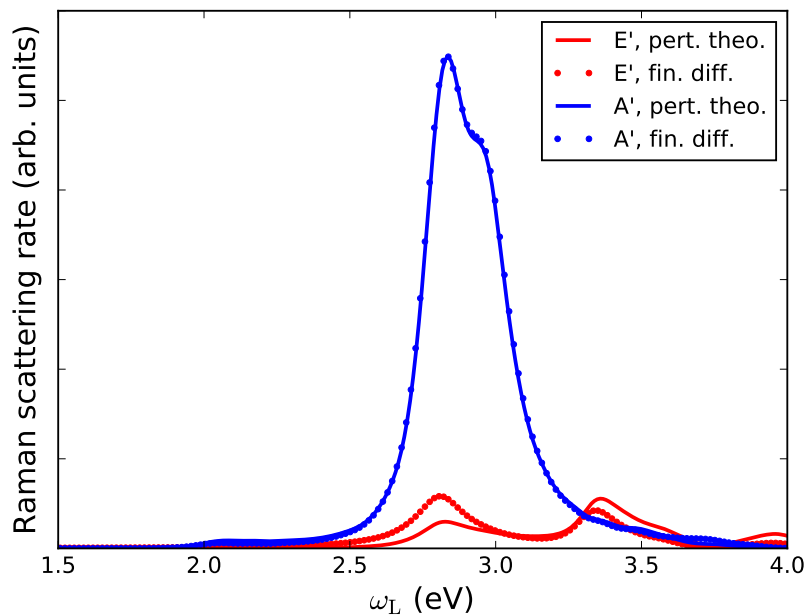


Figure 6.9: **Comparison of the “finite difference” method with the perturbation theory approach.** Calculated Raman scattering rate with both the method of the static, first derivative of the transverse dielectric susceptibility (dots) and the suggested perturbative approach (lines) as a function of excitation energy. The Raman scattering rate for the degenerate in-plane optical phonon mode E' is shown in red, while the scattering rate for the non-degenerate out-of-plane Raman-active mode A' is shown in blue. Both kinds of calculations were done in the independent-particle approximation. In the case of the perturbative method, the screened electron-phonon coupling was taken from DFPT for consistency and we set $\omega_L = \omega_D$ in the perturbative approach to mimic the static nuclear displacements of the first derivative method. (The calculations with the static derivative method as well as the *ab initio* calculations for the building blocks of the perturbative approach were done by H. Miranda.)

approach instead, this contribution to the electron-phonon coupling is missing entirely. How this issue could be fixed still remains to be seen. One possible ansatz for the inclusion of the missing contribution could be the inclusion of additional diagrams involving *Born effective charges*, which couple lattice displacement with transverse electronic dipole moments. In this way, an additional contribution to the Raman scattering rate would arise which would involve the three-current correlation function as compared to the nuclear displacement-two-current correlation function considered in our approach. However, the details of this ansatz still need to be worked out.

In addition to the comparison of the static first derivative and perturbative approaches on the independent-particle level, future work will also be put into an implementation of our suggested method for the inclusion of excitonic effects in the perturbative calculation, which could then also be validated against the already existing results of a finite-difference calculation including excitonic effects. Furthermore, the perturbative approach potentially allows an effective inclusion of temperature via the calculation of the temperature-dependent electron self-energy due to electron-phonon interaction [137]. This approach would lead to temperature-dependent electronic excitation energies and decay widths, which would account for the frequency shift of optical spectra with temperature. However, such an approach can, as of now, only be justified heuristically, as a rigorous treatment of the extension of our suggested theoretical approach to the calculation of Raman scattering rates to the finite-temperature case still needs to be carried out.

Chapter 7

Magneto-Raman Spectroscopy for the Characterization of Graphene

Parts of the content of this chapter have been published in the following publications:

- Neumann, C., Reichardt, S., Drögeler, M., Terrés, B., Watanabe, K., Taniguchi, T., Beschoten, B., Rotkin, S. V. & Stampfer, C. Low B field magneto-phonon resonances in single-layer and bilayer graphene. *Nano Lett.* **15**, 1547–1552 (2015)¹
- Neumann, C., Halpaap, D., Reichardt, S., Banszerus, L., Schmitz, M., Watanabe, K., Taniguchi, T., Beschoten, B. & Stampfer, C. Probing electronic lifetimes and phonon anharmonicities in high-quality chemical vapor deposited graphene by magneto-Raman spectroscopy. *Appl. Phys. Lett.* **107**, 233105 (2015)¹
- Sonntag, J., Reichardt, S., Wirtz, L., Beschoten, B., Katsnelson, M. I., Libisch, F. & Stampfer, C. Impact of many-body effects on Landau levels in graphene. *Phys. Rev. Lett.* **120**, 187701 (2018)¹

¹Contributions of the author of this thesis to the cited work:

Provided key ideas for interpretation of the experimental results; implemented theoretical models for the description and visualization of the data; extensively discussed the results with the co-authors; co-wrote the manuscript.

In the previous chapters, we focused entirely on the theoretical and computational aspects of Raman spectroscopy. We will now turn to a more application-oriented aspect of it and discuss how it can be used to probe certain properties of a sample, choosing again graphene as a prime example. In particular, we will devote most of our attention to the study of the effects and strength of electron-electron interaction and how to use Raman Spectroscopy under the influence of a magnetic field to extract various quantities, such as electron and phonon lifetimes and the magnitude of the electron-phonon coupling.

The influence of inter-electron Coulomb interactions manifests itself most prominently in its impact on the electronic band structure, i.e., the electronic energy levels. The latter can be probed in a variety of ways, for example, by scanning tunneling microscopy (STM) [156], by transport experiments [78, 79], or by Raman spectroscopy in finite magnetic fields [47, 49, 79]. The basic principle behind all three methods is to study the *resonant* coupling of the electronic levels with a second system that it is in resonance with, i.e., whose characteristic frequency or energy scale matches the energy of an electronic transition. To this end, one varies either the electronic energy levels or the second energy scale by tuning an external quantity and measures a suitable observable that depends on either the electronic transition energies or the second energy scale in a known way.

In the case of STM, one varies the bias voltage of the STM tip and measures the tunneling current, which depends on the electronic density of states. In transport experiments, on the other hand, one applies a weak perpendicular magnetic field and varies the charge carrier density, which allows the observation of “Shubnikov-de Haas oscillations” in the electrical conductivity. The amplitude of these oscillations depends on the ratio of the scale of electronic excitation energies and the thermal excitation energy $k_B T$. By varying the temperature, one can then extract the energy of electronic transitions.

Finally, in Raman spectroscopy, one can extract the electronic energy levels via their resonant coupling to phonons. Since the frequencies of the latter are hard to influence without also modifying the electronic system at the same time, one typically applies high magnetic fields ($B \geq 1$ T) to only tune the electronic transition energies.

When one tunes the magnetic field in such a way that the electronic transition energies match the energy of a Raman-active optical phonon, the lifetime of the latter decreases significantly, which results in a broadening of the Raman peak. By measuring the width of the Raman peak as a function of the external magnetic field, one can thus gain insight into the typical electronic transition energies. When combining this measurement with a way of tuning the effects of electron-electron interaction, such as a change in charge carrier density or the simultaneous excitation of many charge carriers, one can study many-body effects in even more detail.

In this part of this work, we will now foremost focus on this third method to probe many-body effects in more detail, i.e., we will show how the effect of *magneto-phonon resonances*, sketched in the last paragraph, can be used in practice to probe the effects of electron-electron interactions. The very same method can also be applied to probe the lifetimes of electrons and anharmonic effects on the phonon lifetimes.

7.1 Theory of magneto-phonon resonances in graphene

To begin with, we review the theoretical description of magneto-phonon resonance in graphene. Since a purely *ab initio* study of a crystal in a finite magnetic field is not feasible at the time of writing, we will rely on an analytical model instead. To this end, we first introduce an analytical *tight-binding* model of the electronic structure of graphene and the electron-phonon coupling, at first without a magnetic field. In a second step, we will then introduce an external, perpendicular magnetic field, which leads to the formation of discrete electronic states, the so-called *Landau levels*. Thirdly, we study the non-adiabatic coupling of these electronic states to the Raman-active optical phonons in time-dependent perturbation theory within a Green's function formalism, which allows us to describe the phenomenon of magneto-phonon resonances using only a small number of empirical parameters.

7.1.1 Tight-binding model for graphene

We start the description of magneto-phonon resonances by introducing an analytical description of the electronic band structure of graphene and the electron-phonon coupling. Since we are interested in describing the resonant coupling of electronic transitions to the Raman-active optical phonons, which have an energy of around 196 meV, we can restrict ourselves to the low-energy part of the band structure, that is, to a small energy window around the Fermi energy. We thus only need an effective description of the π - and π^* -bands of graphene in the vicinity of the $K^{(\prime)}$ -point in the first Brillouin zone. As remarked in Sections 3.2 and 6.2, the bands in this region of \mathbf{k} -space can be well described by a linear combination of p_z -orbitals. In real space, a good approximation for the Hamiltonian can then be found within a first-nearest-neighbors tight-binding model, in which the electrons are assumed to be tightly bound to one specific atom with a finite probability to “hop” to a neighboring atomic site.

More concretely, we consider the following electronic tight-binding Hamiltonian [157–159]:

$$\hat{H}_{\text{el}} = - \sum_m \sum_{n=1}^3 t_n \left[\hat{c}_{\mathbf{R}_m + \mathbf{d}_n}^\dagger \hat{c}_{\mathbf{R}_m} + \hat{c}_{\mathbf{R}_m}^\dagger \hat{c}_{\mathbf{R}_m + \mathbf{d}_n} \right]. \quad (7.1)$$

Here, m labels the different unit cells of the crystal, \mathbf{R}_m is a lattice vector, and $\mathbf{d}_{1,2,3}$ are three vectors describing the relative position of the three nearest neighbors of a carbon atom on the A -sublattice of the graphene lattice (see Fig. 7.1a for a definition of the sublattices and an illustration of the notation). Explicitly, the lattice vectors and nearest-neighbor vectors are given by

$$\mathbf{R}_m = n_1 \mathbf{t}_1 + n_2 \mathbf{t}_2, \text{ where } \mathbf{t}_1 = a_0 \begin{pmatrix} 1 \\ 0 \\ 0 \end{pmatrix}, \mathbf{t}_2 = a_0 \begin{pmatrix} -1/2 \\ \sqrt{3}/2 \\ 0 \end{pmatrix} \text{ and } n_1, n_2 \in \mathbb{Z}, \quad (7.2)$$

$$\mathbf{d}_1 = a \begin{pmatrix} 0 \\ 1 \\ 0 \end{pmatrix}, \mathbf{d}_2 = a \begin{pmatrix} -\sqrt{3}/2 \\ -1/2 \\ 0 \end{pmatrix}, \mathbf{d}_3 = a \begin{pmatrix} \sqrt{3}/2 \\ -1/2 \\ 0 \end{pmatrix}, \quad (7.3)$$

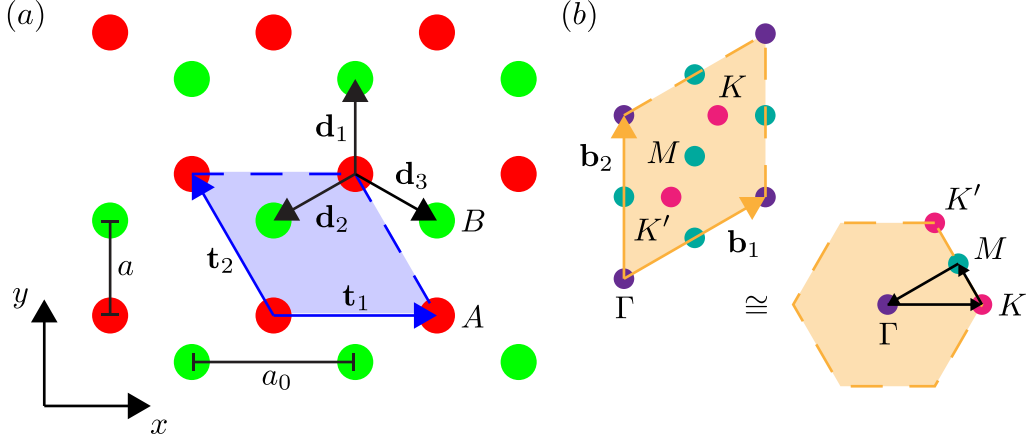


Figure 7.1: **Lattice structure, reciprocal lattice, and first Brillouin zone of graphene.** (a) Lattice structure of graphene. Red (green) dots represent atoms on the A (B) sublattice. The lattice basis vectors $\mathbf{t}_{1,2}$ and the unit cell they span are depicted in blue. Black arrows represent the nearest-neighbor vectors $\mathbf{d}_{1,2,3}$. The nearest-neighbor distance a and lattice constant a_0 are also shown. (b) Reciprocal lattice and first Brillouin zone of graphene. Purple, teal, and magenta points represent the high-symmetry points Γ , M , and $K^{(\prime)}$, respectively. The reciprocal lattice basis vectors $\mathbf{b}_{1,2}$ and the unit cell they span are depicted in orange. The bottom-right corner shows the first Brillouin zone (i.e., the Wigner-Seitz unit cell) of the graphene lattice. Black arrows mark a path along the high-symmetry lines that is commonly used for visualization.

where $a_0 \approx 2.46 \text{ \AA}$ and $a \equiv a_0/\sqrt{3} \approx 1.42 \text{ \AA}$ are the lattice constant and first-nearest-neighbor distance in graphene, respectively. The operator $\hat{c}_{\mathbf{R}}^\dagger$ creates an electron in a p_z -orbital-like state $|\mathbf{R}\rangle$ localized on the atomic site \mathbf{R} . Finally, t_n are the so-called *hopping integrals* defined by

$$t_n \equiv - \int d^3r [\phi_{p_z}(\mathbf{r} - \mathbf{d}_n)]^* [V(\mathbf{r}) - V^{(\text{at})}(\mathbf{r})] \phi_{p_z}(\mathbf{r}) > 0, \quad (7.4)$$

where $V(\mathbf{r})$ is the lattice-periodic total potential and $V^{(\text{at})}(\mathbf{r})$ the potential of an isolated carbon atom located at the origin [160]. To include the effects of electron-electron interaction in an approximative way, the potentials can be replaced by effective potentials that partially include exchange-correlation effects, such as the self-consistent (pseudo-) potentials in Kohn-Sham density functional theory. Lastly, $\phi_{p_z}(\mathbf{r} - \mathbf{R}) \equiv \langle \mathbf{r} | \mathbf{R} \rangle$ is the

wave function of the p_z -like state of the atomic potential $V^{(\text{at})}(\mathbf{r} - \mathbf{R})$ centered on site \mathbf{R} . In the following, we will neglect the overlap of wave functions located on different atomic sites, i.e., $\langle \mathbf{R} | \mathbf{R}' \rangle \approx \delta_{\mathbf{R}, \mathbf{R}'}$ which is sufficient to reproduce the low-energy electronic band structure in the energy range that is needed to describe the phenomenon of magneto-phonon resonances [47, 161–163].

In our case, we will use the definition of t_n only to derive a tight-binding description for the electron-phonon coupling. For the purpose of describing the electronic band structure only, we will treat the t_n as empirical parameters. Note that for the undistorted graphene lattice, we have $t_1 = t_2 = t_3 \equiv t$ by symmetry and t is on the order of 3 eV [51, 157, 158].

To find the eigenstates and eigenvalues of \hat{H}_{el} , we introduce the Fourier-transformed operators

$$\hat{c}_{\mathbf{k},A} \equiv \frac{1}{\sqrt{N}} \sum_m e^{-i\mathbf{k}\cdot\mathbf{R}_m} \hat{c}_{\mathbf{R}_m}, \quad \hat{c}_{\mathbf{k},B} \equiv \frac{1}{\sqrt{N}} \sum_m e^{-i\mathbf{k}\cdot\mathbf{R}_m} \hat{c}_{\mathbf{R}_m + \mathbf{d}_1}, \quad (7.5)$$

which can be interpreted as operators which destroy a Bloch wave-like state with finite amplitude on the A or B sublattice, i.e., on the sites \mathbf{R}_m or $\mathbf{R}_m + \mathbf{d}_1$, only. The inverse transformations are given by

$$\hat{c}_{\mathbf{R}_m} = \frac{1}{\sqrt{N}} \sum_{\mathbf{k}} e^{i\mathbf{k}\cdot\mathbf{R}_m} \hat{c}_{\mathbf{k},A}, \quad \hat{c}_{\mathbf{R}_m + \mathbf{d}_1} = \frac{1}{\sqrt{N}} \sum_{\mathbf{k}} e^{i\mathbf{k}\cdot(\mathbf{d}_1 + \mathbf{R}_m)} \hat{c}_{\mathbf{k},B}. \quad (7.6)$$

In terms of the Fourier-transformed operators, the Hamiltonian takes on the simple form

$$\hat{H}_{\text{el}} = -t \sum_{\mathbf{k}} \left\{ \left[\sum_{n=1}^3 e^{i\mathbf{k}\cdot(\mathbf{d}_n - \mathbf{d}_1)} \right] \hat{c}_{\mathbf{k},A}^\dagger \hat{c}_{\mathbf{k},B} + \left[\sum_{n=1}^3 e^{-i\mathbf{k}\cdot(\mathbf{d}_n - \mathbf{d}_1)} \right] \hat{c}_{\mathbf{k},B}^\dagger \hat{c}_{\mathbf{k},A} \right\}. \quad (7.7)$$

We can thus represent it in sublattice space by a 2×2 -matrix

$$\mathbb{H}_{\mathbf{k}} = \begin{pmatrix} 0 & -tf(\mathbf{k}) \\ -t(f(\mathbf{k}))^* & 0 \end{pmatrix}, \quad (7.8)$$

where we defined $f(\mathbf{k}) \equiv \sum_{n=1}^3 \exp(i\mathbf{k} \cdot (\mathbf{d}_n - \mathbf{d}_1))$. The eigenvalues and -vectors of $\mathbf{H}_{\mathbf{k}}$ are given by

$$\varepsilon_{\mathbf{k},\pi^*} = +t|f(\mathbf{k})|, \quad \chi_{\mathbf{k},\pi^*} = \frac{1}{\sqrt{2}} \begin{pmatrix} 1 \\ -\frac{(f(\mathbf{k}))^*}{|f(\mathbf{k})|} \end{pmatrix}, \quad (7.9)$$

$$\varepsilon_{\mathbf{k},\pi} = -t|f(\mathbf{k})|, \quad \chi_{\mathbf{k},\pi} = \frac{1}{\sqrt{2}} \begin{pmatrix} 1 \\ +\frac{(f(\mathbf{k}))^*}{|f(\mathbf{k})|} \end{pmatrix}. \quad (7.10)$$

For completeness, we note that the function $|f(\mathbf{k})|$ explicitly reads

$$|f(\mathbf{k})| = \sqrt{1 + 4 \cos\left(\frac{1}{2}k_x a_0\right) \left[\cos\left(\frac{1}{2}k_x a_0\right) + \cos\left(\frac{\sqrt{3}}{2}k_y a_0\right) \right]} \quad (7.11)$$

and that it becomes zero at two inequivalent points in the first Brillouin zone (see Fig. 7.1b):

$$\mathbf{K} \equiv \frac{2\pi}{a_0} \begin{pmatrix} 2/3 \\ 0 \\ 0 \end{pmatrix}, \quad \mathbf{K}' \equiv \frac{2\pi}{a_0} \begin{pmatrix} -2/3 \\ 0 \\ 0 \end{pmatrix}, \quad (7.12)$$

which are called *valleys* or also *Dirac points* in the literature.

Since we are only interested in the low-energy electronic excitations around the Fermi surface, for pristine graphene defined by $\varepsilon_{\mathbf{k}} = 0$, we can expand the Hamiltonian into a Taylor series around K and K' . We then obtain the effective, low-energy, matrix Hamiltonians

$$\mathbf{H}^K(\mathbf{k}) = v_F \mathbf{k} \cdot \boldsymbol{\sigma}, \quad \mathbf{H}^{K'}(\mathbf{k}) = -v_F \mathbf{k} \cdot \boldsymbol{\sigma}^*, \quad (7.13)$$

where $\boldsymbol{\sigma} \equiv (\sigma_x, \sigma_y)^T$ is a two-dimensional vector of Pauli matrices acting in sublattice space and we re-defined the wave vector \mathbf{k} to now originate from the points K and K' , respectively. The Hamiltonians in Eq. 7.13 have the same algebraic structure as the *Weyl Hamiltonian*, which describes massless particles of spin 1/2 and definite helicity.² Here, however, the Pauli matrices do not act on the physical spin degree of freedom

²The *helicity* operator is defined as $\hat{\lambda} \equiv \boldsymbol{\sigma} \cdot \hat{\mathbf{p}}/|\hat{\mathbf{p}}|$, i.e., it represents the projection of the (pseudo-) spin in the direction of the momentum.

(which, so far, we have been ignoring in our treatment), but rather act in the space of the sublattices A and B . The corresponding degree of freedom is thus known as *pseudo-spin*.

The effective Hamiltonians have the linearly dispersive spectrum $\varepsilon_{\pm}(\mathbf{k}) = \pm v_F |\mathbf{k}|$, i.e., electrons in graphene with energies around the Fermi energy behave as massless, relativistic particles. The parameter v_F is the slope of the bands, which are in a first approximation linear in $|\mathbf{k}|$ in the vicinity of the K - and K' -points, and it thus has the physical interpretation of the Fermi velocity, i.e., the velocity of electrons at the Fermi surface. It is related to the hopping integral via $v_F = \sqrt{3}ta_0/2$ and is on the order of 10^6 m/s. In the following, however, we will take it to be an empirical parameter.

Next, we turn to a tight-binding-based description of the electron-phonon coupling. To this end, we consider a general displacement of the lattice atoms, which, following the discussion in Section 4.2, can be written as a Fourier series:

$$\mathbf{u}_{\alpha}(\mathbf{R}_m) \equiv \mathbf{u}_{(m,\alpha)} = \frac{1}{\sqrt{N}} \sum_{\mathbf{q}} \mathbf{u}_{\mathbf{q}}^{\alpha} e^{i\mathbf{q}\cdot\mathbf{R}_m}, \quad \alpha = A, B. \quad (7.14)$$

In the approximation that the hopping integral only depends on the distance between the atomic sites [158, 164, 165], the hopping parameter between sites \mathbf{R}_m and $\mathbf{R}_m + \mathbf{d}_n$ changes by the amount

$$\delta t_n(\mathbf{R}_m) = \frac{\partial t}{\partial a} \frac{1}{a} \mathbf{d}_n \cdot [\mathbf{u}_B(\mathbf{R}_m + \mathbf{d}_n - \mathbf{d}_1) - \mathbf{u}_A(\mathbf{R}_m)] \quad (7.15)$$

under a displacement of the lattice atoms. Here, the gradient of the hopping integral has been approximated by its “radial” component in the direction of the unit vector \mathbf{d}_n/a and the change of the nearest-neighbor vector \mathbf{d}_n is the difference between the displacements of an atom on the B sublattice and of an atom on the A sublattice (compare the definition of the direction of \mathbf{d}_n in Figure 7.1). The electron-phonon Hamiltonian in a first-nearest-neighbor tight-binding description and in terms of the

Bloch wave operators $\hat{c}_{\mathbf{k},\alpha}$ then reads:

$$\begin{aligned}
\hat{H}_{\text{el-ph}} &= - \sum_m \sum_{n=1}^3 \delta t_n(\mathbf{R}_m) \left[\hat{c}_{\mathbf{R}_m+\mathbf{d}_n}^\dagger \hat{c}_{\mathbf{R}_m} + \hat{c}_{\mathbf{R}_m}^\dagger \hat{c}_{\mathbf{R}_m+\mathbf{d}_n} \right] \\
&= \frac{\partial t}{\partial a} \sum_{\mathbf{k},\mathbf{q}} \left\{ \left[\left(\sum_{n=1}^3 e^{i\mathbf{k}\cdot(\mathbf{d}_n-\mathbf{d}_1)} \frac{1}{a} \mathbf{d}_n \right) \cdot \frac{1}{\sqrt{N}} \mathbf{u}_{\mathbf{q}}^A \right. \right. \\
&\quad \left. \left. - \left(\sum_{n=1}^3 e^{i(\mathbf{k}+\mathbf{q})\cdot(\mathbf{d}_n-\mathbf{d}_1)} \frac{1}{a} \mathbf{d}_n \right) \cdot \frac{1}{\sqrt{N}} \mathbf{u}_{\mathbf{q}}^B \right] \hat{c}_{\mathbf{k}+\mathbf{q},A}^\dagger \hat{c}_{\mathbf{k},B} \right. \\
&\quad \left. + \left[\left(\sum_{n=1}^3 e^{-i(\mathbf{k}+\mathbf{q})\cdot(\mathbf{d}_n-\mathbf{d}_1)} \frac{1}{a} \mathbf{d}_n \right) \cdot \frac{1}{\sqrt{N}} \mathbf{u}_{\mathbf{q}}^A \right. \right. \\
&\quad \left. \left. - \left(\sum_{n=1}^3 e^{-i\mathbf{k}\cdot(\mathbf{d}_n-\mathbf{d}_1)} \frac{1}{a} \mathbf{d}_n \right) \cdot \frac{1}{\sqrt{N}} \mathbf{u}_{\mathbf{q}}^B \right] \hat{c}_{\mathbf{k}+\mathbf{q},B}^\dagger \hat{c}_{\mathbf{k},A} \right\}. \tag{7.16}
\end{aligned}$$

Expanding the lattice displacements in terms of the vibrational eigenmodes and passing to a quantum-mechanical description,

$$\mathbf{u}_{\mathbf{q}}^\alpha \rightarrow \hat{\mathbf{u}}_{\mathbf{q}}^\alpha = \sum_{\lambda} \sqrt{\frac{1}{2M\omega_{\mathbf{q},\lambda}}} \mathbf{v}_{\mathbf{q},\lambda}^\alpha (\hat{b}_{\mathbf{q},\lambda} + \hat{b}_{-\mathbf{q},\lambda}^\dagger), \tag{7.17}$$

we can write the electron-phonon interaction Hamiltonian for the phonon mode (\mathbf{q}, λ) as a 2×2 -matrix in sublattice space:

$$\mathbf{H}_{\mathbf{k}}^{\mathbf{q},\lambda} = \sqrt{\frac{1}{2NM\omega_{\mathbf{q},\lambda}}} \frac{\partial t}{\partial a} \left[\mathbf{v}_{\mathbf{q},\lambda}^A \cdot \begin{pmatrix} 0 & \mathbf{F}_{\mathbf{k}} \\ (\mathbf{F}_{\mathbf{k}+\mathbf{q}})^* & 0 \end{pmatrix} - \mathbf{v}_{\mathbf{q},\lambda}^B \cdot \begin{pmatrix} 0 & \mathbf{F}_{\mathbf{k}+\mathbf{q}} \\ (\mathbf{F}_{\mathbf{k}})^* & 0 \end{pmatrix} \right], \tag{7.18}$$

where we introduced the abbreviation $\mathbf{F}_{\mathbf{k}} \equiv \sum_{n=1}^3 \exp(i\mathbf{k}\cdot(\mathbf{d}_n-\mathbf{d}_1)) \mathbf{d}_n/a$. The matrix Hamiltonian obeys $\mathbf{H}_{\mathbf{k}}^{\mathbf{q},\lambda} = (\mathbf{H}_{\mathbf{k}+\mathbf{q}}^{-\mathbf{q},\lambda})^\dagger$, which provides a useful link between the matrix elements for phonon absorption and emission.

In the context of magneto-phonon resonances in the one-phonon part of the Raman spectrum, which involves in-plane optical phonons at the Γ -point only, we only need the coupling matrices for the special case $\mathbf{q} = 0$ and $\lambda = \text{LO, TO}$. For the optical phonon

modes at Γ , the polarization vectors $\mathbf{v}_{\mathbf{q}=0,\lambda}^{A,B}$ have the form³ $\mathbf{v}_{\mathbf{q}=0,\lambda}^A = -\mathbf{v}_{\mathbf{q}=0,\lambda}^B = 1/\sqrt{2}\mathbf{v}_\lambda$, where $\mathbf{v}_\lambda = \mathbf{e}_x, \mathbf{e}_y$ for cartesian phonon polarization. Moreover, if we are only interested in the low-energy electrons near the K - and K' -points, we can further simplify the coupling Hamiltonian by letting $\mathbf{k} = \mathbf{K}, \mathbf{K}'$, with the understanding that any product of $(\mathbf{K}^{(\prime)} - \mathbf{k})$ and the lattice displacement would constitute a higher-order contribution. In this approximation, we have $\mathbf{F}_{\mathbf{k}} \approx \mathbf{F}_{\mathbf{K}} = 3/2(i, 1)^T = (\mathbf{F}_{\mathbf{K}'})^*$ and the electron-phonon coupling Hamiltonian takes on the compact form:

$$\mathbf{H}^{K,\lambda} = \sqrt{\frac{1}{2NM\omega_{\text{ph}}}} \frac{3}{\sqrt{2}} \frac{\partial t}{\partial a} \boldsymbol{\sigma} \wedge \mathbf{v}_\lambda, \quad \mathbf{H}^{K',\lambda} = \sqrt{\frac{1}{2NM\omega_{\text{ph}}}} \frac{3}{\sqrt{2}} \frac{\partial t}{\partial a} \boldsymbol{\sigma}^* \wedge \mathbf{v}_\lambda, \quad (7.19)$$

where we defined the wedge product as $\mathbf{a} \wedge \mathbf{b} \equiv a_x b_y - a_y b_x$.

Up to here, we focused on the description of low-energy electronic states and their coupling to phonons. In the next section, we will now introduce a perpendicular magnetic field, which will condense the low-energy continuum of electronic states in a set of discrete electronic states, called *Landau levels*. After deriving the spectrum and the corresponding states of the effective electronic Hamiltonian in the presence of a magnetic field, we will describe their coupling to the optical phonons at the Γ -point.

7.1.2 Landau levels in graphene

In order to describe the behavior of the low-energy electronic states in graphene in the presence of a magnetic field, we start from a model of free Weyl fermions in two spatial dimensions. In the context of graphene, this model is valid only up to an energy cutoff Λ on the order of 1–2 eV, at which point the graphene bands start to strongly deviate from the linear shape of the Weyl electron dispersion. Starting from a model of free Weyl fermions, however, has the advantage that the spectrum of the Hamiltonian in the presence of a homogeneous, perpendicular magnetic field can be derived algebraically in a simple way.

³Also compare the illustration of the vibration pattern in Fig. 4.3a.

Our starting point, therefore, will be the Hamiltonian

$$\hat{H}_{\text{eff}}^K = v_F \left[\hat{\mathbf{p}} + \frac{e}{c} \mathbf{A}(\hat{\mathbf{r}}) \right] \cdot \boldsymbol{\sigma} \equiv v_F \hat{\boldsymbol{\pi}} \cdot \boldsymbol{\sigma}, \quad (7.20)$$

where the vector potential is understood to be chosen such that it yields a magnetic field $\mathbf{B} = \nabla \times \mathbf{A}(\mathbf{r}) = B\mathbf{e}_z$ and we introduced the operator of *kinetic* momentum $\hat{\boldsymbol{\pi}} \equiv \hat{\mathbf{p}} + e/c\mathbf{A}(\hat{\mathbf{r}})$. We also focus solely on the effective Hamiltonian for electrons near the K -point for now and treat all vectors as being two-dimensional, with occurring vector products being understood to be evaluated with inserted vanishing z -components.

Following the discussion in Ref. 159, we pass from the set of operators $\{\hat{r}_x, \hat{r}_y, \hat{p}_x, \hat{p}_y\}$ to the set $\{\hat{R}_x, \hat{R}_y, \hat{X}, \hat{Y}\}$, whose elements are defined by

$$\hat{\mathbf{R}} \equiv \frac{c}{eB} \mathbf{e}_z \times \hat{\boldsymbol{\pi}}, \quad \hat{\mathbf{X}} \equiv \hat{\mathbf{R}} + \hat{\mathbf{r}}, \quad (7.21)$$

where $\hat{\mathbf{X}} = (\hat{X}, \hat{Y})^T$. The two sets of operators are in a one-to-one correspondence and are thus equally valid for a complete quantum mechanical description of the system. The physical motivation for these definitions is the classical description of an electron moving in a constant magnetic field, which moves on a circular orbit and whose classical state can be described either by specifying its position \mathbf{r} and canonical momentum \mathbf{p} or by specifying the center of the orbit, \mathbf{X} , and the position of the electron relative to the center of the orbit, \mathbf{R} [159]. The commutation relations of $\hat{\mathbf{X}}$ and $\hat{\mathbf{R}}$ follow from the fundamental commutation relation $[\hat{r}_i, \hat{p}_j] = i\delta_{i,j}$ and the only two non-vanishing commutators are given by

$$[\hat{R}_x, \hat{R}_y] = -il_B^2, \quad [\hat{X}, \hat{Y}] = +il_B^2, \quad (7.22)$$

where we defined the *magnetic length* $l_B \equiv \sqrt{c/(eB)} \approx 25.7 \text{ nm}/\sqrt{B[\text{T}]}$.

In terms of $\hat{\mathbf{X}}$ and $\hat{\mathbf{R}}$, the effective Hamiltonian reads

$$\hat{H}_{\text{eff}}^K = \frac{v_F}{c} eB \hat{\mathbf{R}} \wedge \boldsymbol{\sigma}, \quad (7.23)$$

with the wedge product having been defined in the previous section. As $\hat{\mathbf{R}}$ and $\hat{\mathbf{X}}$

commute, so do \hat{H}_{eff}^K and $\hat{\mathbf{X}}$ and hence we can choose the eigenstates of \hat{H}_{eff}^K to be eigenstates of any function $f(\hat{X}, \hat{Y})$. Following [159], we introduce two pairs of ladder operators \hat{a}, \hat{a}^\dagger and \hat{b}, \hat{b}^\dagger via

$$\hat{a} \equiv (-i) \frac{1}{\sqrt{2}l_B} (\hat{R}_x - i\hat{R}_y), \quad \hat{a}^\dagger = (+i) \frac{1}{\sqrt{2}l_B} (\hat{R}_x + i\hat{R}_y), \quad (7.24)$$

$$\hat{b} \equiv \frac{1}{\sqrt{2}l_B} (\hat{X} + i\hat{Y}), \quad \hat{b}^\dagger = \frac{1}{\sqrt{2}l_B} (\hat{X} - i\hat{Y}), \quad (7.25)$$

which obey the commutation relations $[\hat{a}, \hat{a}^\dagger] = [\hat{b}, \hat{b}^\dagger] = 1$.

In terms of these, the Hamiltonian takes on the form

$$\hat{H}_{\text{eff}}^K = \frac{v_F}{c} \sqrt{2} e B l_B \begin{pmatrix} 0 & \hat{a} \\ \hat{a}^\dagger & 0 \end{pmatrix}. \quad (7.26)$$

Choosing the eigenstates of \hat{H}_{eff}^K to be eigenfunctions of $\hat{b}^\dagger \hat{b}$ to the eigenvalue $m \in \mathbb{N}_0$, we find (see Ref. 159) that the eigenvalues and eigenstates of the Hamiltonian at the K -point read

$$\varepsilon_n = \text{sgn}(n) \omega_B \sqrt{|n|}, \quad |n, m; K\rangle = C_n \begin{pmatrix} \text{sgn}(n) ||n| - 1\rangle_a \\ ||n|\rangle_a \end{pmatrix} \otimes |m\rangle_b, \quad (7.27)$$

with $n \in \mathbb{Z}$ and we introduced the *cyclotron frequency* $\omega_B \equiv v_F \sqrt{2eB/c}$. The states $||n|\rangle_a$ and $|m\rangle_b$ are eigenstates of the number operators $\hat{a}^\dagger \hat{a}$ and $\hat{b}^\dagger \hat{b}$, respectively, while $C_{n \neq 0} = 1/\sqrt{2}$, $C_0 = 1$ is a normalization factor. For electrons near the K' -point one finds the same spectrum, with the eigenstates being given by $|n, m; K'\rangle = \sigma_x |n, m; K\rangle$. The states $|n, m; K^{(\prime)}\rangle$ are known as *Landau levels* (LLs), after L. Landau, who discussed them for the first time in his 1930 work on diamagnetism in metals [166]. The physical meaning of the quantum numbers n and m can be inferred from their connection to the operators $|\hat{\mathbf{R}}|^2 = l_B^2 (2\hat{a}^\dagger \hat{a} + 1)$ and $|\hat{\mathbf{X}}|^2 = l_B^2 (2\hat{b}^\dagger \hat{b} + 1)$: the principal quantum number n is thus a measure of the mean squared radius of the “orbit” of the electron, whilst the quantum number m is a measure for the mean squared distance of the center of the “orbit” from the origin (the so-called *guiding center*).

As the eigenvalues of the Hamiltonian are independent of the quantum number $m \in \mathbb{N}_0$, the corresponding eigenstates are infinitely degenerate, which has its classical analogue in the independence of the energy of a circulating electron from the position of the center of the orbit. The degeneracy thus is, loosely speaking, linked to the infinitely many ways in which an orbit of fixed mean squared radius can be placed within the graphene sheet. In a finite-sized flake, however, there is an upper limit to the number of orbits that fit into the flake, and hence the degeneracy of the Landau levels is finite. From the condition that the furthest guiding center still fits into the flake (for simplicity assumed to be circular), we obtain the degeneracy of the LLs as $g_{\text{LL}} = 4A/(2\pi l_B^2)$, where the factor of 4 stems from the additional spin and valley (K and K') degeneracy.

In pristine graphene, the Fermi level lies within the zeroth ($n = 0$) Landau level so that half of its degenerate states are occupied and all “negative LLs” ($n < 0$) are filled while all “positive” ones are empty. However, by introducing additional electrons into the sample, for example, by applying an external gate voltage, the occupancies of the LLs can be changed. To describe the relative fillings of the individual LLs, it is then convenient to introduce the concept of the *filling factor*

$$\nu \equiv \Delta N_{\text{el}} 2\pi l_B^2 / A \equiv n_{\text{el}} 2\pi l_B^2, \quad (7.28)$$

where $n_{\text{el}} \equiv \Delta N_{\text{el}} / A$ denotes the excess charge carrier density, i.e., the *doping*, in the sample. Taking into account the additional fourfold degeneracy of the LLs and the fact that the zeroth LL is half-filled in pristine graphene, we find that the fractional occupancy of the n th LL can be described by the *partial filling factor*

$$\bar{\nu}_n \equiv \frac{\nu + 2 - 4n}{4} \in [0, 1] \quad (7.29)$$

with the understanding that $\bar{\nu}_n \equiv 0$ (1) if $(\nu + 2 - 4n)/4 < 0$ (> 1).

As a final ingredient for the description of magneto-phonon resonances, to be presented in the next section, we will also need the electron-phonon coupling matrix elements involving two Landau levels. Combining the previously derived expressions leads to the

following simple result for the needed matrix elements of the electron-phonon interaction Hamiltonian:

$$\langle n, m; v | \mathbf{H}^{v, \lambda=x} | n', m'; v \rangle = C_n^* C_{n'} \frac{3}{2\sqrt{NM\omega_{\text{ph}}}} \frac{\partial t}{\partial a} \left(\text{sgn}(n') \delta_{|n|, |n'|-1} + \text{sgn}(n) \delta_{|n|, |n'+1|} \right) \delta_{m, m'} \quad (7.30)$$

$$\langle n, m; v | \mathbf{H}^{v, \lambda=y} | n', m'; v \rangle = C_n^* C_{n'} \frac{3}{2\sqrt{NM\omega_{\text{ph}}}} \frac{\partial t}{\partial a} i \left(\text{sgn}(n') \delta_{|n|, |n'|-1} - \text{sgn}(n) \delta_{|n|, |n'+1|} \right) \delta_{m, m'} \quad (7.31)$$

This result is independent of the valley $v = K, K'$ and is diagonal in the guiding center quantum numbers m, m' . Furthermore, the only allowed transitions are between Landau levels whose absolute values of their principal quantum numbers differ by ± 1 . This selection rule can be explained in terms of angular momentum conservation, as an LL state $|n, m\rangle$ carries orbital angular momentum $l_z = (|n| - m)\hbar$ [159], while the doubly-degenerate in-plane optical phonon transforms as a vector under in-plane rotations, and hence behaves like possessing an orbital angular momentum of $\pm\hbar$.

Having discussed the description of the behavior of low-energy electrons in a finite magnetic field and their coupling to in-plane optical phonons in graphene, we can now turn to the description of magneto-phonon resonances.

7.1.3 Magneto-phonon resonances

As mentioned in the introduction to this section, the term *magneto-phonon resonance* describes the resonant, non-adiabatic coupling of a phonon to a Landau level transition. This leads to a strong decrease of the lifetime of the phonon, which, in turn, manifests itself in a broadening of the corresponding peak in the Raman spectrum. Before detailing how this effect can be used to experimentally probe the spectrum of electronic excitations and hence of many-body effects, we first review its theoretical background. Our treatment of the theory of magneto-phonon resonances follows the perturbative approach of Ando [161] and Goerbig [162], while we choose a slightly different way of incorporating the effects of partially filled Landau levels.

To describe the response of the position and width of the Raman peak to the non-adiabatic coupling of the Landau level system to the phonon, we determine the non-adiabatic shift and the decay width of the phonon. The frequency and the decay width of the phonon can be determined from the real and imaginary part of the poles of the Fourier-transformed exact phonon Green's function $\tilde{\mathcal{D}}_{\mathbf{q},\lambda,\lambda'}(\omega)$, as defined in Eq. 5.59. As in Section 6.1, we will work in the quasi-particle approximation and approximate $\tilde{\mathcal{D}}_{\mathbf{q},\lambda,\lambda'}(\omega) \approx \delta_{\lambda,\lambda'}\tilde{\mathcal{D}}_{\mathbf{q},\lambda}(\omega)$, where the diagonal part will be written as $\tilde{\mathcal{D}}_{\mathbf{q},\lambda}(\omega)$ from now on. We will also only be concerned with the $\mathbf{q}=\mathbf{0}$ -case, as, within the dipole approximation, these are the only phonons that contribute to the one-phonon-induced Raman process.

As discussed in Section 5.3, the exact phonon Green's function can be most easily calculated in time-dependent perturbation theory. For this, we split up the the total Hamiltonian as described in Section 5.1 into three parts:

$$\hat{\mathcal{H}} = \hat{\mathcal{H}}_{\text{el}} + \hat{\mathcal{H}}_{\text{ph}} + \hat{\mathcal{H}}_{\text{el-ph}}. \quad (7.32)$$

If we are only interested in the resonant coupling of the two in-plane optical phonons at the Γ -point to electrons moving in a strong magnetic field, we can approximate the electronic part of the Hamiltonian with the effective LL Hamiltonian

$$\hat{\mathcal{H}}_{\text{el}} \approx \left(\sum_{n,m,v} \varepsilon_n \hat{c}_{n,m,v}^\dagger \hat{c}_{n,m,v} \right) \otimes \mathbb{1}_n, \quad (7.33)$$

where $\hat{c}_{n,m,v}^\dagger$ creates an electron in the LL state $|n, m; v\rangle$ defined in the previous section ($v = K, K'$ again denotes the valley index and we suppressed any reference to the electronic spin for now). Likewise, we take the phonon part of the Hamiltonian as

$$\hat{\mathcal{H}}_{\text{ph}} \approx \mathbb{1}_e \otimes \left(\sum_{\lambda=x,y} \omega_{\text{ph}} \hat{b}_\lambda^\dagger \hat{b}_\lambda \right), \quad (7.34)$$

where $\hat{b}_\lambda \equiv \hat{b}_{\mathbf{q}=\mathbf{0},\lambda}$ and $\omega_{\text{ph}} \equiv \omega_{\mathbf{q}=\mathbf{0},\lambda=x,y}$ is the frequency of the doubly degenerate in-

plane optical phonon at Γ and we omitted the constant zero-point energy. Lastly, we approximate the electron-phonon interaction Hamiltonian as:

$$\begin{aligned} \hat{\mathcal{H}}_{\text{el-ph}} \approx & \sum_{\substack{n,n', \\ m,v}} \sum_{\lambda=x,y} g_{n,n'}^\lambda \hat{c}_{n,m,v}^\dagger \hat{c}_{n',m,v} \left(\hat{b}_\lambda + \hat{b}_\lambda^\dagger \right) \\ & - \mathbb{1}_e \otimes \left(\sum_{\lambda=x,y} \frac{1}{2} \omega_{\text{ph}}^{(\text{el,ad.})} \left(\hat{b}_\lambda + \hat{b}_\lambda^\dagger \right)^2 \right). \end{aligned} \quad (7.35)$$

Here, $\omega_{\text{ph}}^{(\text{el,ad.})}$ (to be explicitly specified later) denotes the electronic part of the phonon frequency ω_{ph} in the adiabatic approximation at zero magnetic field and zero Fermi energy⁴ and $g_{n,n'}^\lambda \equiv \langle n, m; v | \mathbf{H}^{v,\lambda} | n', m; v \rangle$ is the non-adiabatic electron-phonon coupling constant, given in Eqs. 7.30 and 7.31.

As seen from Eq. 5.68, the exact one-phonon Green's function is found to have the form

$$\tilde{\mathcal{D}}_\lambda(\omega) \equiv \int_{-\infty}^{+\infty} dt e^{i\omega t} \mathcal{D}_\lambda(t) = \frac{2\omega_{\text{ph}}}{\omega^2 - \omega_{\text{ph}}^2 - 2\omega_{\text{ph}} \tilde{\Pi}_\lambda(\omega)}, \quad (7.36)$$

where $\tilde{\Pi}_\lambda(\omega)$ is the phonon self-energy defined as the sum of all terms occurring in an expansion of $\tilde{\mathcal{D}}_\lambda(\omega)$ in powers of $\hat{\mathcal{H}}_{\text{el-ph}}$ that can be represented by Feynman diagrams that are one-phonon line-irreducible. To lowest non-vanishing order in the electron-



Figure 7.2: **Leading-order Feynman diagrams for the phonon self-energy.** The diagram on the left represents the *non-adiabatic* part of the phonon self-energy, while the diagram on the right represents its *adiabatic* part. The latter is akin to the “counterterms” used in high-energy physics to enforce certain renormalization conditions, which in this context corresponds to the requirement that the self-energy vanishes in the adiabatic limit. Compare also the discussion in Section 5.3.

phonon coupling, the phonon self-energy can be represented by the sum of diagrams in

⁴In terms of the quantities used in Chapter 5, $\omega_{\text{ph}}^{(\text{el,ad.})}$ corresponds to the diagonal matrix element of the electronic part of the adiabatic dynamical matrix for the phonon branches $\lambda = x, y$.

Fig. 7.2, which corresponds to

$$\tilde{\Pi}_\lambda(\omega) = \tilde{\Pi}_\lambda^{(\text{NA})}(\omega) - \tilde{\Pi}_\lambda^{(\text{ad.})}. \quad (7.37)$$

Here, the static, adiabatic part of the self-energy is simply given by

$$\tilde{\Pi}_\lambda^{(\text{ad.})} = \omega_{\text{ph}}^{(\text{el,ad.})}, \quad (7.38)$$

while the dynamic, non-adiabatic part reads

$$\tilde{\Pi}_\lambda^{(\text{NA})}(\omega) = \sum_m \sum_{\substack{n,n'; v=K,K'; \\ s=\pm}} \int \frac{d\omega'}{2\pi i} |g_{n,n'}^\lambda|^2 \tilde{G}_{n,m,v,s}(\omega + \omega') \tilde{G}_{n',m,v,s}(\omega'). \quad (7.39)$$

The sums run, in order, over the principal LL quantum numbers n, n' , the guiding center quantum number m , the valley index $v = K, K'$, and the spin $s = \pm$. The Fourier-transformed non-interacting electron Green's function reads [159]:

$$\begin{aligned} \tilde{G}_{n,m,v,s}(\omega) &\equiv \int_{-\infty}^{+\infty} dt e^{i\omega t} (-i) \langle 0 | \mathcal{T} \left\{ \hat{c}_{n,m,v,s;I}(0) \hat{c}_{n,m,v,s;I}^\dagger(t) \right\} | 0 \rangle \\ &= \frac{n_{n,m,v,s}}{\omega - \varepsilon_n - i\eta} + \frac{1 - n_{n,m,v,s}}{\omega - \varepsilon_n + i\eta}, \end{aligned} \quad (7.40)$$

with $n_{n,m,v,s}$ being the occupancy of the state $|n, m, v, s\rangle$ in the ground state and $\eta = 0^+$ being a positive infinitesimal. Evaluation of the frequency integral using the residue theorem then yields:

$$\tilde{\Pi}_\lambda^{(\text{NA})}(\omega) = \sum_m \sum_{\substack{n,n'; v=K,K'; \\ s=\pm}} |g_{n,n'}^\lambda|^2 \frac{n_{n',m,v,s} - n_{n,m,v,s}}{\omega - \varepsilon_n + \varepsilon_{n'}} \quad (7.41)$$

when the sum of the occupancies over the degenerate LL states, i.e., the sums over m , v , and s , can be expressed in terms of the partial filling factors as $g_{\text{LL}} \times (\bar{\nu}_{n'} - \bar{\nu}_n)$. It is customary [159, 161] to then also express the prefactor $g_{\text{LL}} |g_{n,n'}^\lambda|^2$ in terms of the

dimensionless electron-phonon coupling constant:

$$\lambda \equiv g_{\text{LL}} \left| \frac{3}{2\sqrt{NM}\omega_{\text{ph}}} \frac{\partial t}{\partial a} \right|^2 \bigg/ \omega_B^2 = \frac{9\sqrt{3}\beta^2}{\pi} \frac{1}{2M\omega_{\text{ph}}a_0^2} \sim 3 - 4 \times 10^{-3}, \quad (7.42)$$

where $\beta \equiv -(\text{d log } t)/(\text{d log } a) \approx 2$ is the logarithmic derivative of the first-nearest-neighbor hopping integral with respect to the nearest-neighbor distance and we used the fact that the factor A/N yields the unit cell area $A_{\text{uc}} = \sqrt{3}a_0^2/2$. Putting everything together, one obtains the following compact expression for the non-adiabatic part of the phonon self-energy:

$$\tilde{\Pi}_\lambda^{(\text{NA})}(\omega) = \lambda\omega_B^2 \sum_{n,n'} |C_n|^2 |C_{n'}|^2 \delta_{|n|,|n'|-1} (\bar{\nu}_{n'} - \bar{\nu}_n) \frac{2(\varepsilon_n - \varepsilon_{n'})}{\omega^2 - (\varepsilon_n - \varepsilon_{n'})^2}, \quad (7.43)$$

which is independent of the cartesian phonon polarization and hence we will drop the index λ from now on. In a final step, we can split the double sum over $n, n' \in \mathbb{Z}$ into two contributions, one from *inter*-band transitions $-n \rightarrow +(n+1)$ and $-(n+1) \rightarrow +n$ with energies $T_n \equiv \varepsilon_{n+1} + \varepsilon_n$, where $n \in \mathbb{N}_0$, and one from *intra*-band transitions $+n \rightarrow +(n+1)$ and $-(n+1) \rightarrow -n$ with energies $S_n \equiv \varepsilon_{n+1} - \varepsilon_n$, where $n \in \mathbb{N}$:

$$\tilde{\Pi}^{(\text{NA})}(\omega) = \frac{\lambda\omega_B^2}{2} \left\{ \sum_{n=0}^{\infty} \bar{\nu}_{T_n} \frac{2T_n}{\omega^2 - T_n^2} + \sum_{n=1}^{\infty} \bar{\nu}_{S_n} \frac{2S_n}{\omega^2 - S_n^2} \right\}. \quad (7.44)$$

For brevity, we introduced effective partial filling factors for the inter- and intra-band transitions via

$$\bar{\nu}_{T_n} \equiv (1 + \delta_{n,0})(\bar{\nu}_{-(n+1)} - \bar{\nu}_{+n} + \bar{\nu}_{-n} - \bar{\nu}_{+(n+1)})/2, \quad (7.45)$$

$$\bar{\nu}_{S_n} \equiv (\bar{\nu}_{-(n+1)} - \bar{\nu}_{-n} + \bar{\nu}_{+n} - \bar{\nu}_{+(n+1)})/2, \quad (7.46)$$

which are defined in such a way that $\bar{\nu}_{T_n} \rightarrow 1$ and $\bar{\nu}_{S_n} \rightarrow 0$ for all n in case of $n_{\text{el}} = 0$.

Note that for large n , we have $S_n \rightarrow 0$ and $T_n \simeq 2\omega_B\sqrt{n}$, and hence the sum over the contributions from inter-band transitions diverges, since $\sum_{n=0}^N 1/\sqrt{n} \simeq \sqrt{N}$ in the limit of large N . However, this divergence is merely an artifact of our usage of a model

of free, relativistic electrons in a magnetic field, which is unsuitable to describe high-energy excitations of electrons in graphene, for which the effective model can only be reasonably applied at lower energies. We thus cut off the sum at an index $n_{\max} = \Lambda/\omega_B$, where $\Lambda \sim 2 - 3$ eV is an excitation energy scale above which the effective, relativistic model is no longer applicable.

Having calculated the non-adiabatic contribution to the phonon self-energy, we can now easily pass to the *adiabatic* contribution, which is given by the electronic contribution to the phonon frequency in the adiabatic limit at zero Fermi energy and in the $B \rightarrow 0$ -limit. According to the considerations in Section 5.3, this contribution can also be calculated in a Green's function formalism and then reduces to the $\omega \rightarrow 0$ -limit of $\tilde{\Pi}^{(\text{NA})}(\omega)$ for $n_{\text{el}} = 0$ and $B \rightarrow 0$. At zero Fermi energy, all intra-band transitions are blocked by virtue of the Pauli principle and the contribution of inter-band transitions in the $B \rightarrow 0$ -limit can be shown to be given by [159, 161]:

$$\omega_{\text{ph}}^{(\text{el,ad.})} = \Pi^{(\text{NA})}(\omega = 0)|_{n_{\text{el}}=0} = -\lambda\omega_B^2 \sum_{n=0}^{\infty} \frac{1}{T_n}. \quad (7.47)$$

Again, the sum over n is divergent and needs to be cut off at the energy scale Λ .

By subtracting the non-adiabatic and adiabatic contributions, we arrive at the total phonon self-energy

$$\tilde{\Pi}(\omega) = \frac{\lambda\omega_B^2}{2} \left\{ \sum_{n=0}^{\infty} \left[\bar{\nu}_{T_n} \frac{2T_n}{\omega^2 - T_n^2} + \frac{2}{T_n} \right] + \sum_{n=1}^{\infty} \bar{\nu}_{S_n} \frac{2S_n}{\omega^2 - S_n^2} \right\}. \quad (7.48)$$

This expression is now perfectly finite at large energies, as the high-energy divergences of the adiabatic and non-adiabatic parts cancel each other, as long as the Fermi energy is not large enough to block high-energy inter-band transitions, when the cancelation would be prohibited. This behavior is physically sensible as a variation of the high-energy degrees of freedom, i.e., states deep inside the valence and conduction bands, should not influence the physical behavior of the system if the Fermi energy is only varied within the low-energy regime and if the magnetic field is kept small enough so that the cyclotron frequency $\omega_B \ll \Lambda$. Also note that in the adiabatic and zero-Fermi

energy limit, the phonon self-energy vanishes and the fully interacting Green's function has a pole at the adiabatic phonon frequency ω_{ph} , as required.

To provide a wider perspective, we want to point out that in many works [161–163], the adiabatic term in the Hamiltonian, proportional to $\omega_{\text{ph}}^{(\text{el,ad.})}$ (last term in Eq. 7.35), is simply omitted. However, this approach then requires the application of a regularization and renormalization procedure to render the physical predictions finite. This is typically done by introducing a co-called counterterm [88, 115] into the Lagrangian by rescaling the unperturbed phonon frequency $\omega_{\text{ph}} \rightarrow Z_\omega \omega_{\text{ph}} = \omega_{\text{ph}} + (Z_\omega - 1)\omega_{\text{ph}}$. This then leads to another term in the perturbation series, which can be represented by the second diagram in Fig. 7.2. The constant Z_ω is taken to also depend on the high-energy cutoff Λ . Its Λ -dependent part is then adjusted such that the phonon self-energy remains independent of the cutoff parameter Λ and its Λ -independent part is adjusted such that the phonon self-energy vanishes in the adiabatic, zero-doping, and zero- B -field limit. In this sense, the reasoning and the derivation presented here is equivalent to renormalization-based approaches typically employed in field theory.

In regards to the low-energy physics contained in the expression for the phonon self-energy, we note that $\tilde{\Pi}(\omega)$ has poles at the LL transition energies. The phonon thus *resonantly* couples to LL transitions when the magnetic field is such that the unperturbed (adiabatic) phonon frequency ω_{ph} matches one of the transition energies T_n or S_n . These resonances are known as *magneto-phonon resonances* (MPRs). The damping of the resonance can be taken into account by ascribing a finite lifetime or, equivalently, decay width to the transitions via $\Delta\varepsilon \rightarrow \Delta\varepsilon - i\gamma_\varepsilon/2$, where $\varepsilon = T_n, S_n$. While in principle the decay width could be calculated perturbatively, in the context of this work, we will take them as empirical parameters to be determined from experiment. In fact, as we will see in the next section, the MPR effect can be used to *experimentally determine* these electronic lifetimes.

To determine the change of the phonon frequencies when the non-adiabatic, resonant coupling to electronic transitions becomes important, one solves Dyson's equation to find the complex poles of the exact phonon Green's function:

$$\omega^2 - \omega_{\text{ph}}^2 - 2\omega_{\text{ph}}\tilde{\Pi}(\omega) = 0, \quad (7.49)$$

where $\omega = \omega_{\text{ph}}^{(\text{NA})} - i\gamma_{\text{ph}}^{(\text{tot})}/2$ is the complex phonon frequency, whose real part is the phonon frequency including non-adiabatic corrections and whose imaginary part equals half of the negative, total phonon decay width. To account for a finite lifetime of the phonon beyond its decay into an electron-hole pair, for example through anharmonic effects, i.e., phonon-phonon scattering, we also let $\omega_{\text{ph}} \rightarrow \omega_{\text{ph}} - i\gamma_{\text{ph}}/2$, where γ_{ph} is understood to capture the non-electron-phonon interaction-induced part of the phonon decay width. Like the electronic decay width, we will treat γ_{ph} as an empirical parameter, which can also be extracted from experiment.

Finally, we account for the effects of electron-electron interaction by modifying the transition energies $\Delta\varepsilon(B) = T_n(B), S_n(B)$ via $\Delta\varepsilon(B) \rightarrow \Delta\varepsilon(B) + \delta\Delta\varepsilon(B, n_{\text{el}})$. It has become common practice in the literature [47, 49] to define an *effective Fermi velocity* via

$$T_n \equiv v_{\text{F},T_n}(B, n_{\text{el}}) \sqrt{2eB/c} (\sqrt{n+1} + \sqrt{n}), \quad (7.50)$$

$$S_n \equiv v_{\text{F},S_n}(B, n_{\text{el}}) \sqrt{2eB/c} (\sqrt{n+1} - \sqrt{n}), \quad (7.51)$$

which captures the changes of the overall energy scale of the transition energies and also includes all deviations from the \sqrt{B} scaling law. The effective Fermi velocities can then be probed experimentally by observing the change of the phonon frequency with magnetic field, as we will discuss in the next section.

To summarize, we reviewed an effective model for the resonant coupling of the Raman-active in-plane optical phonon mode to electronic transitions in a finite magnetic field. The model contains only a small set of parameters that have a direct physical meaning: the unperturbed phonon frequency ω_{ph} , which corresponds to the observed phonon frequency at $n_{\text{el}} = 0$ and $B = 0$; the effective Fermi velocities v_{F,T_n} and v_{F,S_n} , which serve as a measure for the strength of many-body effects and can be extracted by probing the evolution of MPRs with magnetic field; the electron lifetimes γ_{T_n} and γ_{S_n} and the anharmonic contribution to the phonon lifetime γ_{ph} , which can be extracted from the “strength” of the MPRs and from the non-resonant phonon decay width, respectively; and finally the dimensionless electron-phonon coupling constant λ , which can be extracted from probing the phonon decay width in the regime where the LLs still form a

quasi-continuum.⁵

7.2 Magneto-phonon resonances as a probe for many-body effects and lifetimes

After we discussed the theoretical description of magneto-phonon resonances in graphene, we will now apply this model to study experimental results obtained from Raman spectroscopy in a finite magnetic field, which directly probes the optical phonon frequency and width. In particular, we will first focus on discussing how a measurement of the latter allows the extraction of electronic transition energies and lifetimes. Afterwards, we will go on to study the behavior of the electronic transition energies and widths when the charge carrier density is tuned via the application of a gate voltage, which allows the tuning of many-body effects by changing the number of free charge carriers in the system. Finally, we show how the same model can be used to quantify electronic lifetimes and anharmonic effects on the phonon lifetime. We will also study their behavior under changes of the number of co-called “hot” charge carriers, i.e., excited charge carriers that populate the conduction band.

7.2.1 Magneto-phonon resonances as a probe for many-body effects

To start with, we detail how the effect of magneto-phonon resonances can be used to probe electronic excitation energies. The basic idea consists of measuring the Raman spectrum of graphene as a function of magnetic field and monitor the evolution of the

⁵Note that so far, we did not discuss the issue of the screening of the electron-phonon interaction, but merely worked with the effective electron-phonon coupling stemming from the derivative of the empirical tight-binding parameter. As pointed out in Sections 4.4 and 5.3, the phonon self-energy in perturbation theory either can be written as the product of two unscreened electron-phonon couplings and the interacting two-particle correlation function or, equivalently, as the product of one screened electron-phonon coupling, an unscreened one and the independent-particle two-particle correlation function. Since we work with the latter, here, λ should actually be thought of as being proportional to the product of one screened and one unscreened electron-coupling. However, since we will treat it as a fitting parameter, this distinction has no consequences for the discussion in this chapter.

position and width of the G -peak. For certain values of the magnetic field B , the energy of an LL transition will match the unperturbed phonon energy ω_{ph} , at which point the two systems are in resonance. When the unperturbed phonon frequency matches the energy of an electronic transition, the lifetime reaches a minimum, as the decay of the phonon into an electronic excitation is energetically possible. Equivalently, the decay width of the phonon reaches a maximum in this case, which results in a broadening of the Raman G -peak. As is typical for a resonance, the frequency of the phonon will correspondingly show an oscillating behavior in the vicinity of the resonance as a function of B . By fitting the previously derived model as a function of B to the experimentally extracted position and full width at half maximum (FWHM) of the Raman G -peak, one can thus obtain values for the model parameters. As such, one can gain insight into, for example, the magnitude of the electron-phonon coupling, the effective Fermi velocities, and the electronic lifetimes.

To start with, we consider a graphene sample encapsulated in hexagonal boron nitride (hBN) and deposited on a silicon dioxide (SiO_2) substrate (see inset of Fig. 7.3a). The boron nitride layers serve both as a protection from detrimental environmental influences and as an atomically flat substrate for graphene. Both are important to ensure sufficiently long electronic lifetimes that allow the observation of magneto-phonon resonances (MPRs). The Raman measurements were carried out⁶ at a temperature of 4.2 K and with a linearly polarized laser beam of wavelength 532 nm, a power of 0.5 mW, and a spot diameter of approximately 500 nm. The scattered light was detected with a CCD camera after having been diffracted by a diffraction grating of 1200 lines/mm.

Fig. 7.3a shows a typical recorded Raman spectrum of the studied device at zero magnetic field. Besides the presence of the G - and $2D$ -peaks of graphene, the spectrum also features a third prominent peak (labeled “hBN”), stemming from the one-phonon Raman response of the hBN layers. The dependence of the Raman spectrum on the magnetic field is shown in Fig. 7.3b, with the recorded Raman intensity being color-encoded. While the $2D$ - and hBN -peaks do not show any noticeable dependence on the magnetic field, the G -peak undergoes a series of magneto-phonon resonances, with

⁶The actual measurements were carried out by C. Neumann.

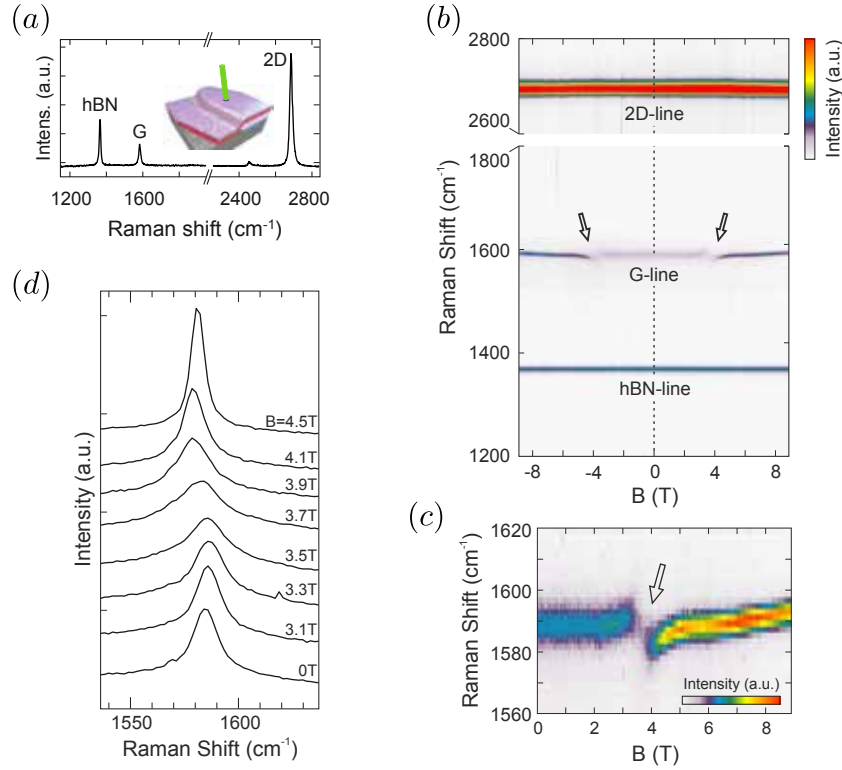


Figure 7.3: **Magneto-Raman spectra of a graphene-boron nitride heterostructure.** (a) Raman spectrum of an hBN-graphene-hBN heterostructure at zero magnetic field. Visible are the G - and $2D$ -peaks of graphene originating from one- and two-phonon scattering processes, respectively, and the one-phonon Raman peak of hBN. The inset shows a sketch of the sample, which consists of an hBN-graphene-hBN heterostructure deposited on a SiO_2 substrate (blue: hBN, red: graphene, grey: SiO_2). (b) Color-encoded Raman spectra as a function of magnetic field, recorded at a temperature of $T=4.2$ K. The arrows mark the occurrence of the MPR associated with the T_1 -LL transition. (c) Zoom-in into the area of panel (b) around the G -peak and for positive values of B only. (d) Evolution of the G -peak as a function of magnetic field. Around the MPR, the peak widens considerably, as expected for resonant coupling. (Figure adapted and reprinted with permission from Neumann, C. *et al.*, *Nano Lett.* **15**, 1547-1552 (2015). Copyright 2015 by the American Chemical Society.)

the most visible one appearing at around $B \approx 3.7$ T (see zoom-in shown in Fig. 7.3 and compare arrows in Fig. 7.3b and c). This MPR corresponds to the resonant coupling of the phonon to the inter-band T_1 -LL transition (see previous section). We will refer

to it as the T_1 -MPR in the following. In order to further analyze the MPRs, we fit the G -peak of each individual spectrum (one for each B -field value) with a Lorentzian. As seen by the sample spectra shown in Fig. 7.3d, this is possible even in the vicinity of the strongest magneto-phonon resonance.

The fitted position and full width at half maximum (FWHM) of the G -peak as a function of magnetic field are depicted in Fig. 7.4a and b, respectively. The evolution of the G -peak with magnetic field features three resonances at $B=2.1$ T, $B=3.7$ T, and $B=5.8$ T, which appear as oscillations in its position and as peaks in its FWHM, as highlighted by arrows in Fig. 7.4b. As illustrated in Fig. 7.4c, the B -field values at which the first two resonances occur correspond well to the expected values from the resonance conditions $\omega_{\text{ph}} = T_2$ and $\omega_{\text{ph}} = T_1$ (compare dashed blue lines), i.e., the corresponding features can be attributed to the magneto-phonon resonances discussed in the previous section. The feature at $B=5.8$ T, however, cannot be explained by the resonance of the unperturbed phonon with the T_n -LL transitions. Instead, its position on the B -field axis matches the value obtained from the resonance condition $\omega_{\text{ph}} = L_1$ (compare dashed red line), where

$$L_n \equiv v_{\text{F},L_n}(B, n_{\text{el}}) \sqrt{2eB/c} (\sqrt{n} + \sqrt{n}) \quad (7.52)$$

denotes the energy of the $-n \rightarrow +n$ inter-band Landau level transition, which we will refer to as L_n . These transitions can only couple to the phonon due to higher-order processes not included in our model derived from an isotropic $B = 0$ band structure and as such the corresponding MPR is much less pronounced. We include it in our model by introducing an effective coupling constant $\lambda_L \sim 0.01 - 0.02\lambda \ll \lambda$ and by modifying the phonon self-energy according to

$$\tilde{\Pi}(\omega) \rightarrow \tilde{\Pi}(\omega) + \frac{\lambda_L \omega_B^2}{2} \sum_{n=1}^{\infty} \left[\bar{\nu}_{L_n} \frac{2L_n}{\omega^2 - L_n^2} + \frac{2}{L_n} \right], \quad (7.53)$$

with $\bar{\nu}_{L_n} \equiv 2(\bar{\nu}_{-n} - \bar{\nu}_{+n})$ being the corresponding effective filling factor for the L_n -transitions.

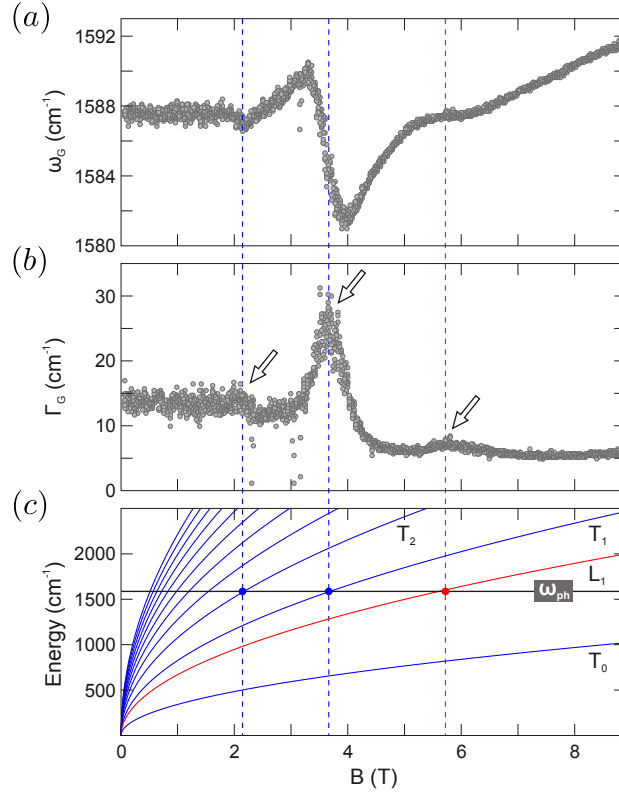


Figure 7.4: **Magneto-phonon resonances in graphene.** (a) and (b) Position and full width at half maximum (FWHM) of the Raman G -peak of graphene as a function of magnetic field, obtained from Lorentzian fits to the data shown in Fig. 7.3. The arrows highlight the magneto-phonon resonances due to the inter-band LL transitions T_1 and T_2 as well as a weaker resonance due to the LL transition $-1 \rightarrow +1$. (c) Inter-band LL transition energies T_1 (blue lines) as a function of magnetic field for effective Fermi velocities $v_{F,T_n} = 1.17 \times 10^6$ m/s. The black line represents the unperturbed phonon frequency $\omega_{\text{ph}} = 1586 \text{ cm}^{-1}$. The red line depicts the energy of the inter-band LL transition $-1 \rightarrow +1$, L_1 , as a function of B . (Figure adapted and reprinted with permission from Neumann, C. *et al.*, *Nano Lett.* **15**, 1547-1552 (2015). Copyright 2015 by the American Chemical Society.)

In order to use the visible magneto-phonon resonances as a probe for certain quantities, we can use the analytical model for MPRs reviewed in the last section. The red traces in Fig. 7.5 represent the result of a calculation of the perturbed phonon fre-

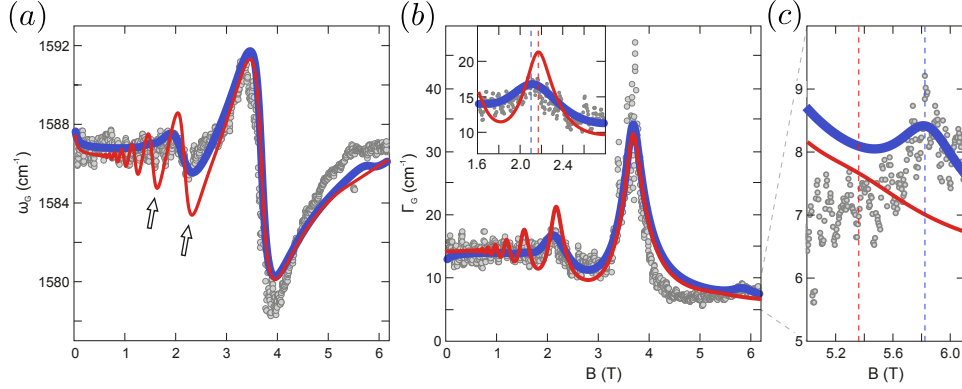


Figure 7.5: **Theoretical description of magneto-phonon resonances in graphene.** (a) and (b) Comparison of the theoretical model (blue and red lines) and the experimental data (grey dots) of the G -peak frequency (panel (a)) and FWHM (panel (b)). The red lines correspond to the solutions of Dyson's equation for a phonon self-energy evaluated at zero charge carrier density and with the parameters set to $\lambda=4\times 10^{-3}$, $\lambda_L = 0.015\lambda$, $\omega_{\text{ph}}=1586 \text{ cm}^{-1}$, $\gamma_{\text{ph}}=5.5 \text{ cm}^{-1}$, $\gamma_{T_n}=\gamma_{L_n}=160 \text{ cm}^{-1}$, and $v_{F,T_n}=v_{F,L_n}=1.17\times 10^6 \text{ m/s}$. The blue lines feature different effective Fermi velocities of $v_{F,T_1}=1.17\times 10^6 \text{ m/s}$, $v_{F,T_2}=1.19\times 10^6 \text{ m/s}$, and $v_{F,L_1}=1.12\times 10^6 \text{ m/s}$ and decay widths of $\gamma_{T_1}=160 \text{ cm}^{-1}$, $\gamma_{T_2}=270 \text{ cm}^{-1}$, and $\gamma_{L_1}=80 \text{ cm}^{-1}$ for the T_1 -, T_2 , and L_1 -MPRs, respectively, while we additionally used values of $\gamma_{T_0}=20 \text{ cm}^{-1}$ and $\gamma_{T_{n\geq 3}}=400 \text{ cm}^{-1}$. The arrows in panel (a) highlight the overestimation of the magneto-phonon resonances due to the T_2 - and T_3 -LL transitions in a model with one common electronic decay width. The inset in panel (b) is a zoom-in into the vicinity of the T_2 -MPR to highlight that a different effective Fermi velocity than that used for the T_1 -transition is needed (compare vertical, dashed lines). (c) Zoom-in into the vicinity of the L_1 -MPR to highlight that a different effective Fermi velocity than that used for the T_1 - and T_2 -transitions is needed (compare vertical, dashed lines). (Figure adapted and reprinted with permission from Neumann, C. *et al.*, *Nano Lett.* **15**, 1547-1552 (2015). Copyright 2015 by the American Chemical Society.)

quency and width at zero Fermi energy where we used the same effective Fermi velocity of $v_{F,T_n}=v_{F,L_n}=1.17\times 10^6 \text{ m/s}$ for all T_n - and L_n -transitions⁷ and assigned the same decay width of $\gamma_{T_n}=\gamma_{L_n}=160 \text{ cm}^{-1}$ to all of them. The values of v_{F,T_n} and γ_{T_n} were chosen such that the T_1 -MPR is described well. The other parameters can be directly read off from the data: $\omega_{\text{ph}}=1586 \text{ cm}^{-1}$ is given by the G -peak position at vanishing

⁷At zero Fermi energy, all S_n -transitions are disallowed by the Pauli principle.

magnetic field; γ_{ph} , which denotes the non-electronic part of the phonon decay width, corresponds to the FWHM of the G -peak at $B \approx 8$ T, where no electronic transitions are energetically matched with the phonon mode and the latter can thus only decay via non-electronic processes; $\lambda=4 \times 10^{-3}$, the dimensionless electron-phonon coupling constant, can be extracted from the requirement that the total decay width of the phonon at zero B -field, which is given by the sum of its electronic and non-electronic parts, matches the FWHM of the G -peak at vanishing magnetic field; and λ_L , which was adjusted to correctly describe the strength of the L_1 -MPR (compare the blue lines in Fig. 7.5).

While the order of magnitude of the electronic decay width and the value of the electron-phonon coupling are in the same range as those measured previously [27, 37, 42–44, 167], the use of a common electronic decay width for all LL transitions overestimates the strength of the MPRs at lower values of the magnetic field (see arrows in Fig. 7.5a, which highlight the T_2 - and T_3 -MPRs). Furthermore, it is not possible to correctly describe the position of all magneto-phonon resonances with one common Fermi velocity (compare vertical dashed lines in the inset of Fig. 7.5b and in Fig. 7.5c), that is to say, many-body effects due to electron-electron interaction affect different LL transitions with different magnitude. To quantify the different magnitude of many-body effects on the transitions visible as MPRs, we assign different effective Fermi velocities of $v_{F,T_1}=1.17 \times 10^6$ m/s, $v_{F,T_2}=1.19 \times 10^6$ m/s, and $v_{F,L_1}=1.12 \times 10^6$ m/s and electronic decay widths of $\gamma_{T_1}=160$ cm $^{-1}$, $\gamma_{T_2}=270$ cm $^{-1}$, and $\gamma_{L_1}=80$ cm $^{-1}$ to the T_1 -, T_2 -, and L_1 -transitions. In addition to that, we also set $\gamma_{T_0}=20$ cm $^{-1}$ and $\gamma_{T_{n \geq 3}}=400$ cm $^{-1}$. The high value for the latter has to be chosen to completely suppress the MPRs due to T_n -transitions with $n \geq 3$, which are not visible in our data. The physical reason for the significantly lower lifetimes⁸ of the higher T_n -transitions can be related to the availability of more phase space in their decay processes.

While the determination of the electronic decay widths is to an extend error-prone due to the strength of the MPRs still being well-described even when the γ_{T_n,L_n} are varied by up to 25%, the determination of the effective Fermi velocities is very accurate, as it is determined from the value of the B -field at which the MPR occurs, which is

⁸Recall that $\tau = 1/\gamma$.

only determined by the sharp resonance condition $\omega_{\text{ph}} = T_n, L_n$. The latter can be inverted to yield the effective Fermi velocity if ω_{ph} and the corresponding B -field value are known (compare Eqs. 7.50 and 7.52). The values of the effective Fermi velocities for different LL transitions vary by up to 7%, indicating that many-body effects indeed influence different LL transitions with different strength, as previously predicted theoretically [168–170].

7.2.2 Tuning many-body effects in graphene

So far, we have shown how the phenomenon of magneto-phonon resonances can be used to gain insight into many-body effects by using it to extract both the coupling of the electronic system to the Raman-active in-plane optical phonon, the electronic decay widths, and, most accurately, the effective Fermi velocities. Note that, in this context, the latter no longer have the meaning of a physical velocity, but rather describe the overall energy scale of the LL transitions. The Fermi velocity, in particular, has been shown both experimentally [78, 156, 171, 172] and theoretically [78, 173–175] to be strongly influenced by many-body effects, as it is very sensitive to changes of the Fermi energy, i.e., of the charge carrier density n_{el} , to the point where it has been shown to *diverge logarithmically* when n_{el} approaches the charge neutrality point *at zero and small magnetic fields*. However, little is known about the impact of many-body effects on the electronic bands in stronger, quantizing magnetic fields. While the behavior of electronic transition energies under changes of the magnetic field has been studied experimentally [49], the influence of changes of the Fermi level, i.e., the number of charge carriers in the system, is still not known.

However, the combination of applying a strong magnetic field, simultaneously tuning the charge carrier density, and actually extracting changes of the many-body effects, typically in the form of the effective Fermi velocity, is experimentally very challenging. The application and especially the tuning of strong magnetic fields requires a superconducting electromagnet, which needs to be operated at cryogenic temperatures. This, however, rules out the method of choice for extracting the effective v_{F} via transport measurements, as the latter is based on measuring the temperature-dependence of the amplitude of the Shubnikov-de Haas oscillations of the electrical conductivity [78, 79].

This only leaves optical methods to probe the effective Fermi velocity. As we have seen in the last section, the effect of magneto-phonon resonances can be used for that purpose. However, the visibility of the MPRs crucially depends on sufficiently long electronic lifetimes, i.e., the sample needs to be sufficiently clean and protected from environmental influences. This can, for instance, be achieved by encapsulating graphene in hexagonal boron nitride, as done for the sample featured in the previous section. By contrast, merely depositing graphene on a standard SiO₂ wafer substrate will result in invisible MPRs [47].

A graphene-hBN heterostructure is thus a perfect choice for the study of many-body effects via MPRs. However, this kind of structure is unfortunately unsuitable for a simultaneous tuning of the charge carrier density. The only practical way to do the latter in a modern experimental setting consists of depositing the heterostructure on a back gate and applying a voltage between the graphene flake (via side contacts [2]) and the back gate (typically consisting of doped silicon). The graphene flake and the back gate then act as the two plates of a plate capacitor and become charged, i.e., the number of charge carrier in the graphene flake can be tuned by tuning the voltage. While this method is extensively used in transport experiments, it cannot be used in optical experiments. The reason for this is the unavoidable presence of defects in hBN, whose electronic states lie inside the normally ~ 7 eV-wide band gap of bulk hBN. These states lead to additional optically active transitions in the visible light spectrum [176], which will be activated in a typical MPR experiment with a laser in the visible light range.⁹ These excited charge carriers are then mobile and will screen the effect of the back gate entirely, thus rendering it useless [177].¹⁰

For this reason, a different sample is required that still offers high electronic lifetimes and thus enables the observation of magneto-phonon resonances and at the same time allows the tuning of the charge carrier density. To this end, we use a *current-annealed*,

⁹The usage of light in the infrared spectrum will result in a too weak Raman signal (see Section 6.2), while the usage of ultraviolet light will either lead to structural damage to the sample when taking the required laser power for a useful signal into account or will excite non-defect transitions in the boron nitride layers.

¹⁰This “photo-induced doping” effect can however be used in a confocal setup to induce different numbers of charge carriers into different parts of a sample by moving the laser across the sample whilst varying the back gate voltage [178].

suspended graphene device,¹¹ which until recently could not be created in that quality. The device consists of an exfoliated graphene flake, contacted by chrome/gold contacts, and suspended over a SiO₂ substrate by etching away ≈ 160 nm of the latter. After cleaning the graphene flake by current annealing [179], the graphene flake features a charge carrier mobility in excess of 400,000 cm²/(Vs) and a charge carrier density inhomogeneity below 10⁹ cm⁻², which are enough to guarantee the observation of MPRs. This device, for the first time, allows both the tuning of many-body effects and their probing in both the low- and the high- B -field regime.

The Raman measurements were done ¹¹ in the same measurement setup, at the same temperature, and with the same laser settings as specified in the previous section. We recorded the Raman spectrum as a function of the magnetic field for various different values of the back gate voltage and in Fig. 7.6a and b, we show the position ω_G and FWHM Γ_G , respectively, of the graphene G -peak as obtained from Lorentzian fits to these spectra. For later use, we note that the back gate voltage V_g can be converted to the charge carrier density n_{el} via the linear relation $n_{el} = \alpha(V_g - V_0)$, where $V_0 = -0.2$ V accounts for the residual doping of the graphene flake. The lever arm $\alpha = 3.15 \times 10^{10}$ cm⁻²/V has been extracted from a Landau fan measurement (see Supplementary Material to Ref. 79).

We observe the typical MPR-behavior in the form of a clearly visible oscillation of the G -peak position around $B \approx 3$ T, accompanied by a strong increase in the broadening of the peak. Just as in the other sample, this most prominent resonance is due to the resonant coupling of the Raman-active in-plane optical phonon with the LL transition T_1 . Focussing on its behavior under changes of the charge carrier density n_{el} , we note that the B -field value at which it occurs, B_{T_1} , shifts towards higher values when n_{el} is increased (compare full, black and dashed, red arrows in Fig. 7.6). In order to quantify the changes induced by a change of n_{el} , we fit single Lorentzians to Γ_G as a function of B (see full black lines in Fig. 7.6b). In this way, we can precisely extract B_{T_1} and the maximum value Γ_G at the resonance, Γ_{G,T_1}^{\max} , as a function of the charge carrier density, as displayed in Fig. 7.7.

¹¹The device fabrication and the measurements were carried out by J. Sonntag.

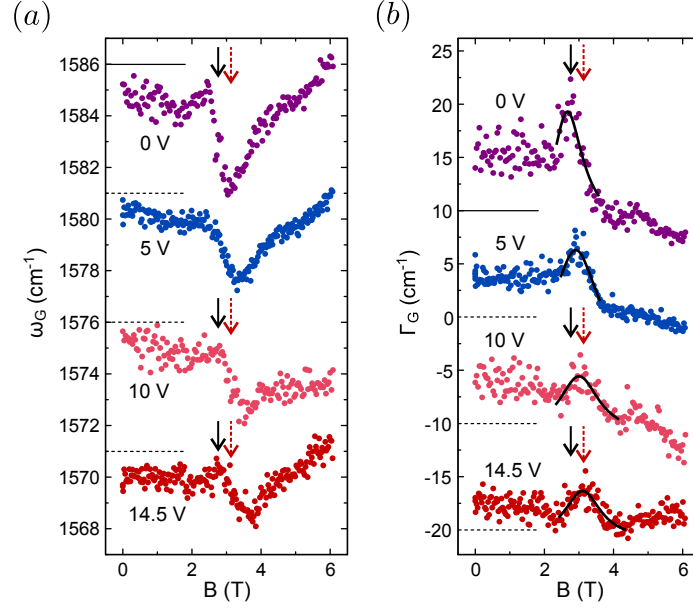


Figure 7.6: **Charge carrier density dependence of magneto-phonon resonances in graphene.** (a) and (b) Position and FWHM, respectively, of the Raman G -peak of suspended graphene as a function of magnetic field for different values of the back gate voltage V_g , which tunes the charge carrier density n_{el} . The different traces are offset by 5 cm^{-1} and 10 cm^{-1} for clarity (see horizontal, dashed lines). The full black lines depict Lorentzian fits to the FWHM around the T_1 -MPR. The full, black and dashed, red arrows highlight the shift of the T_1 -MPR with a change in n_{el} from $V_g=0 \text{ V} \hat{=} n_{\text{el}} \approx 0 \text{ cm}^{-2}$ to $V_g=14.5 \text{ V} \hat{=} n_{\text{el}} \approx 0.5 \times 10^{12} \text{ cm}^{-2}$, respectively. (Figure adapted and reprinted with permission from Sonntag, J. *et al.*, *Phys. Rev. Lett.* **120**, 187701 (2018). Copyright 2018 by the American Physical Society.)

The decrease of $\Gamma_{G,T_1}^{\text{max}}$ with increasing $|n_{\text{el}}|$ can be understood in terms of the increasing filling of the degenerate Landau level states. For small $|n_{\text{el}}|$, the Fermi energy stays within the states belonging to the zeroth LL and hence the T_1 -MPR remains almost unaffected as it only involves the LL transitions $-2 \rightarrow +1$ and $-1 \rightarrow +2$. For higher values of $|n_{\text{el}}|$, the states belonging to the first LL become filled up and as a result more and more of the degenerate transitions contributing to the T_1 -MPR become blocked by the Pauli principle, which results in a decrease of the strength of the T_1 -MPR as measured by $\Gamma_{G,T_1}^{\text{max}}$. This decrease of $\Gamma_{G,T_1}^{\text{max}}$ with $|n_{\text{el}}|$ is in good agreement

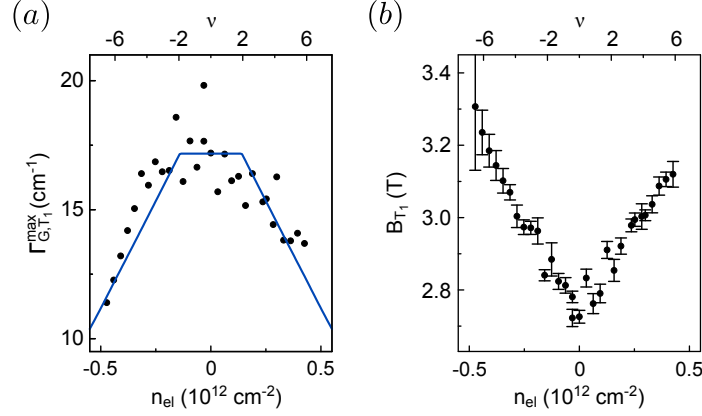


Figure 7.7: **Evolution of the T_1 -MPR with charge carrier density.** (a) Peak width of the Raman G -peak at the T_1 -MPR as a function of charge carrier density n_{el} . The black dots represent experimental data, the blue line represents the theoretical prediction obtained with the parameters $\lambda=4\times 10^{-3}$, $\omega_{\text{ph}}=1584.4 \text{ cm}^{-1}$, $\gamma_{\text{ph}}=7.6 \text{ cm}^{-1}$, $\gamma_{\text{el},T_n}=395 \text{ cm}^{-1}$, and $v_{\text{F},T_n}=1.33\times 10^6 \text{ m/s}$. (b) B -field value at which the T_1 -MPR occurs, B_{T_1} , as a function of n_{el} . The upper axis in both panels shows the filling factor ν at a magnetic field of $B=3 \text{ T}$. (Figure adapted and reprinted with permission from Sonntag, J. *et al.*, *Phys. Rev. Lett.* **120**, 187701 (2018). Copyright 2018 by the American Physical Society.)

with the theoretical predication based on the change of the effective filling factor $\bar{\nu}_{T_1}$ (see Eq. 7.45). The latter is linear in n_{el} and enters linearly into the imaginary part of the phonon self-energy, which in turn enters additively into Γ_G . In consequence, Γ_{G,T_1}^{\max} is expected to decrease linearly with $|n_{\text{el}}|$, as shown as a blue line in Fig. 7.7b, which is in good agreement with the experimental data.

On the other hand, the value of B_{T_1} , i.e., the position on the B -field axis at which the T_1 -MPR occurs, *increases* with $|n_{\text{el}}|$. From the resonance condition

$$\omega_{\text{ph}} = v_{\text{F},T_n}(B_{T_1}, n_{\text{el}}) \sqrt{2eB_{T_1}/c} (\sqrt{n+1} + \sqrt{n}), \quad (7.54)$$

it is clear that the value of B_{T_1} only depends on the unperturbed phonon frequency $\omega_{\text{ph}} = \omega_G(B = 0 \text{ T}, n_{\text{el}} = 0 \text{ cm}^{-2})$ and the effective Fermi velocity $v_{\text{F},T_1}(n_{\text{el}}) \equiv v_{\text{F},T_1}(B = B_{T_1}, n_{\text{el}})$. Changes of ω_{ph} , for example due to tensile strain from electrostatically pulling the graphene sheet, can be ruled out as the source of the change of B_{T_1} as the observed

variation of ω_{ph} on the order of 2 cm^{-1} is negligible (see Supplementary Material to Ref. 79). Furthermore, tensile strain would lead to a *decrease* of ω_{ph} , as the atomic bonds are *softened*, and thus it could only lead to a decrease of B_{T_1} with increasing $|n_{\text{el}}|$. Therefore, the observed change of B_{T_1} can only be attributed to a change of the LL transition energies, which can be described by a change of the effective Fermi velocity $v_{\text{F},T_1}(n_{\text{el}})$ with n_{el} .

In order to be more quantitative about the latter, we use the resonance condition Eq. 7.54 to calculate $v_{\text{F},T_1}(n_{\text{el}})$ from the measured values of B_{T_1} , as shown in Fig. 7.8. The effective Fermi velocity ranges from $v_{\text{F},T_1}(n_{\text{el}}) \approx 1.36 \times 10^6 \text{ m/s}$ at the charge neutrality point $n_{\text{el}} = 0 \text{ cm}^{-2}$ to $v_{\text{F},T_1}(n_{\text{el}}) \approx 1.24 \times 10^6 \text{ m/s}$ at a charge carrier density of $|n_{\text{el}}| \approx 0.4 \times 10^{12} \text{ cm}^{-2}$. Most importantly, we observe a *finite, linear* behavior of $v_{\text{F},T_1}(n_{\text{el}})$ near the charge neutrality point, contrary to the case of the effective Fermi velocity at low magnetic field, which logarithmically diverges (see blue and purple dots in the inset of Fig. 7.8). To understand this linear decrease of v_{F,T_1} as a function of $|n_{\text{el}}|$, we study the renormalization of v_{F,T_1} in more detail from a theoretical point of view.

To this end, we consider the electron self-energy of one Landau level on the level of the Hartree-Fock approximation (compare Sections 3.2 and 3.3.1):

$$\begin{aligned} \Sigma_n^{\text{HF}}(B, n_{\text{el}}) &\equiv \frac{1}{g_{\text{LL}}/2} \sum_{m,v} \Sigma_{n,m,v}^{\text{HF}}(B, n_{\text{el}}) \\ &= \frac{1}{g_{\text{LL}}/2} \sum_{m,v} \sum_{n',m',v'} \bar{\nu}_{n'}(B, n_{\text{el}}) \left(2v_{(n',m',v')}^{\text{Hart.}}(B) - v_{(n,m,v)}^{\text{Fock}}(B) \right). \end{aligned} \quad (7.55)$$

Here, we defined a self-energy for LL n by averaging over the self-energies of all degenerate states belonging to this LL. The sum runs over all guiding center quantum numbers m and the valley index $v = K, K'$.¹² The spin-independent self-energy of one LL state $|n, m; v\rangle$ in the Hartree-Fock approximation is given by the product of the partial filling factor $\bar{\nu}_n$ and the sum of the Hartree (or *direct Coulomb*) contribution,

¹²As the self-energy is independent of spin, we do not need to average over the spin degree of freedom and as such the normalization factor of the sum is given by half of the LL degeneracy only, i.e., $g_{\text{LL}}/2$.

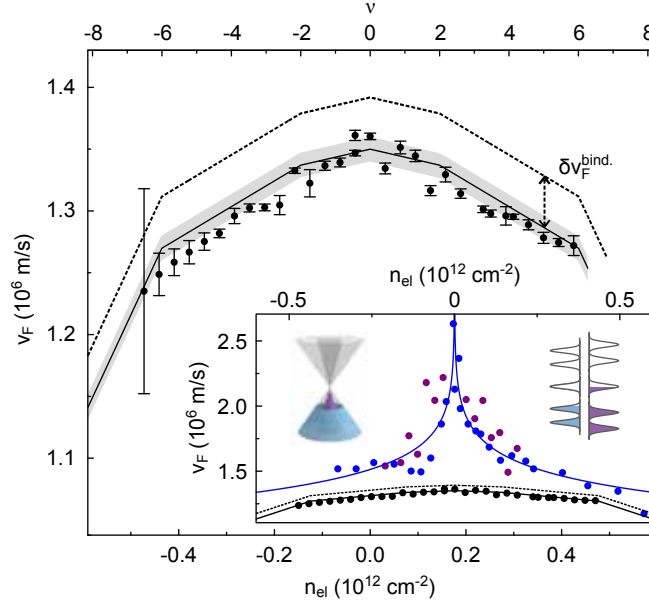


Figure 7.8: **Evolution of the effective Fermi velocity with charge carrier density.** The effective Fermi velocity v_{F,T_1} as a function of charge carrier density n_{el} . The upper axis in both the main figure and the inset shows the filling factor ν at a magnetic field of $B=3$ T. Black dots with error bars denote experimental data, while full and dashed lines represent the results of the theoretical calculation with and without the excitonic binding energy, respectively. The grey-shaded area illustrates the uncertainty related to the B -field-dependent renormalization due to states beyond the high-energy cutoff [49]. Inset: Comparison between effective Fermi velocities as extracted from transport experiments (blue dots from the work by Elias *et al.* [78]; purple dots from the same device as the one of the shown Raman data) and MPR measurements (black dots). The full blue line depicts the theoretically predicted logarithmic renormalization at low magnetic fields. The sketches illustrate the difference between the renormalization of the effective v_F at low (left) and high magnetic field (right) with increasing n_{el} (blue to purple shades). (Figure adapted and reprinted with permission from Sonntag, J. *et al.*, *Phys. Rev. Lett.* **120**, 187701 (2018). Copyright 2018 by the American Physical Society.)

calculated from the matrix elements

$$v_{(n',m',v')}^{Hart.}(n,m,v)(B) = \frac{e^2}{\epsilon} \int d^3r \int d^3r' \frac{|\phi_{n,m,v}(\mathbf{r})|^2 |\phi_{n',m',v'}(\mathbf{r}')|^2}{|\mathbf{r} - \mathbf{r}'|}, \quad (7.56)$$

and the negative Fock (or *exchange*) contribution, computed from the matrix elements

$$v_{\substack{(n,m,v) \\ (n',m',v')}}^{\text{Fock}}(B) = \frac{e^2}{\epsilon} \int d^3r \int d^3r' \frac{\phi_{n,m,v}(\mathbf{r})\phi_{n',m',v'}^*(\mathbf{r})\phi_{n',m',v'}(\mathbf{r}')\phi_{n,m,v}^*(\mathbf{r}')}{|\mathbf{r} - \mathbf{r}'|}, \quad (7.57)$$

where $\phi_{n,m,v}(\mathbf{r}) \equiv \langle \mathbf{r} | n, m; v \rangle$ denotes the wave function of the state $|n, m; v\rangle$. Note that in the Hartree term, the total electron density contributes, which is given by the sum of the (equal) spin-up and spin-down contributions. In the Fock term, by contrast, only one spin polarization contributes, as it has its origins in the Pauli exclusion principle, which affects only electrons in the same spin state and thus gives rise to the absence of the prefactor of 2. We calculated¹³ the LL state wave functions and the Hartree and Fock matrix elements within a third-nearest tight-binding model [180], wherein the magnetic field is included via the Peierls substitution [181–183] and edge states are eliminated by including a finite mass boundary term. The calculations were done for a quadratic 40×40 nm² graphene-flake in a magnetic field of $B=200$ T. The size of the flake was chosen in order to keep the calculations feasible, while the very high magnetic field results in a magnetic length of ≈ 1.8 nm and thus yields a sizable number of degenerate LL states for this flake size. To make the results of this calculation applicable to the experimental case of $B \approx 3$ T, we use the scale invariance of the effective Hamiltonian and the Coulomb matrix elements and appropriately rescale the magnetic field length according to $l_B \propto 1/\sqrt{B}$. The numerical results then effectively correspond to an $\approx 330 \times 330$ nm²-sized flake. Finally, we account for intrinsic screening effects of the graphene flake by introducing an effective dielectric constant of $\epsilon=3.1$.

In terms of the LL self-energy, the single-particle energies become shifted (or *renormalized*): $\varepsilon_n \rightarrow \varepsilon_n + \Sigma_n^{\text{HF}}$. As a result, the effective Fermi velocity $v_{\text{F},T_1}(n_{\text{el}})$ evolves according to

$$v_{\text{F},T_1}(n_{\text{el}}) = v_{\text{F},T_1}(n_{\text{el}}^{(0)}) + \frac{\Delta \Sigma_{n+1}^{\text{HF}}(n_{\text{el}}) - \Delta \Sigma_{-n}^{\text{HF}}(n_{\text{el}})}{\sqrt{2eB_{T_1}/c}(\sqrt{2} + 1)}, \quad (7.58)$$

where $\Delta \Sigma_n^{\text{HF}}(n_{\text{el}}) \equiv \Sigma_n^{\text{HF}}(n_{\text{el}}) - \Sigma_n^{\text{HF}}(n_{\text{el}}^{(0)})$ denotes the difference in self-energies at charge carrier densities of n_{el} and $n_{\text{el}}^{(0)} \equiv 0$ cm⁻². It is important to note that in this difference, all contributions from states outside the energy window defined by $n_{\text{el}}^{(0)}$ and n_{el} drop

¹³The numerical calculations of the wave functions and matrix elements were done by F. Libisch.

out for constant magnetic field, as their occupancies do not change. This applies in particular to contributions from all states not considered in our effective model, i.e., the states deep inside the valence and conduction bands that lie beyond the high-energy cutoff Λ , as they lie outside this n_{el} -defined window. Note that this ensures that the *change* of the renormalized effective Fermi velocity does not depend on the precise choice of the high-energy cutoff Λ , as it must be if the Fermi energy is varied only on an energy scale much less than Λ . The only way in which the states beyond the high-energy cutoff influence the renormalized Fermi velocity is through their contribution to the value of $v_{\text{F},T_1}(n_{\text{el}}^{(0)})$, which we fix to the experimentally extracted value of $v_{\text{F},T_1}(n_{\text{el}}^{(0)})=1.35\times 10^6$ m/s.¹⁴ Note that this value is higher than that found for the hBN-graphene-hBN heterostructure, given in the previous section, due to the absence of screening from the substrate environment.

As seen from the black line in Fig. 7.8, the theoretical results match the experimentally extracted values of v_{F,T_1} (black dots) very well. Note that due to the n_{el} -induced shift of v_{F,T_1} , each value of v_{F,T_1} has experimentally been extracted at a slightly different magnetic field B_{T_1} (compare Eq. 7.54). At different magnetic fields, however, the contribution of states from beyond the high-energy cutoff changes slightly by a logarithmic correction proportional to $\log(B_1/B_2)$ [49]. On the basis of the results of the calculation presented in the Supplementary Material to Ref. 49, we estimate this effect to be on the order of $\delta v_{\text{F},T_1}\approx 0.02\times 10^6$ m/s for the observed range of B_{T_1} -values (2.8 T to 3.2 T) and depict this uncertainty as a grey-shaded band in Fig. 7.8. However, it does not affect any of the conclusions drawn in the following.

The excellent agreement between our calculations and our measurements allow us to give a simple explanation for the observed linear decrease of the effective Fermi velocity with $|n_{\text{el}}|$. As seen from Eq. 7.55, the Hartree and Fock matrix elements only depend on the value of the magnetic field but not on the charge carrier density. Therefore, the only dependence of the Hartree-Fock self-energy on the charge carrier density is through the partial filling factor $\bar{\nu}_n$, which depends linearly on n_{el} . As seen in Section 7.1.2, this

¹⁴In the language of renormalization group (RG) approaches [78, 173, 174], the value of $v_{\text{F},T_1}(n_{\text{el}}^{(0)})$ serves as the initial value for the integration of the RG flow equation and in this sense can also be interpreted as an integration constant that must be fixed such that the renormalization condition $v_{\text{F},T_1}(n_{\text{el}})|_{n_{\text{el}}=n_{\text{el}}^{(0)}} = v_{\text{F},T_1}(n_{\text{el}}^{(0)})$, with $v_{\text{F},T_1}(n_{\text{el}}^{(0)})$ fixed by experiment, is satisfied.

linear dependence has its origins in the degeneracy of the Landau levels. The Hartree and Fock matrix elements merely set the rate of the decrease with n_{el} , i.e., the *slope* of the curve depicted in Fig. 7.8. The slope remains constant as long as the Fermi energy is varied within one LL. When the Fermi level enters the next Landau level, different Hartree and Fock matrix elements start to contribute to the self-energy and as a result the slope changes. This behavior can be found in the curve shown in Fig. 7.8, which features kinks at the filling factors $\nu = \pm 2$ and $\nu = \pm 6$, which correspond to the start of the filling of LLs $n = \pm 1$ and $n = \pm 2$, respectively.

In order to further understand also the overall much smaller magnitude of the v_{F} -renormalization near the charge neutrality point compared to the case of low magnetic fields (compare blue and purple dots in the inset of Fig. 7.8), which were extracted from transport experiments, we first rule out that this difference is merely due to the experimental method used to probe the effective Fermi velocity. To this end, we briefly discuss the previously neglected excitonic effects, i.e., the binding energy between the phonon-excited electron-hole pair, which plays a role in the optically extracted effective v_{F} , but not in the one extracted from transport measurements. In the resonance condition Eq. 7.54 we compare the LL excitation energy T_1 to the unperturbed phonon energy ω_{ph} . When we experimentally measure the former via measuring B_{T_1} , the resulting deduced value of v_{F,T_1} already includes all effects of electron-electron interaction, including the excitonic binding energy, i.e., the energies T_n in Eq. 7.50 are actually given by $T_n = \varepsilon_{n+1} + \varepsilon_n + \varepsilon_{n+1,-n}^{\text{bind.}}$, where $\varepsilon_{n+1,-n}^{\text{bind.}}$ denotes the (negative) binding energy of the LL transition. Consequently, the experimentally extracted value of $v_{\text{F},T_1}(n_{\text{el}}^{(0)})$ invariably contains an excitonic contribution of $\delta v_{\text{F},T_1}^{\text{bind.}} = \varepsilon_{n+1,-n}^{\text{bind.}} / (\sqrt{2eB_{T_1}}/c(\sqrt{2} + 1))$ (compare the definition in Eq. 7.50). In order to enable a sensible comparison to the values of the effective Fermi velocity extracted from transport measurements, we estimate $\varepsilon_{n+1,-n}^{\text{bind.}}$ within our tight-binding model on the level of the Hartree-Fock approximation. For this, we approximate it as the difference of the direct Coulomb and exchange matrix elements, averaged over all possible pairs of degenerate LL states contributing to the

T_1 -transition:

$$\varepsilon_{n+1,-n}^{\text{bind.}}(B) = \frac{1}{(g_{mrLL}/2)^2} \sum_{\substack{m,v \\ m'v'}} \left(v_{(-n,m',v')}^{\text{Hart.}}(B) - v_{(-n,m',v')}^{\text{Fock}}(B) \right). \quad (7.59)$$

A numerical evaluation yields an n_{el} -independent estimate of $\varepsilon_{2,-1}^{\text{bind.}}(B_{T_1}) \approx -6$ meV. If we correct the results of our calculation for the corresponding contribution $\delta v_{\text{F},T_1}^{\text{bind.}}$ to the effective Fermi velocity, we obtain values for v_{F,T_1} without any excitonic effects, as shown as a black dotted line in Fig. 7.8.

Finally, we compare the charge carrier density dependence of the effective Fermi velocity at high magnetic fields ($B \approx 3$ T) to the effective v_{F} at low magnetic fields ($B \lesssim 0.5$ T) in the inset of Fig. 7.8. The purple dots represent the effective Fermi velocity as extracted from temperature-dependent measurements of the amplitude of Shubnikov-de Haas oscillations of the electrical conductivity (compare Supplementary Material to Ref. 79), performed on the same device as the one used for the measurement of the n_{el} -dependence of magneto-phonon resonances. They agree very well with previous measurements by Elias *et al.* [78] and feature a logarithmic divergence at the charge neutrality point, as predicted by theory [78, 173, 174] (compare blue line in the inset of Fig. 7.8). However, the n_{el} -dependence of the effective Fermi velocity at low magnetic fields as extracted from transport experiments is fundamentally different from the n_{el} -dependence of the effective v_{F} at high magnetic fields as extracted from measurements of the T_1 -MPR.

It is crucial to point out that this difference *cannot* be attributed solely to the different experimental methods with which v_{F} has been extracted. While transport experiments do probe the effective Fermi velocity at the energy scale of the Fermi level (in contrast to MPR-measurements, which probe the effective v_{F} at approximately half the phonon energy), the renormalized electronic bands at low B -fields still remain linear [156] (also compare left sketch in the inset of Fig. 7.8). Therefore, the energy scale at which v_{F} is probed is actually irrelevant. The presence of excitonic effects in the measurements of the T_1 -MPR, which are not present in transport experiments, cannot account for the different behavior either, as illustrated by the full blue and dashed black line in the inset of Fig. 7.8. Therefore, the different n_{el} -behavior of the

effective Fermi velocity cannot be ascribed to the different way in which it was probed experimentally. Rather, the underlying reason is of a physical nature, i.e., the electron-electron interaction effects behave differently under the changes of n_{el} in low magnetic fields and when Landau levels are present.

At low magnetic fields, the effective Fermi velocity as a function of n_{el} diverges logarithmically near the charge neutrality point. This divergence is due to a combination of the long-range nature of the Coulomb interaction in the HF self-energy and the delocalized nature of the electronic wave function for states near the $K^{(l)}$ -point, typical for non-bound, Bloch wave-like states. By contrast, in the LL-regime, where the spectrum of the Hamiltonian is discrete and thus the states have a bound state character, the electronic wave functions become exponentially localized, with a decay constant on the order of the magnetic length l_B . As a result, the Coulomb matrix elements are smoothly cut off at a length scale on the order of l_B (compare Supplementary Material to Ref. 79) and rendered finite and therefore the divergence is eliminated.

7.2.3 Probing electronic and phonon lifetimes with magneto-phonon resonances

Up to this point, we solely discussed how magneto-phonon resonances can be used to study the impact of many-body effects on the effective Fermi velocity, i.e., the electronic energy levels and transition energies only. As we have seen in the theoretical section of this chapter, however, the phenomenon of magneto-phonon resonances is also influenced by the electronic and phonon *lifetimes* and the *electron-phonon coupling constant* λ . So far, we merely treated these three quantities as fit parameters to describe the behavior of the G -peak position and width as a function of magnetic field over a large B -field range. In this section, instead, we will focus on extracting these three quantities more precisely from measurements at only a few different values of the magnetic field.

To begin with, we discuss the coupling of the unperturbed phonon to the set of Landau level transitions in the vicinity of a magneto-phonon resonance, i.e., when the magnetic field is such that one LL transition is in resonance with the unperturbed phonon. In the following, we will restrict ourselves to the case of vanishing charge carrier density, i.e.

$n_{\text{el}}=0 \text{ cm}^{-2}$, as is the case when probing MPRs in graphene-boron nitride heterostructures, due to the photo-induced doping effect [172], as described in the introduction to the previous section. We can then focus on the resonant coupling of the phonon to T_n -transitions only. In the vicinity of a T_n -transition, the phonon-self energy can be approximated by one term only:

$$\tilde{\Pi}(\omega) \xrightarrow{\text{Re}(\omega) \rightarrow T_n} \frac{\lambda \omega_B^2}{2} \frac{1}{\omega - T_n + \frac{i}{2} \gamma_{T_n}}. \quad (7.60)$$

Dyson's equation, Eq. 7.49, in the vicinity of the T_n -MPR then simplifies to

$$\left(\omega - \omega_{\text{ph}} + \frac{i}{2} \gamma_{\text{ph}} \right) \left(\omega - T_n + \frac{i}{2} \gamma_{T_n} \right) - g_B^2 = 0, \quad (7.61)$$

where we used the fact that near the MPR we also have $\omega \rightarrow \omega_{\text{ph}}$ and introduced the effective coupling constant $g_B \equiv \sqrt{\lambda/2} \omega_B$. Eq. 7.61 is the secular equation for a non-Hermitian two-level system consisting of a state with energy ω_{ph} and decay width γ_{ph} and a state with energy T_n and decay width γ_{T_n} coupled via a coupling constant g_B . Its complex solutions are given by

$$\begin{aligned} \omega_{\pm} = & \frac{\omega_{\text{ph}} + T_n}{2} - \frac{i}{2} \frac{\gamma_{\text{ph}} + \gamma_{T_n}}{2} \\ & \pm \frac{1}{2} \sqrt{(\omega_{\text{ph}} - T_n)^2 - \frac{1}{4}(\gamma_{\text{ph}} - \gamma_{T_n})^2 - i(\omega_{\text{ph}} - T_n)(\gamma_{\text{ph}} - \gamma_{T_n}) + (2g_B)^2}. \end{aligned} \quad (7.62)$$

Exactly at the resonance, i.e., when the magnetic field is such that $\omega_{\text{ph}} = T_n = \omega_B(\sqrt{n+1} + \sqrt{n})$, this expression simplifies to

$$\omega_{\pm, T_n} = \omega_{\text{ph}} - \frac{i}{2} \frac{\gamma_{\text{ph}} + \gamma_{T_n}}{2} \pm \frac{1}{2} \sqrt{(2g_{T_n})^2 - \left(\frac{\gamma_{\text{ph}} - \gamma_{T_n}}{2} \right)^2}, \quad (7.63)$$

where $g_{T_n} \equiv g_B(B = B_{T_n})$.

Here, we can distinguish between two different regimes:

i) Strong coupling regime: $2g_{T_n} > |\gamma_{\text{ph}} - \gamma_{T_n}|/2$.

In this case, the square root is entirely real, and the energies and decay widths of the

coupled modes are given by:

$$\varepsilon_{\pm, T_n} \equiv \text{Re}(\omega_{\pm, T_n}) = \omega_{\text{ph}} \pm \sqrt{(2g_{T_n})^2 - \left(\frac{\gamma_{\text{ph}} - \gamma_{T_n}}{2}\right)^2}, \quad (7.64)$$

$$\gamma_{\pm, T_n} \equiv -2 \text{Im}(\omega_{\pm, T_n}) = \frac{\gamma_{\text{ph}} + \gamma_{T_n}}{2}. \quad (7.65)$$

At the resonance, there are thus two distinct energy levels with the same decay rate, given by the average of the decay rates of the uncoupled modes. The existence of two non-degenerate levels, i.e., a so-called *anti-crossing*, is well-known from standard quantum mechanical perturbation theory for a coupled, Hermitian two-level system, where two coupled states “repel” each other [86].

ii) Weak coupling regime: $2g_{T_n} < |\gamma_{\text{ph}} - \gamma_{T_n}|/2$.

In the opposite case, i.e., for small values of the coupling constant, the complex energies of the coupled modes read:

$$\varepsilon_{\pm, T_n} \equiv \text{Re}(\omega_{\pm, T_n}) = \omega_{\text{ph}} \quad (7.66)$$

$$\gamma_{\pm, T_n} \equiv -2 \text{Im}(\omega_{\pm, T_n}) = \frac{\gamma_{\text{ph}} + \gamma_{T_n}}{2} \mp \sqrt{\left(\frac{\gamma_{\text{ph}} - \gamma_{T_n}}{2}\right)^2 - (2g_{T_n})^2}. \quad (7.67)$$

Here, the two coupled modes are not long-lived enough, compared to the time scale set by the inverse coupling constant, to allow the energy levels to influence each other and induce a splitting. Instead, the two coupled modes remain degenerate, but decay with different decay widths, centered around the average decay width of the two uncoupled modes.

Note that the effective coupling constant at the T_n -MPR is given by $g_{T_n} = \sqrt{\lambda/2}\omega_{\text{ph}}/(\sqrt{n+1} + \sqrt{n})$. For example, in the case of the T_1 -MPR, which we will mostly be interested in below, we find $g_{T_1} \sim 30 \text{ cm}^{-1}$, for $\lambda \sim 4 \times 10^{-3}$ and $\omega_{\text{ph}} \approx 1586 \text{ cm}^{-1}$. If we compare this value to the typical electronic and phonon decay widths we encountered in the previous two sections, i.e., $\gamma_{\text{ph}} \sim 5\text{-}10 \text{ cm}^{-1}$ and $\gamma_{T_n} > 150 \text{ cm}^{-1}$, it becomes clear that the *magneto-phonon resonances in graphene belong to the weak coupling regime*. We can rearrange the formula for the decay width of the coupled modes to

obtain an expression for the electronic decay width γ_{T_n} :

$$\gamma_{T_n} = \Gamma_{G,T_n}^{\max} + \frac{4g_{T_n}^2}{\Gamma_{G,T_n}^{\max} - \gamma_{\text{ph}}}. \quad (7.68)$$

This formula expresses γ_{T_n} in terms of the decay width of the coupled mode, which is experimentally accessible in the form of the FWHM of the Raman G -peak at the MPR, Γ_{G,T_n}^{\max} (see last section), the effective coupling constant g_{T_n} , and the lifetime of the unperturbed phonon mode γ_{ph} , i.e., the decay width of the phonon due to phonon-phonon scattering, which serves as a measure for anharmonic effects. Since only Γ_{G,T_n}^{\max} is directly observable as the height of the resonance peak in the $\Gamma_G(B)$ curve, at least two independent measurements are required to extract the effective coupling constant g_{T_n} and the anharmonic part of the phonon decay width, γ_{ph} .

To determine the effective coupling constant, we note that exactly at resonance, it is directly proportional to the dimensionless electron-phonon coupling constant λ and the unperturbed phonon frequency ω_{ph} . Note that the latter is directly given by the value of the G -peak position at $B=0$ T and vanishing charge carrier density. The dimensionless electron-phonon coupling constant, on the other hand, is related to the FWHM of the G -peak at $B=0$ T. At vanishing magnetic field, the total decay width of the phonon and thus the FWHM of the G -peak, is given by the sum of two terms:

$$\Gamma_G(B=0 \text{ T}) = \Gamma_G^{(\text{el-ph.})} + \gamma_{\text{ph}}, \quad (7.69)$$

where $\Gamma_G^{(\text{el-ph.})}$ denotes the partial decay width of the phonon due to electron-phonon interaction, i.e., its decay into an electron-hole pair. We can estimate this contribution to the decay width using Fermi's golden rule:

$$\Gamma_G^{(\text{el-ph.})} = \sum_{\mathbf{k}} \sum_{\text{spin}} |\langle \mathbf{k}, \pi^* | \hat{\mathcal{H}}_{\text{el.-ph.}} | \mathbf{k}, \pi; \mathbf{q} = \mathbf{0}, \lambda \rangle|^2 2\pi \delta(\omega_{\text{ph}} - (\varepsilon_{\mathbf{k},\pi^*} - \varepsilon_{\mathbf{k},\pi})), \quad (7.70)$$

where in this context, λ refers to the phonon polarization of the degenerate, in-plane optical phonon. Since the energy of the unperturbed phonon is on the order of 200 meV, the low-energy model of massless Weyl fermions is applicable. We can therefore replace

the integration over the first Brillouin zone by a sum over the two valleys K and K' and a continuum integration up to a high-energy cutoff Λ :

$$\mathbf{k} \rightarrow \mathbf{K}^{(\prime)} + \mathbf{k}, \quad \varepsilon_{\mathbf{k}, \pi^*/\pi} \rightarrow \pm v_F |\mathbf{k}|, \quad \sum_{\mathbf{k}} \rightarrow \sum_{v=K, K'} \int_{v_F |\mathbf{k}| \leq \Lambda} \frac{d^2 k}{(2\pi)^2} A, \quad (7.71)$$

where A denotes the total area of the graphene sheet, and the sum over the valley index v runs over both the K and K' valleys. The matrix element squared can easily be calculated using the explicit form of the wave functions and Hamiltonians given in Section 7.1.1. In the low-energy approximation, the \mathbf{k} -point dependence of the matrix element can be neglected and is to a good approximation given by the one at $\mathbf{k} = \mathbf{K}^{(\prime)}$. The squared matrix element is furthermore independent of the valley and the phonon polarization vector:

$$|\langle \mathbf{K}^{(\prime)}, \pi^* | \hat{\mathcal{H}}_{\text{el.-ph.}} | \mathbf{K}^{(\prime)}, \pi; \mathbf{q} = \mathbf{0}, \lambda \rangle|^2 = \frac{1}{2NM\omega_{\text{ph}}} \frac{9}{2} \left(\frac{\partial t}{\partial a} \right)^2. \quad (7.72)$$

Putting everything together, performing the spin and valley sums, and the integration over the delta function, we find for the partial decay width:

$$\Gamma_G^{(\text{el-ph.})} = \frac{9\sqrt{3}}{2Ma_0^2} \beta^2 = 2\pi\lambda \frac{\omega_{\text{ph}}}{2}, \quad (7.73)$$

where we again identified $\beta \equiv -(\text{d log } t)/(\text{d log } a)$ and the lattice constant $a_0 = \sqrt{3}a$ and expressed the result in terms of the dimensionless electron-phonon coupling constant λ , as defined in Eq. 7.42. We can thus determine λ from a measurement of ω_{ph} , $\Gamma_G(B = 0 \text{ T})$, and γ_{ph} .

Finally, the only other quantity that needs to be determined in order to extract the electron-phonon coupling constant λ and the electronic lifetimes γ_{T_n} is γ_{ph} . Since the latter is defined as the anharmonic contribution to the total phonon decay width, we can measure it directly by completely suppressing the electronic contribution. This can be done with a magnetic field as well, as it quantizes the electronic energy levels and thus also the possible electronic transitions. If the B -field is tuned such that no electronic transition is energetically matched with the phonon mode, the decay of the latter

becomes impossible as it would violate energy conservation. As seen from Fig. 7.4c, a magnetic field of around 8 T is enough to completely suppress all electronic decay channels of the phonon by virtue of energy conservation.

The various parameters discussed and the means to extract them are summarized

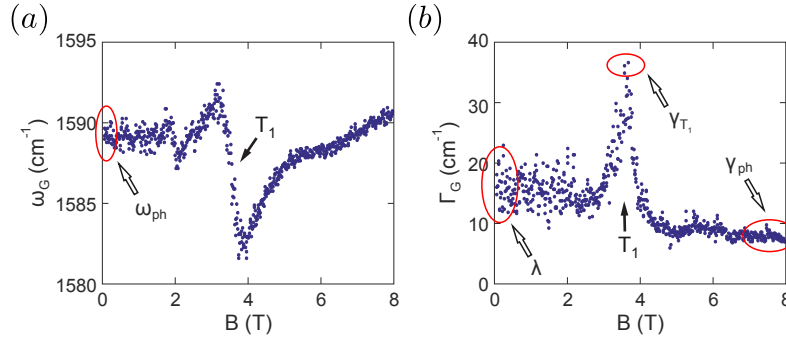


Figure 7.9: **Relation of physical quantities to measurements of magneto-phonon resonances.** (a) and (b) Illustration of the relation of the position and FWHM, respectively, of the G -peak of graphene at different values of the magnetic field to the unperturbed phonon frequency ω_{ph} , the dimensionless electron-phonon coupling constant λ , the anharmonic contribution to the phonon decay width, γ_{ph} , and the decay width of the T_1 -Landau level transition. (Figure adapted and reprinted from Neumann, C. *et al.*, *Appl. Phys. Lett.* **107**, 233105 (2015), with the permission of AIP Publishing.)

and illustrated in Fig. 7.9. The depicted magneto-Raman data were recorded¹⁵ on a graphene flake grown by chemical vapor deposition (CVD) and encapsulated by hexagonal boron nitride, using the same experimental setup, temperature, and laser settings as given in the previous two sections. Applying the theoretical considerations discussed above, we can extract an unperturbed phonon frequency of $\omega_{\text{ph}}=1589.1 \text{ cm}^{-1}$, a partial decay width of the phonon due to anharmonicity of $\gamma_{\text{ph}}=7.6 \text{ cm}^{-1}$, an electron-phonon coupling constant of $\lambda=3.8 \times 10^{-3}$, and a decay width of the T_1 -LL transition of $\gamma_{T_1}=140 \text{ cm}^{-1}$. The extracted parameters are on the same order of magnitude as the ones found above, i.e., the CVD-grown graphene flake is of similar electronic and mechanical quality than the exfoliated graphene flakes in the samples of the previous

¹⁵The measurements were performed by D. Halpaap and C. Neumann.

two sections.

As a final point, we study the evolution of these parameters as a function of an

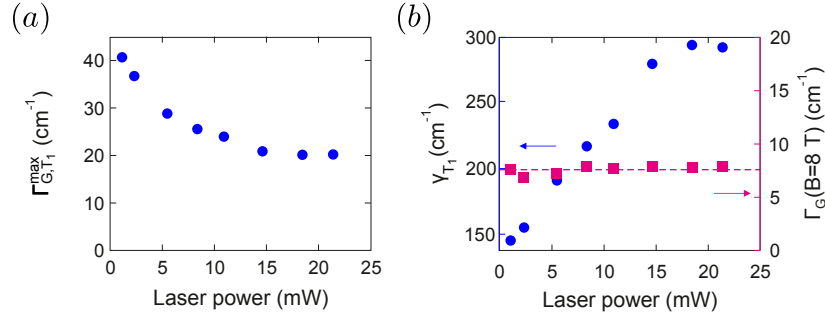


Figure 7.10: **Evolution of MPR-strength and electronic and phonon lifetimes with laser power.** (a) Peak width of the Raman G -peak at the T_1 -MPR as a function of laser power. (b) Laser power dependence of the extracted decay width of the T_1 -LL transition (blue dots) and of the FWHM of the Raman G -peak at $B=8$ T (purple squares). The latter corresponds to the anharmonic contribution to the phonon decay width. (Figure adapted and reprinted from Neumann, C. *et al.*, *Appl. Phys. Lett.* **107**, 233105 (2015), with the permission of AIP Publishing.)

external parameter that influences the many-body effects on them. However, due to the aforementioned photo-induced doping effect in graphene-boron nitride heterostructures, the charge carrier density cannot be tuned in a simple way. Instead, we probe the dependence of the electronic and phonon decay widths on the laser power, which we vary from the previously used 5 mW up to a maximal power of 21.4 mW. In Fig. 7.10a, we show the FWHM of the G -peak at the T_1 -MPR as a function of laser power, while Fig. 7.10b depicts the corresponding electronic decay width γ_{T_1} (blue dots) and the FWHM of the G -peak at a magnetic field of $B=8$ T (purple squares).

The maximum FWHM of the G -peak at the T_1 -MPR decreases with increasing laser power before saturating at approximately half the value measured at low laser power. The decrease of the “strength” of the resonance can be attributed to the stronger damping of the electronic excitations as seen from the increase of the T_1 -excitation decay width with increasing laser power, which approximately doubles from low to high laser power. We associate this strong increase of the decay width, or equivalently the

strong decrease of the lifetime of the excitation, with the stronger presence of so-called “hot charge carriers” in the system. This refers to an electronic system that is not in thermal equilibrium with its low-temperature surroundings, but instead is continuously pumped by the laser and does not have enough time to relax to the thermal equilibrium state. Instead, it reaches a new stationary state at high laser power when the continuous excitation by the laser and the decay of the excited states approaches a steady state equilibrium. By contrast, the value of the FWHM of the G -peak at $B=8$ T is very robust under changes of the laser power. This is consistent with our interpretation of $\Gamma_G(B = 8 \text{ T})$ as the anharmonic part of the phonon decay width, as the latter is not influenced by the electronic system and it is only the latter that can be influenced by an increase of the laser power.

Chapter 8

Conclusions and Outlook

In the preceding six chapters, we have presented part of our work on the theory and application of Raman spectroscopy. Since many of our results and contributions pertaining to the phenomenological, computational, and applied aspects of Raman spectroscopy have already been published elsewhere,¹ in this thesis, we have focused on presenting our recently developed coherent theoretical approach for the description of Raman scattering. In the process, we managed to address many of the open questions that were mentioned in the introduction. In addition, we were able to significantly advance the state of the art of both the theoretical and the computational treatment of Raman spectroscopy. In this final chapter, we summarize the most important achievements presented in this thesis and point out possible future avenues of research.

8.1 Main results of this work

We started our discussion of Raman spectroscopy by devising a correlation function-based approach to the calculation of Raman scattering probabilities and rates. Our theory is potentially applicable to the study of ultra-fast and out-of-equilibrium Raman scattering. However, since some work still needs to be done on the way towards a concrete, practical implementation, we focused on the equilibrium, zero-temperature case first. In this limit, we derived a generalized version of Fermi's golden rule which

¹For a full list of our contributions, see the [List of Publications](#).

relates the Raman scattering rate to the matrix elements of two current density operators between eigenstates of the Hamiltonian that describes a fully interacting system of electrons and nuclei.

In the process of turning this expression into something more concrete, we first reviewed the treatment of the electronic system in the clamped nuclei approximation, its approximative treatment within Kohn-Sham density functional theory, and its perturbative treatment within many-body perturbation theory. We then applied the perturbative technique to derive a novel and concrete approach for the calculation of phonon frequencies within the adiabatic, Born-Oppenheimer approximation that goes beyond the state of the art in the form of density functional perturbation theory.

While DFPT indeed yields good results for non-metallic systems, it fails when electronic correlation and screening effects become important. This is, for example, the case in graphene, but also in many other materials that feature Kohn anomalies, such as the also intensively studied TiSe_2 . Our new approach, which has been developed entirely from first principles, now offers the first fully *ab initio* description of phonons in these kinds of systems, where the current state-of-the-art methods do not work in a satisfactory way. The ability to capture Kohn anomaly-related effects by more accurately describing the screening of the electron-nuclei interaction paves the way, for instance, for a first consistent first-principles calculation of the phonon dispersion of graphene. Besides providing a solution for this long-standing problem, the generality of our approach also permits its application to other highly correlated systems, such as TiSe_2 . For the latter kind of systems, the currently used methods are still restricted to phonons of specific wave vectors only, since they rely on the construction of supercells.

Our approach has been derived entirely from fundamental principles and is thus fully sound from a theoretical point of view. Moreover, we extensively discussed the physical effects captured by our method and in which way it improves on the current state-of-the-art methods. Lastly, it is formulated entirely in terms of quantities that can, in principle, already be computed using currently available *ab initio* codes. However, as of now, no existing code allows the computation of all the necessary ingredients within the same basis set. Nevertheless, once these technical difficulties are overcome,

our method can be implemented timely.

After our extensive, and in large parts, original and novel treatment of phonons in the adiabatic approximation, we set up the exact perturbative formalism for the fully interacting electron-nuclei system, starting from non-interacting Kohn-Sham electrons and non-interacting phonons in the adiabatic approximation. Our systematic, perturbative/diagrammatic approach has allowed us to obtain a comprehensive theoretical description of the screening of the electron-phonon coupling. The latter plays an important role for many material properties. For instance, it determines the (in)stability of crystals that potentially feature Peierls distortions and also influences the line shape and intensities of certain peaks in the Raman spectrum, for example, of graphene.

In order to be able to correctly predict these properties, it is crucial to develop an improved description of the screening of the electron-phonon coupling, as the state-of-the-art methods often fail. Our approach goes beyond the current standard and, for the first time, provides a concrete and comprehensive algorithm for the computation of the screened electron-phonon coupling beyond the level of theory offered by methods such as DFPT. One of its most important features is its promise to yield an accurate description of Kohn anomalies, which are the underlying reason behind the mentioned difficulties in the description of the screened electron-phonon coupling.

In addition to our developments related to the electron-phonon coupling, we have also derived a consistent approach for the calculation of phonon frequencies beyond the adiabatic, Born-Oppenheimer approximation. Such an approach is needed as the latter is expected to fail in systems with a (semi-)metallic character, as the electronic system can be in resonance with the phonon system due to the absence of an electronic band gap. As such, our work provides a concrete computational ansatz for the correct calculation of phonon frequencies in these kinds of systems.

Following the discussion of our developed advancements in the theory of the adiabatic and non-adiabatic electron-phonon interaction, we presented a novel approach to the theory of one-phonon-induced Raman scattering, based on the application of the Lehmann-Symanzik-Zimmermann reduction formula. This approach has enabled us to

obtain a concrete computational algorithm for the computation of one-phonon-induced Raman scattering rates which both includes excitonic effects and a non-static description of lattice vibrations. The inclusion of both at the same time is not possible with currently used methods, which only allow the inclusion of either one or the other. As such, our novel method significantly advances the state-of-the-art description of Raman spectroscopy, as it is the first theory to contain all relevant physical effects and describe them in a unified way.

At the same time, it is both computationally feasible to be realized in the near future, as it essentially relies only on the solution of the standard, one-frequency Bethe-Salpeter equation for zero excitation wave vector. Importantly, our perturbative treatment also only relies on calculations of all involved quantities within one unit cell only. This constitutes a large computational advantage compared to the expensive supercell calculations associated with finite difference methods.

As a first application, we applied our approach to graphene, in which excitonic effects are for the most part negligible, which allows us to test our new approach in a simple system. We implemented our method on the level of the independent-particle approximation for the optical excitation and the DFPT-level approximation for the screened electron-phonon coupling. Our code is completely general and can be applied to any material. The flexibility of our perturbative approach furthermore offers unique possibilities for the analysis of the underlying physical concepts. Additionally, it does not rely on any parameters, but instead is entirely based on first principles. As such, our calculation for graphene constitutes the first time an entirely *ab initio* calculation of the one-phonon Raman peak intensity of graphene has been performed.

In this concrete case, our method allowed us to study both the laser and Fermi energy dependence of the one-phonon Raman peak (*G*-peak) intensity. Our results are in excellent agreement with experiment. Besides this quantitative agreement, however, we have also been able to understand the observed and calculated behavior in terms of approximate symmetries and quantum interference effects. Especially the latter have a large impact on the Raman intensity, not only in the case of graphene, but in other materials as well, for example, in two-dimensional transition metal dichalcogenides.

Moreover, our method has allowed us to unambiguously demonstrate that the naïve assumption that only resonant electronic transitions are important for Raman scattering does not hold in graphene.

The understanding of Raman spectroscopy that we gained during our study of graphene has helped to resolve open problems in Raman spectroscopy of TMDs. More concretely, our methods of analysis and visualization techniques combined with our insight on approximate symmetries and quantum interference effects has allowed us to understand the previously puzzling intensity inversion of the Raman peaks of Davydov multiplets in triple-layer MoTe₂. This feature could not be understood with previously applied methods, such as bond polarizability models, but could now be fully understood in terms of quantum interference effects. This illustrates the general nature of our analysis techniques and additionally sheds further light on the complex quantum mechanical nature of the Raman scattering process. In addition to this, we briefly summarized the current state of our collaborative work on a comparison of our perturbative approach to the previously used method of static first derivatives of the transverse dielectric susceptibility. While this work is still in progress, we already verified that our perturbative method is in excellent agreement with the first derivative approach for phonon modes that are not influenced by polar effects. The latter are so far not fully incorporated in our perturbative treatment and as such there still remain some discrepancies between the two methods for polar phonon modes, which still need to be fully understood and remedied.

We then concluded the main part of this thesis by presenting parts of our work on the use of Raman scattering as a probe of many-body effects in graphene. Concretely, we showed results of our work on the phenomenon of magneto-phonon resonances done in close collaboration with an experimental group. Our work details how magneto-phonon resonances can be used to extract various physical quantities of interest. We first applied this technique to study electronic excitation energies of graphene, which are often described in terms of an effective Fermi velocity, and probed the dependence of the latter on changes of the charge carrier density. While the Fermi velocity is known to diverge at the charge neutrality point in the absence of a magnetic field, we were

able to demonstrate that many-body effects only lead to a finite renormalization in the presence of a magnetic field. We confirmed these curious experimental findings by tight-binding calculations on the level of the Hartree-Fock approximation. Besides the excellent quantitative agreement with experiment, this calculation has also allowed us to provide an intuitive physical explanation of this phenomenon.

We concluded this chapter with a discussion and a practical example of how the effect of magneto-phonon resonances can be used to extract various properties of the electron and phonon system. In particular, our work demonstrates in detail how the electron-phonon coupling, electronic excitation energies and lifetimes, and anharmonic effects on the phonon lifetimes can be extracted from a small number of measurements.

8.2 Outlook

The work presented in this thesis constitutes a considerable advancement in the theory of the coupled electron-phonon system. In particular, it has resulted in concrete expressions for the calculation of both adiabatic and non-adiabatic phonon frequencies and the screened electron-phonon coupling, beyond the current state of the art. Our work thus paves the way for the study of systems in which contemporary methods fail. Among these systems are, for example, graphene, for which a consistent and conclusive calculation of the phonon dispersion is still missing, and strongly correlated systems, such as TiSe_2 , for which a proper calculation of the screened electron-phonon coupling is of vital importance. While our developments were derived entirely from fundamental principles and thus stand on firm ground, our work still remains to be implemented in a computer code and tested on several test systems. The main practical problem as of now is the unavailability of an electronic structure code that allows both the solution of the Bethe-Salpeter equation at finite excitation wave vectors and a computation of the electron-phonon coupling in the same basis set. However, once these technical difficulties are overcome, our derived approaches can be tested on concrete systems. As a first test case, the computation of the screened electron-phonon coupling and the phonon dispersion of graphene suggests itself, for which a fully convincing calculation is still missing.

Regarding the part of our work that pertains to Raman scattering, the next step consists of implementing the part of our suggested approach that allows the inclusion of excitonic effects. Possible systems to test our method on would be transition metal dichalcogenides. In parallel, the independent-particle version of our approach needs to be validated further. From a theoretical point of view, it furthermore needs to be understood how corrections for polar materials can be calculated and included, possibly via the inclusion of Born effective charges in our diagrammatic framework.

In addition to these further computational developments for one-phonon-induced Raman scattering, the extension of our approach to two-phonon Raman scattering is also highly desirable. Again a first test case for this would be graphene, as the latest theoretical works here are not fully consistent, since, as mentioned in the introduction, they omit a large number of terms that arise in the same order of perturbation theory. It still needs to be seen how this approximation can be justified physically, for which concrete work is already in progress.

On a more long-term time scale, it may be worthwhile to extend our concrete formulation of Raman scattering also to finite temperature and non-equilibrium situations beyond the elegant, but still rather abstract correlation function formulation presented at the beginning of this thesis. This will ultimately allow a theoretical description of Raman spectroscopy on ultra-short time scales, which have recently become a topic of interest in optical absorption spectroscopy.

List of Publications

1. Engels, S., Terrés, B., Klein, F., **Reichardt, S.**, Goldsche, M., Kuhlen, S., Watanabe, K., Taniguchi, T. & Stampfer, C. Impact of thermal annealing on graphene devices encapsulated in hexagonal boron nitride. *Phys. Status Solidi B* **251**, 2545–2550 (2014).
2. Terrés, B., **Reichardt, S.**, Neumann, C., Watanabe, K., Taniguchi, T. & Stampfer, C. Raman spectroscopy on mechanically exfoliated pristine graphene ribbons. *Phys. Status Solidi B* **251**, 2551–2555 (2014).
3. Neumann, C., **Reichardt, S.**, Drögeler, M., Terrés, B., Watanabe, K., Taniguchi, T., Beschoten, B., Rotkin, S. V. & Stampfer, C. Low B field magneto-phonon resonances in single-layer and bilayer graphene. *Nano Lett.* **15**, 1547–1552 (2015).
4. Neumann, C., **Reichardt, S.**, Venezuela, P., Drögeler, M., Banszerus, L., Schmitz, M., Watanabe, K., Taniguchi, T., Mauri, F., Beschoten, B., Rotkin, S. V. & Stampfer, C. Raman spectroscopy as probe of nanometre-scale strain variations in graphene. *Nat. Commun.* **6**, 8462 (2015).
5. Neumann, C., Halpaap, D., **Reichardt, S.**, Banszerus, L., Schmitz, M., Watanabe, K., Taniguchi, T., Beschoten, B. & Stampfer, C. Probing electronic lifetimes and phonon anharmonicities in high-quality chemical vapor deposited graphene by magneto-Raman spectroscopy. *Appl. Phys. Lett.* **107**, 233105 (2015).
6. Neumann, C., Rizzi, L., **Reichardt, S.**, Terrés, B., Khodkov, T., Watanabe, K., Taniguchi, T., Beschoten, B. & Stampfer, C. Spatial control of laser-induced dop-

ing profiles in graphene on hexagonal boron nitride. *ACS Appl. Mater. Interfaces* **8**, 9377–9383 (2016).

7. Stampfer, C. & **Reichardt, S.** Correspondence: On the nature of strong piezoelectricity in graphene on SiO₂. *Nat. Commun.* **7**, 11570 (2016).
8. **Reichardt, S.** & Stampfer, C. Modeling charge relaxation in graphene quantum dots induced by electron-phonon interaction. *Phys. Rev. B* **93**, 245423 (2016).
9. Neumann, C., Banszerus, L., Schmitz, M., **Reichardt, S.**, Sonntag, J., Watanabe, K., Taniguchi, T., Beschoten, B. & Stampfer, C. Line shape of the Raman 2D Peak of graphene in van der Waals heterostructures. *Phys. Status Solidi B* **253**, 2326–2330 (2016).
10. **Reichardt, S.** & Wirtz, L. Raman Spectroscopy of Graphene, *Optical Properties of Graphene*, chap. 3, 85–132 (World Scientific, Singapore, 2017).
11. Miranda, H. P. C., **Reichardt, S.**, Froehlicher, G., Molina-Sánchez, A., Berciaud, S. & Wirtz, L. Quantum interference effects in resonant Raman spectroscopy of single- and triple-layer MoTe₂ from first principles. *Nano Lett.* **17**, 2381–2388 (2017).
12. **Reichardt, S.** & Wirtz, L. Ab initio calculation of the G peak intensity of graphene: Laser-energy and Fermi-energy dependence and importance of quantum interference effects. *Phys. Rev. B* **95**, 195422 (2017).
13. Goldsche, M., Sonntag, J., Khodkov, T., Verbiest, G., **Reichardt, S.**, Neumann, C., Ouaj, T., von den Driesch, N., Buca, D., Trellenkamp, S. & Stampfer, C. Tailoring mechanically-tunable strain fields in graphene. *Nano Lett.* **18**, 1707–1713 (2018).
14. Sonntag, J., **Reichardt, S.**, Wirtz, L., Beschoten, B., Katsnelson, M. I., Libisch, F. & Stampfer, C. Impact of many-body effects on Landau levels in graphene. *Phys. Rev. Lett.* **120**, 187701 (2018).

15. Reichardt, S. & Wirtz, L. Many-body perturbation theory approach to the calculation of phonon-induced optical and Raman spectra. *In preparation* (2018).
16. Miranda, H. P. C., Reichardt, S., Molina-Sánchez, A. & Wirtz, L. First-principles calculation of Raman intensities in MoS₂ from a perturbative approach. *In preparation* (2018).
17. Reichardt, S. & Wirtz, L. Efficient ab initio approach for the computation of two-phonon Raman spectra. *In preparation* (2018).

Bibliography

- [1] Novoselov, K. S., Geim, A. K., Morozov, S. V., Jiang, D., Zhang, Y., Dubonos, S. V., Grigorieva, I. V. & Firsov, A. A. Electric field effect in atomically thin carbon films. *Science* **306**, 666–669 (2004).
- [2] Wang, L., Meric, I., Huang, P. Y., Gao, Q., Gao, Y., Tran, H., Taniguchi, T., Watanabe, K., Campos, L. M., Muller, D. A., Guo, J., Kim, P., Hone, J., Shepard, K. L. & Dean, C. R. One-dimensional electrical contact to a two-dimensional material. *Science* **342**, 614–617 (2013).
- [3] Lee, C., Wei, X., Kysar, J. W. & Hone, J. Measurement of the elastic properties and intrinsic strength of monolayer graphene. *Science* **321**, 385–388 (2008).
- [4] Novoselov, K. S., Fal'ko, V. I., Colombo, L., Gellert, P. R., Schwab, M. G. & Kim, K. A roadmap for graphene. *Nature* **490**, 192–200 (2012).
- [5] Novoselov, K. S., Jiang, D., Schedin, F., Booth, T. J., Khotkevich, V. V., Morozov, S. V. & Geim, A. K. Two-dimensional atomic crystals. *Proc. Natl. Acad. Sci. U.S.A.* **102**, 10451–10453 (2005).
- [6] Xu, M., Liang, T., Shi, M. & Chen, H. Graphene-like two-dimensional materials. *Chem. Rev.* **113**, 3766–3798 (2013).
- [7] Radisavljevic, B., Radenovic, A., Brivio, J., Giacometti, V. & Kis, A. Single-layer MoS₂ transistors. *Nat. Nanotechnol.* **6**, 147 (2011).
- [8] Dean, C. R., Young, A. F., Meric, I., Lee, C., Wang, L., Sorgenfrei, S., Watanabe,

K., Taniguchi, T., Kim, P., Shepard, K. L. & Hone, J. Boron nitride substrates for high-quality graphene electronics. *Nat. Nanotechnol.* **5**, 722–726 (2010).

- [9] Ponomarenko, L. A., Gorbachev, R. V., Yu, G. L., Elias, D. C., Jalil, R., Patel, A. A., Mishchenko, A., Mayorov, A. S., Woods, C. R., Wallbank, J. R., M, M.-K., Piot, B. A., Potemski, M., Grigorieva, I. V., Novoselov, K. S., Guinea, F., Fal’ko, V. I., & Geim, A. K. Cloning of Dirac fermions in graphene superlattices. *Nature* **497**, 594–597 (2013).
- [10] Ponomarenko, L. A., Geim, A. K., Zhukov, A. A., Jalil, R., Morozov, S. V., Novoselov, K. S., Grigorieva, I. V., Hill, E. H., Cheianov, V. V., Fal’ko, V. I., Watanabe, K., Taniguchi, T. & Gorbachev, R. V. Tunable metal-insulator transition in double-layer graphene heterostructures. *Nat. Phys.* **7**, 958 (2011).
- [11] Haigh, S. J., Gholinia, A., Jalil, R., Romani, S., Britnell, L., Elias, D. C., Novoselov, K. S., Ponomarenko, L. A., Geim, A. K. & Gorbachev, R. V. Cross-sectional imaging of individual layers and buried interfaces of graphene-based heterostructures and superlattices. *Nat. Mater.* **11**, 764 (2012).
- [12] Geim, A. K. & Grigorieva, I. V. Van der Waals heterostructures. *Nature* **499**, 419 (2013).
- [13] Raman, C. V. & Krishnan, K. S. A new type of secondary radiation. *Nature* **121**, 501–502 (1928).
- [14] Raman, C. V. & Krishnan, K. S. A change of wave-length in light scattering. *Nature* **121**, 619 (1928).
- [15] Raman, C. V. & Krishnan, K. S. The optical analogue of the Compton effect. *Nature* **121**, 711 (1928).
- [16] Ferrari, A. C. & Basko, D. M. Raman spectroscopy as a versatile tool for studying the properties of graphene. *Nat. Nanotechnol.* **8**, 235–246 (2013).

- [17] Ferrari, A. C., Meyer, J. C., Scardaci, V., Casiraghi, C., Lazzeri, M., Mauri, F., Piscanec, S., Jiang, D., Novoselov, K. S., Roth, S. & Geim, A. K. Raman spectrum of graphene and graphene layers. *Phys. Rev. Lett.* **97**, 187401 (2006).
- [18] Graf, D., Molitor, F., Ensslin, K., Stampfer, C., Jungen, A., Hierold, C. & Wirtz, L. Spatially resolved Raman spectroscopy of single- and few-layer graphene. *Nano Lett.* **7**, 238–242 (2007).
- [19] Mohiuddin, T. M. G., Lombardo, A., Nair, R. R., Bonetti, A., Savini, G., Jalil, R., Bonini, N., Basko, D. M., Galotit, C., Marzari, N., Novoselov, K. S., Geim, A. K. & Ferrari, A. C. Uniaxial strain in graphene by Raman spectroscopy: G peak splitting, Grüneisen parameters, and sample orientation. *Phys. Rev. B* **79**, 205433 (2009).
- [20] Huang, M., Yan, H., Heinz, T. F. & Hone, J. Probing strain-induced electronic structure change in graphene by Raman spectroscopy. *Nano Lett.* **10**, 4074–4079 (2010).
- [21] Mohr, M., Maultzsch, J. & Thomsen, C. Splitting of the Raman 2D band of graphene subjected to strain. *Phys. Rev. B* **82**, 201409 (2010).
- [22] Yoon, D., Son, Y.-W. & Cheong, H. Strain-dependent splitting of the double-resonance Raman scattering band in graphene. *Phys. Rev. Lett.* **106**, 155502 (2011).
- [23] Lee, J. E., Ahn, G., Shim, J., Lee, Y. S. & Ryu, S. Optical separation of mechanical strain from charge doping in graphene. *Nat. Commun.* **3**, 1024 (2012).
- [24] Chacon-Torres, J. C., Wirtz, L. & Pichler, T. Manifestation of charged and strained graphene layers in the Raman response of graphite intercalation compounds. *ACS Nano* **7**, 9249–9259 (2013).
- [25] Neumann, C., Reichardt, S., Venezuela, P., Drögeler, M., Banszerus, L., Schmitz, M., Watanabe, K., Taniguchi, T., Mauri, F., Beschoten, B., Rotkin, S. V. & Stampfer, C. Raman spectroscopy as probe of nanometre-scale strain variations in graphene. *Nat. Commun.* **6**, 8462 (2015).

- [26] Ferrari, A. C. Raman spectroscopy of graphene and graphite: disorder, electron–phonon coupling, doping and nonadiabatic effects. *Solid State Commun.* **143**, 47–57 (2007).
- [27] Yan, J., Zhang, Y., Kim, P. & Pinczuk, A. Electric field effect tuning of electron–phonon coupling in graphene. *Phys. Rev. Lett.* **98**, 166802 (2007).
- [28] Pisana, S., Lazzeri, M., Casiraghi, C., Novoselov, K. S., Geim, A. K., Ferrari, A. C. & Mauri, F. Breakdown of the adiabatic Born–Oppenheimer approximation in graphene. *Nat. Mater.* **6**, 198–201 (2007).
- [29] Stampfer, C., Molitor, F., Graf, D., Ensslin, K., Jungen, A., Hierold, C. & Wirtz, L. Raman imaging of doping domains in graphene on SiO₂. *Appl. Phys. Lett.* **91**, 241907 (2007).
- [30] Calizo, I., Balandin, A. A., Bao, W., Miao, F. & Lau, C. N. Temperature dependence of the Raman spectra of graphene and graphene multilayers. *Nano Lett.* **7**, 2645–2649 (2007).
- [31] Balandin, A. A., Ghosh, S., Bao, W., Calizo, I., Teweldebrhan, D., Miao, F. & Lau, C. N. Superior thermal conductivity of single-layer graphene. *Nano Lett.* **8**, 902–907 (2008).
- [32] Zabel, J., Nair, R. R., Ott, A., Georgiou, T., Geim, A. K., Novoselov, K. S. & Casiraghi, C. Raman spectroscopy of graphene and bilayer under biaxial strain: bubbles and balloons. *Nano Lett.* **12**, 617–621 (2012).
- [33] Engels, S., Terrés, B., Klein, F., Reichardt, S., Goldsche, M., Kuhlen, S., Watanabe, K., Taniguchi, T. & Stampfer, C. Impact of thermal annealing on graphene devices encapsulated in hexagonal boron nitride. *Phys. Status Solidi B* **251**, 2545–2550 (2014).
- [34] Drögeler, M., Volmer, F., Wolter, M., Terrés, B., Watanabe, K., Taniguchi, T., Güntherodt, G., Stampfer, C. & Beschoten, B. Nanosecond spin lifetimes in single- and few-layer graphene–hBN heterostructures at room temperature. *Nano Lett.* **14**, 6050–6055 (2014).

- [35] Casiraghi, C., Hartschuh, A., Qian, H., Piscanec, S., Georgi, C., Fasoli, A., Novoselov, K. S., Basko, D. M. & Ferrari, A. C. Raman spectroscopy of graphene edges. *Nano Lett.* **9**, 1433–1441 (2009).
- [36] Terrés, B., Reichardt, S., Neumann, C., Watanabe, K., Taniguchi, T. & Stampfer, C. Raman spectroscopy on mechanically exfoliated pristine graphene ribbons. *Phys. Status Solidi B* **251**, 2551–2555 (2014).
- [37] Faugeras, C., Amado, M., Kossacki, P., Orlita, M., Sprinkle, M., Berger, C., De Heer, W. A. & Potemski, M. Tuning the electron-phonon coupling in multi-layer graphene with magnetic fields. *Phys. Rev. Lett.* **103**, 186803 (2009).
- [38] Yan, J., Goler, S., Rhone, T. D., Han, M., He, R., Kim, P., Pellegrini, V. & Pinczuk, A. Observation of magnetophonon resonance of Dirac fermions in graphite. *Phys. Rev. Lett.* **105**, 227401 (2010).
- [39] Faugeras, C., Amado, M., Kossacki, P., Orlita, M., Kühne, M., Nicolet, A. A. L., Latyshev, Y. I. & Potemski, M. Magneto-Raman scattering of graphene on graphite: Electronic and phonon excitations. *Phys. Rev. Lett.* **107**, 036807 (2011).
- [40] Faugeras, C., Kossacki, P., Nicolet, A. A. L., Orlita, M., Potemski, M., Mahmood, A. & Basko, D. M. Probing the band structure of quadri-layer graphene with magneto-phonon resonance. *New. J. Phys.* **14**, 095007 (2012).
- [41] Kossacki, P., Faugeras, C., Kühne, M., Orlita, M., Mahmood, A., Dujardin, E., Nair, R. R., Geim, A. K. & Potemski, M. Circular dichroism of magnetophonon resonance in doped graphene. *Phys. Rev. B* **86**, 205431 (2012).
- [42] Goler, S., Yan, J., Pellegrini, V. & Pinczuk, A. Raman spectroscopy of magneto-phonon resonances in graphene and graphite. *Solid State Commun.* **152**, 1289–1293 (2012).
- [43] Kim, Y. D., Bae, M.-H., Seo, J.-T., Kim, Y. S., Kim, H., Lee, J. H., Ahn, J. R., Lee, S. W., Chun, S.-H. & Park, Y. D. Focused-laser-enabled p–n junctions in graphene field-effect transistors. *ACS Nano* **7**, 5850–5857 (2013).

- [44] Qiu, C., Shen, X., Cao, B., Cong, C., Saito, R., Yu, J., Dresselhaus, M. S. & Yu, T. Strong magnetophonon resonance induced triple G-mode splitting in graphene on graphite probed by micromagneto Raman spectroscopy. *Phys. Rev. B* **88**, 165407 (2013).
- [45] Leszczynski, P., Han, Z., Nicolet, A. A. L., Piot, B. A., Kossacki, P., Orlita, M., Bouchiat, V., Basko, D. M., Potemski, M. & Faugeras, C. Electrical switch to the resonant magneto-phonon effect in graphene. *Nano Lett.* **14**, 1460–1466 (2014).
- [46] Berciaud, S., Potemski, M. & Faugeras, C. Probing electronic excitations in mono- to pentalayer graphene by micro magneto-Raman spectroscopy. *Nano Lett.* **14**, 4548–4553 (2014).
- [47] Neumann, C., Reichardt, S., Drögeler, M., Terrés, B., Watanabe, K., Taniguchi, T., Beschoten, B., Rotkin, S. V. & Stampfer, C. Low B field magneto-phonon resonances in single-layer and bilayer graphene. *Nano Lett.* **15**, 1547–1552 (2015).
- [48] Neumann, C., Halpaap, D., Reichardt, S., Banszerus, L., Schmitz, M., Watanabe, K., Taniguchi, T., Beschoten, B. & Stampfer, C. Probing electronic lifetimes and phonon anharmonicities in high-quality chemical vapor deposited graphene by magneto-Raman spectroscopy. *Appl. Phys. Lett.* **107**, 233105 (2015).
- [49] Faugeras, C., Berciaud, S., Leszczynski, P., Henni, Y., Nogajewski, K., Orlita, M., Taniguchi, T., Watanabe, K., Forsythe, C., Kim, P., Jalil, R., Geim, A. K., Basko, D. M. & Potemski, M. Landau level spectroscopy of electron-electron interactions in graphene. *Phys. Rev. Lett.* **114**, 126804 (2015).
- [50] Miranda, H. P. C., Reichardt, S., Froehlicher, G., Molina-Sánchez, A., Berciaud, S. & Wirtz, L. Quantum interference effects in resonant Raman spectroscopy of single- and triple-layer MoTe₂ from first-principles. *Nano Lett.* **17**, 2381–2388 (2017).
- [51] Reich, S., Maultzsch, J., Thomsen, C. & Ordejon, P. Tight-binding description of graphene. *Phys. Rev. B* **66**, 035412 (2002).

- [52] Grüneis, A., Attaccalite, C., Pichler, T., Zabolotnyy, V., Shiozawa, H., Molodtsov, S., Inosov, D., Koitzsch, A., Knupfer, M., Schiessling, J., Follath, R., Weder, R., Rudolf, P., Wirtz, L. & Rubio, A. Electron-electron correlation in graphite: a combined angle-resolved photoemission and first-principles study. *Phys. Rev. Lett.* **100**, 037601 (2008).
- [53] Lazzeri, M., Attaccalite, C., Wirtz, L. & Mauri, F. Impact of the electron-electron correlation on phonon dispersion: Failure of LDA and GGA DFT functionals in graphene and graphite. *Phys. Rev. B* **78**, 081406 (2008).
- [54] Basko, D. M. Theory of resonant multiphonon Raman scattering in graphene. *Phys. Rev. B* **78**, 125418 (2008).
- [55] Basko, D. M. Calculation of the Raman G peak intensity in monolayer graphene: role of Ward identities. *New. J. Phys.* **11**, 095011 (2009).
- [56] Venezuela, P., Lazzeri, M. & Mauri, F. Theory of double-resonant Raman spectra in graphene: Intensity and line shape of defect-induced and two-phonon bands. *Phys. Rev. B* **84**, 035433 (2011).
- [57] Herziger, F., Calandra, M., Gava, P., May, P., Lazzeri, M., Mauri, F. & Maultzsch, J. Two-dimensional analysis of the double-resonant 2D Raman mode in bilayer graphene. *Phys. Rev. Lett.* **113**, 187401 (2014).
- [58] Hasdeo, E. H., Nugraha, A. R. T., Dresselhaus, M. S. & Saito, R. Fermi energy dependence of first- and second-order Raman spectra in graphene: Kohn anomaly and quantum interference effect. *Phys. Rev. B* **94**, 075104 (2016).
- [59] Reichardt, S. & Wirtz, L. Ab initio calculation of the G peak intensity of graphene: Laser-energy and Fermi-energy dependence and importance of quantum interference effects. *Phys. Rev. B* **95**, 195422 (2017).
- [60] Thomsen, C. & Reich, S. Double resonant Raman scattering in graphite. *Phys. Rev. Lett.* **85**, 5214 (2000).

- [61] Maultzsch, J., Reich, S., Thomsen, C., Requardt, H. & Ordejón, P. Phonon dispersion in graphite. *Phys. Rev. Lett.* **92**, 075501 (2004).
- [62] Maultzsch, J., Reich, S. & Thomsen, C. Double-resonant Raman scattering in graphite: Interference effects, selection rules, and phonon dispersion. *Phys. Rev. B* **70**, 155403 (2004).
- [63] Saito, R., Dresselhaus, G. & Dresselhaus, M. S. Physical Properties of Carbon Nanotubes (World Scientific, Singapore, 1998).
- [64] Reich, S., Thomsen, C. & Maultzsch, J. Carbon Nanotubes: Basic Concepts and Physical Properties (Wiley-VCH, New York, 2004).
- [65] Malard, L. M., Pimenta, M. A., Dresselhaus, G. & Dresselhaus, M. S. Raman spectroscopy in graphene. *Phys. Rep.* **473**, 51–87 (2009).
- [66] Saito, R., Hofmann, M., Dresselhaus, G., Jorio, A. & Dresselhaus, M. S. Raman spectroscopy of graphene and carbon nanotubes. *Adv. Phys.* **60**, 413–550 (2011).
- [67] Reichardt, S. & Wirtz, L. Raman Spectroscopy of Graphene, *Optical Properties of Graphene*, chap. 3, 85–132 (World Scientific, Singapore, 2017).
- [68] Kohn, W. Image of the Fermi Surface in the Vibration Spectrum of a Metal. *Phys. Rev. Lett.* **2**, 393 (1959).
- [69] Umari, P., Pasquarello, A. & Dal Corso, A. Raman scattering intensities in α -quartz: A first-principles investigation. *Phys. Rev. B* **63**, 094305 (2001).
- [70] Luo, X., Zhao, Y., Zhang, J., Xiong, Q. & Quek, S. Y. Anomalous frequency trends in MoS₂ thin films attributed to surface effects. *Phys. Rev. B* **88**, 075320 (2013).
- [71] Luo, X., Zhao, Y., Zhang, J., Toh, M., Kloc, C., Xiong, Q. & Quek, S. Y. Effects of lower symmetry and dimensionality on Raman spectra in two-dimensional WSe₂. *Phys. Rev. B* **88**, 195313 (2013).

- [72] Froehlicher, G., Lorchat, E., Fernique, F., Chaitanya, J., Molina-Sanchez, A., Wirtz, L. & Berciaud, S. Unified description of the optical phonon modes in N-layer MoTe₂. *Nano Lett.* **15**, 6481–6489 (2015).
- [73] Lazzeri, M. & Mauri, F. First-Principles Calculation of Vibrational Raman Spectra in Large Systems: Signature of Small Rings in Crystalline SiO₂. *Phys. Rev. Lett.* **90**, 036401 (2003).
- [74] Veithen, M., Gonze, X. & Ghosez, P. Nonlinear optical susceptibilities, Raman efficiencies, and electro-optic tensors from first-principles density functional perturbation theory. *Phys. Rev. B* **71**, 125107 (2005).
- [75] Gillet, Y., Giantomassi, M. & Gonze, X. First-principles study of excitonic effects in Raman intensities. *Phys. Rev. B* **88**, 094305 (2013).
- [76] Gillet, Y., Kontur, S., Giantomassi, M., Draxl, C. & Gonze, X. Ab Initio Approach to Second-order Resonant Raman Scattering Including Exciton-Phonon Interaction. *Sci. Rep.* **7**, 7344 (2017).
- [77] Hasdeo, E. H., Nugraha, A. R., Dresselhaus, M. S. & Saito, R. Breit-Wigner-Fano line shapes in Raman spectra of graphene. *Phys. Rev. B* **90**, 245140 (2014).
- [78] Elias, D. C., Gorbachev, R. V., Mayorov, A. S., Morozov, S. V., Zhukov, A. A., Blake, P., Ponomarenko, L. A., Grigorieva, I. V., Novoselov, K. S., Guinea, F. & Geim, A. K. Dirac cones reshaped by interaction effects in suspended graphene. *Nat. Phys.* **7**, 701–704 (2011).
- [79] Sonntag, J., Reichardt, S., Wirtz, L., Beschoten, B., Katsnelson, M. I., Libisch, F. & Stampfer, C. Impact of many-body effects on Landau levels in graphene. *Phys. Rev. Lett.* **120**, 187701 (2018).
- [80] Lehmann, H., Symanzik, K. & Zimmermann, W. Zur Formulierung quantisierter Feldtheorien. *Nuovo Cimento* **1**, 205–225 (1955).
- [81] Chen, C.-F., Park, C.-H., Boudouris, B. W., Horng, J., Geng, B., Girit, C., Zettl, A., Crommie, M. F., Segalman, R. A., Louie, S. G. & Wang, F. Controlling

- inelastic light scattering quantum pathways in graphene. *Nature* **471**, 617–620 (2011).
- [82] Miranda, H. P. C., Reichardt, S., Molina-Sánchez, A. & Wirtz, L. First-principles calculation of Raman intensities in MoS₂ from a perturbative approach. *In preparation* (2018).
- [83] Weinberg, S. *The Quantum Theory of Fields: Volume 1, Foundations* (Cambridge University Press, Cambridge, 2005).
- [84] Jackson, J. D. *Classical electrodynamics* (John Wiley & Sons, New York, 2007).
- [85] Yu, P. Y. & Cardona, M. *Fundamentals of Semiconductors* (Springer, Berlin, 2010).
- [86] Cohen-Tannoudji, C., Diu, B. & Laloe, F. *Quantum Mechanics* (Wiley-VCH, Singapore, 1977).
- [87] Fetter, A. L. & Walecka, J. D. *Quantum Theory of Many-Particle Physics* (McGraw-Hill, New York, 1971).
- [88] Peskin, M. E. & Schroeder, D. V. *An Introduction to Quantum Field Theory* (Westview Press, Boulder, 1995).
- [89] Mahan, G. D. *Many-particle physics* (Springer Science & Business Media, New York, 2000).
- [90] Schwabl, F. *Advanced quantum mechanics* (Springer, Berlin, 2005).
- [91] Stefanucci, G. & Van Leeuwen, R. *Nonequilibrium many-body theory of quantum systems: a modern introduction* (Cambridge University Press, Cambridge, 2013).
- [92] Martin, R. M. *Electronic structure: basic theory and practical methods* (Cambridge university press, Cambridge, 2004).
- [93] Hartree, D. R. The wave mechanics of an atom with a non-Coulomb central field. Part I. Theory and methods. *Math. Proc. Camb. Phil. Soc.* **24**, 89–110 (1928).

- [94] Hartree, D. R. The wave mechanics of an atom with a non-Coulomb central field. Part II. Some results and discussion. *Math. Proc. Camb. Phil. Soc.* **24**, 111–132 (1928).
- [95] Fock, V. Näherungsmethode zur Lösung des quantenmechanischen Mehrkörperproblems. *Z. Phys. A* **61**, 126–148 (1930).
- [96] Slater, J. C. A simplification of the Hartree-Fock method. *Phys. Rev.* **81**, 385 (1951).
- [97] Kohn, W. & Sham, L. J. Self-consistent equations including exchange and correlation effects. *Phys. Rev.* **140**, A1133 (1965).
- [98] Hohenberg, P. & Kohn, W. Inhomogeneous electron gas. *Phys. Rev.* **136**, B864 (1964).
- [99] Levy, M. Universal variational functionals of electron densities, first-order density matrices, and natural spin-orbitals and solution of the v-representability problem. *Proc. Natl. Acad. Sci. U.S.A.* **76**, 6062–6065 (1979).
- [100] Levy, M. Electron densities in search of Hamiltonians. *Phys. Rev. A* **26**, 1200 (1982).
- [101] Kohn, W. Highlights of Condensed Matter Theory. In Bassani, F., Fumi, F. & Tosi, M. P. (eds.) *International School of Physics "Enrico Fermi"*, 1–15 (1985).
- [102] Perdew, J. P. & Zunger, A. Self-interaction correction to density-functional approximations for many-electron systems. *Phys. Rev. B* **23**, 5048 (1981).
- [103] Perdew, J. P. & Wang, Y. Accurate and simple analytic representation of the electron-gas correlation energy. *Phys. Rev. B* **45**, 13244 (1992).
- [104] Perdew, J. P., Burke, K. & Ernzerhof, M. Generalized gradient approximation made simple. *Phys. Rev. Lett.* **77**, 3865 (1996).
- [105] Gross, R. & Marx, A. *Festkörperphysik* (de Gruyter, Oldenburg, 2014).

- [106] Bloch, F. Über die Quantenmechanik der Elektronen in Kristallgittern. *Z. Phys. A* **52**, 555–600 (1929).
- [107] Blase, X., Rubio, A., Louie, S. G. & Cohen, M. L. Quasiparticle band structure of bulk hexagonal boron nitride and related systems. *Phys. Rev. B* **51**, 6868 (1995).
- [108] Hellgren, M., Baima, J., Bianco, R., Calandra, M., Mauri, F. & Wirtz, L. Critical Role of the Exchange Interaction for the Electronic Structure and Charge-Density-Wave Formation in TiSe_2 . *Phys. Rev. Lett.* **119**, 176401 (2017).
- [109] Bechstedt, F. Many-Body Approach to Electronic Excitations (Springer, Berlin, 2016).
- [110] Martin, R. M., Reining, L. & Ceperley, D. M. Interacting Electrons (Cambridge University Press, Cambridge, 2016).
- [111] Martin, P. C. & Schwinger, J. Theory of many-particle systems. I. *Phys. Rev.* **115**, 1342 (1959).
- [112] Dyson, F. J. The S matrix in quantum electrodynamics. *Phys. Rev.* **75**, 1736 (1949).
- [113] Schwinger, J. On the Green's functions of quantized fields. I. *Proc. Natl. Acad. Sci. U.S.A.* **37**, 452–455 (1951).
- [114] Schwinger, J. On the Green's functions of quantized fields. II. *Proc. Natl. Acad. Sci. U.S.A.* **37**, 455–459 (1951).
- [115] Srednicki, M. Quantum field theory (Cambridge University Press, Cambridge, 2007).
- [116] Feynman, R. P. Space-time approach to quantum electrodynamics. *Phys. Rev.* **76**, 769 (1949).
- [117] Hedin, L. New method for calculating the one-particle Green's function with application to the electron-gas problem. *Phys. Rev.* **139**, A796 (1965).

- [118] Salpeter, E. E. & Bethe, H. A. A relativistic equation for bound-state problems. *Phys. Rev.* **84**, 1232 (1951).
- [119] Wick, G. C. Properties of Bethe-Salpeter wave functions. *Phys. Rev.* **96**, 1124 (1954).
- [120] Cutkosky, R. E. Solutions of a Bethe-Salpeter equation. *Phys. Rev.* **96**, 1135 (1954).
- [121] Tamm, I. G. Relativistic interaction of elementary particles. *J. Phys. USSR* **9**, 449 (1945).
- [122] Dancoff, S. M. Non-adiabatic meson theory of nuclear forces. *Phys. Rev.* **78**, 382 (1950).
- [123] Brüesch, P. Phonons: theory and experiments I: lattice dynamics and models of interatomic forces (Springer, Berlin, 1982).
- [124] Brüesch, P. Phonons: theory and experiments II: experiments and interpretation of experimental results (Springer, Berlin, 1986).
- [125] Brüesch, P. Phonons: theory and experiments III: phenomena related to phonons (Springer, Berlin, 1987).
- [126] Born, M. & Oppenheimer, R. Zur Quantentheorie der Molekeln. *Ann. Phys. (Berl.)* **389**, 457–484 (1927).
- [127] Paulatto, L., Mauri, F. & Lazzeri, M. Anharmonic properties from a generalized third-order ab initio approach: Theory and applications to graphite and graphene. *Phys. Rev. B* **87**, 214303 (2013).
- [128] Hellmann, H. Einführung in die Quantenchemie (Franz Deuticke, Vienna, 1937).
- [129] Feynman, R. P. Forces in molecules. *Phys. Rev.* **56**, 340 (1939).
- [130] Baroni, S., De Gironcoli, S., Dal Corso, A. & Giannozzi, P. Phonons and related crystal properties from density-functional perturbation theory. *Rev. Mod. Phys.* **73**, 515 (2001).

- [131] Giustino, F. Electron-phonon interactions from first principles. *Rev. Mod. Phys.* **89**, 015003 (2017).
- [132] Mulliken, R. S. Report on notation for the spectra of polyatomic molecules. *J. Chem. Phys.* **23**, 1997–2011 (1955).
- [133] Pócsik, I., Hundhausen, M., Koós, M. & Ley, L. Origin of the D peak in the Raman spectrum of microcrystalline graphite. *J. Non-Cryst. Solids* **227**, 1083–1086 (1998).
- [134] Tan, P., An, L., Liu, L., Guo, Z., Czerw, R., Carroll, D. L., Ajayan, P. M., Zhang, N. & Guo, H. Probing the phonon dispersion relations of graphite from the double-resonance process of Stokes and anti-Stokes Raman scatterings in multiwalled carbon nanotubes. *Phys. Rev. B* **66**, 245410 (2002).
- [135] Mohr, M., Maultzsch, J., Dobardžić, E., Reich, S., Milošević, I., Damnjanović, M., Bosak, A., Krisch, M. & Thomsen, C. Phonon dispersion of graphite by inelastic x-ray scattering. *Phys. Rev. B* **76**, 035439 (2007).
- [136] Wirtz, L. & Rubio, A. The phonon dispersion of graphite revisited. *Solid State Commun.* **131**, 141–152 (2004).
- [137] Molina-Sánchez, A., Palumbo, M., Marini, A. & Wirtz, L. Temperature-dependent excitonic effects in the optical properties of single-layer MoS₂. *Phys. Rev. B* **93**, 155435 (2016).
- [138] Lehmann, H. Über Eigenschaften von Ausbreitungsfunktionen und Renormierungskonstanten quantisierter Felder. *Nuovo Cimento* **11**, 342–357 (1954).
- [139] Källén, G. On the definition of the renormalization constants in quantum electrodynamics. *Helv. Phys. Acta* **25**, 417–434 (1952).
- [140] Caruso, F., Hoesch, M., Achatz, P., Serrano, J., Krisch, M., Bustarret, E. & Giustino, F. Nonadiabatic Kohn Anomaly in Heavily Boron-Doped Diamond. *Phys. Rev. Lett.* **119**, 017001 (2017).

- [141] Saunders, R. W. & Young, W. Raman scattering: one-phonon final states and many-body effects. *J. Phys. C: Solid State Phys.* **13**, 103 (1980).
- [142] Yang, L., Deslippe, J., Park, C.-H., Cohen, M. L. & Louie, S. G. Excitonic effects on the optical response of graphene and bilayer graphene. *Phys. Rev. Lett.* **103**, 186802 (2009).
- [143] Cançado, L. G., Jorio, A. & Pimenta, M. A. Measuring the absolute Raman cross section of nanographites as a function of laser energy and crystallite size. *Phys. Rev. B* **76**, 064304 (2007).
- [144] Grüneis, A., Attaccalite, C., Wirtz, L., Shiozawa, H., Saito, R., Pichler, T. & Rubio, A. Tight-binding description of the quasiparticle dispersion of graphite and few-layer graphene. *Phys. Rev. B* **78**, 205425 (2008).
- [145] Giannozzi, P., Baroni, S., Bonini, N., Calandra, M., Car, R., Cavazzoni, C., Ceresoli, D., Chiarotti, G. L., Cococcioni, M., Dabo, I., Dal Corso, A., de Gironcoli, S., Fabris, S., Fratesi, G., Gebauer, R., Gerstmann, U., Gougoussis, C., Kokalj, A., Lazzeri, M., Martin-Samos, L., Marzari, N., Mauri, F., Mazzarello, R., Paolini, S., Pasquarello, A., Paulatto, L., Sbraccia, C., Scandolo, S., Sclauzero, G., Seitsonen, A. P., Smogunov, A., Umari, P. & Wentzcovitch, R. M. QUANTUM ESPRESSO: a modular and open-source software project for quantum simulations of materials. *J. Phys. Condens. Matter* **21**, 395502 (2009).
- [146] Marzari, N. & Vanderbilt, D. Maximally localized generalized Wannier functions for composite energy bands. *Phys. Rev. B* **56**, 12847 (1997).
- [147] Souza, I., Marzari, N. & Vanderbilt, D. Maximally localized Wannier functions for entangled energy bands. *Phys. Rev. B* **65**, 035109 (2001).
- [148] Marzari, N., Mostofi, A. A., Yates, J. R., Souza, I. & Vanderbilt, D. Maximally localized Wannier functions: Theory and applications. *Rev. Mod. Phys.* **84**, 1419 (2012).

- [149] Mostofi, A. A., Yates, J. R., Pizzi, G., Lee, Y.-S., Souza, I., Vanderbilt, D. & Marzari, N. An updated version of wannier90: A tool for obtaining maximally-localised Wannier functions. *Comput. Phys. Commun.* **185**, 2309–2310 (2014).
- [150] Giustino, F., Cohen, M. L. & Louie, S. G. Electron-phonon interaction using Wannier functions. *Phys. Rev. B* **76**, 165108 (2007).
- [151] Poncé, S., Margine, E. R., Verdi, C. & Giustino, F. EPW: Electron–phonon coupling, transport and superconducting properties using maximally localized Wannier functions. *Comput. Phys. Commun.* **209**, 116–133 (2016).
- [152] Loudon, R. The Raman effect in crystals. *Adv. Phys.* **13**, 423–482 (1964).
- [153] Miranda, H. P. C. Ab initio approaches to resonant raman spectroscopy of transition metal dichalcogenides. Ph.D. thesis, University of Luxembourg (2017).
- [154] Grzeszczyk, M., Golasa, K., Zinkiewicz, M., Nogajewski, K., Molas, M. R., Potemski, M., Wymolek, A. & Babiński, A. Raman scattering of few-layers MoTe₂. *2D Mater.* **3**, 025010 (2016).
- [155] Song, Q. J., Tan, Q. H., Zhang, X., Wu, J. B., Sheng, B. W., Wan, Y., Wang, X. Q., Dai, L. & Tan, P. H. Physical origin of Davydov splitting and resonant Raman spectroscopy of Davydov components in multilayer MoTe₂. *Phys. Rev. B* **93**, 115409 (2016).
- [156] Chae, J., Jung, S., Young, A. F., Dean, C. R., Wang, L., Gao, Y., Watanabe, K., Taniguchi, T., Hone, J., Shepard, K. L., Kim, P., Zhitenev, N. B. & Stroscio, J. A. Renormalization of the graphene dispersion velocity determined from scanning tunneling spectroscopy. *Phys. Rev. Lett.* **109**, 116802 (2012).
- [157] Castro Neto, A. H., Guinea, F., Peres, N. M. R., Novoselov, K. S. & Geim, A. K. The electronic properties of graphene. *Rev. Mod. Phys.* **81**, 109 (2009).
- [158] Katsnelson, M. I. Graphene: carbon in two dimensions (Cambridge University Press, Cambridge, 2012).

- [159] Reichardt, S. Electron-phonon interaction in graphene and graphene quantum dots. Master's thesis, RWTH Aachen University (2014).
- [160] Wallace, P. R. The band theory of graphite. *Phys. Rev.* **71**, 622 (1947).
- [161] Ando, T. Magnetic oscillation of optical phonon in graphene. *J. Phys. Soc. Jpn.* **76**, 024712 (2007).
- [162] Goerbig, M. O., Fuchs, J.-N., Kechedzhi, K. & Fal'ko, V. I. Filling-factor-dependent magnetophonon resonance in graphene. *Phys. Rev. Lett.* **99**, 087402 (2007).
- [163] Kashuba, O. & Fal'ko, V. I. Role of electronic excitations in magneto-Raman spectra of graphene. *New. J. Phys.* **14**, 105016 (2012).
- [164] Suzuura, H. & Ando, T. Phonons and electron-phonon scattering in carbon nanotubes. *Phys. Rev. B* **65**, 235412 (2002).
- [165] Ishikawa, K. & Ando, T. Optical phonon interacting with electrons in carbon nanotubes. *J. Phys. Soc. Jpn.* **75**, 084713 (2006).
- [166] Landau, L. D. Diamagnetismus der Metalle. *Z. Phys. A* **64**, 629–637 (1930).
- [167] Kühne, M., Faugeras, C., Kossacki, P., Nicolet, A. A. L., Orlita, M., Latyshev, Y. I. & Potemski, M. Polarization-resolved magneto-Raman scattering of graphenelike domains on natural graphite. *Phys. Rev. B* **85**, 195406 (2012).
- [168] Iyengar, A., Wang, J., Fertig, H. & Brey, L. Excitations from filled Landau levels in graphene. *Phys. Rev. B* **75**, 125430 (2007).
- [169] Shizuya, K. Many-body corrections to cyclotron resonance in monolayer and bilayer graphene. *Phys. Rev. B* **81**, 075407 (2010).
- [170] Shizuya, K. Renormalization and cyclotron resonance in bilayer graphene with weak electron-hole asymmetry. *Phys. Rev. B* **84**, 075409 (2011).

- [171] Luican, A., Li, G. & Andrei, E. Y. Quantized Landau level spectrum and its density dependence in graphene. *Phys. Rev. B* **83**, 041405 (2011).
- [172] Yu, G. L., Jalil, R., Belle, B., Mayorov, A. S., Blake, P., Schedin, F., Morozov, S. V., Ponomarenko, L. A., Chiappini, F., Wiedmann, S., Zeitler, U., Katsnelson, M. I., Geim, A. K., Novoselov, K. S. & Elias, D. C. Interaction phenomena in graphene seen through quantum capacitance. *Proc. Natl. Acad. Sci. U.S.A.* **110**, 3282–3286 (2013).
- [173] González, J., Guinea, F. & Vozmediano, M. A. H. Non-Fermi liquid behavior of electrons in the half-filled honeycomb lattice (A renormalization group approach). *Nucl. Phys. B* **424**, 595–618 (1994).
- [174] González, J., Guinea, F. & Vozmediano, M. A. H. Marginal-Fermi-liquid behavior from two-dimensional Coulomb interaction. *Phys. Rev. B* **59**, R2474 (1999).
- [175] Stauber, T., Parida, P., Trushin, M., Ulybyshev, M. V., Boyda, D. L. & Schliemann, J. Interacting Electrons in Graphene: Fermi Velocity Renormalization and Optical Response. *Phys. Rev. Lett.* **118**, 266801 (2017).
- [176] Attaccalite, C., Bockstedte, M., Marini, A., Rubio, A. & Wirtz, L. Coupling of excitons and defect states in boron-nitride nanostructures. *Phys. Rev. B* **83**, 144115 (2011).
- [177] Ju, L., Velasco Jr, J., Huang, E., Kahn, S., Nosiglia, C., Tsai, H.-Z., Yang, W., Taniguchi, T., Watanabe, K., Zhang, Y., Zhang, G., Crommie, M., Zettl, A. & Wang, F. Photoinduced doping in heterostructures of graphene and boron nitride. *Nat. Nanotechnol.* **9**, 348–352 (2014).
- [178] Neumann, C., Rizzi, L., Reichardt, S., Terrés, B., Khodkov, T., Watanabe, K., Taniguchi, T., Beschoten, B. & Stampfer, C. Spatial control of laser-induced doping profiles in graphene on hexagonal boron nitride. *ACS Appl. Mater. Interfaces* **8**, 9377–9383 (2016).

- [179] Bolotin, K. I., Sikes, K., Jiang, Z., Klima, M., Fudenberg, G., Hone, J., Kim, P. & Stormer, H. Ultrahigh electron mobility in suspended graphene. *Solid State Commun.* **146**, 351–355 (2008).
- [180] Chizhova, L. A., Burgdörfer, J. & Libisch, F. Magneto-optical response of graphene: Probing substrate interactions. *Phys. Rev. B* **92**, 125411 (2015).
- [181] Peierls, R. Zur Theorie des Diamagnetismus von Leitungselektronen. *Z. Phys. A* **80**, 763–791 (1933).
- [182] Kohn, W. Theory of Bloch electrons in a magnetic field: the effective Hamiltonian. *Phys. Rev.* **115**, 1460 (1959).
- [183] Blount, E. Bloch electrons in a magnetic field. *Phys. Rev.* **126**, 1636 (1962).

Acknowledgments

First of all I would like to thank my two supervisors, Prof. Ludger Wirtz and Prof. Christoph Stampfer, very much for giving me the opportunity to work on this challenging topic and for giving me the freedom and the trust to pursue the new ideas that now made it into this thesis. I am also very grateful for their continuous support and advice and for many scientific and non-scientific discussions we had over the duration of my time as a PhD Student in their groups.

Secondly, I would like to extend my gratitude to Prof. Thomas Schmidt and Prof. Riccardo Mazzarello for joining my thesis advisory committee, including all the commitments this entailed. Likewise, I would like to thank Prof. Claudia Draxl and Prof. Kristian Thygesen for agreeing to serve as external examiners for my defense.

A big thank you also needs to be extended to my main collaborators:

Firstly, Henrique Pereira Coutada Miranda needs to be mentioned for always being there when help was needed. This includes both invaluable help with computer-related issues as well as countless scientific discussions about all kinds of topics, but also extends beyond the work environment to the private level, for which I am immensely grateful.

The same can be said about Christoph Neumann who initially persuaded me to join Christoph Stampfer's group while I was a Master student and thus in a way sparked my interest in condensed matter physics in the first place. Besides that he has been a trusted and always supportive friend throughout our studies and I am also very grateful for our very fruitful scientific collaboration.

Amongst the other collaborators, I would like to thank Jens Sonntag for many discussions about the physics of Raman scattering and graphene and for our productive

collaboration in the magneto-Raman project. Likewise, I thank Bernd Beschoten for many interesting physics discussions and his always insightful and attentive contributions to the various projects and publications we collaborated on. From Aachen, I would also like to thank Gerard Verbiest, Matthias Goldsche, Tymofiy Khodkov, Donatus Halpaap, and Leo Rizzi, for a very pleasant collaboration. For our collaboration on the magneto-Raman project, but also for various insight-generating physics discussions, I am also indebted to Prof. Florian Libisch. Finally, as far as collaborators go, I thank Alejandro Molina-Sánchez for a productive collaboration on the MoTe₂ project and for contributing to the social life of the group in Luxembourg in a very positive way.

Besides these scientific collaborators, I have been extremely fortunate to be able to work in two institutes with excellent administrative support personnel that allowed me to focus entirely on work with a minimum of distracting administrative things to care about. In that regard, I first of all need to mention Frédérique Bertrand, who, as our group secretary in Luxembourg, did an excellent job at organizing basically everything that was needed with a minimum of involvement of the rest of the group. Similarly, I would like to thank her successor Stéphanie Metry, as well as Yoanna Koleva and Astrid Tobias for their very good administrative support. Likewise, I would like to thank their counterpart in Aachen, Beatrix Dangela, for her help in organizing my extended stay in Aachen and for various other administrative matters.

Besides the above mentioned people, I would also like to extend my thanks to all those who contributed to the overall very pleasant time I had in Luxembourg and in Aachen.

The first one that needs to be mentioned in this context is Fulvio Paleari, with whom I had the pleasure to share the office for over two years and whom I would like to thank for many discussions about physics, movies, and literally everything in-between and of course for the hundreds (thousands?) of cookies we shared. In addition, I would like to express my gratitude for his support during times when things were not looking so bright.

Similarly, I thank the other current and past members of the Luxembourg group,

who contributed to the great atmosphere in our small building: Thomas Galvani for plenty of shared cups of tea and many discussions about mathematics, quantum mechanics, tight-binding models, and the merits of the French and German languages; Engin Torun and Matteo Barborini for the various bits of advice they shared, for providing alternative points of view during various discussions about physics and life, and for taking the time to read some parts of this thesis; Francesco Naccarato and Alexandre Morlet for contributing to the scientific and social life in the group; and Maria Hellgren for sharing the office with me during my first year in Luxembourg and the nice work atmosphere.

From Aachen, I would additionally like to thank my former office mates Jan Dauber and Regine Ockelmann for the great and productive atmosphere there and the latter also for her support during difficult times.

In addition to the above mentioned people, I would like to mention the many other people that enriched my life in both Luxembourg in Aachen in various, mostly social, ways and who, in that way, also contributed to this piece of work. Our Indian internship students: Chaitanya Joshi, Chaitanya Nuthalapati, Ashish Nanda, Suvajit Majumder, and, most of all, Anuj Shetty, Kumar Ayush, and Amal Vats; the various members of Thomas Schmidt's group, who I had the pleasure to share the office floor and many coffee breaks with: Giacomo Dolcetto, Alexia Rod, Patrick Haughian, Solofo Groenendijk, Alessio Calzona, Kristof Moors, Johann Ekström, Hugo Tschirhart, and first and foremost Christopher Pedder, who I would also like to thank for various bits of advice about life and always insightful discussions about physics beyond the boundaries of our work projects; the "people from upstairs": Martin Stoehr, Katerine Saleme Rios, Dmitry Fedorov, Fernaz Heider-Zadeh, Igor Poltavsky, Johannes Hoja, and especially Yasmine Al-Hamdani, Mainak Sadhukhan, and Dennis Barton, for the many teas and coffees we shared as well as for various exchanges of views on life; the "people from downstairs": Marko Mravlak, Mohit Dixit, and Artur Wachtel for various interesting discussions during coffee breaks; and several members of Christoph Stampfer's group in Aachen for the many discussions and their contributions to a productive, inspiring, and nice work atmosphere there, in particular: Alexander Epping, Stephan Engels, Luca Banszerus, Michael Schmitz, and Christian Volk.

Finally, on a more personal note, I am immensely grateful for the friendship of Martin Oellers and Efterpi Kalesaki, who continued to support me in any possible way throughout my time as a PhD Student, irrespective of how they fared themselves.

Last, but most certainly not least, I thank my parents for their continuous, unconditional support and love, both throughout my entire life but especially during the darker periods in Luxembourg. Without them, this thesis and the work it is based on would not exist.